Probing the Progression, Properties, and Progenies of Magnetic Reconnection

Thesis by
Young Dae Yoon

In Partial Fulfillment of the Requirements for the
Degree of
Doctor of Philosophy

CALIFORNIA INSTITUTE OF TECHNOLOGY
Pasadena, California

2020
Defended April 23rd, 2020

Young Dae Yoon
ORCID: 0000-0001-8394-2076

ACKNOWLEDGEMENTS

I must begin by cherishing my roots and thanking my family. My parents' unwavering support, commitment, and wisdom are the pillar and base upon which I am merely standing. I am so proud of my younger brother for all he has accomplished despite the sacrifices he has had to make because of me. I also thank every single one of my relatives for always rooting for me along the way. Without their love and faith amidst all the hardships, I would not have made it this far.

To paraphrase Sir Isaac Newton, if I have seen any bit further, it is by standing on the shoulders of Professor Paul Bellan. He is a brilliant experimentalist as well as an excellent theorist having both breath and depth of knowledge in physics. I admire his accessibility as he always drops whatever he is doing at the time to pay attention to what the students have to say. There is just one time slot when he is not available, and that is 30 minutes before his plasma physics class; I am still amazed by his constant effort in preparing for a class he has been teaching for decades. He is very patient and understanding, but also enthusiastic and motivational. I sincerely feel extremely lucky to have chosen Paul as my advisor.

I would like to thank my candidacy committee—Professors E. Sterl Phinney, Gregg Hallinan, and Kerry Vahala—and my thesis committee—Professors E. Sterl Phinney, Gregg Hallinan, and Marco Velli—for their helpful feedback and insightful questions.

Ryan Marshall and Pakorn (Tung) Wongwaitayakornkul joined the group with me in 2014, and we will all be graduating at the same time. We have made so many fond memories in class, in the lab, at conferences, and at bars. I thank Ryan for keeping the office lively, offsetting my laziness, and having probably the most beers with me at conferences. I thank Tung for all the fun lunch conversations; however, I do NOT thank him for his insane badminton and pool skills.

I have benefited greatly from the senior members of the group. I thank Xiang Zhai, Vernon Chaplin, and Bao Ha for effectively transferring their abundant knowledge and skills to an ignorant first-year student while finishing up their graduate studies. I deeply thank Magnus Haw for being the senior graduate student for the longest time so that I could make use of his "senior aura" that magically fixes everything. I am also greatly indebted to Gunsu Yun, who has helped me so much career-wise by taking my matter into his own hands.

I have greatly enjoyed working with and learning from the post-docs in our group: Kil-Byoung Chai, Amelia Greig, and Byonghoon Seo. In particular, I have greatly benefited from our two Korean post-docs, Kil-Byoung Chai and Byonghoon Seo, whose work ethic, enthusiasm, and knowledge have shaped how I think and what I know. The numerous everyday conversations that we have had over a cup of coffee ("the Korean Coffee Break," as Ryan calls it) have amounted to a big chunk of ideas.

The lab will now be managed by Yi Zhou, Yang Zhang, and André Nicolov, from whom I have also learned a lot. Yi rightfully questions seemingly obvious statements; I tell myself to be more like Yi when I seem to be overlooking important assumptions underlying a problem. Yang and André are also very passionate, intelligent, and diligent. I am happy that the lab is in good hands.

I have never met an administrative hurdle during my time at Caltech, largely thanks to Connie Rodriguez, Christy Jenstad, and Jennifer Blankenship. I especially thank Connie for dealing with all the purchases and travel reports and for furnishing the office with leftover pizza from APh 110.

I also thank Dave Felt for imparting his outstanding electrical engineering wisdom when I was building my RF plasma source.

The Korean society at Caltech has been a big part of my graduate life. There are so many of you to name here, so I will try my best not to leave anyone out. I thank those you who started out graduate life at Caltech with me: Young Joon Choi, Kibeom Kim, Sangjun Lee, Gyu Baek Rah, Jaeyun Moon, Serim Ryou, Sung Won Ahn, Jong Hun Kang, and Hyunjun Cho. I also thank Hyeong Chan Jo, Jeongmin Kim, Sanghyun Yi, Jihong Min, Juhyun Kim, Hyungjoo Row, Jinmo Koo, Jieun Shin for being good friends with me all these years. Special shout-out to the travelling/drinking/dawdling crew Hee Jeong Ahn, Jonghun Lim, Hye Young Shin, Areum Kim, without whom I would have been a lot more productive.

The Wednesday tennis club made tennis my favorite sport, although tennis may have been an excuse to gather people for drinks. I tremendously thank Peter Lee for his leadership, without which the club would not function. I am not sure whether I will ever have a chance to play tennis regularly again, so I will miss the club dearly.

I cannot describe with words my gratitude to the Kim family—Mr. and Mrs. Kim, Wonchan Kim and Robin Kim, who made me feel at home even when I am on the other side of the globe from mine. Thanks for all the delicious food and fun times.

Finally, I would like to thank Ha-Rry for being there with me through all the ups and downs. You have done much more for me than you could ever imagine.

ABSTRACT

Magnetic reconnection is a plasma phenomenon in which opposing magnetic fields annihilate and release their magnetic energy into other forms of energy. In this thesis, various aspects of collisionless magnetic reconnection are studied analytically and numerically, and an experimental diagnostic for magnetic fields in a plasma is described.

The progression of magnetic reconnection is first illustrated through the formulation of a framework that revolves around canonical vorticity flux, which is ideally a conserved quantity. The reconnection instability, electron acceleration, and whistler wave generation are explained in an intuitive manner by analyzing the dynamics of canonical vorticity flux tubes. The validity of the framework is then extended down to first principles by the inclusion of the electron canonical battery effect. The importance of this effect during reconnection determines the overall structure and evolution of the process.

A crucial property of magnetic reconnection is its accompaniment by anomalous ion heating much faster than conventional collisional heating. Stochastic heating is a mechanism in which, under a sufficiently strong electric field, particles undergo chaotic motion in phase space and heat up dramatically. Using the previously established canonical vorticity framework, it is demonstrated that the Hall electric fields that develop during reconnection satisfy the stochastic ion heating criterion and that the ions involved indeed undergo chaotic motion. This mechanism is then kinetically verified via exact analyses and particle simulations and is thus ultimately established as the main ion heating mechanism in magnetic reconnection.

An important progeny of magnetic reconnection is whistler waves. These waves interact with energetic particles and scatter their pitch-angles, triggering losses of magnetic confinement. A previous study demonstrated via exact relativistic analyses that if a particle undergoes a "two-valley" motion, it undergoes drastic changes in its pitch-angle. This analysis is extended to a relativistic thermal distribution of particles. The condition for two-valley motion is first derived; it is then shown that a significant fraction of the particle distribution meets this condition and thus undergoes large pitch-angle scatterings. The scaling of this fraction with the wave amplitude suggests that relativistic microburst events may be explained by the two-valley mechanism. It is also found that the widely-used second-order trapping theory

is an inaccurate approximation of the theory presented.

A new method of probing the magnetic field in a plasma is described and developed to some extent. It utilizes the two-photon Doppler-free laser-induced fluorescence technique, where two counter-propagating laser beams effectively cancel out the Doppler effect and excite electron populations. The fluorescence resulting from the subsequent de-excitation is then measured, enabling the resolution of Zeeman splitting of the spectral lines from which the magnetic field information can be inferred. A high-power, repetitively-pulsed radio-frequency plasma source was developed as the subject of diagnosis, and preliminary results are presented.

PUBLISHED CONTENT AND CONTRIBUTIONS

[1] Young Dae Yoon and Paul M. Bellan. A generalized two-fluid picture of non-driven collisionless reconnection and its relation to whistler waves. *Physics of Plasmas*, 24(5):052114, May 2017. ISSN 1070-664X. doi: 10.1063/1.4982812. URL http://aip.scitation.org/doi/10.1063/1.4982812. Y.D.Y. performed the analytical calculations, built and conducted the numerical simulations, and wrote the manuscript.

[2] Young Dae Yoon and Paul M. Bellan. An intuitive two-fluid picture of spontaneous 2D collisionless magnetic reconnection and whistler wave generation. *Physics of Plasmas*, 25(5):055704, May 2018. ISSN 1070-664X. doi: 10.1063/1.5016345. URL http://aip.scitation.org/doi/10.1063/1.5016345. Y.D.Y. performed the analytical calculations, built and conducted the numerical simulations, and wrote the manuscript.

[3] Young Dae Yoon and Paul M. Bellan. Fast Ion Heating in Transient Collisionless Magnetic Reconnection via an Intrinsic Stochastic Mechanism. *The Astrophysical Journal Letters*, 868(2):L31, Nov 2018. ISSN 2041-8213. doi: 10.3847/2041-8213/aaf0a3. URL http://stacks.iop.org/2041-8205/868/i=2/a=L31?key=crossref.559ad6f22dfdfcdfe3b6e580c7240456. Y.D.Y. performed the analytical calculations, built and conducted the numerical simulations, and wrote the manuscript.

[4] Young Dae Yoon and Paul M Bellan. Kinetic Verification of the Stochastic Ion Heating Mechanism in Collisionless Magnetic Reconnection. *The Astrophysical Journal Letters*, 887(2):L29, Dec 2019. ISSN 2041-8213. doi: 10.3847/2041-8213/ab5b0a. URL https://iopscience.iop.org/article/10.3847/2041-8213/ab5b0a. Y.D.Y. performed the analytical calculations, conducted the numerical simulations, and wrote the manuscript.

[5] Young Dae Yoon and Paul M. Bellan. The electron canonical battery effect in magnetic reconnection: Completion of the electron canonical vorticity framework. *Physics of Plasmas*, 26(10):100702, Oct 2019. ISSN 1070-664X. doi: 10.1063/1.5122225. URL http://aip.scitation.org/doi/10.1063/1.5122225. Y.D.Y. performed the analytical calculations, built and conducted the numerical simulations, and wrote the manuscript.

[6] Young Dae Yoon and Paul M. Bellan. Non-diffusive pitch-angle scattering of a distribution of energetic particles by coherent whistler waves. *Submitted*, 2020. Y.D.Y. performed the analytical calculations, built and conducted the numerical simulations, and wrote the manuscript.

TABLE OF CONTENTS

LIST OF ILLUSTRATIONS

LIST OF TABLES

Chapter 1

INTRODUCTION TO PLASMA PHYSICS

A plasma is often dubbed the "fourth state of matter" and is a mixture of ions, electrons, and possibly neutral atoms. Because the constituents of a plasma mutually interact with one another, a plasma tends to develop collective behavior. Plasma physics is the study of this behavior in various circumstances. The majority of the observable matter in the Universe is in the plasma state, examples of which include stars, planetary nebulae, the Earth's magnetosphere, astrophysical accretion disks and jets, and the interstellar medium. Naturally occurring plasmas on the Earth include lightning and flames, while man-made plasmas are found in fusion-grade experiments, research experiments, semiconductor manufacturing, and so on. In contrast to conventional gas or liquid dynamics which are dominated by inter-particle binary collisions, plasma dynamics are dominated by long-range electric and magnetic fields. The coupling of these fields with fluid effects leads to complex plasma behavior.

Plasma dynamics can be described by four different models, which are — in order of decreasing fundamentality — single-particle theory, Vlasov theory, two-fluid theory, and magneto-hydrodynamics (MHD). Single-particle theory is the most fundamental and follows individual dynamics of all mutually-interacting particles in the plasma and their interaction with electromagnetic fields. Vlasov theory constructs velocity distribution functions from a statistically large number of particles and follows the temporal evolution of these functions. Two-fluid theory treats the plasma as a system of finite-pressure fluids, one for each species. MHD treats the plasma as a single conducting fluid with finite pressure. The most suitable model to use depends on the given situation; the specified plasma regime and the underlying assumptions determine which toolkit is the most appropriate in solving the particular problem.

All four plasma models will be used in pertinent places throughout the thesis. In this chapter, the fundamentals of each model are first presented as a proper introduction and background. Then, an introduction to magnetic reconnection — the main subject of this thesis — will be presented.

1.1 Single-Particle Theory

The equation of motion for a particle with charge q and mass m acted on by electric and magnetic fields $\mathbf{E}$ and $\mathbf{B}$ is given by the Lorentz equation

$$m\frac{d\mathbf{v}}{dt} = q\mathbf{E} + q\mathbf{v}\times\mathbf{B}, \tag{1.1}$$

where $\mathbf{v}$ is the particle velocity. This equation will now be solved iteratively to obtain a hierarchy of slow and fast motions. The derivations will be more detailed than usually necessary in order to highlight the underlying assumptions, the violation of which will be important in Chapter 4. $\mathbf{E}$ and $\mathbf{B}$ are assumed to evolve adiabatically, i.e., slowly change in space and time.

Cyclotron motion

Dividing Eq. 1.1 by $q|\mathbf{B}|$ yields

$$\frac{1}{\omega_c}\frac{d\mathbf{v}}{dt} = \frac{\mathbf{E}}{|\mathbf{B}|} + \mathbf{v}\times\frac{\mathbf{B}}{|\mathbf{B}|}, \tag{1.2}$$

where $\omega_c = q|\mathbf{B}|/m$ is the cyclotron frequency. Assuming $\mathbf{E} = 0$, we have

$$\frac{1}{\omega_c}\frac{d\mathbf{v}_c}{dt} = \mathbf{v}_c\times\frac{\mathbf{B}}{|\mathbf{B}|}, \tag{1.3}$$

which yields the cyclotron motion with velocity $\mathbf{v}_c$ and frequency ω_c.

$\mathbf{E}\times\mathbf{B}$ drift

Let us now define $\mathbf{v}_E$ to be a steady drift on top of $\mathbf{v}_c$ so that $|d\mathbf{v}_E/dt| \ll |d\mathbf{v}_c/dt|$. Writing $\mathbf{v} = \mathbf{v}_c + \mathbf{v}_E$ and using $|d\mathbf{v}_E/dt| \ll |d\mathbf{v}_c/dt|$, Equation 1.2 now becomes

$$\frac{1}{\omega_c}\frac{d\mathbf{v}_c}{dt} = \frac{\mathbf{E}}{|\mathbf{B}|} + (\mathbf{v}_c + \mathbf{v}_E)\times\frac{\mathbf{B}}{|\mathbf{B}|}. \tag{1.4}$$

Using Eq. 1.3, this becomes

$$\mathbf{E} + \mathbf{v}_E\times\mathbf{B} = 0, \tag{1.5}$$

and the solution is

$$\mathbf{v}_E = \frac{\mathbf{E}_\perp\times\mathbf{B}}{B^2}, \tag{1.6}$$

where $\mathbf{E}_\perp$ is the electric field perpendicular to $\mathbf{B}$. This steady drift is called the $\mathbf{E}\times\mathbf{B}$ *drift*.

Polarization drift

Next, let us define $\mathbf{v}_p$ to be the next-order correction to $\mathbf{v}_E$ so that $|d\mathbf{v}_p/dt| \ll |d\mathbf{v}_E/dt|$. After writing $\mathbf{v} = \mathbf{v}_c + \mathbf{v}_E + \mathbf{v}_p$ and averaging out the cyclotron motion, Eq. 1.2 becomes

$$\frac{1}{\omega_c}\frac{d\left(\mathbf{v}_E + \mathbf{v}_p\right)}{dt} = \frac{\mathbf{E}}{|\mathbf{B}|} + \left(\mathbf{v}_E + \mathbf{v}_p\right) \times \frac{\mathbf{B}}{|\mathbf{B}|}. \tag{1.7}$$

Using the assumption $|d\mathbf{v}_p/dt| \ll |d\mathbf{v}_E/dt|$ and Eq. 1.5, we have

$$\frac{1}{\omega_c}\frac{d\mathbf{v}_E}{dt} = \mathbf{v}_p \times \frac{\mathbf{B}}{|\mathbf{B}|}, \tag{1.8}$$

for which the solution is

$$\mathbf{v}_p = \frac{m}{qB^2}\frac{d\mathbf{E}_\perp}{dt}. \tag{1.9}$$

This drift is called the polarization drift.

μ conservation

The motion of the particle after averaging out the cyclotron motion is called *guiding-center motion*. In the frame of reference moving with the guiding-center velocity $\mathbf{v}_{gc} = \mathbf{v}_E + \mathbf{v}_p$, the magnetic moment

$$\mu = \frac{mv_c^2}{2B} \tag{1.10}$$

is a conserved quantity.

Breakdown of Hierarchy

The drift solutions presented here rely on a delicate set of assumptions which, if violated, lead to non-adiabatic particle behavior. In fact, it will be shown in detail in Chapter 4 that if the drift hierarchy breaks down, chaotic behavior arises. In this case, a fast, strong heating of associated particles occurs.

1.2 Vlasov Theory

Let us now consider the dynamics of a statistically large number of particles. The instantaneous particle density in phase space is called *the distribution function* and is denoted $f(\mathbf{x}, \mathbf{v}, t)$. Conservation of the number of particles signifies that the rate of change of f must equal the flux of f in and out of the phase space volume. Consideration of this fact yields the *Vlasov equation* [11]:

$$\frac{\partial f}{\partial t} + \mathbf{v} \cdot \frac{\partial f}{\partial \mathbf{x}} + \frac{\partial}{\partial \mathbf{v}} \cdot (\mathbf{a} f) = 0, \tag{1.11}$$

where $\mathbf{a}(\mathbf{x}, \mathbf{v}, t)$ is the particle acceleration.

Charged particles are subject to the Lorentz force, i.e.,

$$\mathbf{a}_L = \frac{q}{m}(\mathbf{E} + \mathbf{v} \times \mathbf{B}). \tag{1.12}$$

Although $\mathbf{a}_L$ is a function of $\mathbf{v}$, $\mathbf{a}_L$ commutes with the velocity derivative because $(\mathbf{v} \times \mathbf{B})_i = v_j B_k - v_k B_i$ does not depend on v_i. Therefore, Eq. 1.11 becomes

$$\frac{\partial f}{\partial t} + \mathbf{v} \cdot \frac{\partial f}{\partial \mathbf{x}} + \frac{q}{m}(\mathbf{E} + \mathbf{v} \times \mathbf{B}) \cdot \frac{\partial f}{\partial \mathbf{v}} = 0, \tag{1.13}$$

which, together with Maxwell's equations, is called the *Vlasov-Maxwell system of equations*.

1.3 Two-Fluid Theory

Because $\mathbf{x}$ and $\mathbf{v}$ are independent quantities in phase space, Eq. 1.11 can be expressed as

$$\frac{\partial f}{\partial t} + \frac{\partial}{\partial \mathbf{x}} \cdot (\mathbf{v} f) + \frac{\partial}{\partial \mathbf{v}} \cdot (\mathbf{a} f) = 0. \tag{1.14}$$

By taking moments of Eq. 1.14, fluid equations can now be obtained.

Continuity Equation

Since f is the instantaneous density in phase-space, taking its zeroth moment yields the instantaneous spatial density, i.e.,

$$n(\mathbf{x}, t) = \int f d^3\mathbf{v}. \tag{1.15}$$

Taking the first moment yields the mean fluid velocity:

$$\mathbf{u}(\mathbf{x}, t) = \frac{\int \mathbf{v} f d^3\mathbf{v}}{n(\mathbf{x}, t)}. \tag{1.16}$$

Also, by Gauss's Law,

$$\int \frac{\partial}{\partial \mathbf{v}} \cdot (\mathbf{a} f)\, d^3\mathbf{v} = \int \mathbf{a} f\, d\mathbf{s}_\mathbf{v}, \tag{1.17}$$

where $\mathbf{s}_\mathbf{v}$ is the surface vector at $\mathbf{v} \to \infty$. Because the distribution function must vanish at $\mathbf{v} \to \infty$ (i.e., $f(\mathbf{v} \to \infty) = 0$), this is equal to zero.

Integrating Eq. 1.14 in three-dimensional velocity space, i.e., taking the zeroth moment and recalling that $\mathbf{x}$, $\mathbf{v}$, and t are independent variables thus yield the *continuity equation*

$$\frac{\partial n_\sigma}{\partial t} + \frac{\partial}{\partial \mathbf{x}_\sigma} \cdot (n_\sigma \mathbf{u}_\sigma) = 0, \tag{1.18}$$

where the subscript σ represents each species, e.g., $\sigma = i, e$ respectively for ions and electrons.

Fluid Equation of Motion

Let us now write velocity $\mathbf{v}$ is the sum of its mean value and its random part so that $\mathbf{v} = \mathbf{u} + \mathbf{v}'$ and define the *pressure tensor*

$$\overleftrightarrow{\mathbf{p}} = m \int \mathbf{v}'\mathbf{v}' f d^3\mathbf{v}'. \tag{1.19}$$

Here $d^3\mathbf{v} = d^3\mathbf{v}'$ and $\int \mathbf{v}' f d^3\mathbf{v}' = 0$ because the mean value of the random part is zero. Then, taking the first moment of Eq. 1.13 and integrating the third term by parts yield the *fluid equation of motion*

$$n_\sigma m_\sigma \frac{D\mathbf{u}_\sigma}{Dt} = n_\sigma q_\sigma \left(\mathbf{E} + \mathbf{u}_\sigma \times \mathbf{B}\right) - \nabla \cdot \overleftrightarrow{\mathbf{p}}_\sigma, \tag{1.20}$$

where

$$\frac{D}{Dt} = \frac{\partial}{\partial t} + \mathbf{u}_\sigma \cdot \nabla \tag{1.21}$$

is the *convective derivative*.

Equations 1.18 and 1.20 for ions and electrons constitute the system of *two-fluid equations*.

1.4 Magneto-Hydrodynamics (MHD)

Equation 1.20 yields two equations involving $\mathbf{u}_i$ and $\mathbf{u}_e$ for ions and electrons, respectively. Magneto-hydrodynamics (MHD) involves two new variables which are linear combinations of $\mathbf{u}_i$ and $\mathbf{u}_e$. These are the current density

$$\mathbf{J} = \sum_\sigma n_\sigma q_\sigma \mathbf{u}_\sigma, \tag{1.22}$$

and the center-of-mass velocity

$$\mathbf{U} = \frac{1}{\rho} \sum_\sigma m_\sigma n_\sigma \mathbf{u}_\sigma, \tag{1.23}$$

where

$$\rho = \sum_\sigma m_\sigma n_\sigma \tag{1.24}$$

is the mass density. Writing particle velocity $\mathbf{v}$ as a sum of the center-of-mass velocity and a random part, i.e., $\mathbf{v} = \mathbf{U} + \mathbf{v}'$, the MHD pressure tensor is defined as

$$\overleftrightarrow{\mathbf{P}}_{\mathrm{MHD}} = \sum_\sigma m_\sigma \int \mathbf{v}'\mathbf{v}' f_\sigma d^3\mathbf{v}'. \tag{1.25}$$

Multiplying Eq. 1.13 by m_σ, taking its zeroth and first moment and summing over all species, we obtain respectively the MHD continuity equation

$$\frac{\partial \rho}{\partial t} + \nabla \cdot (\rho \mathbf{U}) = 0, \tag{1.26}$$

and the MHD equation of motion

$$\rho \left(\frac{\partial \mathbf{U}}{\partial t} + \mathbf{U} \cdot \nabla \mathbf{U} \right) = \mathbf{J} \times \mathbf{B} - \nabla \cdot \overleftrightarrow{\mathbf{P}}_{\mathrm{MHD}}. \tag{1.27}$$

These equations, together with Maxwell's equations,

$$\nabla \cdot \mathbf{E} = \frac{\rho_c}{\epsilon_0}, \tag{1.28}$$

$$\nabla \cdot \mathbf{B} = 0, \tag{1.29}$$

$$\nabla \times \mathbf{E} = -\frac{\partial \mathbf{B}}{\partial t}, \tag{1.30}$$

$$\nabla \times \mathbf{B} = \mu_0 \mathbf{J}, \tag{1.31}$$

constitute the set of MHD equations. Note that the pre-Maxwell form of Ampère's law was used because MHD usually deals with phenomena with characteristic velocities much slower than the light speed, so the displacement current can be ignored. Unless specified otherwise, this form of Ampère's law will be used throughout the thesis.

It can be seen from Eq. 1.27 that MHD plasma motion is determined by two forces: the magnetic force $\mathbf{J} \times \mathbf{B}$ and the hydrodynamic force $\nabla \cdot \overleftrightarrow{\mathbf{P}}_{\mathrm{MHD}}$. Since Ampère's law gives $\mathbf{J} = \nabla \times \mathbf{B}/\mu_0$, we can define *plasma beta* as

$$\beta = \frac{P}{B^2/2\mu_0} \sim \frac{\nabla \cdot \overleftrightarrow{\mathbf{P}}}{\mathbf{J} \times \mathbf{B}}. \tag{1.32}$$

As long as the scale length of the two forces are comparable, β measures the ratio of the hydrodynamic force to the magnetic force. Low-β plasmas are therefore dominated by magnetic forces and vice versa.

Generalized Ohm's Law

Dividing the electron fluid equation by $n_e q_e = -ne$ and rearranging give

$$\mathbf{E} + \mathbf{u}_e \times \mathbf{B} = -\frac{m_e}{e} \frac{D\mathbf{u}_e}{Dt} - \frac{\nabla \cdot \overleftrightarrow{\mathbf{p}}_e}{ne}. \tag{1.33}$$

Since $\mathbf{u}_e = \mathbf{u}_i - \mathbf{J}/n_e e$ and $\mathbf{u}_i \simeq \mathbf{U}$ due to the much heavier ion mass, Eq. 1.33 becomes the *generalized Ohm's law*

$$\mathbf{E} + \mathbf{U} \times \mathbf{B} = \frac{\mathbf{J} \times \mathbf{B}}{ne} - \frac{m_e}{e} \frac{D\mathbf{u}_e}{Dt} - \frac{\nabla \cdot \overleftrightarrow{\mathbf{p}}_e}{ne} + \eta \mathbf{J}, \tag{1.34}$$

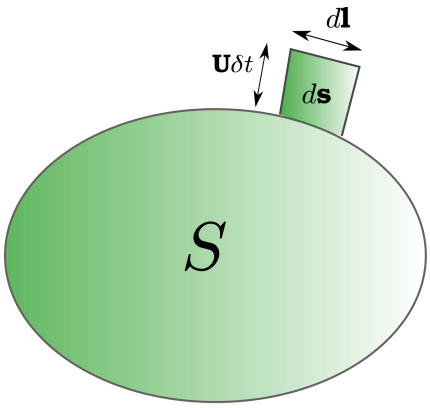

Figure 1.1: Incremental change in surface area due to a displacement $\mathbf{U}\delta t$ of a line segment $d\mathbf{l}$.

where $\eta\mathbf{J}$ is introduced to represent resistive effects due to collisions. The terms on the right-hand side are respectively called the Hall term, the electron inertia term, the pressure term, and the resistive term. The roles these terms play in plasma dynamics will become apparent in Chapters 2 and 3.

Ideal Ohm's Law and Frozen-in Flux

If the right-hand side of Eq. 1.34 is neglected, then we obtain the *ideal Ohm's law*

$$\mathbf{E} + \mathbf{U} \times \mathbf{B} = 0. \tag{1.35}$$

In regimes where this equation is valid — typically involving very slow time scales and very large spatial scales — the plasma acts as a perfectly conducting fluid and is thus said to be *ideal*. Taking the curl of Eq. 1.35 and using Faraday's law $\nabla \times \mathbf{E} = -\partial\mathbf{B}/\partial t$ yield the *plasma induction equation*

$$\frac{\partial \mathbf{B}}{\partial t} = \nabla \times (\mathbf{U} \times \mathbf{B}) \,. \tag{1.36}$$

The induction equation signifies an important aspect of ideal MHD, namely that *magnetic flux through any surface moving with the plasma is conserved*. To prove this property, we define the magnetic flux through a moving surface $S(t)$ bounded by $C(t)$ as

$$\Phi_B = \int_S \mathbf{B} \cdot d\mathbf{s}. \tag{1.37}$$

The rate of change of Φ_B is determined by that of $\mathbf{B}$ and that of S. The former is simply $\partial\mathbf{B}/\partial t$. The latter can be found by noting that the incremental change in surface area due to a displacement $\mathbf{U}\delta t$ of a line segment $d\mathbf{l}$ of the bounding contour

C is $\mathbf{U}\delta t \times d\mathbf{l}$ (illustrated in Fig. 1.1). Therefore, the rate of change of S is $\mathbf{U} \times d\mathbf{l}$, and

$$\frac{d\Phi_B}{dt} = \int_S \frac{\partial \mathbf{B}}{\partial t} \cdot d\mathbf{s} + \int_C \mathbf{B} \cdot \mathbf{U} \times d\mathbf{l}, \tag{1.38}$$

$$= \int_S \frac{\partial \mathbf{B}}{\partial t} \cdot d\mathbf{s} + \int_C \mathbf{B} \times \mathbf{U} \cdot d\mathbf{l}, \tag{1.39}$$

$$= \int_S \left[\frac{\partial \mathbf{B}}{\partial t} + \nabla \times (\mathbf{B} \times \mathbf{U}) \right] \cdot d\mathbf{s}. \tag{1.40}$$

It can be seen that if Eq. 1.36 is true, then $d\Phi_B/dt = 0$. This property of ideal MHD is called the *frozen-in flux* phenomenon.

Magnetic Flux Tubes

The concept of frozen-in flux in ideal MHD equivalently means that magnetic fields lines are frozen into the plasma. By connecting a continuous sequence of surfaces, a tube-like structure can be constructed. If magnetic field lines penetrate this structure, it is called a *magnetic flux tube*. Figure 1.2 shows a sketch of two deforming magnetic flux tubes. The frozen-in field lines move with the tubes as they deform.

It should be noted that magnetic flux tubes are flux tubes associated with the magnetic field $\mathbf{B}$, and that these are not the only kind of flux tubes. In fact, it will be shown in Chapter 2 that we can also define flux tubes associated with a quantity called the canonical vorticity $\mathbf{Q}$ and that these $\mathbf{Q}$ flux tubes have similar but separate dynamics from those of magnetic flux tubes.

Magnetic Helicity

Magnetic helicity is an important concept in MHD and is defined as

$$K = \int_V \mathbf{A} \cdot \mathbf{B} d^3\mathbf{r}, \tag{1.41}$$

where $\mathbf{A}$ is the vector potential associated with the magnetic field $\mathbf{B}$ and V is the plasma volume. This quantity measures the linkage and twist of magnetic flux tubes. Although $\mathbf{A}$ is undefined with respect to a gauge, K turns out to be gauge-independent if magnetic field lines do not penetrate the boundary of the volume.

Magnetic helicity is a conserved quantity in ideal MHD. To prove this, consider the

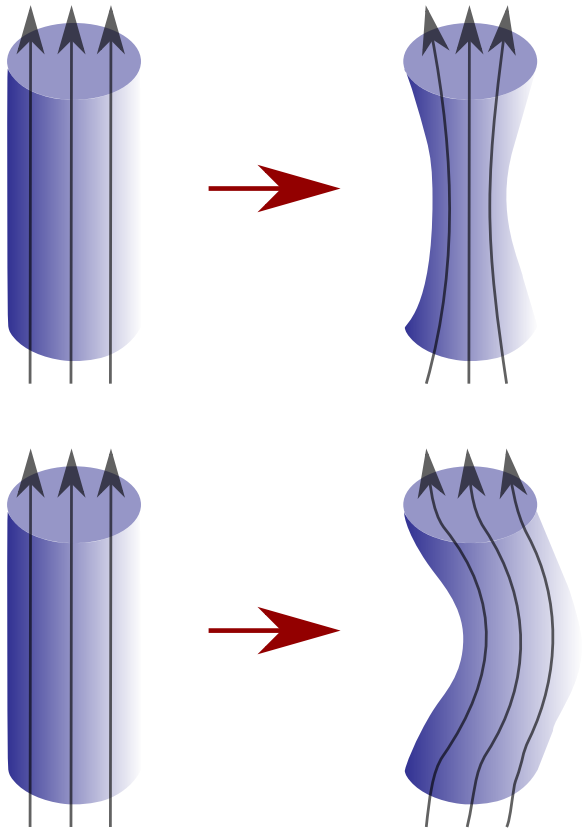

Figure 1.2: Frozen-in magnetic field lines within deforming magnetic flux tubes.

time evolution of the helicity density $\kappa = \mathbf{A} \cdot \mathbf{B}$

$$\frac{\partial \kappa}{\partial t} = \frac{\partial \mathbf{A}}{\partial t} \cdot \mathbf{B} + \mathbf{A} \cdot \frac{\partial \mathbf{B}}{\partial t}, \tag{1.42}$$

$$= -(\mathbf{E} + \nabla\phi) \cdot \mathbf{B} - \mathbf{A} \cdot (\nabla \times \mathbf{E}), \tag{1.43}$$

$$= -2\mathbf{E} \cdot \mathbf{B} - \nabla \cdot (\phi\mathbf{B} + \mathbf{E} \times \mathbf{A}). \tag{1.44}$$

Dotting ideal Ohm's law (Eq. 1.35) with $\mathbf{B}$ shows that $\mathbf{E} \cdot \mathbf{B} = 0$. Integrating Eq. 1.44 over the entire volume, we obtain the helicity conservation equation

$$\frac{\partial K}{\partial t} + \int d\mathbf{s} \cdot (\phi\mathbf{B} + \mathbf{E} \times \mathbf{A}) = 0, \tag{1.45}$$

where $\int d\mathbf{s}$ is the closed surface integral over the enclosed volume. Assuming that the magnetic field and the plasma flow do not penetrate the volume, i.e., $\mathbf{B}$ and $\mathbf{U}$ are tangential to the boundary at the boundary, $\mathbf{E} = -\mathbf{U} \times \mathbf{B}$ is purely perpendicular to the boundary (i.e., $\mathbf{E} \parallel d\mathbf{s}$, so $d\mathbf{s} \cdot (\mathbf{E} \times \mathbf{A}) = 0$). Thus, the surface integral in Eq. 1.45 vanishes and

$$K = const., \tag{1.46}$$

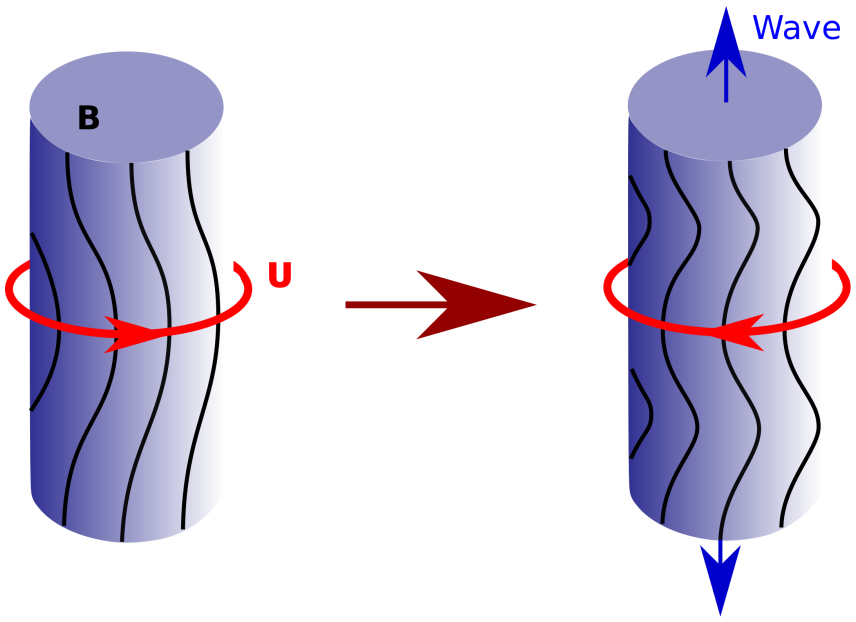

Figure 1.3: A graphical description of a torsional Alfvén wave.

so the total magnetic helicity is conserved for an ideal plasma.

Alfvén Wave

The normal mode of ideal MHD is called the Alfvén wave [3], and there are two modes of this wave: the compressional mode and the shear mode. The former involves compressions and rarefactions of the magnetic field and the latter involves transverse perturbations to the magnetic field. Both modes travel with the Aflvén velocity

$$v_A = \frac{B}{\sqrt{\mu_0 \rho}}, \tag{1.47}$$

where B is the magnetic field strength and ρ is the plasma mass density.

A particular mode of Alfvén waves is called a "torsional Alfvén wave," which is a class of shear Alfvén waves. A graphical description is shown in Fig. 1.3. An azimuthal source (red circle) twists the magnetic field lines (black lines) within a magnetic flux tube, and this twist propagates away from the source as torsional Alfvén waves. This twist mechanism will be an analogy to the generation mechanism of another wave named "whistler waves" in Section 2.5.

1.5 Magnetic Reconnection

Magnetic reconnection is a plasma process in which opposing magnetic field lines come together, annihilate, reconnect, and release their stored magnetic potential

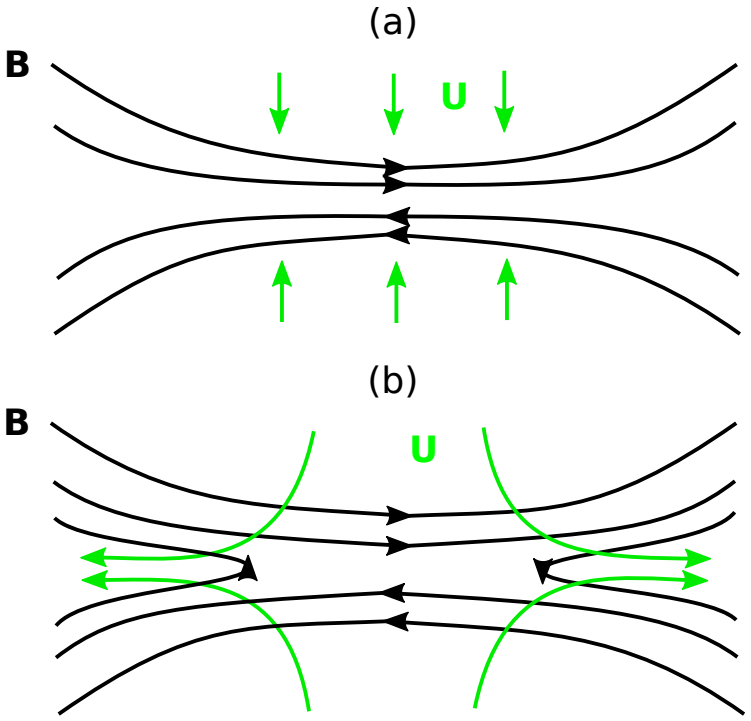

Figure 1.4: (a) Non-reconnecting magnetic field lines (black) and stagnating flows (green). (b) Reconnecting magnetic field lines and plasma inflow/outflow.

energy as other forms of energy, such as kinetic, thermal, and/or wave energies [165]. This process is observed in a variety of space and astrophysical situations — solar flares, coronal mass ejections, the Earth's magnetopause and magnetotail, etc [40, 53, 86, 124]. It is also frequent in laboratory plasmas, such as tokamaks, spheromaks, and reversed-field pinches [13, 29, 109, 161, 163]. Magnetic reconnection is almost always accompanied by strong ion and electron acceleration and heating, as evidenced by ion jets [85], abnormally high ion temperatures [74], and extreme-ultraviolet and X-ray emissions [29, 105]. Since reconnection acts to lower the magnetic energy in a plasma while nearly preserving magnetic helicity, it is an important part of relaxation processes that lead to equilibrium plasma states with minimum magnetic energy [147].

In ideal MHD, magnetic field lines are frozen into the plasma. Therefore, opposing field lines cannot annihilate or break because two counter-propagating plasma flows stagnate at some point in the middle. This can be seen graphically in Fig. 1.4a, where opposing magnetic field lines (black) pile up at the center due to stagnating plasma inflows (green). Thus, magnetic reconnection is forbidden in ideal MHD due to the ideal Ohm's law (Eq. 1.35) and can only happen if the frozen-in condition

is violated.

Sweet-Parker Reconnection

One means of breaking the frozen-in condition is finite resistivity. If only the resistive term in Eq. 1.34 is kept, we have the *resistive Ohm's law*

$$\mathbf{E} + \mathbf{U} \times \mathbf{B} = \eta \mathbf{J}. \tag{1.48}$$

The mechanism by which the resistive term allows for reconnection becomes clear after taking the curl of the above equation, using Faraday's law to eliminate the electric field, and rearranging:

$$\frac{\partial \mathbf{B}}{\partial t} = \nabla \times (\mathbf{U} \times \mathbf{B}) + \frac{\eta}{\mu_0} \nabla^2 \mathbf{B}, \tag{1.49}$$

where Ampère's law was used so $\nabla \times \mathbf{J} = \mu_0^{-1} \nabla \times (\nabla \times \mathbf{B}) = \mu_0^{-1} \nabla (\nabla \cdot \mathbf{B}) - \mu_0^{-1} \nabla^2 \mathbf{B} = -\mu_0^{-1} \nabla^2 \mathbf{B}$. The first term on the right-hand side portrays the frozen-in condition. The second term, on the other hand, is a diffusion-like term with the diffusion coefficient η/μ_0. Therefore, finite resistivity allows for magnetic field diffusion across plasma and thus magnetic reconnection as shown in Fig. 1.4b.

Using this picture, Sweet and Parker [119] made quantitative predictions of the reconnection rate, i.e., how fast the magnetic field lines reconnect. However, the theory predicted reconnection rates that were far slower than what had been observed. For example, magnetic field diffusion predicted the time scale of solar coronal eruptions to be months to years, whereas the actual observed time scale is minutes to hours. As enticing as this theory is, it does not accurately describe what is actually happening in most physical situations.

Fast Collisionless Reconnection

Since resistivity is not a fast enough source for magnetic reconnection, one must look to other terms in Eq. 1.34,

$$\mathbf{E} + \mathbf{U} \times \mathbf{B} = \frac{\mathbf{J} \times \mathbf{B}}{ne} - \frac{m_e}{e} \frac{D\mathbf{u}_e}{Dt}, \tag{1.50}$$

where only the Hall term and the electron inertia term are kept, and a low-β plasma is assumed so the pressure term is dropped. Let us now investigate the conditions for which the non-ideal terms on the right-hand side become important.

First, the Hall term will be compared with the $\mathbf{U} \times \mathbf{B}$ term. Assuming $\mathbf{U}$ is of the order of the Alfvén velocity $v_A = B/\sqrt{\mu_0 \rho} \simeq B/\sqrt{\mu_0 n m_i}$ and using $\mathbf{J} \sim B/\mu_0 L$

where L is the length scale of the magnetic field, the following comparison applies:

$$\mathbf{U}\times\mathbf{B} : \frac{\mathbf{J}\times\mathbf{B}}{ne}, \tag{1.51}$$

$$\frac{B^2}{\sqrt{\mu_0 n m_i}} : \frac{B^2}{\mu_0 n e L}, \tag{1.52}$$

$$L : \sqrt{\frac{m_i}{\mu_0 n e^2}}, \tag{1.53}$$

$$L : d_i, \tag{1.54}$$

where $d_i = c/\sqrt{ne^2/m_i\epsilon_0} = c/\omega_{pi}$ is the ion collisionless skin depth. Therefore, if the length scale of the magnetic field becomes comparable to the ion skin depth, i.e., $L \sim d_i$, the Hall term becomes important. Note that if $L \ll d_i$, then the Hall term dominates, so the ions can be assumed to be stationary because $|\mathbf{u}_i| \simeq |\mathbf{U}| \ll |\mathbf{J}/ne|$.

Second, the electron inertia term will be compared with the Hall term. Since electrons are much lighter than ions, they carry most of the current, so $\mathbf{u}_e \simeq -\mathbf{J}/ne \sim B/\mu_0 neL$. Considering the time-dependent part of the inertia term, writing $\partial/\partial t \sim \omega$,

$$\frac{\mathbf{J}\times\mathbf{B}}{ne} : \frac{m_e}{e}\frac{\partial \mathbf{u}_e}{\partial t}, \tag{1.55}$$

$$\frac{B^2}{\mu_0 neL} : \frac{m_e}{e}\frac{\omega B}{\mu_0 neL}, \tag{1.56}$$

$$\omega_{ce} : \omega, \tag{1.57}$$

where $\omega_{ce} = eB/m_e$ is the electron cyclotron frequency. Now considering the time-independent part of the inertia term,

$$\frac{\mathbf{J}\times\mathbf{B}}{ne} : \frac{m_e}{e}\mathbf{u}_e\cdot\nabla\mathbf{u}_e, \tag{1.58}$$

$$\frac{B^2}{\mu_0 neL} : \frac{m_e}{e}\frac{B^2}{\mu_0^2 n^2 e^2 L^3}, \tag{1.59}$$

$$L^2 : \frac{m_e}{\mu_0 n e^2}, \tag{1.60}$$

$$L^2 : d_e^2, \tag{1.61}$$

where $d_e = c/\sqrt{ne^2/m_e\epsilon_0} = c/\omega_{pe}$ is the electron collisionless skin depth. Thus, the electron inertia term becomes as important as the Hall term if $\omega \sim \omega_{ce}$ and/or $L \sim d_e$. Reconnection phenomena mostly involve $\omega \ll \omega_{ce}$, so we conclude that *the Hall term is important at d_i length scales and the electron inertia term is important at d_e length scales*. Thus, at length scales comparable to or smaller

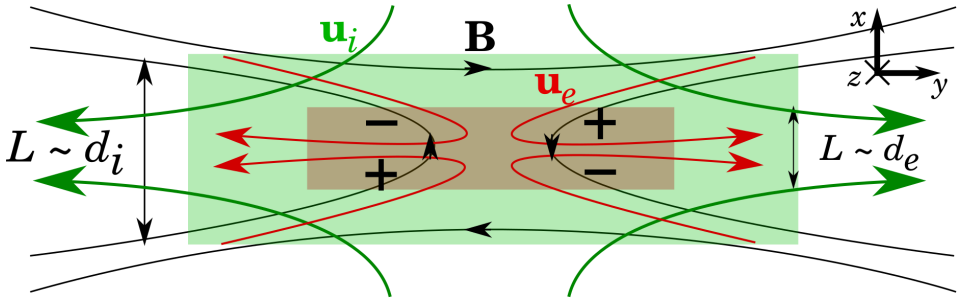

Figure 1.5: Fast reconnection geometry.

than d_i, fast, collisionless magnetic reconnection consistent with observations may occur. Henceforth, the term "magnetic reconnection" will be used interchangeably with "fast reconnection" and/or "collisionless reconnection."

A graphical description of fast reconnection is shown in Fig. 1.5. The inset shows the set of coordinates that will be used throughout the analysis. The initial opposing magnetic field lines are in the y-direction and the reconnected fields are in the x-direction. The particle inflow is mainly in the x-direction and the outflow is mainly in the y-direction. The z-direction represents the out-of-plane components. Since the Hall term signifies the difference between ion and electron flows and becomes important at $L \sim d_i$, ions "unfreeze" from the magnetic field below these scales and flow outwards (green arrows). Electrons, on the other hand, are still frozen to the magnetic field down to $L \sim d_e$. Only below these scales can the magnetic fields reconnect and the electrons flow outwards (red arrows). The particular shape of the electron flow creates quadrupole out-of-plane magnetic fields (plus and minus), which are characteristic of fast reconnection. The origin of these fields as well as other facets of reconnection will be explained more intuitively in Chapter 2.

The question of how the macroscopic system couples to the microscopic scales required for collisionless reconnection naturally arises. There are various ways this could be achieved, and some examples include the kink-induced Rayleigh-Taylor instability [109], the sausage-to-kink instability [136], ideal tearing instability [148], and plasmoid/fractal instabilities [99, 138].

Figure 1.5 represents two directly opposing magnetic fields. If a background out-of-plane magnetic field exists, this is called the *guide field*. Effects due to the guide field as well as finite electron pressure will be discussed in Chapter 3.

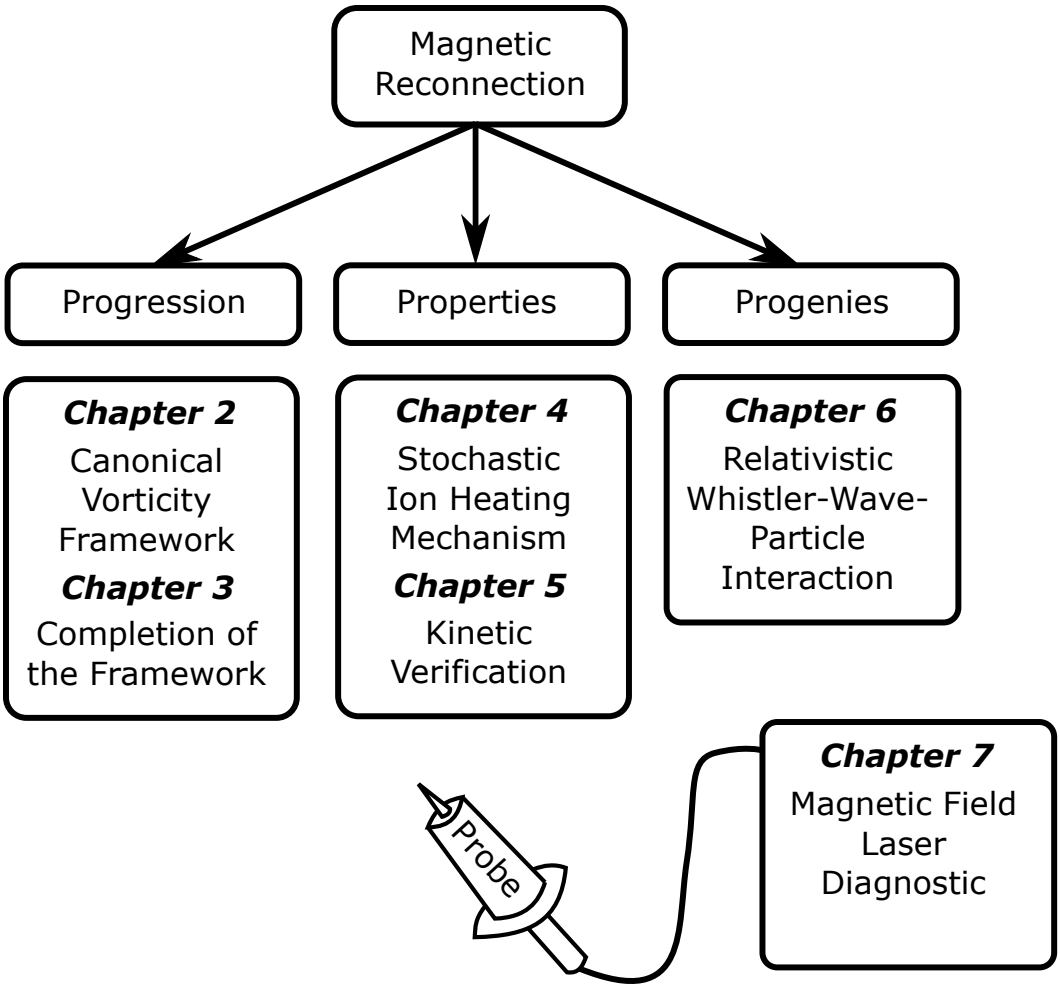

Figure 1.6: Thesis outline.

1.6 Thesis Outline

Figure 1.6 shows the outline of this thesis. The progression of magnetic reconnection will be studied in Chapters 2 and 3. In Chapter 2, the *canonical vorticity* framework will be constructed and collisionless magnetic reconnection will be described using this framework in an intuitive manner. In Chapter 3, the framework will be extended to kinetic regimes by the introduction of the *canonical battery* term.

A crucial property of magnetic reconnection, namely its accompaniment by anomalous, extreme ion heating, will be studied in Chapters 4 and 5. In Chapter 4, the canonical vorticity framework will be used to establish the existence and importance of the *stochastic ion heating* mechanism in collisionless reconnection. In Chapter 5, this mechanism will be analytically and numerically verified to be the main ion heating mechanism up to moderate guide fields.

An important progeny of collisionless reconnection is *whistler waves*, and their generation mechanism will be discussed in Chapter 2. In Chapter 6, the interaction between whistler waves and relativistic particles will be studied in detail. In particular, how coherent waves significantly scatter the pitch-angle of relativistic particles will be illustrated.

A new method of probing magnetic fields is described in Chapter 7. This method uses two laser beams to excite the electron population in a plasma while suppressing thermal broadening effects in order to resolve the magnetic field information.

Chapter 2

CANONICAL VORTICITY FRAMEWORK OF MAGNETIC RECONNECTION: AN INTUITIVE DESCRIPTION

As shown in Section 1.5, collisionless magnetic reconnection is an extremely complicated process involving different length scales and multiple spatial dimensions. In this Chapter, a relatively intuitive description of collisionless reconnection will be given. This is achieved by considering the dynamics of a quantity called the canonical vorticity, which is a combination of the particle flow and the magnetic field, instead of focusing solely on the magnetic field. Unlike the Sweet-Parker description in Chapter 1 where a steady magnetic diffusion is the main process, collisionless reconnection will be shown to be an exponentially growing instability.

2.1 Canonical Vorticity

The quantity "canonical vorticity" is defined as

$$\mathbf{Q}_\sigma = m_\sigma \nabla \times \mathbf{u}_\sigma + q_\sigma \mathbf{B}, \tag{2.1}$$

$$= m_\sigma \mathbf{w}_\sigma + q_\sigma \mathbf{B}, \tag{2.2}$$

where $\mathbf{u}_\sigma$ is the flow velocity of each species σ and $\mathbf{w}_\sigma = \nabla \times \mathbf{u}_\sigma$ is the vorticity of each species. By writing $\mathbf{B} = \nabla \times \mathbf{A}$,

$$\mathbf{Q}_\sigma = \nabla \times (m_\sigma \mathbf{u}_\sigma + q_\sigma \mathbf{A}), \tag{2.3}$$

$$= \nabla \times \mathbf{P}_\sigma, \tag{2.4}$$

where $\mathbf{P}_\sigma = m_\sigma \mathbf{u}_\sigma + q_\sigma \mathbf{A}$ is the canonical momentum of each species. Therefore, canonical vorticity $\mathbf{Q}_\sigma$ is the curl of the species canonical momentum $\mathbf{P}_\sigma$, hence the name. $\mathbf{Q}_\sigma$ is a combination of the inertial term which involves finite species mass, and the magnetic term which involves the magnetic field.

Frozen-in Property of Canonical Vorticity

Consider the two-fluid equation (Eq. 1.20)

$$m_\sigma \frac{\partial \mathbf{u}_\sigma}{\partial t} + m_\sigma \mathbf{u}_\sigma \cdot \nabla \mathbf{u}_\sigma = q_\sigma (\mathbf{E} + \mathbf{u}_\sigma \times \mathbf{B}) - \frac{\nabla \cdot \overleftrightarrow{\mathbf{p}}_\sigma}{n_\sigma}, \tag{2.5}$$

where the convective derivative was decomposed into partial derivatives. The pressure term will now be dropped by simply assuming low β, or by assuming both

isotropic ($\nabla \cdot \overleftrightarrow{\mathbf{p}} = \nabla p$) and barotropic ($\nabla p \times \nabla n = 0$) pressure when intending to take the curl of this equation so that

$$\nabla \times \frac{\nabla \cdot \overleftrightarrow{\mathbf{p}}_\sigma}{n_\sigma} = \nabla \times \frac{\nabla p_\sigma}{n_\sigma} = \frac{1}{n_\sigma^2} \nabla p_\sigma \times \nabla n_\sigma = 0. \tag{2.6}$$

Taking the curl of Eq. 2.5 and using Faraday's law to eliminate $\mathbf{E}$,

$$m_\sigma \frac{\partial \nabla \times \mathbf{u}_\sigma}{\partial t} + m_\sigma \nabla \times (\mathbf{u}_\sigma \cdot \nabla \mathbf{u}_\sigma) = -q_\sigma \frac{\partial \mathbf{B}}{\partial t} + q_\sigma \nabla \times (\mathbf{u}_\sigma \times \mathbf{B}) \,. \tag{2.7}$$

Using the identities $\nabla \left(V^2/2\right) = \mathbf{V} \cdot \nabla \mathbf{V} + \mathbf{V} \times \nabla \times \mathbf{V}$ and $\nabla \times \nabla S = 0$ for any vector $\mathbf{V}$ and scalar S,

$$m_\sigma \frac{\partial \nabla \times \mathbf{u}_\sigma}{\partial t} - m_\sigma \nabla \times (\mathbf{u}_\sigma \times \nabla \times \mathbf{u}_\sigma) = -q_\sigma \frac{\partial \mathbf{B}}{\partial t} + q_\sigma \nabla \times (\mathbf{u}_\sigma \times \mathbf{B}) \,. \tag{2.8}$$

Writing $\nabla \times \mathbf{u}_\sigma = \mathbf{w}_\sigma$ and rearranging,

$$\frac{\partial \left(m_\sigma \mathbf{w}_\sigma + q_\sigma \mathbf{B}\right)}{\partial t} = \nabla \times (\mathbf{u}_\sigma \times [m_\sigma \mathbf{w}_\sigma + q_\sigma \mathbf{B}]), \tag{2.9}$$

or

$$\frac{\partial \mathbf{Q}_\sigma}{\partial t} = \nabla \times (\mathbf{u}_\sigma \times \mathbf{Q}_\sigma), \tag{2.10}$$

which is the *canonical induction equation*. Equation 2.10 is an extremely important result in that it has the same form as the plasma induction equation (Eq. 1.36). Because the plasma induction equation means that the magnetic field $\mathbf{B}$ is frozen into the plasma flow $\mathbf{U}$, Eq. 2.10 means that the canonical vorticity $\mathbf{Q}_\sigma$ is frozen into the species flow $\mathbf{u}_\sigma$. It also equivalently means that the flux associated with $\mathbf{Q}_\sigma$,

$$\Phi_Q = \int_S \mathbf{Q}_\sigma \cdot d\mathbf{s}, \tag{2.11}$$

is a conserved quantity, and that flux tubes associated with $\mathbf{Q}_\sigma$ can therefore be defined. Each species has its own flux tubes that convect with the respective species flow. The conservation of $\mathbf{Q}_\sigma$ flux is a combination of Kelvin's circulation theorem [149] in hydrodynamics which states that $\int_S \nabla \times \mathbf{u}_\sigma \cdot d\mathbf{s} = \oint_C \mathbf{u}_\sigma \cdot d\mathbf{l} = const.$, and the plasma induction equation which states that magnetic flux is conserved.

Because Φ_Q, not Φ_B, is the conserved quantity, $\mathbf{B}$ is free to annihilate, reconnect, and be converted to vorticity $\mathbf{w}_\sigma$ while preserving Φ_Q. In other words, collisionless magnetic reconnection is allowed because the topological constraint on $\mathbf{B}$ in MHD is relieved in the two-fluid regime.

The frozen-in property of $\mathbf{Q}_\sigma$ and the interchangeability between $\mathbf{w}_\sigma$ and $\mathbf{B}$ within $\mathbf{Q}_\sigma$ are the crux of the intuitive description of collisionless reconnection that will be given in this chapter.

2.2 Assumptions

A couple of assumptions will now be made in order to readily relate the concept of canonical vorticity to collisionless reconnection.

Stationary Ion Assumption

The region of interest in this chapter is the region where $L < d_i$ (green box in Fig. 1.5). In this region, the Hall term dominates over the $\mathbf{U} \times \mathbf{B}$ term, so the ions can be assumed to be stationary; detailed ion dynamics will be presented in Chapter 4. The stationary ion assumption implies that the current is carried solely by the electrons, i.e.,

$$\mathbf{u}_e = -\frac{\mathbf{J}}{n_e e} = -\frac{\nabla \times \mathbf{B}}{\mu_0 n_e e}. \tag{2.12}$$

The electron canonical vorticity then becomes

$$\begin{aligned}
\mathbf{Q}_e &= m_e \nabla \times \mathbf{u}_e + q_e \mathbf{B}, && (2.13)\\
&= -\frac{m_e}{\mu_0 n_e e} \nabla \times (\nabla \times \mathbf{B}) - e\mathbf{B}, && (2.14)\\
&= e\left(-\frac{m_e}{\mu_0 n_e e^2} \nabla \times (\nabla \times \mathbf{B}) - \mathbf{B}\right), && (2.15)\\
&= e\left(d_e^2 \nabla^2 \mathbf{B} - \mathbf{B}\right), && (2.16)
\end{aligned}$$

where

$$\frac{m_e}{\mu_0 n_e e^2} = \frac{1}{\epsilon_0 \mu_0} \frac{m_e \epsilon_0}{n_e e^2} = \frac{c^2}{\omega_{pe}^2} = d_e^2 \tag{2.17}$$

and $\nabla \times (\nabla \times \mathbf{B}) = \nabla (\nabla \cdot \mathbf{B}) - \nabla^2 \mathbf{B} = -\nabla^2 \mathbf{B}$ were used. Writing $\nabla \sim 1/L$, the Laplacian term which arises from finite electron inertia scales as d_e^2/L^2. Therefore, at length scales much larger than the electron skin depth, i.e., $L \gg d_e$, the magnetic term dominates and $\mathbf{Q}_e$ is topologically indistinguishable from $\mathbf{B}$. At $L \ll d_e$, the inertial term dominates so $\mathbf{Q}_e \simeq m_e \mathbf{w}_e = e d_e^2 \nabla^2 \mathbf{B}$. At $L \sim d_e$, both the inertial and magnetic terms are important.

Incompressibility Assumption

Since ions are assumed to be stationary, a local change in electron density will result in a local change in the charge density. This violates a fundamental plasma assumption that plasmas are *quasi-neutral*, i.e., charge-neutral over scale lengths much larger than the Debye length λ_D. Now, λ_D/d_e scales as v_{Te}/c where v_{Te} is the electron thermal velocity, so $v_{Te} \ll c$ means that $\lambda_D \ll d_e$. Since d_e is the smallest length scale in our analysis of collisionless reconnection, incompressibility

is a valid assumption as long as the electron thermal velocity is much smaller than the speed of light. Thus, a time-independent, spatially uniform electron density will be used throughout the analysis.

Mathematically, incompressibility means that

$$\nabla \cdot \mathbf{u}_e = 0. \tag{2.18}$$

This can be seen by rearranging the electron continuity equation,

$$\frac{\partial n_e}{\partial t} + \nabla \cdot (n_e \mathbf{u}_e) = 0, \tag{2.19}$$

$$\frac{\partial n_e}{\partial t} + \mathbf{u}_e \cdot \nabla n_e + n_e (\nabla \cdot \mathbf{u}_e) = 0. \tag{2.20}$$

Therefore, $Dn_e/Dt = 0$ if and only if $\nabla \cdot \mathbf{u}_e = 0$.

Assuming incompressibility is equivalent to assuming that the displacement current is negligible. This fact is illustrated by taking the divergence of the Ampère's law including the displacement current assuming stationary ions:

$$\nabla \cdot \nabla \times \mathbf{B} = -\nabla \cdot (\mu_0 n_e e \mathbf{u}_e) + \mu_0 \epsilon_0 \frac{\partial \nabla \cdot \mathbf{E}}{\partial t}, \tag{2.21}$$

$$0 = -\nabla \cdot (n_e \mathbf{u}_e) - \frac{\partial n_e}{\partial t}, \tag{2.22}$$

where Gauss's law was used so $\epsilon_0 \nabla \cdot \mathbf{E} = (n_i - n_e)\, e$ and $\partial n_i/\partial t = 0$ because ions are stationary. This result clearly shows that the time-dependence of n_e is equivalent to finite displacement current.

This set of assumptions and the ensuing system of equations have historically been called electron-magnetohydrodynamics (EMHD) [25]. Studies of magnetic reconnection in similar formulations have been done before [17, 25, 27], albeit not in the three-dimensional, intuitive manner that will be presented here.

2.3 Numerical Construction

A numerical simulation was developed in order to verify the ensuing analysis and graphically represent the results. The algorithm that solves Eq. 2.10 will now be presented. The code was written in Python 3.6.

Normalization

In order to facilitate the scaling of the simulation to real-life situations, relevant equations must be made dimensionless, i.e., normalized with respect to a set of

dimensional quantities. For example, dividing Eq. 2.12 by $d_e\,|\omega_{ce}|$ where $|\omega_{ce}| = eB_0/m_e$ and B_0 is a reference magnetic field,

$$\frac{\mathbf{u}_e}{d_e\,|\omega_{ce}|} = -\frac{m_e \nabla \times \mathbf{B}}{\mu_0 n_e e^2 B_0 d_e}, \tag{2.23}$$

$$= -d_e \nabla \times \frac{\mathbf{B}}{B_0}. \tag{2.24}$$

Normalizing each quantity, i.e., $\bar{\mathbf{u}}_e = \mathbf{u}_e/d_e\,|\omega_{ce}|$, $\bar{\mathbf{B}} = \mathbf{B}/B_0$, and $\bar{\nabla} = d_e\nabla$, we have the normalized Ampère's law,

$$\bar{\nabla} \times \bar{\mathbf{B}} = -\bar{\mathbf{u}}_e. \tag{2.25}$$

Likewise, length is normalized to d_e, time to $|\omega_{ce}|^{-1}$, and magnetic field to B_0. Normalizing electron canonical vorticity $\mathbf{Q}_e$ by eB_0,

$$\bar{\mathbf{Q}}_e = \bar{\nabla} \times \bar{\mathbf{u}}_e - \bar{\mathbf{B}}, \tag{2.26}$$

$$= \bar{\nabla}^2 \bar{\mathbf{B}} - \bar{\mathbf{B}}. \tag{2.27}$$

The normalized electron canonical induction equation is

$$\frac{m_e}{e^2 B_0^2}\frac{\partial \mathbf{Q}_e}{\partial t} = \frac{m_e}{e^2 B_0^2}\nabla \times (\mathbf{u}_e \times \mathbf{Q}_e) \tag{2.28}$$

$$\frac{\partial \bar{\mathbf{Q}}_e}{\partial \bar{t}} = d_e \nabla \times \left(\frac{\mathbf{u}_e}{d_e\,|\omega_{ce}|} \times \bar{\mathbf{Q}}_e\right) \tag{2.29}$$

$$\frac{\partial \bar{\mathbf{Q}}_e}{\partial \bar{t}} = \bar{\nabla} \times \left(\bar{\mathbf{u}}_e \times \bar{\mathbf{Q}}_e\right), \tag{2.30}$$

where $\bar{t} = eB_0 t/m_e = |\omega_{ce}|\,t$. Using Eqs. 2.25 and 2.27, Eq. 2.30 can be written entirely in terms of $\bar{\mathbf{B}}$:

$$\frac{\partial}{\partial \bar{t}}\left(\bar{\nabla}^2 \bar{\mathbf{B}} - \bar{\mathbf{B}}\right) = -\bar{\nabla} \times \left(\left[\bar{\nabla} \times \bar{\mathbf{B}}\right] \times \left[\bar{\nabla}^2 \bar{\mathbf{B}} - \bar{\mathbf{B}}\right]\right). \tag{2.31}$$

Therefore, the entire system can be expressed solely as a function of the magnetic field.

From this point on the bars will be dropped to reduce notational clutter. Only normalized quantities will be used unless specified otherwise. A summary of the normalizations used in this chapter is illustrated in Table 2.1.

Discretization

2.5D Cartesian coordinates are used. This means that any quantity σ at any given time t is defined on a 2D grid as $\sigma^t_{i,j}$, where i and j are the x and y coordinates, and

Quantity	Normalization
t	$\|\omega_{ce}\|^{-1}$
$\mathbf{x}$	d_e
$\mathbf{u}_e$	$d_e\|\omega_{ce}\|$
$\mathbf{B}$	B_0
$\mathbf{Q}_e$	eB_0

Table 2.1: Dimensional quantities and their normalization parameters in Chapter 2.

any vector $\mathbf{V}$ has three components, namely V_x, V_y, and V_z. Also, the z coordinate is an ignorable coordinate so that $\partial/\partial z \to 0$. The central differentiation scheme is used for the spatial derivative in the x-direction, i.e.,

$$\frac{\partial \sigma}{\partial x} \to \frac{\sigma^t_{i+1,j} - \sigma^t_{i-1,j}}{2\Delta x} \tag{2.32}$$

for any quantity q and similarly for the y-direction. The second spatial derivative is expressed as

$$\frac{\partial^2 \sigma}{\partial x^2} \to \frac{\sigma^t_{i+1,j} + 2\sigma^t_{i,j} - \sigma^t_{i-1,j}}{\Delta x^2}. \tag{2.33}$$

The explicit forward differentiation scheme is used for the time derivative, i.e.,

$$\frac{\partial \sigma}{\partial t} = s \to \frac{\sigma^{t+1}_{i,j} - \sigma^t_{i,j}}{\Delta t} = s^t_{i,j} \tag{2.34}$$

for any source term s.

Algorithm

The following algorithm is used to solve Eq. 2.30 and equivalently Eq. 2.31.

1. Given $\bar{\mathbf{B}}^t$, calculate $\bar{\mathbf{u}}^t_e$ and $\bar{\mathbf{Q}}^t_e$ using Eqs. 2.25 and 2.27, respectively.
2. Obtain $\bar{\mathbf{Q}}^{t+1}_e$ using Eq. 2.30.
3. Obtain $\bar{\mathbf{B}}^{t+1}$ by solving Eq. 2.27 iteratively using the relaxation method [84] .
4. Repeat.

The relaxation method in step 3 can be explained as follows. Consider the discretized form of Eq. 2.27 at any given time:

$$\mathbf{Q}_{i,j} = \frac{\mathbf{B}_{i+1,j} + 2\mathbf{B}_{i,j} - \mathbf{B}_{i-1,j}}{\Delta x^2} + \frac{\mathbf{B}_{i,j+1} + 2\mathbf{B}_{i,j} - \mathbf{B}_{i,j+1}}{\Delta y^2} - \mathbf{B}_{i,j}. \tag{2.35}$$

This equation can be iteratively solved for $\bar{\mathbf{B}}_{i,j}$:

$$\left(\mathbf{B}_{i,j}\right)_{n+1} = \left(\frac{2}{\Delta x^2} + \frac{2}{\Delta y^2} - 1\right)^{-1} \left(\mathbf{Q}_{i,j} - \frac{\left(\mathbf{B}_{i+1,j}\right)_n - \left(\mathbf{B}_{i-1,j}\right)_n}{\Delta x^2} - \frac{\left(\mathbf{B}_{i,j+1}\right)_n - \left(\mathbf{B}_{i,j-1}\right)_n}{\Delta y^2}\right), \tag{2.36}$$

where n is each iterative step. The iteration is halted when the difference of $\mathbf{B}$ at any two consecutive iterative steps reaches below a specified value of tolerance. This method does not always yield a converging, stable solution; convergence tests must be first conducted in order to avoid spurious numerical solutions.

Algorithm Test

The normal mode of Eq. 2.31 is a plasma wave called a "whistler wave." Therefore, the algorithm should reproduce whistler waves, and relevant tests were conducted to validate the code. In Appendix A, an analytical solution for whistler waves is presented in detail. In Appendix B, tests of the algorithm against the prediction are conducted and confirm that the code produces whistler waves.

Initial Conditions

The magnetic field profile is the Harris magnetic shear profile [66] (see Appendix E), or

$$B_y = \tanh \frac{x}{\lambda}, \tag{2.37}$$

where λ is the shear length scale. This profile represents two regions of opposing magnetic fields separated by a region of magnetic null.

By Ampère's law, this magnetic field is produced by the out-of-plane current profile

$$u_{ez} = -J_z = -\frac{\partial B_y}{\partial x} = -\frac{1}{\lambda} \cosh^{-2} \frac{x}{\lambda}, \tag{2.38}$$

so the electrons are flowing in the $-z$-direction near $x = 0$. This configuration is frequently called a "current sheet" because of this current profile.

Reconnection is initiated by a 2D-localized vector potential perturbation of the form

$$A_z = \epsilon \exp\left(-\frac{x^2}{2\lambda^2} - \frac{y^2}{2\sigma_y^2}\right), \tag{2.39}$$

where ϵ is the perturbation strength and is a small number, e.g., 10^{-5}, and σ_y is the perturbation length scale in the y-direction. The perturbation magnetic fields from

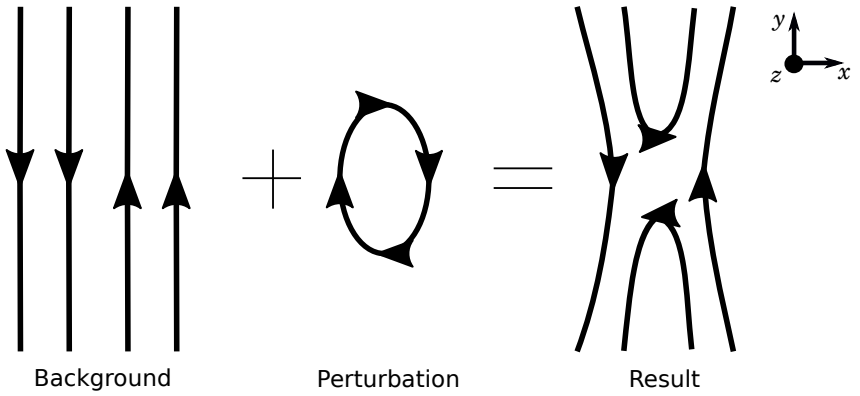

Figure 2.1: The background and perturbation magnetic fields and their sum as the initial condition for magnetic reconnection.

this vector potential are

$$\tilde{B}_x = \frac{\partial A_z}{\partial y} = -\epsilon \frac{y}{\sigma_y^2} \exp\left(-\frac{x^2}{2\lambda^2} - \frac{y^2}{2\sigma_y^2}\right), \tag{2.40}$$

$$\tilde{B}_y = -\frac{\partial A_z}{\partial x} = \epsilon \frac{x}{\lambda^2} \exp\left(-\frac{x^2}{2\lambda^2} - \frac{y^2}{2\sigma_y^2}\right). \tag{2.41}$$

The background and perturbation magnetic fields and their sum are shown graphically in Fig. 2.1. The perturbation adds to the background field in such a way that field lines close to the center ($x = 0$) are reconnected; those that are further away come closer together to the center at a localized point in y; i.e., the field lines bow toward the center.

This initial condition triggers the instability that is fast magnetic reconnection; analytical and intuitive explanations for why an instability occurs will be illustrated in Section 2.5.

Typical grid dimensions were $x \times y = 150 \times 600 = 30d_e \times 120d_e$. Neumann boundary conditions were used, but the simulation was halted before any significant physical change reached the boundary.

2.4 Simulation Results

Figure 2.2 shows the time evolution of the magnetic field during collisionless reconnection. As shown by the streamlines, the in-plane magnetic fields spontaneously come together at $x = 0$ and reconnect, accelerating electrons to high velocities (red arrows). The quadrupole out-of-plane magnetic fields, represented by the yellow

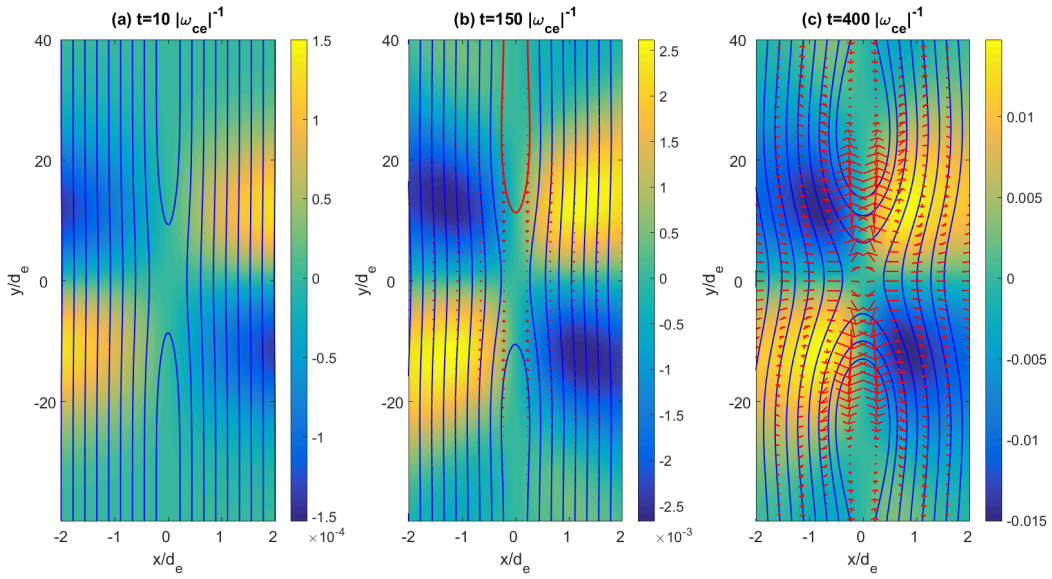

Figure 2.2: Time evolution of the magnetic field during collisionless reconnection. The colors and blue lines are the out-of-plane and in-plane magnetic fields, respectively, and the red arrows are the electron flow vectors.

and blue colors, also come together and grow in magnitude (note the different color scales). These results — quadrupole Hall magnetic fields and the geometry of the electron flow — are consistent with previous numerical and experimental studies of Hall-mediated collisionless reconnection [45, 54, 129, 166].

Figures 2.3a and 2.3b show the in-plane (blue lines) and out-of-plane (colors) components of $\mathbf{B}$ and $\mathbf{Q}_e$, respectively. It can be clearly seen that while $\mathbf{B}$ field lines reconnect, $\mathbf{Q}_e$ field lines do not reconnect and pile up near the center. The slight reconnection of $\mathbf{Q}_e$ is due to the initial perturbation and finite numerical resistivity that originates from unavoidable small numerical error.

Figures 2.3c and 2.3d show three-dimensional views of $\mathbf{B}$ and $\mathbf{Q}_e$, respectively. This is done by stacking the 2D simulation results in the z-direction and plotting the 3D vectors. It can be seen from Fig. 2.3c that the magnetic field lines generally move in the direction of the out-of-plane electron flow u_{ez} (red arrow; recall that the magnetic field shear is created by the out-of-plane current profile in Eq. 2.38), but they do not exactly convect with u_{ez}. This fact is obvious in comparison to Fig. 2.3d, where $\mathbf{Q}_e$ field lines stay connected and exactly convect with u_{ez} in the $-z$-direction. This exact downward convection is an important process that will be examined in the next Section.

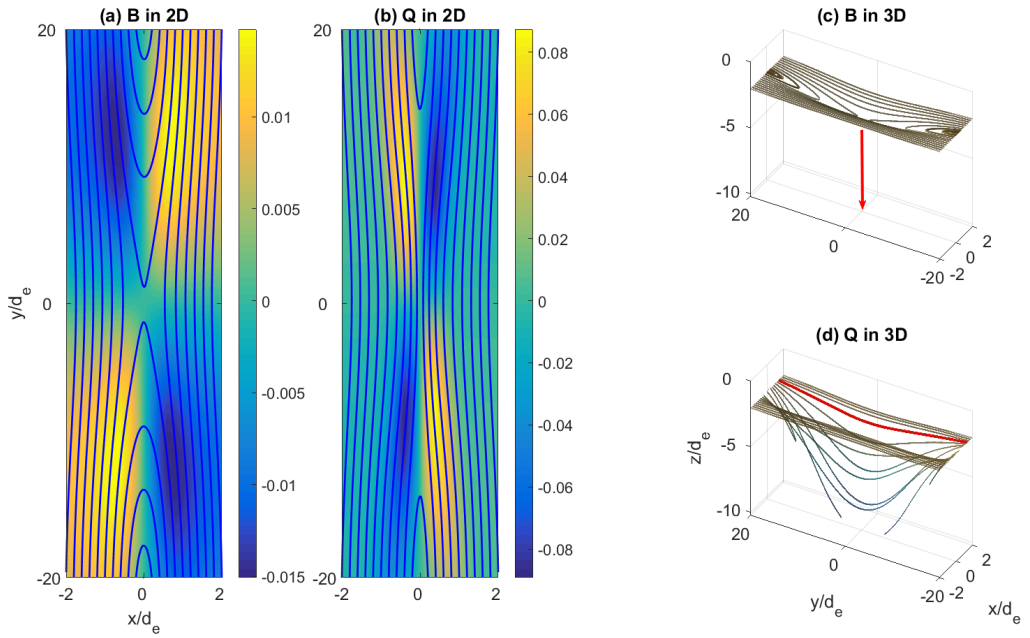

Figure 2.3: In-plane (blue lines) and out-of-plane (colors) components of (a) **B** and (b) $\mathbf{Q}_e$. Corresponding 3D views are shown in (c) and (d), respectively. The color of the lines represent the height in z. The red arrow in (c) is the direction of the out-of-plane electron velocity u_{ez}.

2.5 Intuitive Description

Instability and Quadrupole Fields

Under the assumptions presented in Section 2.2, collisionless reconnection is a purely growing instability with an exponential growth rate that depends on the system parameters. This fact was demonstrated in Bellan [12] via an extensive analytical calculation involving a pair of second-order differential equations that form a fourth-order eigensystem. Here, an intuitive explanation of the exponential growth using $\mathbf{Q}_e$ flux tube dynamics is presented, followed by an analytical proof much simpler than that in Bellan [12]. The origin of the quadrupole magnetic fields in Fig. 2.3a will also be explained.

A $\mathbf{Q}_e$ flux tube is first defined by picking a $\mathbf{Q}_e$ field line, .e.g., the red line in Fig. 2.3d, and bunching up the field lines around it. The temporal evolution of this $\mathbf{Q}_e$ flux tube is shown in Fig. 2.4. The small insets show the side-on and overhead views of the flux tube. The progression of this flux tube is as follows:

1. Initially due to the perturbation, a localized section of the flux tube bows towards the center where electrons are flowing downwards (red arrow; Fig.

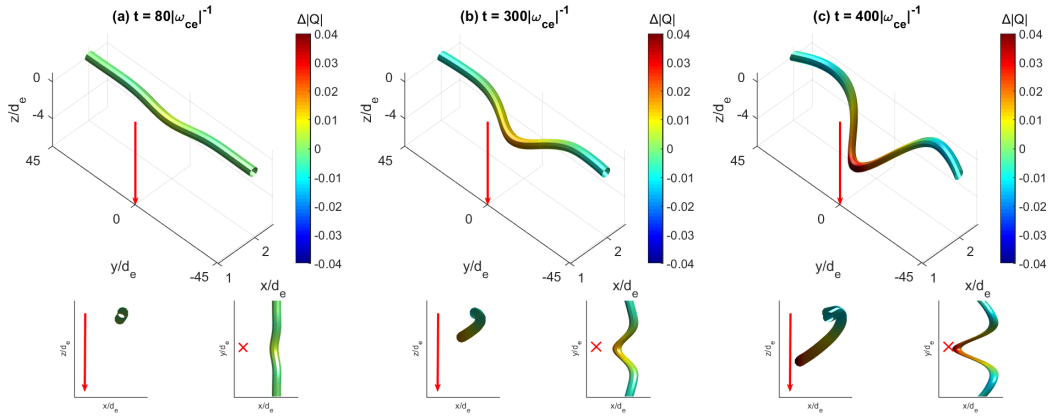

Figure 2.4: Temporal evolution of a $\mathbf{Q}_e$ flux tube. The insets are side-on and overhead views of the flux tube. The red arrow represents the direction and location of electron flow $\mathbf{u}_e$. The color of the flux tube represents the change of $|\mathbf{Q}_e|$.

2.4a).

2. This section "feels" a stronger electron flow than other parts of the flux tube and so convects downwards faster (Figs. 2.4b and 2.4c).

3. This downward convection creates Q_{ez} fields and thus B_z fields that scale like $B_z \sim xy$ near the origin (colors in Fig. 2.3a). These are the quadrupole Hall fields that are generic to collisionless reconnection.

4. Because $B_z \sim xy$ in the vicinity of the origin, $u_{ex} = -\partial B_z/\partial y \sim -x$, so the electron flow in the x-direction corresponds to inflow towards the center. Thus, more $\mathbf{Q}_e$ field lines bow toward the center, and the process repeats to yield an instability.

It is now clear why an instability occurs, but to prove exponential growth, an analytical calculation must be done.

Let us first explicitly prove that $\mathbf{Q}_e$ does not reconnect by proving that Q_{ex} is zero on the y-axis. Reconnection of $\mathbf{Q}_e$ would require development of finite Q_{ex} on the y-axis, so $(Q_{ex})_{x=0} = 0$ means that $\mathbf{Q}_e$ field lines stay connected. Expanding the right-hand side of Eq. 2.30,

$$\frac{\partial \mathbf{Q}_e}{\partial t} = \mathbf{Q}_e \cdot \nabla \mathbf{u}_e + \mathbf{u}_e \left(\nabla \cdot \mathbf{Q}_e\right) - \mathbf{u}_e \cdot \nabla \mathbf{Q}_e - \mathbf{Q}_e \left(\nabla \cdot \mathbf{u}_e\right), \tag{2.42}$$

$$= \mathbf{Q}_e \cdot \nabla \mathbf{u}_e - \mathbf{u}_e \cdot \nabla \mathbf{Q}_e, \tag{2.43}$$

where $\nabla \cdot \mathbf{Q}_e = 0$ by the definition of $\mathbf{Q}_e$ (Eq. 2.26) and $\nabla \cdot \mathbf{u}_e = 0$ by the incompressibility assumption. Expressing this equation using the convective derivative,

$$\frac{D\mathbf{Q}_e}{Dt} = \mathbf{Q}_e \cdot \nabla \mathbf{u}_e, \tag{2.44}$$

and its x-component is

$$\frac{DQ_{ex}}{Dt} = Q_{ex}\frac{\partial u_{ex}}{\partial x} + Q_{ey}\frac{\partial u_{ex}}{\partial y}, \tag{2.45}$$

where $\partial/\partial z \to 0$ was used. We now examine what happens at $x = 0$ if $(Q_{ex})_{x=0,t=0} = 0$. The first term is obviously zero at $t = 0$. Because u_{ex} represents the electron inflow and so is zero everywhere on the y-axis, the second term is also zero. Thus at $t = 0$,

$$\frac{DQ_{ex}}{Dt} = 0. \tag{2.46}$$

Therefore, if $(Q_{ex})_{x=0}$ starts out with zero, it will remain zero. It has thus been explicitly established that $\mathbf{Q}_e$ does not reconnect, and equivalently that Q_{ex} at or near $x = 0$ is zero or extremely small.

Next, consider the y-component of Eq. 2.44:

$$\frac{DQ_{ey}}{Dt} = Q_{ex}\frac{\partial u_{ey}}{\partial x} + Q_{ey}\frac{\partial u_{ey}}{\partial y}. \tag{2.47}$$

Near $x = 0$, $Q_{ex} \simeq 0$, so

$$\left(\frac{DQ_{ey}}{Dt}\right)_{x\approx 0} = \left(Q_{ey}\right)_{x\approx 0}\left(\frac{\partial u_{ey}}{\partial y}\right)_{x\approx 0}, \tag{2.48}$$

where $x \approx 0$ means near but not exactly at $x = 0$. The solution is

$$\left(Q_{ey}\right)_{x\approx 0,t} = \left(Q_{ey}\right)_{x\approx 0,t=0}\left[\exp\left(\int_0^t \frac{\partial u_{ey}}{\partial y}dt\right)\right]_{x\approx 0}, \tag{2.49}$$

which is a purely growing solution ($\partial u_{ey}/\partial y > 0$) because B_z has the profile $B_z \sim \gamma xy$ near $x = 0$ where γ is a positive value as can be seen from Fig. 2.2, and $\partial u_{ey}/\partial y = \partial^2 B_z/\partial x \partial y \sim \gamma > 0$ using Eq. 2.25.

This exponential growth propagates to other variables as well. Figure 2.5 shows the time evolution of Q_{ez}, B_z, and $(\nabla \times \mathbf{u}_e)_z$ at $(x, y) = (1, 2)d_e$. The y-axis is in natural logarithmic scale. Because the initial conditions are not an eigenfunction of the system, all relevant quantities relax to an eigenstate before $t = 100\,|\omega_{ce}|^{-1}$. However, after $t = 100\,|\omega_{ce}|^{-1}$, it can be seen that all relevant quantities exponentially grow in time.

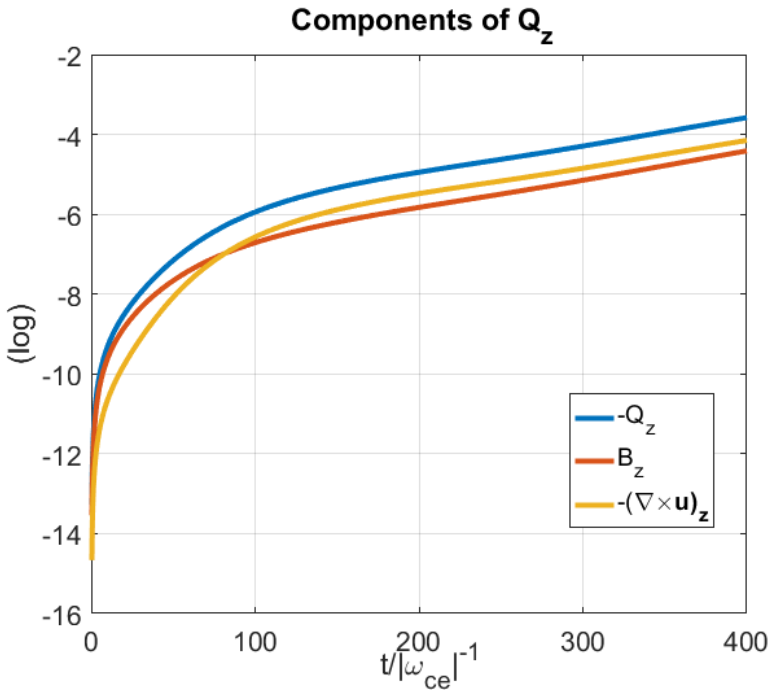

Figure 2.5: Time evolution of Q_{ez}, B_z, and $(\nabla \times \mathbf{u}_e)_z$ at $(x, y) = (1, 2)d_e$. The y-axis is in natural logarithmic scale.

Thus, we can conclude that *any slight gradient of electron velocity along* $\mathbf{Q}_e$ *field lines* is a sufficient condition for this instability that provides collisionless reconnection.

Bellan [12] predicted the growth rate in collisionless reconnection as (writing in terms of the normalized variables used in this chapter)

$$\gamma = \frac{\sqrt{2}}{10}\frac{1}{\lambda\sigma_y}. \tag{2.50}$$

Now, incompressibility dictates that the electron outflow u_{ey} satisfies $u_{ey}\lambda = const.$, i.e., if the flow channel narrows, the outflow must be faster and vice-versa. Thus, the growth rate in Eq. 2.49 scales as

$$\gamma \simeq \frac{\partial u_{ey}}{\partial y} \simeq \frac{u_{ey}}{\sigma_y} \sim \frac{1}{\lambda\sigma_y}, \tag{2.51}$$

which is in agreement with Eq. 2.50.

Table 2.2 shows the comparison between the calculated growth rate in Bellan [12] (γ_c) and the simulated growth rate γ_s obtained by linearly fitting through the lines in, e.g., Fig. 2.5. The agreement between the two rates is evident.

λ	σ_y	γ_s	γ_c
1	10	40.19 ± 0.40	43.40
2	10	17.56 ± 0.10	22.08
2	16	12.95 ± 0.50	13.80
5	16	5.21 ± 0.05	4.01

Table 2.2: Comparison of simulated γ_s and calculated γ_c for different length parameters of the current sheet

Electron Acceleration

$\mathbf{Q}_e$ flux tube dynamics also explains how collisionless reconnection triggers extreme electron acceleration. As the flux tube convects downward with the electron flow, the tube lengthens and stretches like a rubber band as in Fig. 2.4c. Due to the assumed incompressibility, the total volume of the flux tube must remain the same, so an increase in flux tube length must be accompanied by a decrease in its circumference, i.e., thinning. However, because $\mathbf{Q}_e$ field lines are frozen-in, flux tube thinning means that the $\mathbf{Q}_e$ lines bunch up together as in the top flux tube in Fig. 1.2. This bunching-up signifies that the magnitude of $\mathbf{Q}_e$ increases, as can be seen from the colors of the tube in Fig. 2.4. Because $\mathbf{Q}_e \simeq \nabla \times \mathbf{u}_e$ at small length scales, this leads to an increase of $\mathbf{u}_e$, i.e., electron acceleration.

This process can be more simply understood by recalling that Φ_Q is a conserved quantity, so

$$\Phi_Q = \int_S \mathbf{Q}_e \cdot d\mathbf{s}, \tag{2.52}$$

$$= \int_S \nabla \times \mathbf{u}_e \cdot d\mathbf{s} - \int_S \mathbf{B} \cdot d\mathbf{s}, \tag{2.53}$$

$$= \oint_C \mathbf{u}_e \cdot d\mathbf{l} - \int_S \mathbf{B} \cdot d\mathbf{s}. \tag{2.54}$$

Magnetic reconnection involves the reduction of $\mathbf{B}$, and flux tube thinning involves the reduction of S and C. Therefore, as $\mathbf{B} \to 0$ and $C \to 0$, $\mathbf{u}_e \to \infty$ in order to conserve Φ_Q.

Thus, extreme electron acceleration is due to *a combination of interchange between the magnetic field and the electron vorticity within* $\mathbf{Q}_e$, *and* $\mathbf{Q}_e$ *amplification due to flux tube thinning*.

Generation of Whistler Waves

Whistler waves are right-handed circularly polarized electromagnetic plasma waves in the frequency range $\omega_{ci}, \omega_{pi} \ll \omega \ll \omega_{ce}, \omega_{pe}$ with the dispersion relation

$$\frac{c^2k^2}{\omega^2} = \frac{\omega_{pe}^2/\omega^2}{\frac{|\omega_{ce}|}{\omega}\cos\theta - 1}, \tag{2.55}$$

where θ is the wave propagation angle with respect to the background magnetic field $\mathbf{B}_0 = B_0\hat{z}$. In terms of normalized quantities used in this chapter, this dispersion relation becomes

$$k^2 = \frac{1}{\frac{\cos\theta}{\omega} - 1}, \tag{2.56}$$

where bars are dropped to reduce notational clutter. Whistler waves are frequently observed in association with magnetic reconnection in both laboratory [29, 67] and space [40] plasmas.

Because the wave frequency is much larger than any ion-related frequency, ions can be assumed to be stationary for a whistler wave. Incompressibility can then also be assumed due to quasi-neutrality. Thus, a whistler wave is the normal mode of Eq. 2.31 upon which the present theory on reconnection is built upon.

To prove this, let us linearize $\mathbf{B}$ so that it is expressed as a sum of the normalized background field $\hat{z}$ and the normalized perturbed field $\mathbf{B}_1$, i.e., $\mathbf{B} = \hat{z} + \mathbf{B}_1$. Equation 2.31 then becomes, to first order,

$$\frac{\partial}{\partial t}\left(\nabla^2\mathbf{B}_1 - \mathbf{B}_1\right) = \nabla \times \left([\nabla \times \mathbf{B}_1] \times \hat{z}\right). \tag{2.57}$$

Assuming $\mathbf{B}_1 \sim \exp(i\mathbf{k}\cdot\mathbf{x} - i\omega t)$ so that $\partial/\partial t \to -i\omega$ and $\nabla \to i\mathbf{k}$,

$$i\omega\left(1 + k^2\right)\mathbf{B}_1 = \mathbf{k} \times ([\mathbf{k} \times \mathbf{B}_1] \times \hat{z}), \tag{2.58}$$

$$= \mathbf{k} \times (k_z\mathbf{B}_1 - \mathbf{k}B_{1z}), \tag{2.59}$$

$$= k_z\mathbf{k} \times \mathbf{B}_1. \tag{2.60}$$

Crossing both sides by $\mathbf{k}$ and using Eq. 2.60 to eliminate $\mathbf{k} \times \mathbf{B}$,

$$i\omega\left(1 + k^2\right)\mathbf{k} \times \mathbf{B}_1 = k_z\mathbf{k} \times (\mathbf{k} \times \mathbf{B}), \tag{2.61}$$

$$-\omega^2\left(1 + k^2\right)^2\mathbf{B}_1/k_z = k_z\left(\mathbf{k}\,[\mathbf{k}\cdot\mathbf{B}_1] - k^2\mathbf{B}_1\right), \tag{2.62}$$

$$\omega^2\left(1 + k^2\right)^2 = k_z^2k^2, \tag{2.63}$$

$$\omega\left(1 + k^2\right) = k^2\cos\theta, \tag{2.64}$$

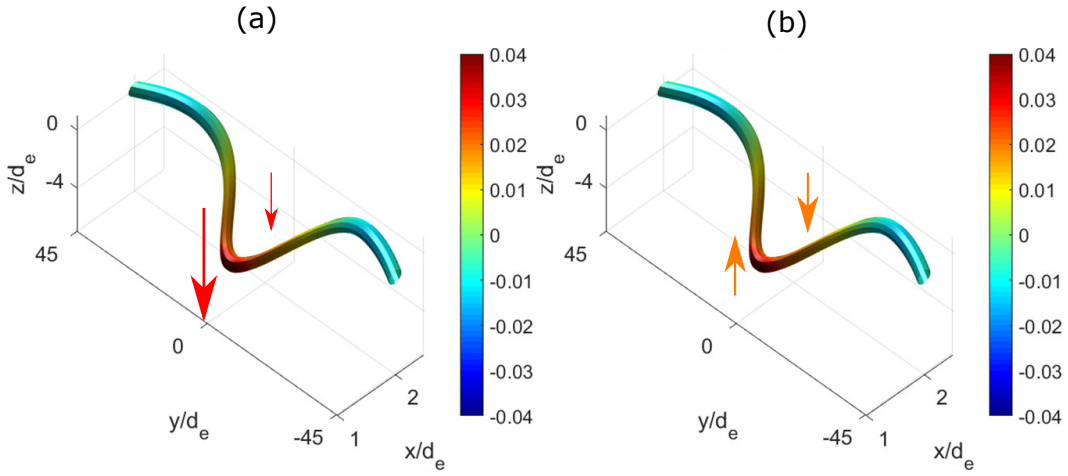

Figure 2.6: (a) A $\mathbf{Q}_e$ flux tube and the spatial variation of the magnitudes of u_{ez} (red arrows). (b) The the direction of u_{ez} in a frame traveling in the $-z$-direction with the center portion of the flux tube.

where $k_z = k\cos\theta$ was used. Solving this equation in terms of k^2 gives

$$k^2 = \frac{1}{\frac{1}{\cos\theta} - 1}, \tag{2.65}$$

which is Eq. 2.56. Therefore, the whistler wave is the normal mode of Eq. 2.31.

The wave source for magnetic reconnection is the central electron current, which induces a u_{ez} shear along a $\mathbf{Q}_e$ flux tube. In Fig. 2.6a , the magnitude difference between u_{ez} at two different locations is apparent (red arrows). Now, in a frame traveling in the $-z$-direction with the center portion of the flux tube, u_{ez} at the two locations have different directions, as can be seen from the orange arrows in Fig. 2.6b. Because $\mathbf{Q}_e$ field lines convect with $\mathbf{u}_e$, this relative shear induces a $\mathbf{Q}_e$ flux tube twist, which acts as a source for whistler waves. This is analogous to how torsional Alfvén waves are excited (Fig. 1.3).

To demonstrate this mathematically, the normalized electron canonical helicity density $\kappa_Q = \mathbf{P}_e \cdot \mathbf{Q}_e$ is first defined in analogy to magnetic helicity density $\kappa = \mathbf{A} \cdot \mathbf{B}$. κ_Q evolves in time as follows (proof in Appendix C):

$$\frac{D\kappa_Q}{Dt} = \mathbf{Q}_e \cdot \nabla\left(\frac{u_e^2}{2} - p_e - \mathbf{u}_e \cdot \mathbf{A}\right), \tag{2.66}$$

$$= \mathbf{Q}_e \cdot \nabla\mathcal{L}, \tag{2.67}$$

where p_e is scalar electron pressure assuming pressure isotropy, and $\mathcal{L} = \frac{u_e^2}{2} - p_e - \mathbf{u}_e \cdot \mathbf{A}$ is the Lagrangian density of the system. This is the canonical helicity

conservation equation[13, 172] for this specific regime. The central electron flow is a source of $\nabla\mathcal{L}$ along the $\mathbf{Q}$ field lines, so it is in turn a source of canonical helicity density. Whistler waves therefore represent a dynamic winding/unwinding of $\mathbf{Q}_e$ field lines just as torsional Alfvèn waves do of $\mathbf{B}$ lines. Therefore, whistler wave generation and propagation in collisionless reconnection can be seen as *the central electron flow curling up the* $\mathbf{Q}_e$ *flux tubes and whistler waves propagating this helicity density in the* $\pm y$*-directions*.

Now we will focus on how the whistler wave manifests itself in $\mathbf{B}$ fields. Figure 2.2 shows that there is an additional region of out-of-plane magnetic fields that develops near the outflow regions (e.g. black box in Fig. 2.2c). These fields, which have been previously observed by other numerical studies as well [45, 54] but generally not discussed in three-dimensional detail, suggest wave-like behavior, so it is worth examining how a typical reconnected $\mathbf{B}$ field line (e.g. red line in Fig. 2.2b) evolves taking these fields into account.

Figure 2.7 shows the 3D time evolution of a typical reconnected $\mathbf{B}$ field line. We can regard the initial field line as the background field, and the final field line as the background field plus the perturbations to this field. If the initial field line is stretched so that it mimics a uniform background field (as in the bottom subfigure), we can see that the spatial polarization of the final field corresponds to the area of strong u_{ez} (red rectangle) acting as the source of two temporally right-handed circularly polarized whistler waves propagating away from this source in the $\pm y$ directions.

2.6 Summary

A quantity called "canonical vorticity" $\mathbf{Q}_\sigma$ frozen into each species' flow, and the $\mathbf{Q}_\sigma$ flux of each species is therefore conserved. By examining the dynamics of $\mathbf{Q}_e$ flux tubes, various aspects of collisionless magnetic reconnection have been explained. First, the reason why collisionless reconnection is an exponentially growing instability has been explained through the interaction of a perturbed $\mathbf{Q}_e$ flux tube with the central out-of-plane electron flow. Second, the electron acceleration mechanism has been explained through the lengthening and thinning of a $\mathbf{Q}_e$ flux tube in conjunction with conversion from the magnetic field to electron vorticity while preserving $\mathbf{Q}_e$ flux. Third, the generation of whistler waves has been explained by the twisting of a $\mathbf{Q}_e$ flux tube by the out-of-plane electron flow shear and the subsequent propagation of this twist.

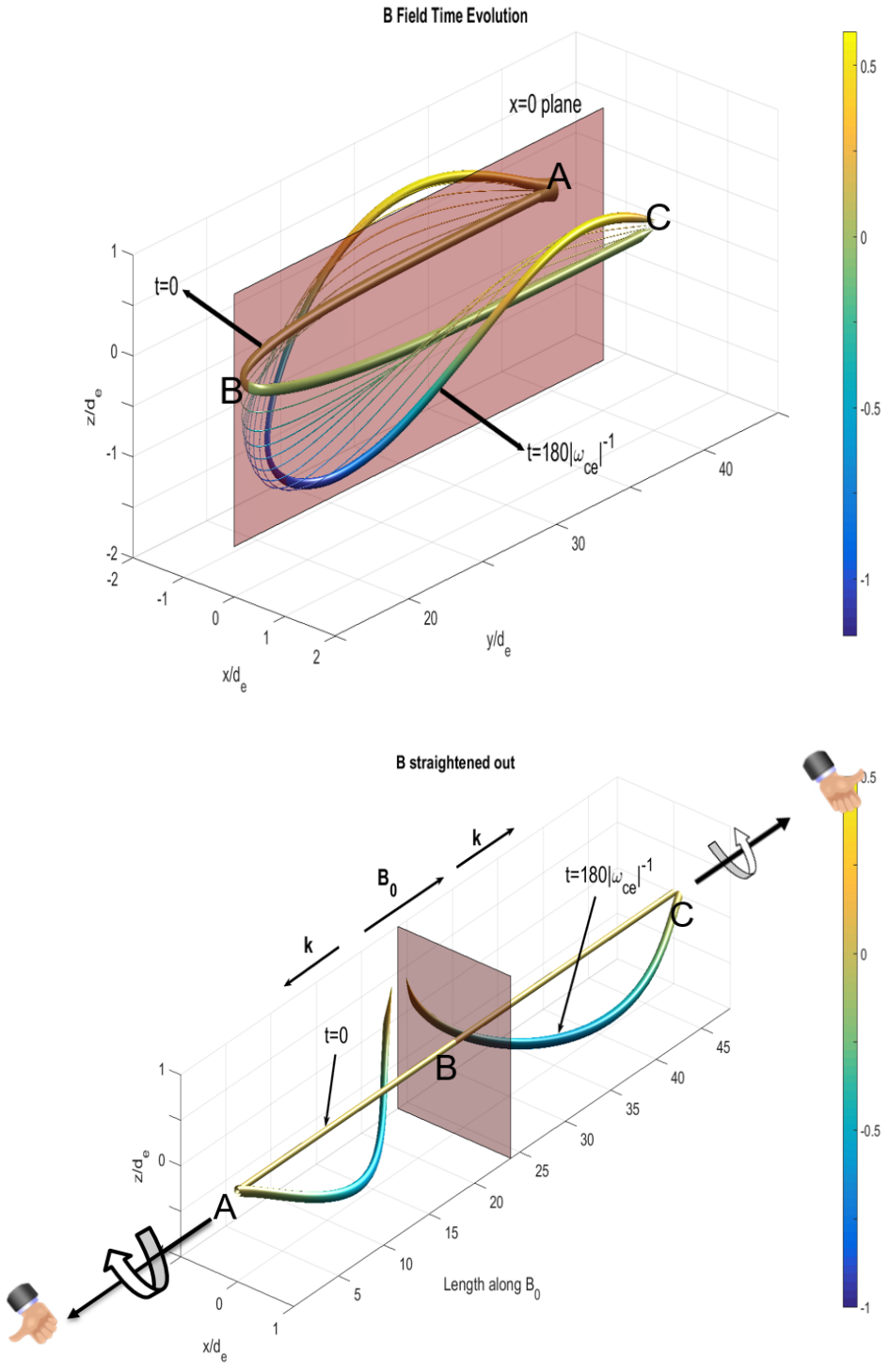

Figure 2.7: Temporal evolution of one of the reconnected magnetic field lines (e.g. red line in Figure 2.2). The bottom figure shows the same field lines when the initial field line is straighted out. The A, B, and Cs in both figures correspond to identical locations along the field line. The colors represent the height in z.

Chapter 3

ELECTRON CANONICAL BATTERY TERM: COMPLETION OF THE CANONICAL VORTICITY FRAMEWORK

In Chapter 2, the pressure term was dropped by either assuming low-β or isotropic and barotropic electron pressure. This allowed the expression of the electron equation of motion in the form of an ideal induction equation (Eq. 2.10). In this chapter, the effects of a finite pressure tensor will be investigated. By including the pressure tensor, the validity of the canonical vorticity framework extends to the Vlasov frame of reference (Section 1.2). It will be shown that the pressure tensor acts as a battery term that generates additional canonical vorticity, and that its competition with the convective term determines the structure and stability of the electron-diffusion-region (EDR; red box in Fig. 1.5).

The EDR structure during reconnection, which is strongly correlated with the shape of the electron out-of-plane flow, has long been a subject of controversy. It was initially presumed that stable electron-scale current layers could not exist because various instabilities would break up these layers [37, 43, 44]. However, spacecraft observations showed that, in fact, the EDR has a highly elongated stable structure [121]. The stability of this elongated structure was interpreted via numerical simulations as resulting from the divergence of the pressure tensor [79, 121, 137]. However, this interpretation assumed a zero initial out-of-plane **B** field (guide field) and later numerical simulations showed that a small guide field alters the structure completely [57]. Another study showed that different regimes of the EDR exist depending on a magnetization parameter [89].

In the completed canonical vorticity framework, these disparities are not only easily resolved but also unified. In fact, the examination of canonical vorticity dynamics is essential for the correct interpretation of the physical origin of the current structure. Different kinetic effects contribute to the canonical battery term, which then competes with the convective term to determine the progression of the electron canonical vorticity. This progression in turn determines the overall structure, evolution, and stability of the EDR. This framework provides a simpler and clearer alternative to the traditional approach where each of the multitude of terms in the electron momentum equation is examined separately.

3.1 The Completed Canonical Vorticity Framework

Assumption

The sole assumption is that the ions are stationary, which is valid for $L < d_i$ corresponding to the green box in Fig. 1.5. While the theory to be presented is similar in many respects to classical electron-magnetohydrodynamics (EMHD; Chapter 2) [25], the minimal restriction of this stationary-ion assumption causes the theory to differ substantively from EHMD because the assumption permits finite displacement current and the full electron pressure tensor $\mathbf{p}_e = m_e \int \mathbf{v}'_e \mathbf{v}'_e f(\mathbf{v}_e)\, d^3\mathbf{v}_e$ where $\mathbf{v}'_e$ is the random part of $\mathbf{v}_e$. Because new quantities will be introduced in this Chapter, unnormalized quantities will first be used and will be normalized later.

The Generalized Canonical Induction Equation

The electron equation of motion is

$$e\mathbf{E} + e\mathbf{u}_e \times \mathbf{B} = -m_e \frac{D\mathbf{u}_e}{Dt} - \frac{\nabla \cdot \overleftrightarrow{\mathbf{p}}_e}{n_e}. \tag{3.1}$$

Recall from Eq. 2.2 that the electron canonical vorticity is defined as

$$\mathbf{Q}_e = m_e \nabla \times \mathbf{u}_e - e\mathbf{B} = m_e \mathbf{w}_e - e\mathbf{B}, \tag{3.2}$$

where $\mathbf{w}_e = \nabla \times \mathbf{u}_e$ is the electron fluid vorticity. Then, Eq. 3.1 can be expressed as

$$e\mathbf{E} = \mathbf{u}_e \times \mathbf{Q}_e - m_e \frac{\partial \mathbf{u}_e}{\partial t} - m_e \nabla \left(\frac{u_e^2}{2} \right) - \frac{\nabla \cdot \overleftrightarrow{\mathbf{p}}_e}{n_e}. \tag{3.3}$$

Taking the curl of Eq. 3.3 and using Faraday's law $\nabla \times \mathbf{E} = -\partial \mathbf{B}/\partial t$ yields the *generalized canonical induction equation*

$$\frac{\partial \mathbf{Q}_e}{\partial t} = \nabla \times (\mathbf{u}_e \times \mathbf{Q}_e) - \nabla \times \left(\frac{\nabla \cdot \overleftrightarrow{\mathbf{p}}_e}{n_e} \right). \tag{3.4}$$

It should be noted that Eq. 3.4 is also valid for any plasma species.

The electron canonical vorticity dynamics governing electron physics is thus reduced to just the two terms on the right hand side of Eq. 3.4. The $\nabla \times (\mathbf{u}_e \times \mathbf{Q}_e)$ term is a convective term which prescribes that $\mathbf{Q}_e$ flux is frozen into $\mathbf{u}_e$, and thus provides an intuitive understanding of the temporal development of $\mathbf{Q}_e$ as demonstrated in Chapter 2. Since the convective term describes freezing-in of the vorticity flux to the flow, $-\nabla \times \left(\nabla \cdot \overleftrightarrow{\mathbf{p}}_e / n_e \right)$ is the only term in Eq. 3.4 that enables diffusion of $\mathbf{Q}_e$

Quantity	Normalization
t	$\|\omega_{ce}\|^{-1}$
$\mathbf{x}$	d_e
$\mathbf{u}_e$	$d_e\|\omega_{ce}\|$
$\mathbf{B}$	B_0
$\mathbf{Q}_e$	eB_0
$\mathbf{E}$	$d_e\|\omega_{ce}\|B_0$
$\overleftrightarrow{\mathbf{p}}_e$	B_0^2/μ_0
n_e	n_0

Table 3.1: Dimensional quantities and their normalization parameters in Chapter 3.

across $\mathbf{u}_e$ or vice-versa. This term will be called the "electron canonical battery" term because in the limit of isotropic pressure, i.e. $\overleftrightarrow{\mathbf{p}}_e = p_e\overleftrightarrow{\mathbf{I}} = n_eT_e\overleftrightarrow{\mathbf{I}}$,

$$-\nabla\times\left(\frac{\nabla p_e}{n_e}\right)=\frac{\nabla n_e\times\nabla T_e}{n_e} \tag{3.5}$$

is the Biermann battery term [14], and because $-\nabla\times\left(\nabla\cdot\overleftrightarrow{\mathbf{p}}_e/n_e\right)$ generates $\mathbf{Q}_e$ as indicated by Eq. 3.4. Since Eq. 3.1 results from the collisionless Vlasov equation without approximations, *Eq. 3.4 is kinetically exact.*

3.2 Fluid Simulation

In order to illustrate how the competition between the convective term and the canonical battery term governs magnetic reconnection, a fluid simulation was developed that includes compressibility, displacement current, and kinetic effects. Because of the added complexity, the relatively simple algorithm used in Section 2.3 cannot be used. A new algorithm was devised, whose details will now be illustrated.

Normalization of Relevant Equations

Quantities are normalized as follows: $\mathbf{B}$ to the background field strength B_0, length to d_e, time to $|\omega_{ce}|^{-1}$, $\overleftrightarrow{\mathbf{p}}_e$ to B_0^2/μ_0, density n_e to the background density n_0, and $\mathbf{E}$ to $v_{Ae}B_0 = d_e\,|\omega_{ce}|\,B_0$. A summary of the normalizations used in this chapter is illustrated in Table 3.1.

Dividing the equation of motion by $ed_e\left|\omega_{ce}\right|B_0$, we have

$$\frac{\mathbf{E}}{d_e\left|\omega_{ce}\right|B_0}+\frac{\mathbf{u}_e}{d_e\left|\omega_{ce}\right|}\times\frac{\mathbf{B}}{B_0}=-\frac{m_e}{eB_0d_e\left|\omega_{ce}\right|}\frac{D\mathbf{u}_e}{Dt}-\frac{\nabla\cdot\overleftrightarrow{\mathbf{p}}_e}{d_e\left|\omega_{ce}\right|B_0n_ee}, \tag{3.6}$$

$$\bar{\mathbf{E}}+\bar{\mathbf{u}}_e\times\bar{\mathbf{B}}=-\frac{D\bar{\mathbf{u}}_e}{D\bar{t}}-\frac{\nabla\cdot\overleftrightarrow{\mathbf{p}}_e}{d_e\left|\omega_{ce}\right|B_0n_ee}, \tag{3.7}$$

$$\bar{\mathbf{E}}+\bar{\mathbf{u}}_e\times\bar{\mathbf{B}}=-\frac{D\bar{\mathbf{u}}_e}{D\bar{t}}-\frac{m_e\bar{\nabla}\cdot\overleftrightarrow{\mathbf{p}}_e}{d_e^2B_0^2n_ee^2}, \tag{3.8}$$

$$\bar{\mathbf{E}}+\bar{\mathbf{u}}_e\times\bar{\mathbf{B}}=-\frac{D\bar{\mathbf{u}}_e}{D\bar{t}}-\frac{\mu_0\bar{\nabla}\cdot\overleftrightarrow{\mathbf{p}}_e}{\bar{n}_eB_0^2}, \tag{3.9}$$

$$\bar{\mathbf{E}}+\bar{\mathbf{u}}_e\times\bar{\mathbf{B}}=-\frac{D\bar{\mathbf{u}}_e}{D\bar{t}}-\frac{\bar{\nabla}\cdot\overleftrightarrow{\mathbf{p}}_e}{\bar{n}_e}, \tag{3.10}$$

where the barred quantities are dimensionless, and

$$\frac{m_e}{d_e^2e^2}=\frac{m_e\omega_{pe}^2}{c^2e^2}=\frac{m_en_0e^2}{m_e\epsilon_0c^2e^2}=n_0\mu_0 \tag{3.11}$$

was used.

Faraday's law is normalized as follows:

$$d_e\nabla\times\frac{\mathbf{E}}{d_e\left|\omega_{ce}\right|B_0}=-\frac{1}{\left|\omega_{ce}\right|B_0}\frac{\partial\mathbf{B}}{\partial t}, \tag{3.12}$$

$$\bar{\nabla}\times\bar{\mathbf{E}}=-\frac{\partial\bar{\mathbf{B}}}{\partial\bar{t}}. \tag{3.13}$$

Ampère's law, including the displacement current, is normalized as follows:

$$\frac{d_e}{B_0}\nabla\times\mathbf{B}=-\frac{d_e}{B_0}\mu_0n_ee\mathbf{u}_e+\frac{d_e}{B_0}\frac{1}{c^2}\frac{\partial\mathbf{E}}{\partial t}, \tag{3.14}$$

$$\bar{\nabla}\times\bar{\mathbf{B}}=-\frac{d_e\omega_{pe}^2}{\left|\omega_{ce}\right|c^2}\bar{n}_e\mathbf{u}_e+\frac{\left|\omega_{ce}\right|}{\omega_{pe}^2}\frac{\partial}{\partial t}\frac{\mathbf{E}}{d_e\left|\omega_{ce}\right|B_0}, \tag{3.15}$$

$$\bar{\nabla}\times\bar{\mathbf{B}}=-\bar{n}_e\bar{\mathbf{u}}_e+\frac{\omega_{ce}^2}{\omega_{pe}^2}\frac{\partial\bar{\mathbf{E}}}{\partial t}, \tag{3.16}$$

where $\mathbf{j}=-n_ee\mathbf{u}_e$ due to the stationary ion assumption.

The continuity equation is normalized as follows:

$$\frac{1}{n_0\left|\omega_{ce}\right|}\frac{\partial n_e}{\partial t}+d_e\nabla\cdot\left(\frac{n_e}{n_0}\frac{\mathbf{u}_e}{d_e\left|\omega_{ce}\right|}\right)=0, \tag{3.17}$$

$$\frac{\partial\bar{n}_e}{\partial\bar{t}}+\bar{\nabla}\cdot(\bar{n}_e\bar{\mathbf{u}}_e)=0. \tag{3.18}$$

Unless specified otherwise, the bars will be dropped to reduce notational clutter, and only normalized quantities and dimensionless equations will be used throughout this chapter.

Expression in terms of j

In order to facilitate the application of the algorithm to be presented, the relevant equations must first be expressed in terms of the current density $\mathbf{j} = -n_e\mathbf{u}_e$ (recall that ions are assumed to be stationary). It is obvious how Faraday's Law, Ampère's law, and the electron continuity equation are expressed in terms of $\mathbf{j} = -n_e\mathbf{u}_e$, but how the equation of motion (Eq. 3.10) is expressed is not and so will be derived here.

Multiplying Eq. 3.10 by n_e,

$$n_e\mathbf{E} + n_e\mathbf{u}_e \times \mathbf{B} = -n_e\frac{\partial \mathbf{u}_e}{\partial t} - n_e\mathbf{u}_e \cdot \nabla\mathbf{u}_e - \nabla \cdot \overleftrightarrow{\mathbf{p}}_e, \tag{3.19}$$

$$n_e\mathbf{E} - \mathbf{j} \times \mathbf{B} = -n_e\frac{\partial \mathbf{u}_e}{\partial t} - \mathbf{u}_e\frac{\partial n_e}{\partial t} - \mathbf{u_e}\nabla \cdot (n_e\mathbf{u}_e) + \mathbf{j} \cdot \nabla\mathbf{u}_e - \nabla \cdot \overleftrightarrow{\mathbf{p}}_e, \tag{3.20}$$

$$n_e\mathbf{E} - \mathbf{j} \times \mathbf{B} = \frac{\partial \mathbf{j}}{\partial t} - \mathbf{u_e}\nabla \cdot (n_e\mathbf{u}_e) + \mathbf{j} \cdot \nabla\mathbf{u}_e - \nabla \cdot \overleftrightarrow{\mathbf{p}}_e, \tag{3.21}$$

$$n_e\mathbf{E} - \mathbf{j} \times \mathbf{B} = \frac{\partial \mathbf{j}}{\partial t} - \frac{\mathbf{j}}{n_e}\nabla \cdot \mathbf{j} - \mathbf{j} \cdot \nabla\frac{\mathbf{j}}{n_e} - \nabla \cdot \overleftrightarrow{\mathbf{p}}_e, \tag{3.22}$$

$$n_e\mathbf{E} - \mathbf{j} \times \mathbf{B} = \frac{\partial \mathbf{j}}{\partial t} - \nabla \cdot \left(\frac{\mathbf{jj}}{n_e}\right) - \nabla \cdot \overleftrightarrow{\mathbf{p}}_e. \tag{3.23}$$

Therefore, the set of relevant dimensionless equations are

$$\begin{aligned}
\frac{\partial \mathbf{B}}{\partial t} &= -\nabla \times \mathbf{E}, \\
\frac{\partial \mathbf{E}}{\partial t} &= \frac{\omega_{pe}^2}{\omega_{ce}^2}(\nabla \times \mathbf{B} - \mathbf{j}), \\
\frac{\partial n_e}{\partial t} &= \nabla \cdot \mathbf{j}, \\
\frac{\partial \mathbf{j}}{\partial t} &= n_e\mathbf{E} - \mathbf{j} \times \mathbf{B} + \nabla \cdot \left(\frac{\mathbf{jj}}{n_e}\right) + \nabla \cdot \mathbf{p}_e.
\end{aligned} \tag{3.24}$$

The set of Eqs. 3.24 solves Eq. 3.4 exactly and includes finite displacement current and non-uniform density.

Numerical Method

The numerical method is a two-dimensional finite-domain time-difference (FDTD) method [167]. The spatial grid is a 2D staggered grid, or the 2D Yee grid [167], as shown in Fig. 3.1; the x and y components are defined on the edges, the z component is defined at the center, and scalars are defined at the corners. For example, the z-component of a curl is computed as, for any vector $\mathbf{V}$ and its curl $\mathbf{W} = \nabla \times \mathbf{V}$,

$$(W_z)_{i,j} = \frac{(V_y)_{i+1/2,j} - (V_y)_{i-1/2,j}}{\Delta x} - \frac{(V_x)_{i,j+1/2} - (V_y)_{i,j-1/2}}{\Delta y}. \tag{3.25}$$

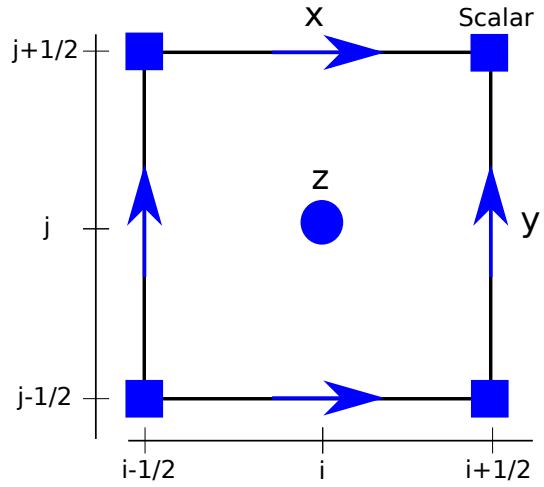

Figure 3.1: The staggered spatial grid used for the fluid simulation.

This grid allows for a second-order accuracy ($\sim \Delta x^2$) in spatial derivatives, and satisfies the divergence-free condition of **B** to floating point precision.

The time grid is also staggered as shown in Fig. 3.2; **B** and **j** are defined on integer time steps, and **E**, n_e, and $\overleftrightarrow{\mathbf{p}}_e$ are defined on half-integer time steps. The time derivatives of quantities on integer steps are defined on half-integer steps, and those of quantities on half-integer steps are defined on integer steps.

The time advancement algorithm is shown in Fig. 3.2 and can be described as follows.

1. Advance **B** in time using Faraday's law.
2. Calculate $\overleftrightarrow{\mathbf{p}}_e$ using a closure of choice relating $\overleftrightarrow{\mathbf{p}}_e$ to n_e and B. The average of B^t and B^{t+1} is used to obtain $B^{t+1/2}$.
3. **j** is advanced in time using an iterative procedure, which will be explained shortly.
4. Using the new values of **B** and **j** at $t + 1$, advance **E** using Ampère's law.
5. Similarly, advance n_e using the continuity equation.
6. Repeat.

In step 3, $\partial \mathbf{j}/\partial t$ depends on **j**, but the former is defined on half-integer time steps while the latter is defined on integer time steps. Therefore, an iterative procedure is

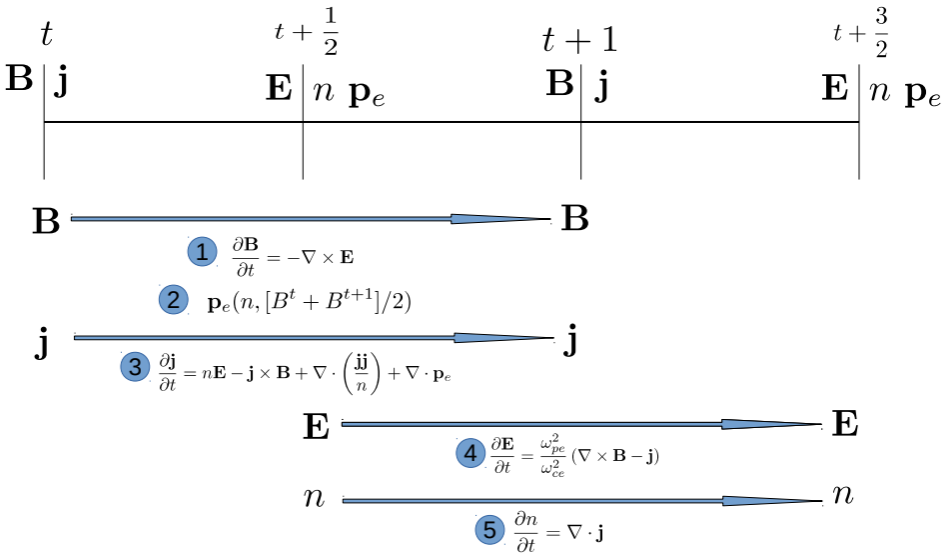

Figure 3.2: The staggered time grid and the time advancement algorithm for the fluid simulation.

used to solve the equation. Discretizing the equation for $\mathbf{j}$,

$$\frac{\mathbf{j}^{t+1}-\mathbf{j}^{t}}{\Delta t} = n_e\mathbf{E} - \frac{\mathbf{j}^{t+1}+\mathbf{j}^{t}}{2}\times\mathbf{B} + \nabla\cdot\left(\frac{\left[\mathbf{j}^{t+1}+\mathbf{j}^{t}\right]\left[\mathbf{j}^{t+1}+\mathbf{j}^{t}\right]}{4n_e}\right) + \nabla\cdot\overleftrightarrow{\mathbf{p}}_e, \tag{3.26}$$

where quantities without superscripts are all defined at half-integer time steps, and $\mathbf{B}^{t+1/2} = \left(\mathbf{B}^{t}+\mathbf{B}^{t+1}\right)/2$. This is then iteratively solved for $\mathbf{j}^{t+1}$, i.e.,

$$\frac{\mathbf{j}_{n+1}^{t+1}-\mathbf{j}^{t}}{\Delta t} = n_e\mathbf{E} - \frac{\mathbf{j}_{n}^{t+1}+\mathbf{j}^{t}}{2}\times\mathbf{B} + \nabla\cdot\left(\frac{\left[\mathbf{j}_{n}^{t+1}+\mathbf{j}^{t}\right]\left[\mathbf{j}_{n}^{t+1}+\mathbf{j}^{t}\right]}{4n_e}\right) + \nabla\cdot\overleftrightarrow{\mathbf{p}}_e, \tag{3.27}$$

where the subscript n denotes the iteration number, and $\mathbf{j}_0^{t+1} = \mathbf{j}^t$. For the reconnection problem, it took 5 to 10 iterations before the solution converged to within floating point precision.

Kinetic Effects

Two different kinetic effects are considered, namely pressure anisotropy and electron viscosity. Pressure anisotropy is modeled using the following closure which is described in Egedal et al. [49] and Le et al. [88]:

$$\tilde{p}_{e\parallel} = \tilde{n}_e\frac{2}{2+\alpha} + \frac{\pi\tilde{n}_e^3}{6\tilde{B}^2}\frac{2\alpha}{2\alpha+1}, \tag{3.28}$$

$$\tilde{p}_{e\perp} = \tilde{n}_e\frac{1}{1+\alpha} + \tilde{n}_e\tilde{B}\frac{\alpha}{\alpha+1}. \tag{3.29}$$

In Eqs. 3.28 and 3.29 the tilde represents normalization to far upstream values (e.g., $\tilde{n}_e = n_e/n_0$) and the parameter $\alpha = \tilde{n}_e^3/\tilde{B}^2$ acts as a switch between having an isothermal (small α) or a double adiabatic (large α) equation of state. Equations 3.28 and 3.29 are approximations of second order moments of an electron distribution function derived from an analysis of electron trapping by a combination of parallel electric fields and magnetic mirrors. The situation where $\alpha \gg 1$ represents trapped electrons because magnetic mirrors trap electrons at regions of low **B** and these trapped electrons increase the local electron density. The trapped electrons conserve their first and second adiabatic invariants and thus obey Chew-Goldberg-Low [35] closure. On the other hand, $\alpha \ll 1$ represents untrapped electrons that provide an isothermal closure. This closure given by Eqs. 3.28 and 3.29, valid in the regime $v_{Te} \gg v_A$, enables fluid models to exhibit kinetic effects missing from an isotropic pressure closure by allowing for pressure anisotropy to have both spatial and temporal dependence as given by the local instantaneous value of α [111].

Equations 3.28 and 3.29 contribute to the pressure tensor as

$$\overleftrightarrow{\mathbf{p}}_{e,aniso} = p_{e\perp}\overleftrightarrow{\mathbf{I}} + \frac{\left(p_{e\parallel} - p_{e\perp}\right)}{B^2}\mathbf{BB}, \tag{3.30}$$

$$= p_{e\perp}\overleftrightarrow{\mathbf{I}} + \sigma\mathbf{BB}. \tag{3.31}$$

The effect of electron viscosity is expressed as

$$\overleftrightarrow{\mathbf{p}}_{e,vis} = -\mu\nabla\mathbf{u}_e, \tag{3.32}$$

where μ is the dynamic viscosity. Because conventional viscosity is in many cases negligible, μ represents an effective viscosity that includes, for example, turbulent viscosity [23] and/or hyper-resistivity [143]. The total pressure tensor is then the sum of the partial pressures; i.e., $\mathbf{p}_e = \mathbf{p}_{e,aniso} + \mathbf{p}_{e,vis}$.

Initial Conditions

The simulation was initiated by imposing a magnetic perturbation in the form of Eq. 2.39 on a periodic force-free equilibrium used in Drake [42] and Ohia et al. [111], given by

$$B_y \simeq \tanh\left(\frac{x}{\lambda}\right) - \tanh\left(\frac{x - x_{max}/2}{\lambda}\right) - 1, \tag{3.33}$$

$$B_z = \sqrt{1 + B_g^2 - B_y^2\,(x)}, \tag{3.34}$$

where x_{max} is the size of the domain, B_g is the out-of-plane field far from the reconnection region, and λ is the half-thickness of the shear and $\lambda \ll x_{max}$. Equation

3.33 characterizes two separate current sheets, but only one of the sheets is examined; the second current sheet just facilitates the application of the periodic boundary conditions used in the simulation. Equation 3.34 characterizes a guide field that renders $B^2 = B_y^2 + B_z^2$ uniform everywhere. Uniform initial pressure and density are also imposed, so the equilibrium system is initially force-free. The system is solved in 2.5D where $\partial/\partial z = 0$, and the grid size is 512×1024 with 25 grid points per d_e in the x direction and 10 per d_e in the y direction. Fixed parameters are $\omega_{ce}/\omega_{pe} = 1/2$, $B_g = 0.4$, and $\lambda = 2$. This extremely thin current sheet not only models the small scale of the EDR, but is also highly relevant in space plasma phenomena such as electron-only reconnection in the turbulent magnetosheath [122].

3.3 Particle-in-cell Simulation

Simulating plasmas by following every single particle is practically impossible with the contemporary computing power due to the typically astronomical number of particles involved. A particle-in-cell (PIC) simulation is a practical alternative and follows the trajectories of a much smaller number of quasi-particles that each represents a collection of real particles. These quasi-particles have an artificially-imposed shape function S that represents how each quasi-particle motion affects values on the numerical grid. More specifically, the distribution function of each species is

$$f_\sigma(\mathbf{x}, \mathbf{p}, t) = \sum_{p=1}^{N} w_p S(\mathbf{x} - \mathbf{x}_p)\delta(\mathbf{p} - \mathbf{p}_p), \tag{3.35}$$

where $p \in [1, N]$ is the quasi-particle number, w_p is the statistical weight of the particle, and $\mathbf{x}_p$ and $\mathbf{p}_p$ are respectively the position and momentum of each particle. This distribution function can be used to calculate ρ and $\mathbf{j}$ using the following relations:

$$\rho(\mathbf{x}, t) = \sum_\sigma q_\sigma \int f_\sigma(\mathbf{x}, \mathbf{p}, t) d^3\mathbf{p}, \tag{3.36}$$

$$\mathbf{j}(\mathbf{x}, t) = \sum_\sigma q_\sigma \int \mathbf{v} f_\sigma(\mathbf{x}, \mathbf{p}, t) d^3\mathbf{p}. \tag{3.37}$$

These are used to calculate $\mathbf{E}$ and $\mathbf{B}$, which are in turn used to advance the quasi-particles in time using the relativistic equation of motion for each quasi-particle:

$$\frac{d\mathbf{x}}{dt} = \frac{\mathbf{p}}{\gamma m_\sigma}, \tag{3.38}$$

$$\frac{d\mathbf{p}}{dt} = q_\sigma \left(\mathbf{E} + \frac{\mathbf{p}}{\gamma m_\sigma} \times \mathbf{B} \right), \tag{3.39}$$

where $\gamma = \sqrt{1 + p^2/m_\sigma^2 c^2}$ is the Lorentz factor of the quasi-particle. The new positions and momenta can be used to calculate f_σ again, and the process can be repeated. A PIC simulation is usually considered to have the capability to resolve physical phenomena down to first-principles, although extreme caution is required when equating these simulations to real-life situations because inevitable limitations exist such as numerical dissipation and error.

In order to verify the results from the fluid simulation, the open-source PIC code SMILEI [41] was used to simulate reconnection with the same parameters as the fluid simulation. The realistic ion to electron mass ratio, $m_i/m_e = 1836$, was used with $\sim 2 \times 10^8$ ions and the same number of electrons. The results from the fluid simulation are mainly presented because of the ability to include, exclude, or control particular physics, and because of the clarity of presentation.

3.4 Results

Viscosity Dependence

We first examine how electron viscosity affects the evolution of $\mathbf{Q}_e$. First recall from Chapter 2 and Eq. 2.27 that $\mathbf{Q}_e \simeq -\mathbf{B}$ for $\nabla^{-1} \sim L \gg 1$ whereas $\mathbf{Q}_e \simeq \mathbf{w}_e$ for $L \ll 1$. For regions where $L \sim 1$ such as the EDR, both $\mathbf{w}_e$ and $\mathbf{B}$ are important. Now, electron viscosity contributes to the canonical battery term as

$$-\nabla \times \left(\frac{\nabla \cdot [-\mu \nabla \mathbf{u}_e]}{n_e} \right) = \nabla \times \left(\frac{\mu \nabla^2 \mathbf{u}_e}{n_e} \right) \simeq \frac{\mu \nabla^2 \mathbf{w}_e}{n_e}, \tag{3.40}$$

assuming density variations are not too large. If $L \ll 1$ so that $\mathbf{Q}_e \simeq \mathbf{w}_e$ and thus $\nabla^2 \mathbf{w}_e \simeq \nabla^2 \mathbf{Q}_e$, Eq. 2.10 becomes

$$\frac{\partial \mathbf{Q}_e}{\partial t} = \nabla \times (\mathbf{u}_e \times \mathbf{Q}_e) + \frac{\mu}{n_e} \nabla^2 \mathbf{Q}_e, \tag{3.41}$$

which has the same form as the resistive-MHD induction equation (Eq. 1.49),

$$\frac{\partial \mathbf{B}}{\partial t} = \nabla \times (\mathbf{U} \times \mathbf{B}) + \frac{\eta}{\mu_0} \nabla^2 \mathbf{B}. \tag{3.42}$$

Thus at electron scales, electron viscosity allows $\mathbf{Q}_e$ to reconnect, similar to how resistivity allows $\mathbf{B}$ to reconnect.

Figure 3.3 shows, for three different values of viscosity, the out-of-plane electron flow u_{ez} (color), in-plane $\mathbf{B}$ (black lines), and in-plane $\mathbf{Q}_e$ (red lines) for a situation with isotropic pressure (initially $\beta_e = 0.3$). Note that the orientation of the plots is rotated by 90° in comparison to those in Chapter 2 to conform to the popular

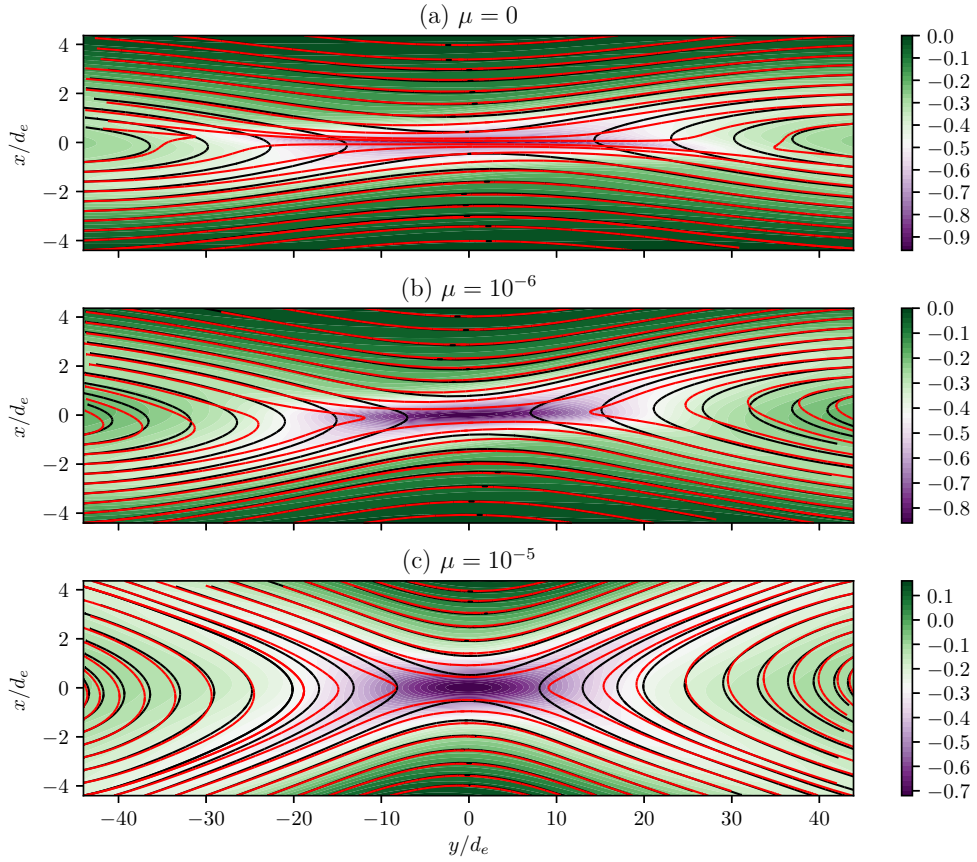

Figure 3.3: In-plane $\mathbf{Q}_e$ (red), in-plane $\mathbf{B}$ (black) and u_{ez} (color) for varying μ values and isotropic pressure at t = (a) 380, (b) 450, (c) 560.

orientation in the literature. The shape of the EDR corresponds to the shape of the purple color. Different times are chosen for each viscosity value because viscosity changes how much time is required for the EDR to display its characteristic structure. For $\mu = 0$ (Fig. 3.3a) the system is ideal, so $\mathbf{Q}_e$ lines remain connected and pile up near the $x = 0$ line in contrast to $\mathbf{B}$ lines which reconnect, as seen in Chapter 2. For finite μ (Figs. 3.3b and 3.3c), $\mathbf{Q}_e$ lines reconnect as well.

It is apparent from Fig.3.3 that the out-of-plane electron current structure (i.e., color contours) is well manifested by in-plane $\mathbf{Q}_e$ but not by $\mathbf{B}$ — a feature that is an important advantage of using $\mathbf{Q}_e$ over $\mathbf{B}$ at electron scales. Fine structures (i.e. small L) of $\mathbf{u}_e$ are not manifested by $\mathbf{B}$ because $|\mathbf{B}| \sim |\mathbf{j}|\, L \sim |\mathbf{u}_e|\, L$ by Ampére's law, whereas they are well manifested by $\mathbf{Q}_e$ because $|\mathbf{Q}_e| \sim |\mathbf{u}_e|\, /L$.

Another important feature is that the local increase of Q_{ey} shear corresponds to the local increase of u_{ez}. To illustrate this point we consider the implications

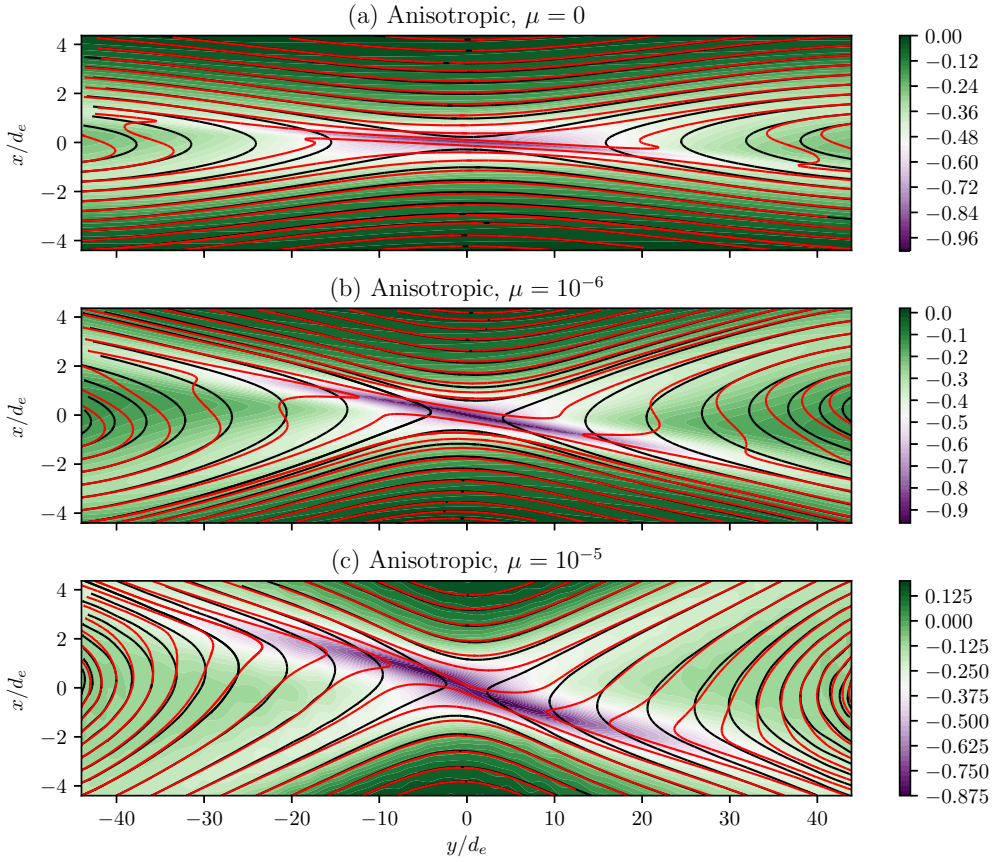

Figure 3.4: Same as Fig. 3.3 with pressure anisotropy and varying μ values at t = (a) 400, (b) 500, (c) 630.

of an assumed hypothetical toy scenario where $Q_{ey} \sim A(t)\, x \exp\left(-x^2\right)$ where $A(t)$ increases in time. This profile represents locally sheared Q_{ey}. Using $u_{ez} = -\int w_{ey} dx \simeq -\int Q_{ey} dx$ for $L \ll 1$ gives $u_{ez} \sim A(t) \exp\left(-x^2\right)$, corresponding to a local increase in u_{ez}.

Anisotropy Dependence

We next examine how pressure anisotropy affects $\mathbf{Q}_e$. In order to bring the system to an anisotropy-driven state faster, an initial pressure anisotropy with $\beta_{e\parallel} = 0.6$ and $\beta_{e\perp} = 0.1$ was imposed. The results for different μ are shown in Figs. 3.4a-c. In comparison to the isotropic case it is seen that pressure anisotropy greatly distorts the in-plane $\mathbf{Q}_e$ lines so that they pile up in the upper-left and lower-right quadrants; this corresponds to the anisotropic regime in Ohia et al. [111]. Again, the out-of-plane current structure is correlated with $\mathbf{Q}_e$ rather than with $\mathbf{B}$; u_{ez} is enhanced at locations where Q_{ey} is sheared. The distortion of $\mathbf{Q}_e$ field lines and the

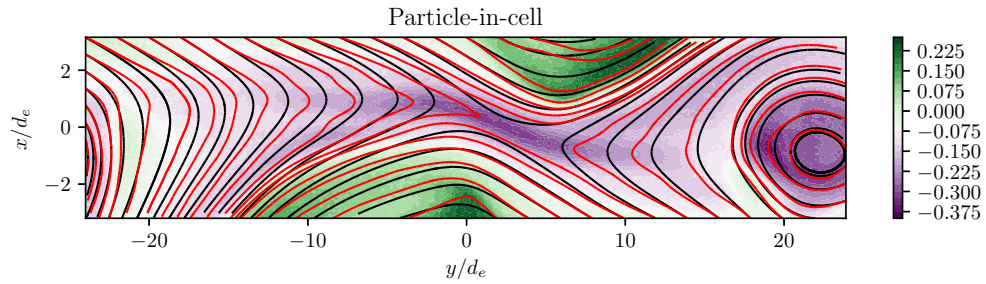

Figure 3.5: Same as 3.3 from the particle-in-cell simulation at $t = 300$.

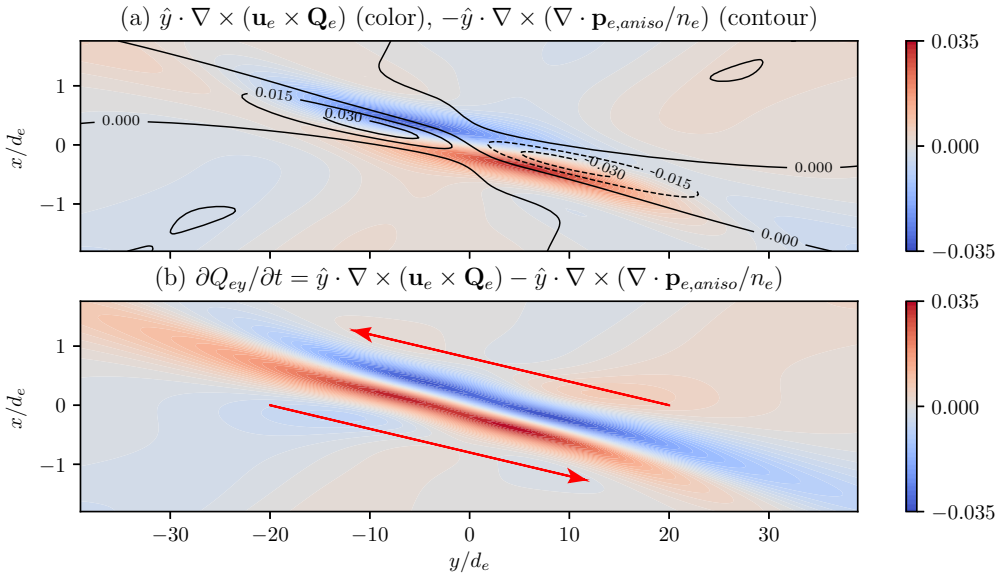

Figure 3.6: (a) The y-component of the convective term $\hat{y} \cdot \nabla \times (\mathbf{u}_e \times \mathbf{Q}_e)$ (color) and the anisotropic contribution to the canonical battery term $-\hat{y} \cdot \nabla \times \left(\nabla \cdot \mathbf{p}_{e,aniso}/n_e\right)$ (contour) for the simulation corresponding to Fig. 3.4b. (b) The sum of $\hat{y} \cdot \nabla \times (\mathbf{u}_e \times \mathbf{Q}_e)$ and $-\hat{y} \cdot \nabla \times \left(\nabla \cdot \mathbf{p}_{e,aniso}/n_e\right)$, which is equal to $\partial Q_{ey}/\partial t$. The red arrows represent the direction of Q_{ey}.

corresponding elongation and tilt of the out-of-plane current are reproduced by the PIC simulation, as shown in Fig. 3.5.

The anisotropic contribution to the electron canonical battery term explains the origin of the distortion of $\mathbf{Q}_e$ and equivalently of the elongation of u_{ez}. Figure 3.6a shows the convective term $\hat{y} \cdot \nabla \times (\mathbf{u}_e \times \mathbf{Q}_e)$ (color) and the battery term $-\hat{y} \cdot \nabla \times \left(\nabla \cdot \mathbf{p}_{e,aniso}/n_e\right)$ (contour). Figure 3.6b shows the sum of the two terms which is equal to $\partial Q_{ey}/\partial t$, and the red arrows show the direction of Q_{ey}. It can be seen that $-\hat{y} \cdot \nabla \times \left(\nabla \cdot \mathbf{p}_{e,aniso}/n_e\right)$ adds to $\hat{y} \cdot \nabla \times (\mathbf{u}_e \times \mathbf{Q}_e)$ and increases the spatial

extent of $\partial Q_{ey}/\partial t$; this in turn elongates the structure of u_{ez}.

To further understand the distortion of $\mathbf{Q}_e$ due to anisotropy, we examine the anisotropic contribution to the canonical battery term, which is equal to

$$\begin{aligned} -\nabla \times \left(\nabla \cdot \mathbf{p}_{e,aniso}/n_e\right) &\simeq -\nabla \times \left(\nabla \cdot [\sigma \mathbf{B}\mathbf{B}]\right) \\ &= -\nabla \times \left(\mathbf{B}\left[\mathbf{B} \cdot \nabla\sigma\right] + \sigma \mathbf{B} \cdot \nabla \mathbf{B}\right). \end{aligned} \tag{3.43}$$

Since an increase of Q_{ey} shear corresponds to an increase in u_{ez}, we consider the y-component of the canonical induction equation (Eq. 3.4) and thus of Eq. 3.43 which is

$$\frac{\partial}{\partial x}\left(\mathbf{B}[\mathbf{B} \cdot \nabla\sigma] + \sigma \mathbf{B} \cdot \nabla \mathbf{B}\right)_z = \frac{\partial}{\partial x}\left(B_z[\mathbf{B} \cdot \nabla\sigma] + \sigma \mathbf{B} \cdot \nabla B_z\right). \tag{3.44}$$

Here, σ depends on $|\mathbf{B}|$ and B_z is of the same order of magnitude as B_y. Therefore, since B_y has the shortest spatial scale of the components of $\mathbf{B}$, it follows that $|\nabla\sigma|/\sigma \gg |\nabla B_z|/B_z$, so

$$\frac{\partial}{\partial x}\left(B_z[\mathbf{B} \cdot \nabla\sigma] + \sigma \mathbf{B} \cdot \nabla B_z\right) \simeq \frac{\partial(B_z[\mathbf{B} \cdot \nabla\sigma])}{\partial x} \simeq B_z \frac{\partial \mathbf{B} \cdot \nabla\sigma}{\partial x}. \tag{3.45}$$

Therefore, we have

$$-\hat{y} \cdot \nabla \times \left(\frac{\nabla \cdot \mathbf{p}_{e,aniso}}{n_e}\right) \simeq B_z \frac{\partial \mathbf{B} \cdot \nabla\sigma}{\partial x} \tag{3.46}$$

Figure 3.7 shows various quantities involved in the calculation of $B_z \partial\left[\mathbf{B} \cdot \nabla\sigma\right]/\partial x$. The quadrupole out-of-plane Hall fields (plus and minus signs in Fig. 1.5) add and subtract to the background guide field B_z prescribed by Eq. 3.34. This, together with the reduction of $|\mathbf{B}|$ due to reconnection, generates a region of low $|\mathbf{B}|$ (Fig. 3.7a) with a pronounced tilt. Because $p_\parallel \sim n_e^3/B^2$ and $p_\perp \sim n_e B$, this $|\mathbf{B}|$ tilt generates a tilted region of finite σ (Fig. 3.7b; color). The quantity $\mathbf{B} \cdot \nabla\sigma$, which is the variation of σ along the in-plane $\mathbf{B}$ (Fig. 3.7b; lines), is shown in Fig. 3.7c (color), and its gradient $\nabla\left(\mathbf{B} \cdot \nabla\sigma\right) \simeq \hat{x}\partial\left[\mathbf{B} \cdot \nabla\sigma\right]/\partial x$ is represented by the black arrows. The resultant $-\hat{y} \cdot \nabla \times \left(\nabla \cdot \mathbf{p}_{e,aniso}/n_e\right) \simeq B_z \partial\left[\mathbf{B} \cdot \nabla\sigma\right]/\partial x$ is shown in Fig. 3.7d (contour). The convective term $\hat{y} \cdot \nabla \times (\mathbf{u}_e \times \mathbf{Q}_e)$ (Fig. 3.7d; color) enhances Q_{ey} shear (Fig. 3.7d; red arrows) as expected from Eq. 2.49, and $-\hat{y} \cdot \nabla \times \left(\nabla \cdot \mathbf{p}_{e,aniso}/n_e\right)$ further enhances this shear in spatial extent in the y direction. The resultant $\partial Q_{ey}/\partial t = \hat{y} \cdot \nabla \times (\mathbf{u}_e \times \mathbf{Q}_e) - \hat{y} \cdot \nabla \times \left(\nabla \cdot \mathbf{p}_{e,aniso}/n_e\right)$ is shown in Fig. 3.7e; this increase in Q_{ey} shear is the origin of the elongated out-of-plane flow u_{ez}.

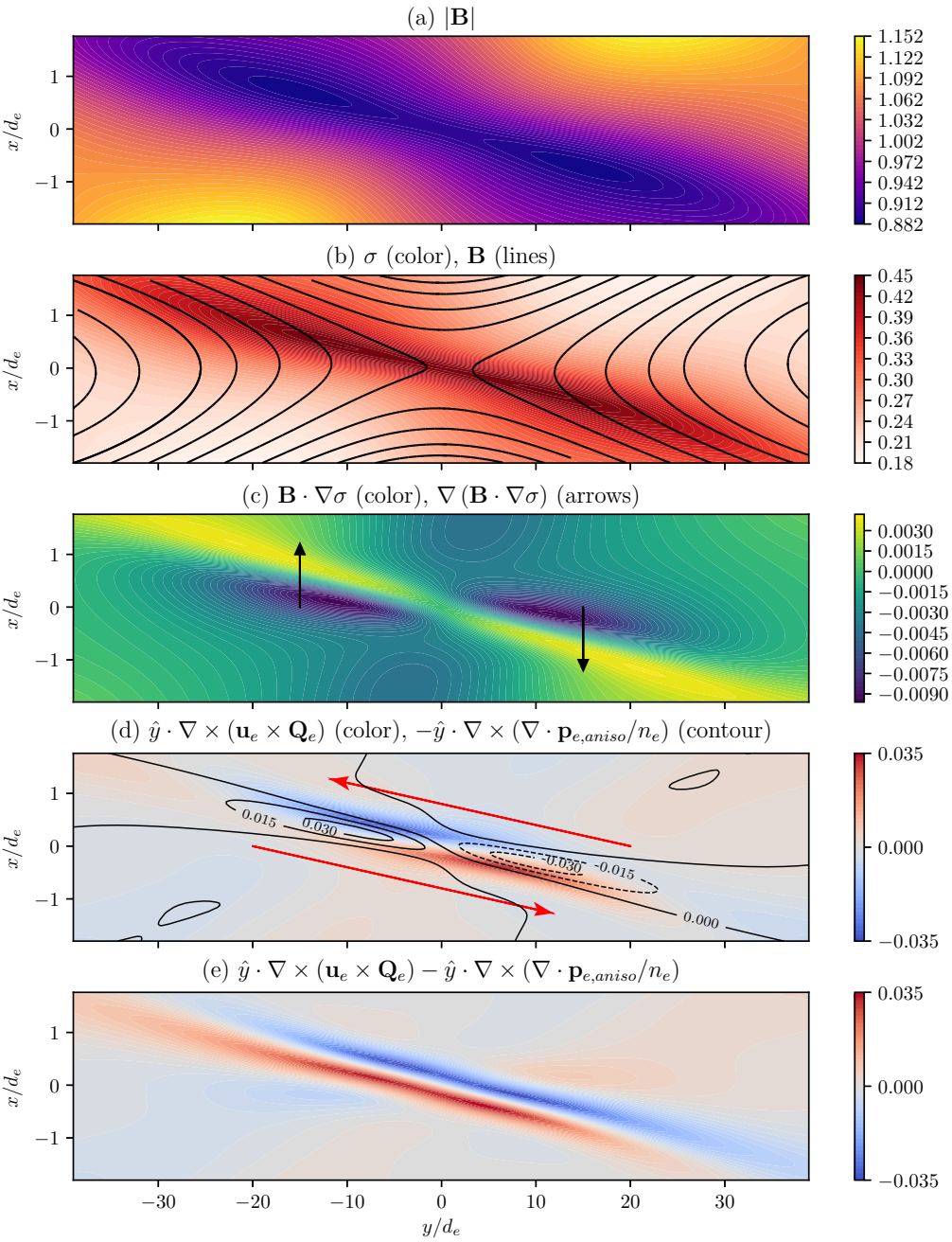

Figure 3.7: (a-c) Various quantities involved in the calculation of $-\hat{y}\cdot\nabla\times\left(\nabla\cdot\mathbf{p}_{e,aniso}/n_e\right)\simeq B_z\partial\left[\mathbf{B}\cdot\nabla\sigma\right]/\partial x$ for the simulation corresponding to Fig. 3.4b. (d) The y-component of the convective term $\hat{y}\cdot\nabla\times(\mathbf{u}_e\times\mathbf{Q}_e)$ and the anisotropic contribution to the canonical battery term $-\hat{y}\cdot\nabla\times\left(\nabla\cdot\mathbf{p}_{e,aniso}/n_e\right)$, and (e) their sum.

3.5 Discussion

The examination of $\mathbf{Q}_e$ dynamics and the electron canonical battery term is not only advantageous but in fact essential for the correct interpretation of a given EDR structure. For example, Ohia et al. [111] observed that imposing isotropic pressure deformed the out-of-plane current structure to be less elongated, which seemingly contradicts Fig. 3.3a. However, in Ohia et al. [111], an effective electron viscosity of 1.5×10^{-5} with the same normalized units as this study was imposed, approximately corresponding to Fig. 3.3c. Thus, it is not isotropic pressure that leads to an out-of-plane current localized at the origin; instead, the current localization results from the reconnection of $\mathbf{Q}_e$ by electron viscosity.

Another such example is the origin of elongated EDR structures. The elongated structure in Fig. 3.3a results from the pile-up of $\mathbf{Q}_e$ field lines due to the lack of significant electron viscosity, whereas the elongated structures in Fig. 3.4 result from pressure anisotropy. Therefore, in order to give correct physical interpretations, the scrutinization of the electron canonical battery term and the ensuing canonical vorticity dynamics is vital.

In Ohia et al. [111], it was found that the plasma approaches the firehose condition, which is the condition for the firehose instability [131], along the elongated current layer. This phenomenon can be simply explained by a direct comparison between the convective term and the electron canonical battery term. On scales $L > d_e$, the convective term goes like $\nabla\times(\mathbf{u}_e\times\mathbf{Q}_e)\simeq\nabla\times(\mathbf{u}_e\times\mathbf{B})\simeq-\nabla\times([\nabla\times\mathbf{B}]\times\mathbf{B})\sim B^2/L^2$, and the anisotropic contribution to the canonical battery term goes like $\nabla\times(\nabla\cdot[\sigma\mathbf{BB}])\sim\sigma B^2/L^2$. It follows that $\sigma\sim1$ or $\left(p_{e\parallel}-p_{e\perp}\right)/B^2\sim1$ in order for the two terms to be commensurate; thus, the parallel and perpendicular electron pressures approach the firehose criterion.

Equation 3.41 stipulates the condition for the instability of the EDR. Because $\mathbf{Q}_e\simeq\mathbf{w}_e$ for $L\ll1$, Eq. 3.41 is equivalent to the electron fluid vorticity equation

$$\frac{\partial\mathbf{w}_e}{\partial t}=\nabla\times(\mathbf{u}_e\times\mathbf{w}_e)+\frac{\mu}{n_e}\nabla^2\mathbf{w}_e. \tag{3.47}$$

It then naturally follows from fluid dynamics that turbulent flow develops at a sufficiently high Reynolds number $Re\sim n_e/\mu$. This unstable regime corresponds to the regimes in Drake et al. [44] and Del Sarto et al. [37]. All fluid runs and PIC runs eventually become unstable to turbulence, in accordance with Drake et al. [44] and Del Sarto et al. [37] in that electron-scale current sheets are unstable to various instabilities.

Equation 2.10 also clarifies the distinction between reconnection models where the magnetic field is broken only by electron inertia [27] and those where it is broken also by pressure tensor effects such as electron viscosity [69]. If only the electron inertia term is included, then the system is entirely described by the convective term in Eq. 2.10, whereas the electron viscosity is manifested by the electron canonical battery term. A possible scenario is that electron inertia breaks the magnetic fields during earlier times, but the EDR is subject to instabilities and turbulence due to the high Reynolds number at latter times. These instabilities increase the effective viscosity, which makes the canonical battery term break both the magnetic field and the canonical vorticity field. Whether a particular reconnection event is affected by mostly the convective term or by both the convective term and the canonical battery term depends on the parameters and the time-scale of the system.

The advantage of the canonical vorticity framework is now clear. The convective term in Eq. 2.10 signifies the convection of $\mathbf{Q}_e$ with $\mathbf{u}_e$, which intuitively explains reconnection electron physics for zero beta (no pressure), as in Chapter 2. One can then study how a particular kinetic effect, such as electron pressure anisotropy, viscosity, or distribution function foliation [97], influences reconnection by examining how that effect is manifested in the canonical battery term and then competes with the convective term. This is not only much simpler than examining multiple terms in the generalized Ohm's law (Eq. 1.34), but also exhaustive because Eq. 2.10 is a direct consequence of the collisionless Vlasov equation.

3.6 Summary

In summary, the electron canonical battery term completes the canonical vorticity framework of the electron physics in magnetic reconnection. As demonstration of the power of this approach, the growth, saturation, stability, and morphology of the EDR have been reinterpreted, expanded, and unified within this framework. In particular, the framework illustrates how the changes in the electron fluid closure (Eqs. 3.28 and 3.29) affect the current structure through the electron canonical battery term. The distinction between electron-inertia-driven and pressure-tensor-driven models of reconnection is also clearly demonstrated. The simple yet complete nature of this framework makes it an appealing alternative to the traditional magnetic-field-based approach to magnetic reconnection.

Chapter 4

STOCHASTIC ION HEATING IN MAGNETIC RECONNECTION

Magnetic reconnection is ultimately a process in which magnetic energy is converted to particle energies. Although magnetic reconnection has been the focus of many studies for decades, the mechanisms underlying this energy conversion from the magnetic field to particles are still poorly understood. In particular, anomalous ion heating much faster than conventional collisional heating has frequently been observed in various astrophysical and laboratory reconnection events [29, 50, 65, 74, 96, 117, 118, 124, 141, 168], and resolving the fundamental cause of this heating remains a crucial objective of reconnection research. The resolution of this problem is an important key to tackling critical conundrums such as the coronal heating problem [59], i.e., why the solar atmosphere is over a million degrees while the solar surface is only about a few thousand degrees.

Five features of ion heating are observed in reconnection simulations, experiments, and observations: (i) correlation with in-plane Hall electric fields [7, 120, 141, 168], (ii) temperature anisotropy ($T_{i\perp} \neq T_{i\parallel}$) [47, 70, 95, 103], (iii) non-conservation of the ion magnetic moment μ [46, 47, 82], (iv) preferential heating of ions with higher mass-to-charge ratios m_i/q_i [51, 106, 128], and (v) reduction of the heating amount under a finite guide field (background out-of-plane magnetic field) [46]. Since anomalous ion heating occurs over a broad range of plasma parameters, the heating mechanism is expected to involve physical quantities that are intrinsic to the reconnection process. So far, numerous mechanisms have been proposed to explain ion heating; examples include pick-up [46, 47], turbulent interaction [107, 138], interactions with fluctuating electric fields [51], remagnetization [168], and shocks or viscous damping [118]. However, the proposed mechanisms are still under serious debate; there is no general consensus among the community on what the fundamental ion heating mechanism is.

In this chapter, it is shown that stochastic ion heating is intrinsic to transient collisionless magnetic reconnection because stochastic ion heating will always occur at length scales smaller than the ion skin depth $d_i = c/\omega_{pi}$ when there is a perturbation of a Harris-type magnetic equilibrium [16, 66]. It is shown via analytic methods supplemented by numerical calculations that the in-plane electric fields near the magnetic

separatrices (lines that separate regions of reconnected and non-reconnected fields) satisfy the condition for stochastic ion heating. Thus, the correlation of anomalous heating with the in-plane Hall electric fields will be established; the other four features of ion heating in reconnection will be explicitly demonstrated in Chapter 5. The stochastic nature of ions will also be demonstrated via single-particle simulations. Comparisons to laboratory experiments support the analytical calculations presented here. Hall electric fields have been attributed to ion energization seen in previous numerical [7, 46, 125], observational [162] and experimental [141, 168] reconnection studies, but the specific mechanism linking the fields to the heating has not been identified.

4.1 Stochastic Heating

Stochastic heating occurs when a particle in a magnetic field is subject to a perpendicular potential gradient so strong that it causes a breakdown of the guiding-center approximation [10, 11, 108, 142]. The particle then experiences a large potential difference within an orbital period and its motion becomes chaotic. When this happens to a large number of particles, the velocity distribution function broadens and this broadening is observationally equivalent to heating. Stochastic heating has been proposed to be an ion heating source in the solar wind via Alfvén wave interactions [22, 30, 31, 142, 156–159] and has been observed in laboratory experiments [29, 108, 133] . The threshold in Coulomb gauge for ion stochastic heating is [10, 108, 142],

$$\alpha = \frac{m_i}{q_i \left|\mathbf{B}\right|^2} \left|\nabla_\perp^2 \phi\right| = \frac{m_i}{q_i \left|\mathbf{B}\right|^2} \left|\nabla_\perp \cdot \mathbf{E}_\perp\right| > 1, \tag{4.1}$$

where ϕ is the electrostatic potential and $\nabla_\perp$ is the gradient perpendicular to $\mathbf{B}$.

Breakdown of the Guiding-Center Approximation

In order to understand this mechanism, consider particle guiding-center motion under the electromagnetic fields

$$\mathbf{E} = E\hat{y} \sin\left(ky - \omega t\right), \tag{4.2}$$

$$\mathbf{B} = B\hat{z}. \tag{4.3}$$

The $\mathbf{E} \times \mathbf{B}$ drift is

$$\mathbf{v}_E = \frac{\mathbf{E} \times \mathbf{B}}{B^2} = \hat{x}\frac{E}{B} \sin\left(ky - \omega t\right), \tag{4.4}$$

and the polarization drift is

$$\mathbf{v}_p = \frac{m}{qB^2}\frac{d\mathbf{E}_\perp}{dt}, \tag{4.5}$$

$$= \hat{y}\frac{mE}{qB^2}\frac{d}{dt}\sin(ky - \omega t), \tag{4.6}$$

$$= \hat{y}\frac{mE}{qB^2}\left(k\frac{dy}{dt} - \omega\right)\cos(ky - \omega t). \tag{4.7}$$

Here, $dy/dt = v_y$ is the velocity in the y-direction. Since $\mathbf{v}_E$ is in the x-direction and $\mathbf{v}_p$ is in the y-direction, $\hat{y}dy/dt = \mathbf{v}_p$. Solving Eq. 4.7 in terms of $\mathbf{v}_p$ gives

$$\mathbf{v}_p = -\hat{y}\frac{\omega mE}{qB^2}\frac{\cos(ky - \omega t)}{1 - \alpha\cos(ky - \omega t)}, \tag{4.8}$$

where

$$\alpha = \frac{mkE}{qB^2} \tag{4.9}$$

is the stochastic heating condition in Eq. 4.1 assuming that the particle is an ion and $|\nabla_\perp \cdot \mathbf{E}_\perp| \simeq kE$. It can clearly be seen from Eq. 4.8 that when $\alpha > 1$, the denominator vanishes when $\cos(ky - \omega t) = \alpha^{-1}$. However, when deriving the polarization drift in Section 1.1, it was explicitly assumed that $|d\mathbf{v}_E/dt| \gg |d\mathbf{v}_p/dt|$. Because $\mathbf{v}_E$ is finite as in Eq. 4.4, this assumption breaks down if $\mathbf{v}_p \to \infty$ along with the guiding-center approximation. The drift equations in Section 1.1 therefore cannot be used, and the magnetic moment μ is not conserved.

Chaotic Motion

It will now be shown that the satisfaction of Eq. 4.1 leads to chaotic particle motion. According to the concept of Lyapunov exponents [100], chaotic behavior entails the spatial divergence of two particles that have an infinitesimal initial separation in phase space. Now consider the motion of the spatial difference of two particles, $\delta\mathbf{r} = \mathbf{r}_1 - \mathbf{r}_2$ and its time derivatives. As above, the electric field is in the y-direction and the magnetic field is in the z-direction. The Lorentz force equation yields

$$\delta\ddot{x} = \frac{qB}{m}\delta\dot{y}, \tag{4.10}$$

$$\delta\ddot{y} = \frac{q}{m}\frac{\partial E}{\partial y}\delta y - \frac{qB}{m}\delta\dot{x}, \tag{4.11}$$

$$\delta\ddot{z} = 0. \tag{4.12}$$

Differentiating the second equation in time and substituting the first equation in,

$$\frac{d^3\delta y}{d^3t} = \frac{q}{m}\frac{\partial E}{\partial y}\frac{d\delta y}{dt} - \frac{q^2B^2}{m^2}\frac{d\delta y}{dt}, \tag{4.13}$$

$$\frac{d^3\delta y}{d^3t} = \frac{q}{m}\left(\frac{\partial E}{\partial y} - \frac{qB^2}{m}\right)\frac{d\delta y}{dt}, \tag{4.14}$$

which yields an exponentially growing solution for $d\delta y/dt$ when

$$\frac{m}{qB^2}\frac{\partial E}{\partial y} = \alpha > 1. \tag{4.15}$$

Therefore, satisfaction of Eq. 4.1 signifies that particles undergo chaotic motion.

Stochastic heating does not require the fields to be incoherent — it is a mechanism that causes particle trajectories to become chaotic in coherent fields. Thus, stochastic heating should not be confused with mechanisms where the fields themselves are stochastic. It should be noted, however, that there has been extensive work on ion acceleration via stochastic interaction with magnetic islands [48, 61, 72, 90, 91, 174, 175]. The present work shows that stochastic ion heating occurs at a single reconnection region, but it will also work in the context of stochastic fields with multiple reconnection regions if the condition in Eq. 4.1 remains satisfied.

4.2 Relevant Equations

We begin the analysis by noting that the electric field acting on the ions can be determined from the two-fluid electron equation of motion. Using this equation to prescribe the electric field is equivalent to invoking the generalized Ohm's law with the Hall, electron inertia, and electron pressure terms all included. The normalization of quantities is the same as in Chapter 3 and thus Table 3.1; the magnitude of the magnetic field far from the reconnection region is denoted B_0 and this defines a reference electron cyclotron frequency $\omega_{ce} = q_e B_0/m_e$. On normalizing length by the electron collisionless skin depth $d_e = c/\omega_{pe}$, time by $|\omega_{ce}|^{-1}$, magnetic field by B_0, density by the background density n_0, electric field by $d_e\,|\omega_{ce}|\,B_0$, and pressure by B_0^2/μ_0, the two-fluid electron equation of motion can be expressed as

$$\bar{\mathbf{E}} + \bar{\mathbf{u}}_e \times \bar{\mathbf{B}} = -\frac{D\bar{\mathbf{u}}_e}{D\bar{t}} - \frac{\bar{\nabla}\bar{p}_e}{\bar{n}_e}, \tag{4.16}$$

where barred quantities are dimensionless. The pressure has been assumed to be scalar. To reduce clutter, the bars will be dropped from now on. Under this normalization, Eq. 4.1 becomes

$$\frac{1}{\varepsilon B^2}\left|\nabla_\perp^2\phi\right| > 1, \tag{4.17}$$

where $\varepsilon = m_e/m_i$ is the electron-to-ion mass ratio.

Recall from Chapter 2 that assuming negligible pressure term by positing either cold electrons (low β_e) or barotropic pressure, and invoking Faraday's law yield the ideal electron canonical induction equation:

$$\frac{\partial \mathbf{Q}_e}{\partial t} = \nabla \times (\mathbf{u}_e \times \mathbf{Q}_e), \tag{4.18}$$

where $\mathbf{Q}_e \equiv \nabla \times \mathbf{u}_e - \mathbf{B}$ is the electron canonical vorticity. An important consequence of Eq. 4.18 was that $\mathbf{Q}_e$ field lines remain connected whereas $\mathbf{B}$ field lines may reconnect.

It should be noted that as seen in Chapter 3, the canonical battery term can be important and will add an additional term to Eq. 4.18, allowing for the reconnection of $\mathbf{Q}_e$. However, this effect will be disregarded in the present analysis because omitting the canonical battery term keeps the analysis simple and enables focusing on more dominant effects. Also for simplicity, a zero guide-field will be assumed. It will be shown in Chapter 5 that this stochastic heating mechanism is still valid in the kinetic regime that includes the canonical battery term and under the presence of moderate guide fields.

Recall that by decomposing the convective derivative using $\mathbf{u}_e \cdot \nabla \mathbf{u}_e = \nabla u_e^2/2 - \mathbf{u_e} \times \nabla \times \mathbf{u_e}$, Equation 4.16 may be expressed in terms of $\mathbf{Q}_e$ rather than $\mathbf{B}$, i.e.,

$$\mathbf{E} = -\frac{\partial \mathbf{u}_e}{\partial t} + \mathbf{u}_e \times \mathbf{Q}_e - \nabla\left(\frac{u_e^2}{2}\right) - \frac{\nabla p_e}{n_e}. \tag{4.19}$$

The connected nature of $\mathbf{Q}_e$ will be now used to simplify Eq. 4.19 in a way that enables checking whether the condition given by Eq. 4.1 for stochastic ion heating is satisfied in transient reconnection situations. The cold electron assumption will be used so that the hydrodynamic pressure term in Eq. 4.19 may be ignored; justification for this assumption will be given later.

In Chapter 2, it was shown that the nominal growth rate of this system near the electron diffusion region (EDR) can be expressed in terms of gradients of components of the electron flow. It is seen from the definition of $\mathbf{Q}_e$ that $\nabla \cdot \mathbf{Q}_e = 0$ and it is also seen that $\nabla \cdot \mathbf{u}_e \sim \nabla \cdot \mathbf{J} \sim \nabla \cdot \nabla \times \mathbf{B} = 0$. Using these properties and $Q_{ex}\,(x = 0) = 0$, expansion of the y-component of Eq. 4.18 gives an exponentially growing solution for Q_{ey} with a growth rate

$$\frac{\partial}{\partial t} \simeq \frac{\partial u_{ey}}{\partial y} \simeq -\frac{\partial u_{ex}}{\partial x}. \tag{4.20}$$

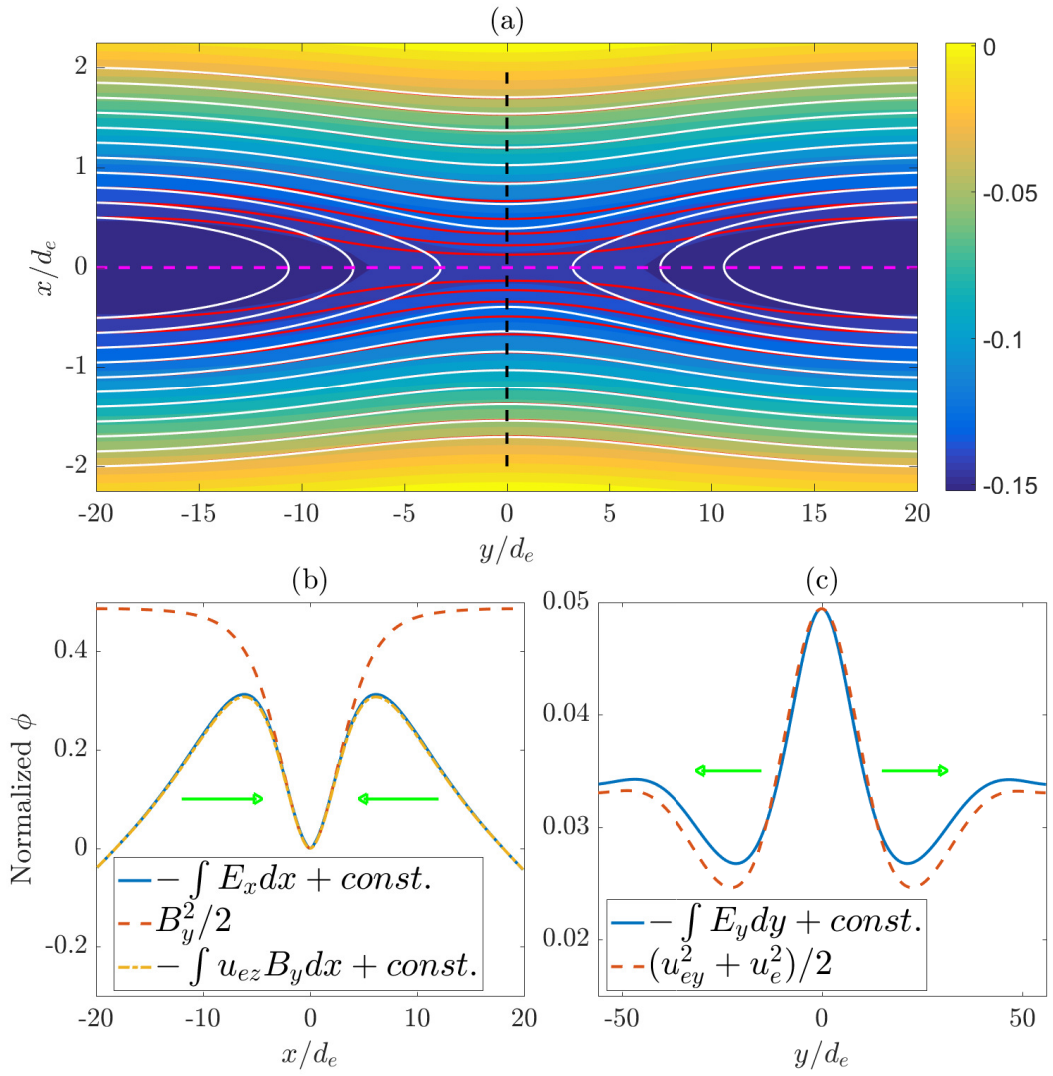

Figure 4.1: (a) Reconnected in-plane **B** field lines (white) and connected in-plane $\mathbf{Q}_e$ field lines (red) in the reconnection geometry. The effective potential (color) was calculated from the cold version of Eq. 4.19. The inflows and outflows are respectively in the $\pm x$ and $\pm y$ directions. The x-axis and the y-axis have different scales to show the field lines more evidently. (b) Comparison of $B_y^2/2$ with $-\int E_x dx$ and $-\int u_{ez} B_y dx$ along the black dotted line in (a). (c) Comparison of $\left(u_{ey}^2 + u_e^2\right)/2$ with $-\int E_y dy$ along the magenta line in (a).

The growth rate is always positive since $\partial u_{ey}/\partial y \simeq \partial^2 B_z/\partial x \partial y$ and the quadrupole out-of-plane Hall magnetic field has the dependence $B_z \sim xy$ in the EDR. This growth rate will be used to rewrite the $\partial \mathbf{u}_e/\partial t$ term in Eq. 4.19.

4.3 Numerical Simulation and Results

To validate the predictions of the model presented here, the EMHD simulation that was developed in Chapter 2.2 was used. Again, a perturbation to the background Harris-type magnetic field

$$B_y = \tanh \frac{x}{\lambda} \tag{4.21}$$

initialized the simulation.

Figure 4.1a shows the numerically calculated reconnected in-plane **B** field lines (white) and the connected in-plane $\mathbf{Q}_e$ field lines (red). The distinction between the reconnection of **B** and the non-reconnection of $\mathbf{Q}_e$ is clearly evident. Specifically, $B_x(x = 0)$ is finite but $Q_{ex}(x = 0) = 0$, so **B** reconnects but $\mathbf{Q}_e$ remains connected. The electric field is calculated numerically using the values of $\mathbf{u}_e$ and $\mathbf{Q}_e$ on the right-hand side of Eq. 4.19, and the associated electrostatic potential (color) is plotted for reference. The potential is saddle-shaped with contours approximately following the **B** field lines in agreement with previous simulations [46, 79, 125] and laboratory experiments [168].

4.4 Stochastic Heating Condition Analysis

Inflow

We first consider the inflow (i.e., flow on $y = 0$, black dashed line in Fig. 4.1a. The **B** field is in the y-direction here, so the perpendicular electric field relevant to stochastic heating is E_x. Although E_z is also perpendicular to B_y, we need not consider E_z for the purposes of analyzing stochastic heating because $\partial/\partial z = 0$ in 2D, so E_z is irrelevant to Eq. 4.1. Using the cold electron assumption (to be justified later), the x-component of Eq. 4.19 becomes

$$E_x = -\frac{\partial u_{ex}}{\partial t} + u_{ey}Q_{ez} - u_{ez}Q_{ey} - \frac{\partial}{\partial x}\left(\frac{u_e^2}{2}\right). \tag{4.22}$$

On invoking Eq. 4.20, the first term on the right-hand side of Eq. 4.22 is $-\partial u_{ex}/\partial t \simeq u_{ex}\partial u_{ex}/\partial x = \partial\left(u_{ex}^2/2\right)/\partial x$. The second term disappears because $u_{ey}(y = 0) = Q_{ez}(y = 0) = 0$ due to the antisymmetry of the outflow and the quadrupole nature of the out-of-plane $\mathbf{Q}_e$ fields as seen in Chapter 2. On expanding the third term using $Q_{ey} = -\partial u_{ez}/\partial x - B_y$ and the fourth term using $u_e^2 = u_{ex}^2 + u_{ez}^2$ at $y = 0$, Eq. 4.22 simplifies to

$$E_x = u_{ez}B_y \tag{4.23}$$

$$\simeq -\frac{\partial}{\partial x}\left(\frac{B_y^2}{2}\right). \tag{4.24}$$

In the last line, we have used $\mathbf{u}_e \simeq -\nabla \times \mathbf{B}$ so $u_{ez} = \partial B_x/\partial y - \partial B_y/\partial x$ and $\partial B_y/\partial x >> \partial B_x/\partial y$ in the EDR; these assumptions are true because $B_y > B_x$ and also $\partial/\partial x >> \partial/\partial y$. Therefore, $B_y^2/2$ acts as an effective electrostatic potential in the x-direction (this is equivalent to Eq. 3 in Li and Horiuchi [93]). This conclusion regarding the effective potential is shown graphically in Fig. 4.1b, where $-\int E_x dx$ and $-\int u_{ez} B_y dx$ are compared with $B_y^2/2$, calculated from the simulation. Outside the EDR, $\partial B_y/\partial x \longrightarrow 0$, so the approximation fails, but for the purposes of analyzing the slope of the potential valley into which the ions fall (ion inflow directions represented by the green arrows) and thus for the purpose of investigating the existence of stochastic heating, $B_y^2/2$ remains a good approximation for the electrostatic potential. The integration constant was set so that the three functions coincide at $x = 0$ in Fig. 4.1b.

Equation 4.17, the condition for ion stochasticity in the inflow direction, can thus be written as

$$\frac{1}{\epsilon B_y^2}\left|\frac{\partial^2}{\partial x^2}\left(\frac{B_y^2}{2}\right)\right| > 1. \tag{4.25}$$

Using $B_y(x) \simeq B_0 x/\lambda$ for $x < \lambda$ and $d_e^2/\varepsilon = d_i^2$, Eq. 4.25 in dimensioned quantities becomes $x^2 < d_i^2$. A sufficient condition to satisfy $x^2 < d_i^2$ while $x < \lambda$ is

$$\lambda^2 < d_i^2. \tag{4.26}$$

Therefore, at sub-ion-skin-depth length scales, at which collisionless reconnection occurs, the condition for stochastic heating in the inflow direction is satisfied.

The cold electron assumption in the inflow direction and thus the validity of Eq. 4.24 is justified by the fact that numerical [93] and experimental [168] studies show that the magnetic force on the electron fluid is balanced by the electric field corresponding to Eq. 4.23 and thus Eq. 4.24.

Outflow

We now consider the outflow (flow along the $x = 0$ line, magenta dashed line in Fig. 4.1a). Because the magnitude of $\mathbf{B}$ is very small on this line, the cold electron assumption in principle cannot be used. However, it will be shown later that including the electron pressure term has little effect on the stochasticity condition, so for now electrons will be assumed cold. Along the outflow (i.e., on the y-axis, $x = 0$), the magnetic field is in the x-direction, so the perpendicular electric field relevant to stochastic heating is E_y. The magnetic field component B_x at $x = 0$ has

small amplitude and its being finite is what constitutes the reconnection. E_z again plays no role in Eq. 4.1 because $\partial/\partial z = 0$. The y-component of Eq. 4.19 with the cold electron assumption invoked is

$$E_y = -\frac{\partial u_{ey}}{\partial t} + u_{ez}Q_{ex} - u_{ex}Q_{ez} - \frac{\partial}{\partial y}\left(\frac{u_e^2}{2}\right). \tag{4.27}$$

Using Eq. 4.20, the first term on the right-hand side of Eq. 4.27 is $-\partial u_{ey}/\partial t \simeq -u_{ey}\partial u_{ey}/\partial y = -\partial\left(u_{ey}^2/2\right)/\partial y$. The second term disappears because $Q_{ex}\,(x=0) = 0$ since $\mathbf{Q}_e$ does not reconnect. The third term disappears because of the antisymmetry of u_{ex} and the quadrupole nature of Q_{ez}. Equation 4.27 now simplifies to

$$E_y \simeq -\frac{\partial}{\partial y}\left(\frac{u_{ey}^2 + u_e^2}{2}\right). \tag{4.28}$$

Thus, $\left(u_{ey}^2 + u_e^2\right)/2$ acts as an effective potential in the y-direction. A comparison between $-\int E_y dx$ and $\left(u_{ey}^2 + u_e^2\right)/2$ along $x = 0$ shows that the latter is a good approximation, as shown in Figure 4.1c. The potential forms a hill off of which the ions fall downwards (ion outflow directions represented by green arrows). The integration constant was set in Fig. 4.1c so that the two functions coincide at $y = 0$. The normalized stochasticity condition (Eq. 4.17) in the outflow direction is

$$\frac{1}{\varepsilon B_x^2}\left|\frac{\partial^2}{\partial y^2}\left(\frac{u_{ey}^2 + u_e^2}{2}\right)\right| > 1. \tag{4.29}$$

Here the connected nature of $\mathbf{Q}_e$ gives $Q_{ex}\,(x=0) = \partial u_{ez}/\partial y - B_x \simeq u_{ez}/L_y - B_x = 0$, so using $\partial/\partial y \sim 1/L_y = B_x/u_{ez}$ on Eq. 4.29 gives

$$\frac{1}{\varepsilon}\left(\frac{u_{ey}^2 + u_e^2}{2u_{ez}^2}\right) > 1. \tag{4.30}$$

However, $\left(u_{ey}^2 + u_e^2\right)/u_{ez}^2 \geq 1$ since $u_e^2 = u_{ey}^2 + u_{ez}^2$, so Eq. 4.30 reduces to

$$\frac{m_i}{m_e} > 1, \tag{4.31}$$

which is of course satisfied. Consequently, the stochasticity condition in the outflow direction is always satisfied by a wide margin.

The cold electron assumption in the outflow direction will now be justified. Recalling that $\bar{p}_e = n_e k_B T_e/(B_0^2/\mu_0)$ gives $\bar{p}_e = \bar{n}_e \bar{v}_{Te}^2/2$ where $\bar{v}_{Te}^2 = (2k_B T_e/m_e)/(d_e\,|\omega_{ce}|)^2$. Dropping bars, the pressure term in Eq. 4.19 becomes $\frac{\nabla p_e}{n_e} = \nabla\left(\frac{v_{Te}^2}{2}\right) + \frac{v_{Te}^2}{2}\frac{\nabla n_e}{n_e} \simeq$

$\nabla\left(\frac{v_{Te}^2}{2}\right)$. The $\frac{v_{Te}^2}{2}\frac{\nabla n_e}{n_e}$ term was dropped by invoking the quasi-neutrality condition; because the normalized Poisson's equation gives $\nabla\cdot\mathbf{E} = -\frac{c^2}{v_{Ae}^2}(n_e - n_0)$ where $v_{Ae}^2 = B^2/\mu_0 m_e n_e$ is the electron Alfvén velocity, taking the gradient of both sides and requiring $\nabla\cdot\mathbf{E}$ to be small by quasi-neutrality yields $\nabla n_e << v_{Ae}^2/c^2$. Using this new pressure term in Eq. 4.19 and applying the same reasoning used to derive Eq. 4.28, E_y approximates to

$$E_y \simeq -\frac{\partial}{\partial y}\left(\frac{u_{ey}^2 + u_e^2 + v_{Te}^2}{2}\right). \tag{4.32}$$

Equation 4.32 implies that if there is electron heating in the exhaust region, the potential becomes flatter and thus less conducive to stochastic heating. This is not a problem in guide-field reconnection in which electron heating is localized near the EDR [146]. For zero guide-field reconnection, however, if the exhaust region (finite y) is hotter than the EDR ($y \approx 0$) [166], the potential is a well centered around $y = 0$ which is not conducive to stochastic heating. Nevertheless, temperature effects do not negate the stochastic condition being satisfied for the following reasons.

Consider the worst case scenario where the outflow becomes completely thermalized, i.e., $u_{ey}^2 + v_{Te}^2 = const$. In this case, only u_e^2 is left in Eq. 4.32 so Eq. 4.30 becomes $\frac{1}{\varepsilon}\left(\frac{u_e^2}{2u_{ez}^2}\right) > 1$, which is always satisfied because $u_e^2 \geq u_{ez}^2$.

Furthermore, previous studies are consistent with the cold electron assumption. Several numerical studies [79, 125] have shown that $|e\Phi/T_e|$ — which corresponds to $\sim u_e^2/v_{Te}^2$ — increases to be $10 \sim 20$ inside the saddle potential, which means that the electron flow is cold and laminar. A previous experimental study [168] measured the plasma potential including electron temperature effects and showed that the potential is a hill in the y-direction with the peak at $y = 0$, confirming the shape given in Fig. 4.1(c).

The fact that Eqs. 4.26 and 4.31 do not depend on the magnetic field signifies that stochastic heating is intrinsic to collisionless reconnection. ϕ in Eq. 4.17 has a dependence on $\mathbf{B}$ in such a way that this dependence cancels out $\mathbf{B}$ in the denominator. Thus, Eq. 4.17 is always met given that the assumptions in the present analysis are met as well.

4.5 Test Particle Simulation

In order to verify ion stochastic heating, 6000 test ion particle trajectories were simulated using an implicit particle integrator [15]. The details of the algorithm

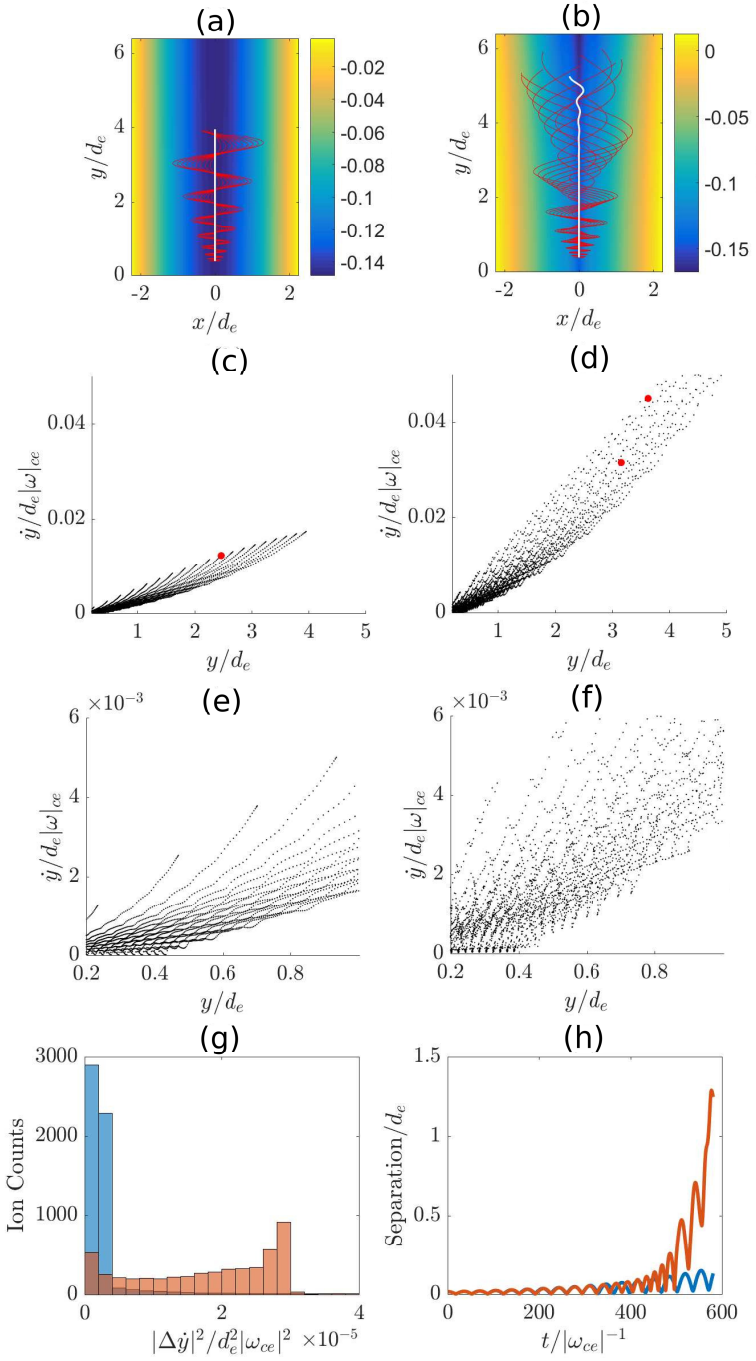

Figure 4.2: (a) Ten coherent ion trajectories undergoing Speiser-like orbits, and (b) their stochastic counterparts. (c) Positions in y phase space of all 6000 ions at $t = 580\,|\omega_{ce}|^{-1}$, and (d) their stochastic counterparts. (e), (f) Zoom-ins of (c) and (d), respectively. (g) Distribution of $|\Delta\dot{y}|^2$ for the coherent case (blue) and the stochastic case (red). (h) Time-dependent 3D separation distances between two selected particles with the minimum initial separation distance, $0.015d_e$, under the stationary electric field (blue line; particles are red dots in (b)) and the growing electric field (red line; particles are red dots in (f)).

are described in Appendix D. Trajectories were calculated for both stationary and growing electric fields. These two cases should respectively give ordered and stochastic ion motions. The particles were started at rest from a rectangular grid $(x, y) = (0, 0) - (4.5, 0.4)d_e$, spaced by $(\Delta x, \Delta y) = (0.015, 0.02)d_e$. Such a small spatial separation was chosen because stochasticity is defined by particles' having disparate trajectories with slightly different initial conditions. The results presented in Fig. 4.2 are based on a mass ratio $m_i/m_e = 10$. While this mass ratio is small, the purpose of the simulation is to reveal the distinction between coherent and stochastic situations. Simulations with higher mass ratios (20, 50, 100) have also been conducted and exhibit similar qualitative behavior; mass and time scalings are subject to future investigations.

The growing electric field was the time-dependent numerically calculated field, and the stationary electric field was chosen to have the value of the time-dependent field at $t = 5\,|\omega_{ce}|^{-1}$. A small value for this reference time was chosen because the particles were started at rest from different positions. This means that they all have different initial total energies, so a small potential was chosen to keep the ions initially cold in order to explicitly show the thermal energy gain due to stochastic heating. Coherence was not destroyed by choosing the electric field at a later time. The focus will be on the outflow direction since Eq. 4.31 is met by a large margin so the stochastic evolution in this direction is more evident.

Particle Trajectories and Phase Mixing

Figure 4.2a shows ten selected ion trajectories (red) in the stationary electric field case, and Figure 4.2b shows the stochastic counterpart. The effective potential at (a) $t = 5\,|\omega_{ce}|^{-1}$ and (b) $580\,|\omega_{ce}|^{-1}$ is plotted (color) for reference. The ions have Speiser-type (bouncing) orbits, consistent with previous numerical studies [7, 46]. In the stationary electric field case (i.e., Fig. 4.2a, the trajectories show a coherent motion. In the growing electric field case (i.e., Fig. 4.2b), the trajectories clearly diverge and undergo phase mixing, the signature of stochastic motion. Stochasticity is further demonstrated by the central trajectory (white) which starts at $x = 0$ in both situations and which, in principle, should have no motion in the x-direction. While the central trajectory in Fig. 4.2a (stationary electric field) is a straight, stable outflow, the trajectory in Fig. 4.2b (growing electric field) becomes unstable indicating stochasticity, where the seed for the instability is the ever-present small numerical error.

Ion Phase Space

Examination of the ion phase space indicates chaotic motion. Figure 4.2c shows the positions in y phase space of all ions at $t = 580\,|\omega_{ce}|^{-1}$ for the stationary electric field case, and Fig. 4.2d shows the counterpart in the growing electric field case. Figures 4.2e and 4.2f show zoomed-in versions of Figs. 4.2c and 4.2d, respectively. The left plots (stationary electric field) clearly show a periodic order, whereas the right plots (growing electric field) exhibit unpredictability and chaos.

The two red dots in Fig. 4.2c (which look like one dot due to their proximity) represent the phase space positions of two selected particles that started with the minimal separation of $0.015d_e$ for the stationary electric field case, and those in Fig. 4.2d represent their stochastic counterpart (growing electric field). The time-dependent 3D separation distance is plotted in Fig. 4.2h as blue (ordered) and red (stochastic). It can be seen in both phase and physical space that the two particles in the stochastic case separate rapidly from one another, a behavior which is the characteristic of chaotic motion and in accordance with the concept of Lyapunov exponents [100].

Effective Heating

The stochasticity results in an effective heating. Figure 4.2g shows for ordered (blue) and stochastic (red) ions the distribution of the squared deviation of the ion outflow velocity $|\Delta\dot{y}|^2$, a proxy for thermal energy. Significant heating is clearly seen for the stochastic case. The distribution is non-Maxwellian, however, because collisions are not included.

Initial Temperature

In reality, ions have a finite initial temperature. Another simulation was conducted where the ions start with a thermal velocity of 0.01 $d_e|\omega_{ce}|$, and the results are shown in Fig. 4.3. The phase space as shown in Fig. 4.3b is much broader than that in Fig. 4.3a. The separation between the two red dots are again much larger in Fig. 4.3b than in Fig. 4.3a. The thermal spread can be seen explicitly in Fig. 4.3d in contrast to Fig. 4.3c. Also, in comparison with Figs. 4.2c and 4.2d, it can be seen that an initial temperature makes the ions spatially travel further and faster.

It should be said that the purpose of this test particle simulation is to explicitly show the contrast between coherent and stochastic ion motion, and the results presented here reflect the initial stage of stochastic evolution. A temporal limitation exists due to the time scale separation between the ions and electrons, so the simulation must

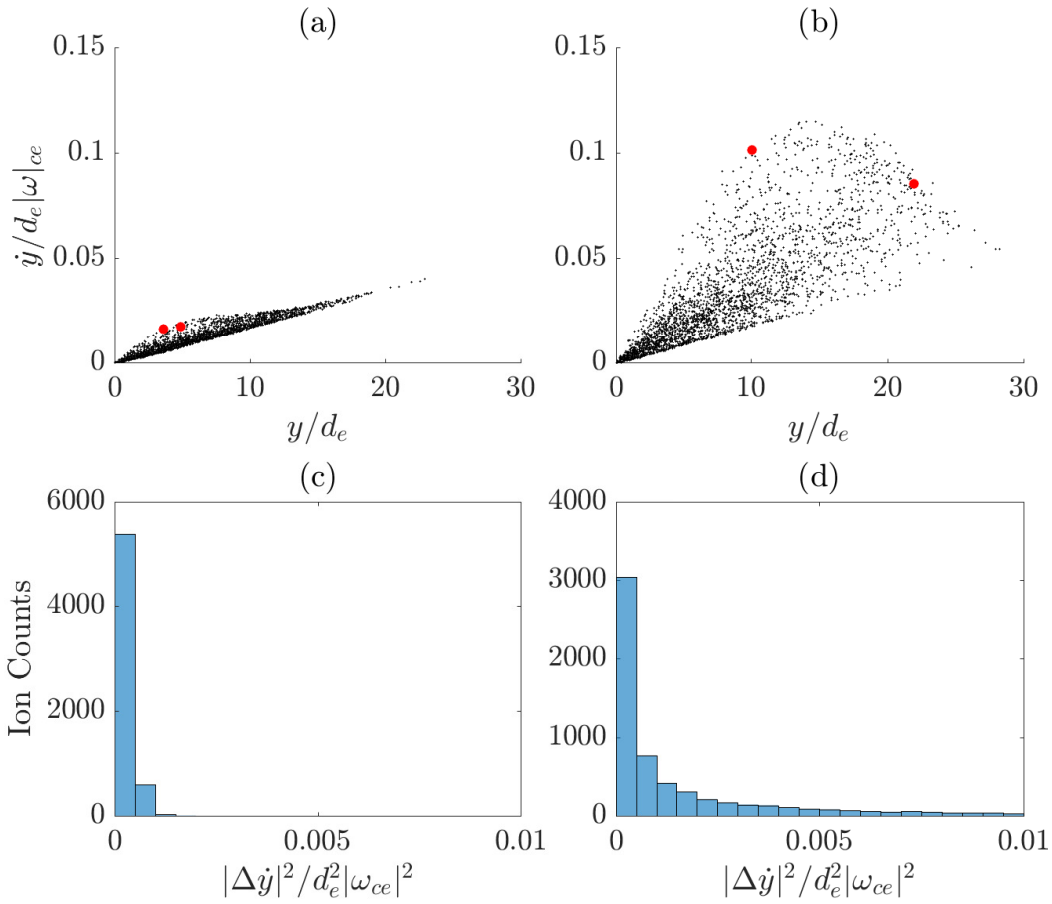

Figure 4.3: Positions in y phase space of ions that started with a thermal velocity of 0.01 $d_e|\omega_{ce}|$ in (a) the coherent case and (b) the stochastic case. Distribution of $|\Delta\dot{y}|^2$ in (c) the coherent case and (d) the stochastic case.

be halted before the ions are exhausted from the reconnection region. This also means that the ions have yet to gain all the available energy from this mechanism.

4.6 Discussion

Heating Rate

An order-of-magnitude estimate for the heating rate and strength in a reconnection situation will be given as follows. A proxy for the exponential heating rate from this mechanism in a reconnection situation is its Lyapunov exponent

$$\gamma_E = \sqrt{\frac{q_i E}{m_i a}}, \tag{4.33}$$

where a is the length scale of the electric field E [10]. Here,

$$\sqrt{\frac{q_i E}{m_i a}} = \frac{q_i B_0}{m_i}\frac{B_\perp}{B_0}\sqrt{\frac{m_i E}{q_i B_\perp^2 a}} \tag{4.34}$$

and noting that the quantity inside the square root is equivalent α of the stochastic heating criterion (Eq. 4.1), $\gamma \approx \omega_{ci}\frac{B_\perp}{B_0}\frac{d_i}{L_x}$ for the inflow and $\approx \omega_{ci}\frac{B_\perp}{B_0}\sqrt{\frac{m_i}{m_e}}$ for the outflow. Assuming $B_\perp \lesssim B_0$ and $L_x \lesssim d_i$, the theoretical heating rate γ is in the range $\omega_{ci} < \gamma < \sqrt{\omega_{ci}\omega_{ce}}$. This is much faster than the MHD time scale governing the macrophysics of the solar environment.

As noted in Sanders et al. [133], the maximally achieved ion thermal velocity due to stochastic heating is $v_T = \omega_{ci} a(\alpha + 1.9)$, where α is defined in Eq. 4.1 and thus satisfies $\alpha > 1$. Using $a \simeq d_i$, the upper bound on the local beta is $\beta_{local} = v_T/v_A = \alpha + 1.9$, at a time scale faster than the ion cyclotron frequency. Since the reconnected magnetic field magnitude is less than the that of upstream field, the global beta may still stay sub-unity. A more detailed analysis on the heating amount is subject to future investigations.

Heating Profile

Our results are consistent with a recent particle-in-cell calculation of ion temperature profile in collisionless reconnection. Haggerty et al. [63, Figure 2] shows a sharp ion temperature increase across the magnetic separatrix where the potential drop occurs, and a further increase in the ion outflow jet. This is congruous with the fact that the inflow condition (Eq. 4.26) is marginally satisfied and the outflow condition (Eq. 4.31) is satisfied by a wide margin; therefore, the temperature increase is more dramatic along the outflow.

Comparisons to Experiments

The claim that Eq. 4.1 is satisfied in collisionless reconnection is also supported by experimental observations. In the Magnetic Reconnection eXperiment [166], the measured in-plane electric field was 700 V/m with a 1 cm length scale. Using the upstream magnetic field $B_0 = 0.1$ kG, Eq. 4.1 becomes $14.6 >> 1$ and so the condition for ion stochastic heating is satisfied by a wide margin. The condition was also met in the spontaneous collisionless reconnection event in the Caltech MHD-driven jet experiment [29].

The calculated heating rate also agrees with experiments. Defining γ_{obs} to be the inverse e-folding time scale of the ion temperature based on experimental observations,

$\gamma_{obs} \approx 10^5$ s^{-1} for MRX [166] and $\gamma_{obs} \approx 10^6$ s^{-1} for the Caltech jet experiment [29]. Calculation of γ range for both experiments gives $\gamma \approx 1\text{–}30 \times 10^6$ s^{-1} for the former and $\gamma \approx 1\text{–}100 \times 10^6$ s^{-1} for the latter. Therefore, stochastic ion heating is fast enough to account for the observations in both experiments.

4.7 Summary

It has been shown that ion stochastic heating, which had already been established as an important heating mechanism in the solar wind, atmosphere, and flares, is also inherent to collisionless magnetic reconnection. The connected nature of electron canonical vorticity has been exploited to show that the electric fields near the magnetic separatrix satsify the stochastic heating criterion. The approximations for the electric field were verified by an electron fluid simulation, and ion stochasticity was demonstrated by test particle simulations. Comparisons to laboratory reconnection experiments also support the existence of this mechanism.

Chapter 5

KINETIC VERIFICATION OF STOCHASTIC ION HEATING IN MAGNETIC RECONNECTION

In Chapter 4, it was demonstrated via a two-fluid, zero-beta analysis of the generalized Ohm's law that stochastic heating is intrinsic to anti-parallel (zero guide field) collisionless reconnection. Although the demonstration provided useful insights into the fundamental ion heating mechanism in reconnection, a fully self-consistent kinetic verification of this mechanism was not demonstrated. Also, four of the five features of ion heating in reconnection, namely temperature anisotropy ($T_{i\perp} \neq T_{i\parallel}$), μ violation, preferential heating of higher m/q particles, and reduction of the heating amount in the presence of a guide field, were not explicitly illustrated in terms of stochastic heating.

In this chapter, it is unambiguously shown via exact kinetic analyses and particle-in-cell simulations that stochastic heating [10, 108, 133, 142] is the main ion heating mechanism in a generic collisionless reconnection process up to moderate guide fields and exhibits all five features of anomalous ion heating.

Recall from Chapter 4 that the criterion for stochastic ion heating is given by a single dimensionless parameter $\alpha(\mathbf{x}, t)$ where

$$\alpha(\mathbf{x}, t) = \frac{m_i}{q_i |\mathbf{B}|^2} \left|\nabla_\perp^2 \phi\right| > 1; \tag{5.1}$$

here $\nabla_\perp$ is the gradient perpendicular to the local magnetic field $\mathbf{B} = \mathbf{B}(\mathbf{x}, t)$, and $\phi = \phi(\mathbf{x}, t)$ is the local electrostatic potential. Equation 5.1 provides a spatio-temporal prediction for stochastic heating. Stochastic heating involves the breakdown of the guiding-center approximation and causes associated non-conservation of the magnetic moment μ. Since μ involves $v_\perp$, this mechanism preferentially increases $T_\perp$. In addition, according to Eq. 5.1, ions with higher m_i/q_i more easily satisfy the $\alpha > 1$ criterion and so are expected to be more readily heated. Thus, stochastic heating is an enticing candidate for the anomalous ion heating mechanism in magnetic reconnection.

This chapter fills the gap between the prediction of stochastic ion heating in magnetic reconnection in Chapter 4 and a self-consistent verification by confirming the exis-

tence and inherent features of stochastic ion heating through fully kinetic analyses and simulations.

5.1 Stochastic Heating in the Harris Equilibrium Plasma Sheath

We begin with an analysis of the existence of stochastic heating in the Harris equilibrium sheath [66], which is often used as the initial condition for reconnection analyses and simulations. Although the Harris-type hyperbolic tangent magnetic field profile has been used in previous chapters, the exact Harris equilibrium is more complicated and will now be briefly derived.

Harris Equilibrium Plasma Sheath

The Harris equilibrium plasma sheath is a kinetically exact specific solution for a steady-state velocity distribution function that simultaneously satisfies Poisson's equation, Ampère's law, and the Vlasov equation (Eq. 1.13). A sheath refers to the region of plasma sandwiched between regions of oppositely-directed magnetic fields. Using the specific distribution function, ϕ and $\mathbf{A}$ can be calculated, and from these the equilibrium electric and magnetic field can be derived. For a more detailed derivation, see Appendix E.

The equilibrium is initially solved in a frame where ions and electrons are moving at equal and opposite velocities in the z direction, i.e., $V_{iz} = -V_{ez} = V$. Assuming uniform $T = T_i = T_e$,

$$\phi = 0 \tag{5.2}$$

in this frame, so

$$\mathbf{E} = 0. \tag{5.3}$$

The equilibrium magnetic field is determined to have the profile [66]

$$B_y(x) = 2\sqrt{\mu_0 n_0 k_B T}\tanh\frac{x}{\lambda}, \tag{5.4}$$

where

$$\lambda = \frac{\sqrt{2}c}{V}\lambda_D \tag{5.5}$$

$$= \frac{\sqrt{2}c}{V}\frac{1}{\sqrt{\lambda_{Di}^{-2} + \lambda_{De}^{-2}}} \tag{5.6}$$

$$= \frac{c}{V}\sqrt{\frac{\epsilon_0 k_B T}{n_0 e^2}} \tag{5.7}$$

is the sheath half-thickness and n_0 is the peak density of the sheath. The density profile is

$$n_i(x) = n_e(x) = n_0 \cosh^{-2} \frac{x}{\lambda}. \tag{5.8}$$

Lorentz tranforming to a frame where $V_{iz} = 0$, which is approximately the center-of-mass frame (i.e., the lab frame due to $m_i \gg m_e$), a lab-frame electric field with the following profile develops [66]:

$$E_x(x) = -VB_y(x) = -2V\sqrt{\mu_0 n_0 k_B T}\tanh\left(\frac{x}{\lambda}\right), \tag{5.9}$$

where we have assumed $V \ll c$, so the Lorentz factor $\gamma = 1$. The magnetic field stays the same after the transformation.

In this lab frame, $V_{iz} = 0$ and $V_{ez} = -2V$, so $J_z(x) = 2n(x)eV$. Thus, Eq. 5.9 is of the same order of magnitude as the Hall component of the electric field $E_{x,Hall}(x) = -J_z(x)B_y/n(x)e = -2VB_y(x)$ in the lab frame. In the vicinity of the reconnection region, the in-plane electric field is mainly balanced by the Hall component [93, 171], so whether Eq. 5.9 satisfies Eq. 5.1 is important for determining the existence of stochastic heating.

Stochastic Ion Heating Condition

To make the analysis more general, a guide field $B_z = b_g B_y(x \to \infty)$ is now included as well where b_g is the ratio of the guide field to the asymptotic value of B_y. Since only $E_x(x)$, $B_y(x)$, and B_z are involved, Eq. 5.1 becomes

$$\frac{m_i}{q_i\left[B_y^2(x) + B_z^2\right]}\left|\frac{\partial E_x(x)}{\partial x}\right| > 1, \tag{5.10}$$

which, after inserting the Harris profiles (Eqs. 5.4 and 5.9), becomes

$$2\frac{\lambda^2}{d_i^2}\cosh^2\left(\frac{x}{\lambda}\right)\left[\tanh^2\left(\frac{x}{\lambda}\right) + b_g^2\right] < 1, \tag{5.11}$$

where d_i is the ion skin depth. Denoting $\bar{x} = x/d_i$ and $\bar{\lambda} = \lambda/d_i$, the solution to Eq. 5.11 is $\bar{x} < \bar{x}_{sh}\left(\bar{\lambda}, b_g\right)$ where

$$\bar{x}_{sh} = \frac{\bar{\lambda}}{2}\ln\frac{\bar{\lambda}^2\left(1 - b_g^2\right) + 1 + \sqrt{\left(1 - 2\bar{\lambda}^2 b_g^2\right)\left(2\bar{\lambda}^2 + 1\right)}}{\bar{\lambda}^2\left(1 + b_g^2\right)}. \tag{5.12}$$

A more detailed derivation of this solution is in Appendix E. Figure 5.1a shows contours of $\bar{x}_{sh}\left(\bar{\lambda}, b_g\right)$, and the inset plots $\bar{x}_{sh}$ as a function of b_g for $\bar{\lambda} = 0.5, 1, 2$.

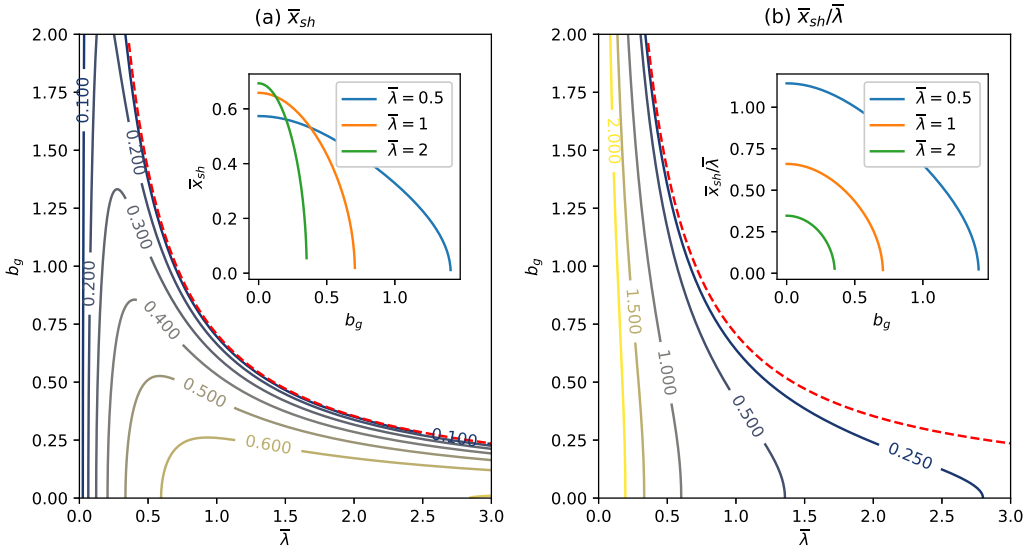

Figure 5.1: (a) Contours of $\bar{x}_{sh}\left(\bar{\lambda}, B_g\right)$. Inset plots $\bar{x}_{sh}$ as a function of B_g for three $\bar{\lambda}$ values. (b) Same as (a), but for $\bar{x}_{sh}/\bar{\lambda}$.

Figure 5.1b shows similar plots, but for $\bar{x}_{sh}/\bar{\lambda}$, the fractional extent of the sheath that is subject to stochastic ion heating. For $b_g = 0$ and $\bar{x} \ll \bar{\lambda}$ so that $\sinh\left(\bar{x}/\bar{\lambda}\right) \simeq \bar{x}/\bar{\lambda}$, Eq. 5.11 simplifies to $\bar{x} < 1/\sqrt{2}$, which shows that stochastic ion heating is intrinsic to a Harris sheath. Figure 5.1b shows that the fractional heating extent increases as the sheath becomes thinner. However, Figs. 5.1a and 5.1b show that for each $\bar{\lambda}$ there exists a maximum guide field value above which stochastic ion heating does not occur (red dashed lines). This corresponds to the argument of the square root in Eq. 5.12 becoming negative when $b_g > \left(\sqrt{2}\bar{\lambda}\right)^{-1}$, so no real solution for $\bar{x}_{sh}$ exists. For $\bar{\lambda} = 1$, the maximum b_g is $1/\sqrt{2} \simeq 0.7$.

This analytical result regarding the Harris equilibrium does not directly apply to an evolving reconnection sheet since the Harris sheath does not by itself involve reconnection. However, because the Harris electric field (Eq. 5.9) is comparable to the Hall electric field, and the reconnecting magnetic field profile is closely related to the Harris profile [164], one can extrapolate a general trend that the fractional extent of stochastic ion heating decreases as the guide field or the sheath width increases.

Quantity	Normalization
t	ω_{ci}^{-1}
$\mathbf{x}$	d_i
$\mathbf{u}$	$d_i\omega_{ci} = v_{Ai}$
$\mathbf{B}$	B_0
$\mathbf{E}$	$d_i\omega_{ci}B_0 = v_{Ai}B_0$
n	n_0
$\overleftrightarrow{\mathbf{p}}$	B_0^2/μ_0
T	$m_i v_{Ai}^2$
μ	$m_i v_{Ai}^2/B_0$

Table 5.1: Dimensional quantities and their normalization parameters in Chapter 5.

5.2 Particle-in-cell verification

Setup

In order to test the prediction that stochastic ion heating is intrinsic to collisionless reconnection, fully kinetic particle-in-cell simulations were conducted using the SMILEI code [41]. The simulations were conducted in 2D, i.e., $\partial/\partial z \to 0$. Lengths were normalized to d_i, time to ω_{ci}, velocity to $v_{Ai} = d_i\omega_{ci}$, $\mathbf{B}$ to the upstream B_0, density to the peak density n_0, T to $m_i v_{Ai}^2$, and the magnetic moment μ to $m_i v_{Ai}^2/B_0$. A summary of the normalizations used in the simulation in this Chapter is detailed in Table 5.1.

Double periodic Harris sheaths were employed as initial conditions, i.e.,

$$B_y = B_0\left[\tanh\left(\frac{\bar{x}}{\bar{\lambda}}\right) - \tanh\left(\frac{\bar{x} - \bar{x}_{max}/2}{\bar{\lambda}}\right) - 1\right] \tag{5.13}$$

and

$$n = n_0\left[\cosh^{-2}\left(\frac{\bar{x}}{\bar{\lambda}}\right) + \cosh^{-2}\left(\frac{\bar{x} - \bar{x}_{max}/2}{\bar{\lambda}}\right) + n_b\right], \tag{5.14}$$

where $\bar{x}_{max}$ is the simulation box size in the x direction, $n_b = 0.2$ the relative upstream density, $\bar{\lambda} = 1$ the half-thickness, and $T = T_i = T_e$ the temperature. Only one of the two sheaths is examined; the double sheath facilitates the application of periodic boundary conditions. We work in the lab-frame, so an initial Harris-type electric field in the form of Eq. 5.9 is employed. The ion-to-electron mass ratio was $m_i/m_e = 100$ and the grid size was $1024 \times 2048 = 40.96d_i \times 81.92d_i$. The number of particles per cell ranged from 100 to 600 depending on the local density, and $c/v_A = 20$. Although $\bar{x}_{sh}$ depends on both $\bar{\lambda}$ and b_g, changing $\bar{\lambda}$ requires significant alterations in simulation parameters such as the domain, and the current sheet tends

to be more unstable for smaller $\bar{\lambda}$. Thus, in order to facilitate the analysis, b_g was chosen to be the variable parameter.

From now on, the bars will be dropped and only normalized quantities will be used unless specified otherwise.

Calculation of $T_{i\perp}$ and $T_{i\parallel}$

Pressure and temperature are not variables that are intrinsic to the particle-in-cell algorithm (Section 3.3) and therefore must be post-processed. The mean ion flow velocity is first calculated as

$$\mathbf{u}_i = \int \mathbf{v}_i f_i d^3\mathbf{v}_i, \tag{5.15}$$

where f_i is calculated from Eq. 3.35.

Now, the ion pressure tensor is defined as

$$\overleftrightarrow{\mathbf{p}}_i = \int \mathbf{v}_i' \mathbf{v}_i' f_i d^3\mathbf{v}_i, \tag{5.16}$$

where $\mathbf{v}_i' = \mathbf{v}_i - \mathbf{u}_i$ is the random part of the ion velocity. Consider the following integral:

$$\int \mathbf{v}_i \mathbf{v}_i f_i d^3\mathbf{v}_i = \int (\mathbf{u}_i + \mathbf{v}_i')(\mathbf{u}_i + \mathbf{v}_i') f_i d^3\mathbf{v}_i, \tag{5.17}$$

$$= \int (\mathbf{u}_i\mathbf{u}_i + \mathbf{u}_i\mathbf{v}_i' + \mathbf{v}_i'\mathbf{u}_i + \mathbf{v}_i'\mathbf{v}_i') f_i d^3\mathbf{v}_i, \tag{5.18}$$

$$= \mathbf{u}_i\mathbf{u}_i \int f_i d^3\mathbf{v}_i + \int \mathbf{v}_i'\mathbf{v}_i' f_i d^3\mathbf{v}_i \tag{5.19}$$

$$= \mathbf{u}_i\mathbf{u}_i + \overleftrightarrow{\mathbf{p}}_i, \tag{5.20}$$

where $\int \mathbf{v}_i' f_i d^3\mathbf{v}_i = 0$ by the definition of $\mathbf{v}_i'$ which is the random part of $\mathbf{v}_i$. Therefore,

$$\overleftrightarrow{\mathbf{p}}_i = \int \mathbf{v}_i \mathbf{v}_i f_i d^3\mathbf{v}_i - \mathbf{u}_i\mathbf{u}_i, \tag{5.21}$$

where the right-hand side can be calculated from the variables explicitly used in the PIC algorithm.

Now, in terms of $p_{i\perp}$ and $p_{i\parallel}$,

$$\overleftrightarrow{\mathbf{p}}_i = p_{i\perp}\overleftrightarrow{\mathbf{I}} + (p_{i\parallel} - p_{i\perp})\hat{B}\hat{B}, \tag{5.22}$$

where $\hat{B}$ is the local unit vector in the direction of the local magnetic field $\mathbf{B}$. It is easy to see that

$$p_{i\parallel} = \hat{B} \cdot \overleftrightarrow{\mathbf{p}}_i \cdot \hat{B}, \tag{5.23}$$

$$= \frac{\mathbf{B} \cdot \overleftrightarrow{\mathbf{p}}_i \cdot \mathbf{B}}{B^2}. \tag{5.24}$$

Since $p_{i\parallel}$ is now known, $p_{i\perp}$ can be calculated by simply using the fact that the trace of a tensor does not change under coordinate transformations, i.e.,

$$\mathrm{Tr}\,\overleftrightarrow{\mathbf{p}}_i = 2p_{i\perp} + p_{i\parallel}, \tag{5.25}$$

or

$$p_{i\perp} = \frac{\mathrm{Tr}\,\overleftrightarrow{\mathbf{p}}_i - p_{i\parallel}}{2}. \tag{5.26}$$

$T_{i\parallel}$ and $T_{i\perp}$ can then be found simply by dividing $p_{i\parallel}$ and $p_{i\perp}$ by $n_i = \int f_i d^3\mathbf{v}_i$, respectively.

Hall Electric Fields

Figure 5.2 shows $\mathbf{B}$ (black lines) and E_x (color) for b_g = (a) 0, (b) 0.1, (c) 0.3, and (d) 0.5. Times are chosen so that significant reconnection has taken place but the periodicity of the domain has not yet affected the local system. It is well-known that the Hall term in the generalized Ohm's law is important in collisionless reconnection [16]. Thus, strong in-plane Hall electric fields $E_x \sim (\mathbf{J} \times \mathbf{B})_x$ (color) develop; these have also been seen in previous studies [7, 47, 93, 125, 162, 171]. Although a finite guide field alters the structure, E_x is generally pointing toward $x = 0$, meaning that ions are falling down a potential valley along the inflow. A Hall E_y (not plotted) also develops but is smaller in spatial extent and magnitude.

Comparison of the Stochastic Heating Criterion to the Ion Temperature Profile

α as defined by Eq. 5.1 can be calculated from the electric and magnetic field information. Figure 5.3 shows $\ln\alpha$; regions where $\ln\alpha$ is above zero (red and yellow) represent the spatial extent of predicted stochastic ion heating. It is seen that the spatial extent decreases as the guide field increases, and at $b_g = 0.5$ (Fig. 5.3d), the stochasticity onset criterion is not satisfied anywhere.

Figure 5.4 shows the spatial profile of the ion temperature $T_i = \left(2T_{i\perp} + T_{i\parallel}\right)/3$. Figures 5.4a and 5.4b show strong heating around the regions predicted by Figs. 5.3a and 5.3b. Figure 5.4c also shows heating, but its amount is much reduced, as

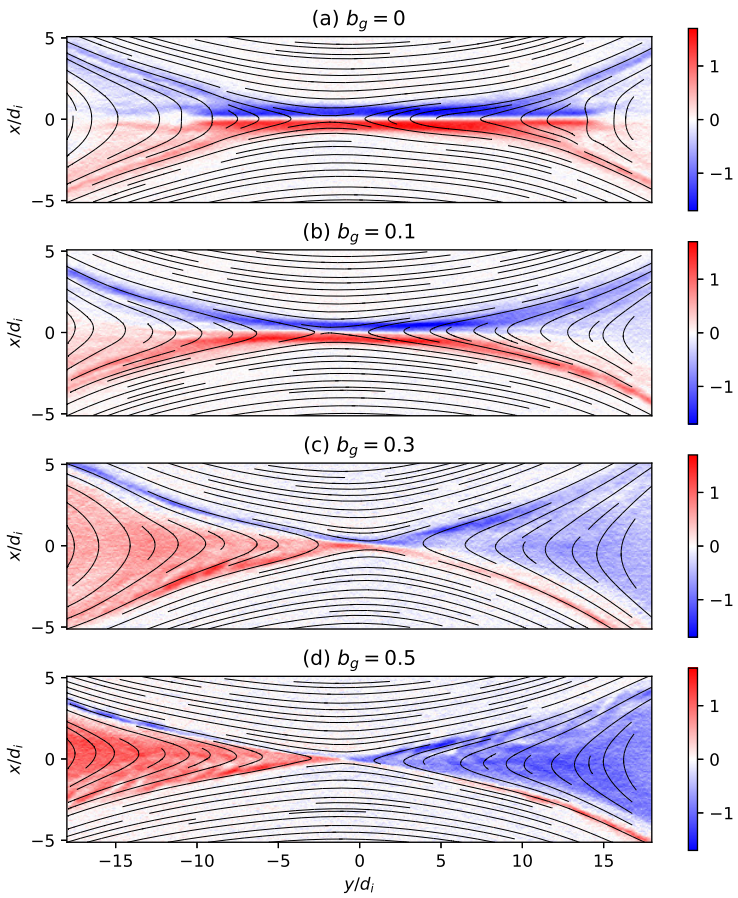

Figure 5.2: **B** (black lines) and E_x (color) for (a) $b_g = 0$, (b) 0.1, (c) 0.3, and (d) 0.5.

predicted from there being only sparse red regions in Fig. 5.3c. Figure 5.4d shows that there is no strong heating at $b_g = 0.5$, in agreement with the prediction of Fig. 5.3d. As previously mentioned, this heating amount reduction with increasing guide field is an observed feature of ion heating in reconnection.

Temperature Anisoptropy

Figures 5.5 and 5.6 show $T_{i\perp}$ and $T_{i\parallel}$, respectively. It can clearly be seen that the two temperature profiles are vastly different, confirming the temperature anisotropy that is an observed feature of ion heating in reconnection. Also, $T_{i\perp}$ is more consistent with the prediction in Fig. 5.3 than $T_{i\parallel}$. Although $T_{i\perp}$ is generally lower in magnitude than $T_{i\parallel}$, the spatial profile of T_i resembles that of $T_{i\perp}$ more because $T_{i\perp}$ contributes to T_i twice as much as $T_{i\parallel}$ does (recall that $T_i = (2T_{i\perp} + T_{i\parallel})/3$).

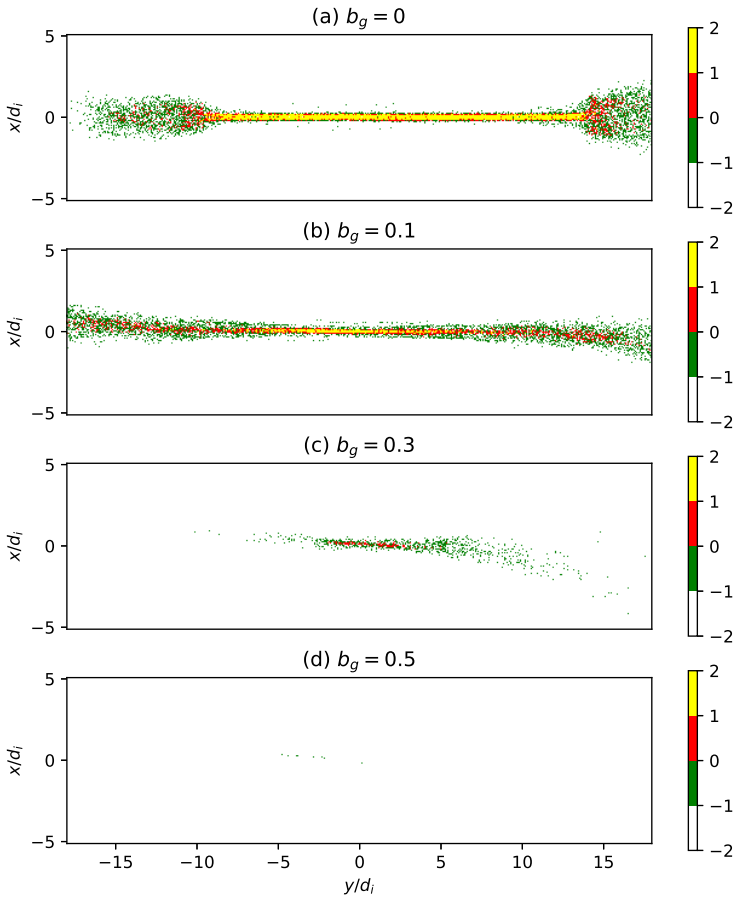

Figure 5.3: $\ln \alpha$ for $b_g = 0$, 0.1, 0.3, and 0.5, respectively.

5.3 Confirmation of Stochastic Motion

The correlation between perpendicular heating and the stochastic criterion involves the non-conservation of the ion magnetic moment $\mu = m_i v_c^2/2B$, where v_c is the cyclotron velocity that must be calculated in the frame moving with the guiding-center velocity [11, pages 96-98]. However, the guiding-center under zero guide field is ill-defined for outflowing ions because they are not magnetized. Therefore, we define a pseudo-moment $\mu_{\mathbf{E}\times\mathbf{B}} = m_i \left|\mathbf{v}_{i\perp} - \mathbf{v}_{\mathbf{E}\times\mathbf{B}}\right|^2 /2B$, whose non-conservation measures the departure from guiding center motion and thus the breakdown of the drift hierarchy. Stochastic heating involves this very breakdown [10], so the correlation between $\mu_{\mathbf{E}\times\mathbf{B}}$ and α indicates the existence of stochastic heating.

Another indication of stochastic heating is the Lyapunov exponent [100], which describes the rate of separation of two initially infinitesimally close particles. As seen in Chapter 4, a positive Lyapunov exponent is characteristic of chaotic behavior.

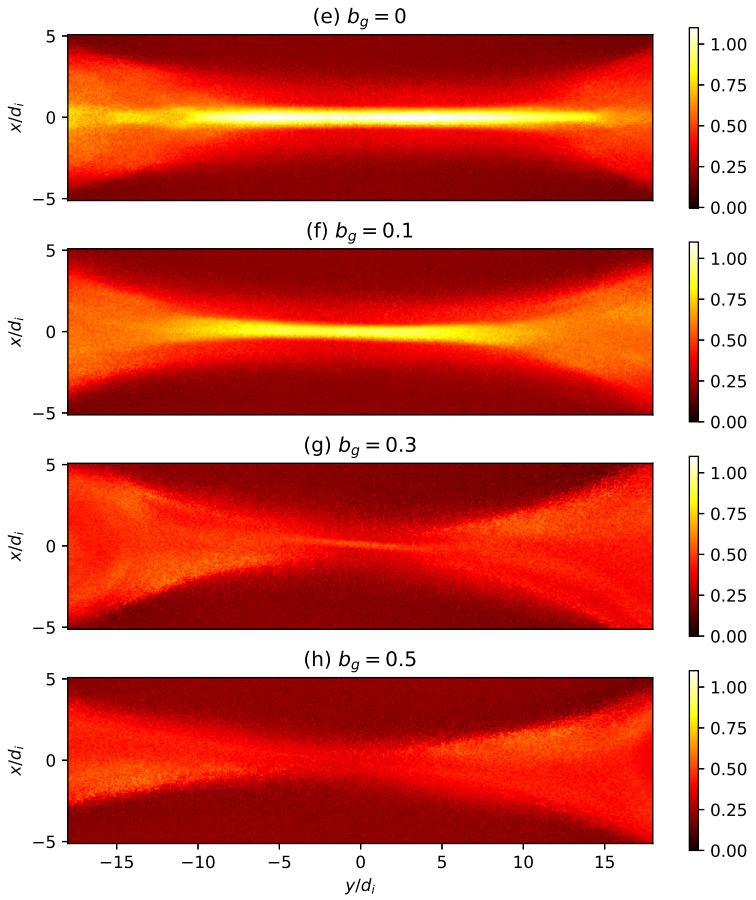

Figure 5.4: T_i for $b_g = 0$, 0.1, 0.3, and 0.5, respectively.

$\mu_{\mathbf{E}\times\mathbf{B}}$ violation

To verify stochastic heating at a single-particle level, test-particle simulations were conducted with the algorithm in Appendix D. Figure 5.7a shows two typical ion outflow trajectories (black solid and dashed line) with an initial spatial separation of $0.04d_i$ for $b_g = 0$. Both ions undergo oscillatory motion in the x-direction under the Hall electric field (color) [7, 47, 162, 168, 171]. Figure 5.7b shows the time-dependent spatial ion separation, which exhibits divergence and thus a positive Lyapunov exponent. Figure 5.7c shows $\mu_{\mathbf{E}\times\mathbf{B}}$ (blue) and $\ln \alpha$ (red) along the particle trajectory represented by the black solid line in Fig. 5.7a. The red dashed line represents the stochastic heating criterion, above which $\mu_{\mathbf{E}\times\mathbf{B}}$ violation is expected. The locations where the stochastic criterion is satisfied coincides with kicks in $\mu_{\mathbf{E}\times\mathbf{B}}$. This $\mu_{\mathbf{E}\times\mathbf{B}}$ is an observed feature of ion heating in reconnection.

The correlation between α and chaotic behavior becomes even more obvious in Figs. 5.7d, 5.7e, and 5.7f, which are respectively the same as Figures 5.7a, 5.7b, and 5.7c

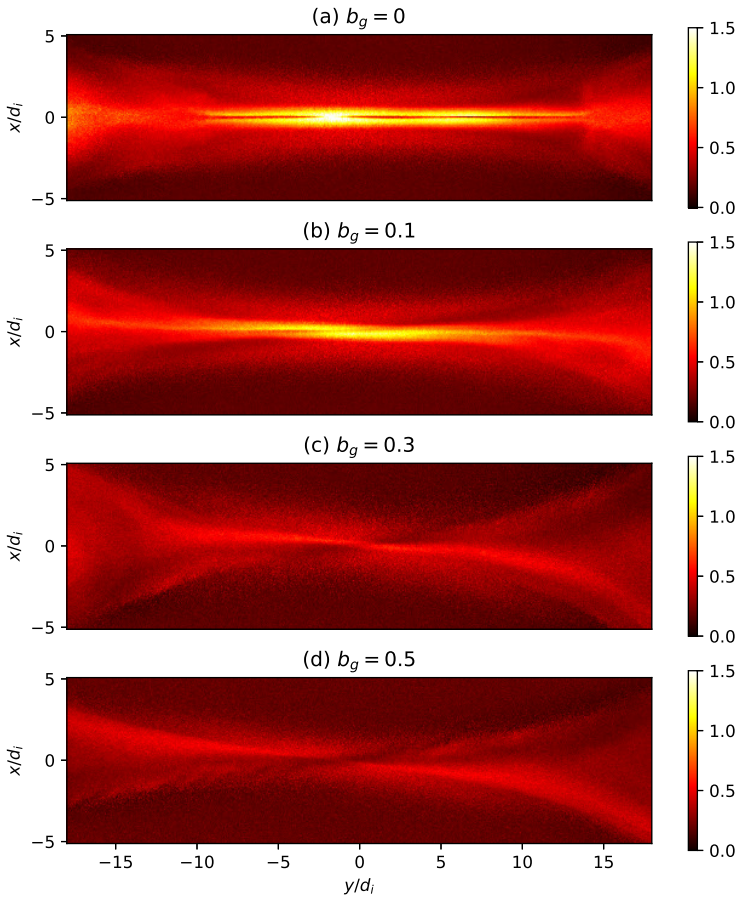

Figure 5.5: $T_{i\perp}$ for $b_g = 0$, 0.1, 0.3, and 0.5, respectively.

except for $b_g = 0.3$ (recall from Fig. 5.4c that there is limited stochastic heating in this case). In Fig. 5.7e, it is apparent that the spatial separation of the ions does not diverge, illustrating non-stochastic behavior. In Fig. 5.7f, $\ln \alpha$ rarely goes above zero, and $\mu_{\mathbf{E}\times\mathbf{B}}$ is relatively conserved.

5.4 Heavy Ions

Finally, Equation 5.1 predicts that ions with larger m_i/q_i more easily satisfy the stochastic heating criterion — an observed feature of ion heating in reconnection. A simulation containing a mix of heavy ions ($m_i/m_e = 500$) of density $0.1n$ and light ions ($m_i/m_e = 100$) of density $0.9n$ for $b_g = 0.3$ was run. Figure 5.4a shows $\ln \alpha$ for the heavy ions, which, because of their larger m_i/q_i, satisfy the stochastic heating criterion across a broader range compared to the light ions in Fig. 5.3c. Figure 5.4b shows T_i for the heavy ions, which, in comparison to the light ions in Fig. 5.4c, undergo stronger stochastic heating. The spatial profile of T_i agrees with Fig.

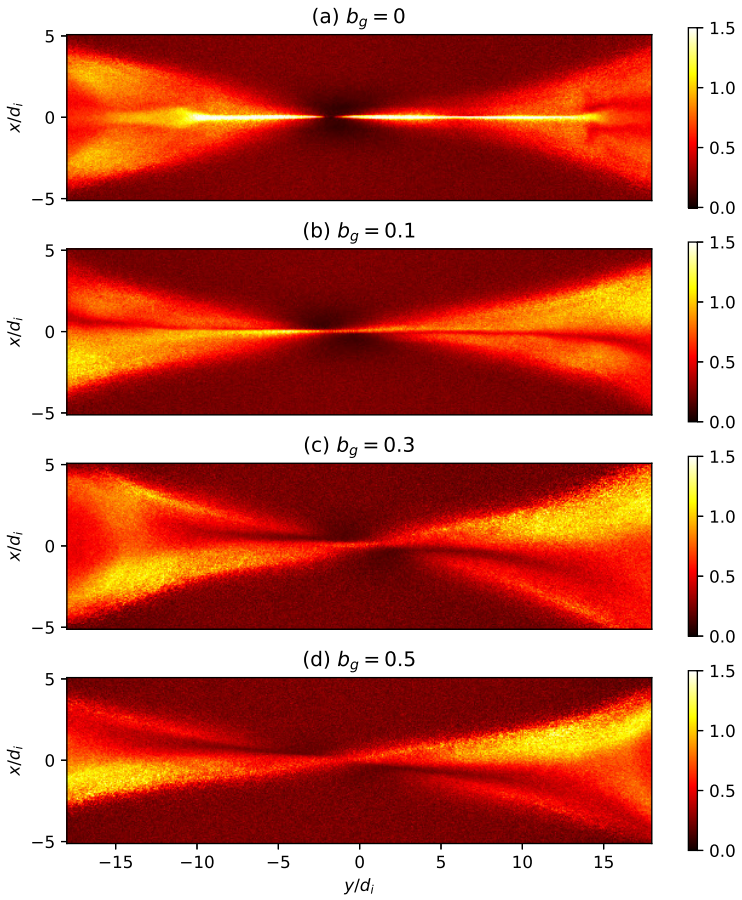

Figure 5.6: $T_{i\|}$ for $b_g = 0$, 0.1, 0.3, and 0.5, respectively.

5.4a, but there is additional heating (blue arrows) that is not due to the stochastic mechanism and which will be subject to future investigations. Figure 5.4c shows that $T_{i\perp}$ agrees well with the prediction from Fig. 5.4a, hinting that the additional heating comes from $T_{i\|}$.

Single-particle trajectories of the heavy ions confirm that stochastic heating is occurring. Figure 5.7g is the same as Figure 5.7d, but for the heavy ions. The separation divergence (Fig. 5.7h) and the kicks in $\mu_{\mathbf{E}\times\mathbf{B}}$ in correlation with α (Fig. 5.7i) verify chaotic behavior. At $t\omega_{ci} > 20$, $\ln\alpha$ is positive only sporadically, so the kicks are smaller, whereas at $t\omega_{ci} < 20$, $\ln\alpha$ stays positive for longer times, so the kicks are bigger.

5.5 Summary

The study presented in this chapter provides strong confirmation that stochastic heating is the fast ion heating mechanism in collisionless magnetic reconnection

up to moderate guide fields. The heating is consistent with calculations based on the properties of the in-plane Hall electric fields that intrinsically develop during reconnection. Ion temperature profiles were found to agree with the predictions. The stochastic nature of ions was confirmed through the examination of Lyapunov exponents and the correlation between $\mu_{\mathbf{E}\times\mathbf{B}}$ violation and the stochastic heating criterion. Heavier ions were found to be heated more strongly because they more easily satisfy the criterion.

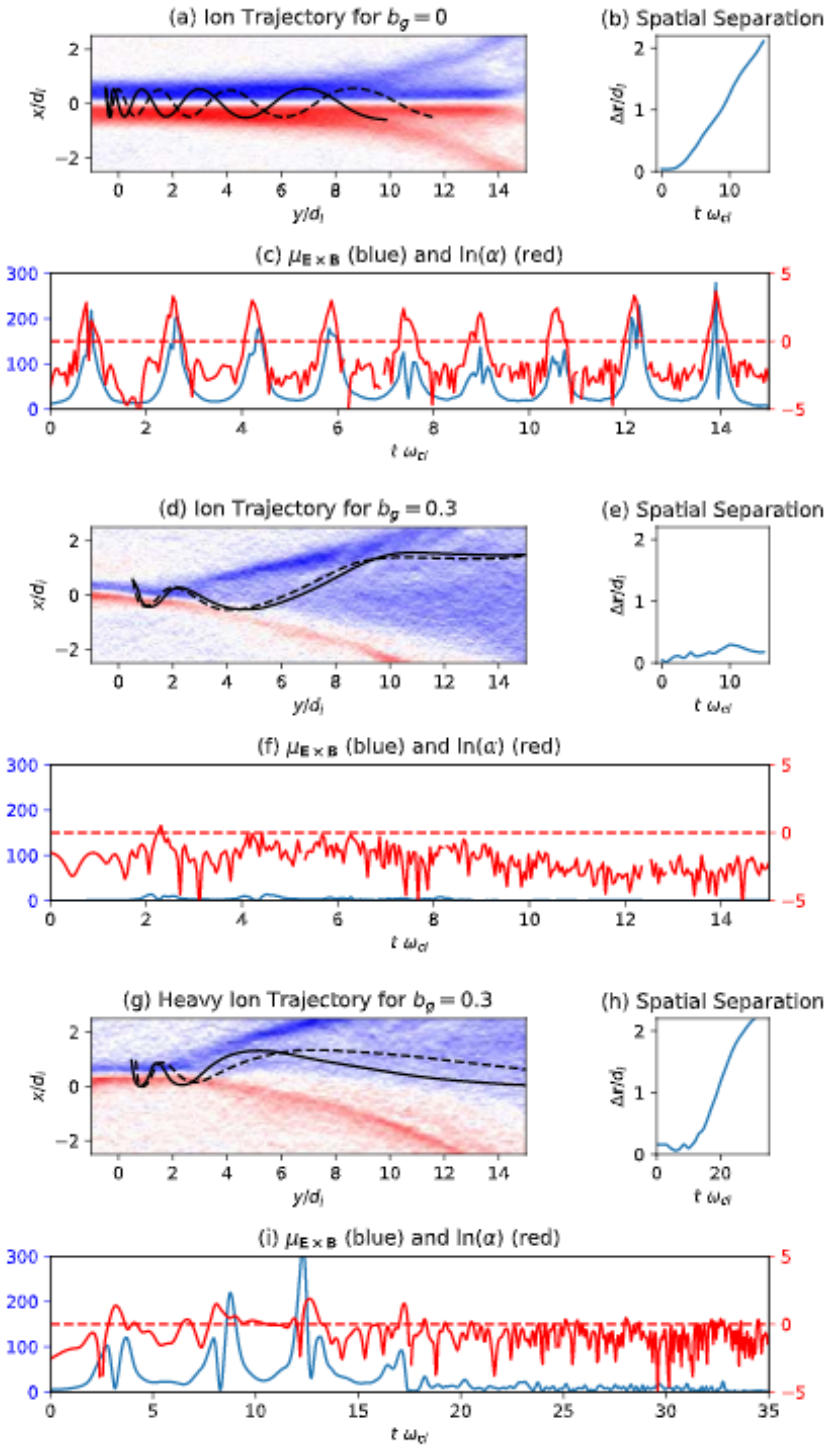

Figure 5.7: (a) Two test ion trajectories (black solid and dashed lines) and E_x (color) under $b_g = 0$. (b) The time-dependent spatial separation between the ions in (a). (c) $\mu_{\mathbf{E}\times\mathbf{B}}$ (blue) and $\ln \alpha$ (red) along the particle trajectory represented by the black solid line in (a). The red dashed line represents the stochastic heating criterion, above which stochastic heating is expected. (d)-(f) are the same as (a)-(c), respectively, except for $b_g = 0.3$. (g)-(i) are the same as (d)-(f), except for $m_i/m_e = 500$.

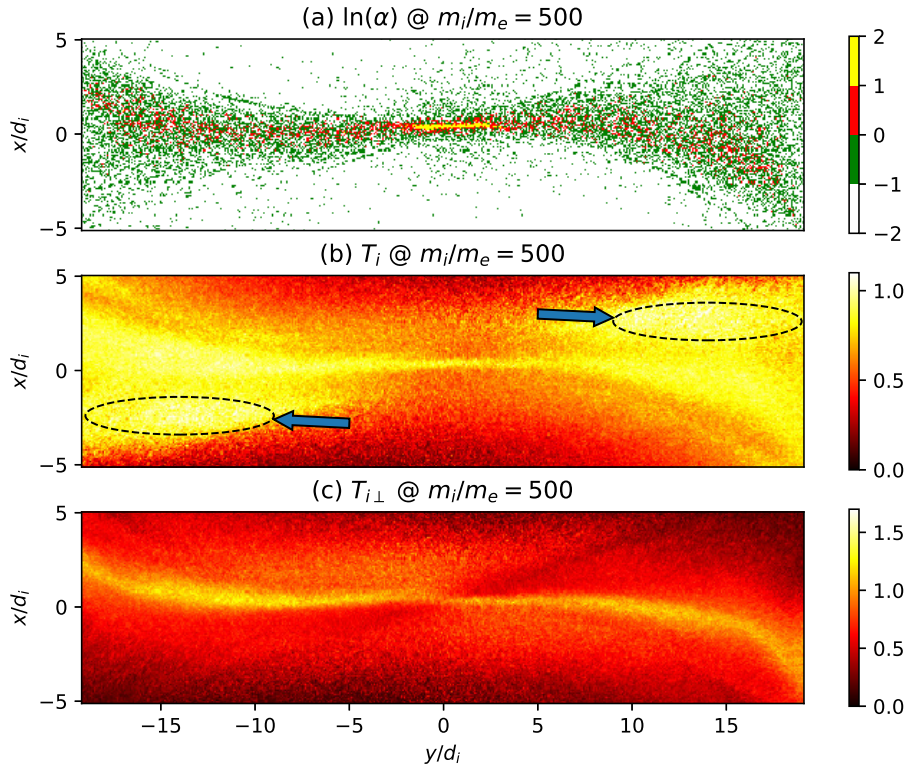

Figure 5.8: (a) $\ln \alpha$, (b) T_i, (c) $T_{i\perp}$ for ions with $m_i/m_e = 500$ under $b_g = 0.3$.

Chapter 6

PITCH-ANGLE SCATTERING OF ENERGETIC PARTICLES BY COHERENT WHISTLER WAVES

In Chapter 2, it was seen that whistler waves are generated as a result of collisionless magnetic reconnection. Because reconnection is ubiquitous in magnetized plasma environments, whistler waves are also ubiquitous in the Earth's magnetosphere [26, 62, 132, 151], Jupiter's magnetosphere [92, 135, 152], and Saturn's magnetosphere [1, 8, 73]. These waves are also important in the solar wind [36, 155], fast magnetic reconnection [12, 29, 67, 104, 169, 170], and helicon plasma sources [20, 33]. In particular, the interaction between energetic charged particles and magnetospheric whistler waves is important since the interaction can change the pitch-angle of the particles, potentially scattering them into the loss cone of a magnetic mirror configuration such as the Earth's dipole magnetic field. Because the escaped energetic particles can cause pulsating auroras at the Earth's poles and energetic particles in general can damage spacecraft, this interaction has been the focus of many studies for decades [2, 5, 6, 68, 71, 80, 81, 101, 114, 145, 154].

Relativistic wave-particle resonance has been known to be an important element of particle energization and pitch-angle scattering. Resonant interaction arises when

$$\omega - k v_z = \frac{\Omega}{\gamma}. \tag{6.1}$$

Here, ω is the wave frequency, k is the wavenumber parallel to the background magnetic field B_0 which is oriented in the z direction, v_z is the parallel particle velocity, and $\Omega = qB_0/m$ is the cyclotron frequency of the particle with charge q and mass m. Also, $\gamma = \left(1 - v^2/c^2\right)^{-1/2}$ is the particle Lorentz factor where v is the particle speed and c is the speed of light. Kennel and Petschek [80] first quantified the scattering mechanism by which incoherent whistler waves lead to velocity space diffusion, and numerous studies have further developed this mechanism [2, 81, 101, 153]. However, recent spacecraft measurements indicate that the observed chorus bursts are, in fact, extremely coherent and that these waves, especially large-amplitude ones ($\delta B/B_0 \sim 0.01$ where δB is the wave magnetic field), are directly linked to electron energization, loss, and microbursts [4, 24, 28, 55, 153, 154]. This linkage suggests that a non-diffusive process could be governing what is observed.

There has thus been a continuing and substantial theoretical effort to investigate the dynamics of energetic particles under coherent whistler waves. Bortnik et al. [19] numerically investigated *ad hoc* the coherent interaction between large-amplitude whistler waves and relativistic particles. Lakhina et al. [87] showed via calculations of pitch-angle diffusion coefficients that coherent chorus subelements can cause rapid pitch angle scattering, although Lakhina et al. [87] used diffusion coefficients calculated from incoherent whistler waves [80] and used non-relativistic equations of motion whereas the actual wave-particle interaction involves relativistic particles (10 keV to MeV [24, 154]). Bellan [9] presented an exact analytical calculation involving a relativistic particle in a right-handed circularly polarized electromagnetic wave. This calculation showed that a certain class of particles undergo quick, drastic pitch-angle scattering depending on whether the individual particle's initial conditions meet a certain criterion, which will be discussed in the next section. Also note that other studies have investigated this single-particle problem via various methods [21, 56, 126, 130]. However, an analysis of the importance of this mechanism for a distribution of particles has not yet been done. To demonstrate importance, one must show that a significant fraction of the particles in the distribution experiences this drastic scattering. If this can be demonstrated, then the particle interaction with coherent whistler waves will be a dominant pitch-angle scattering mechanism.

In this chapter, the analysis presented in Bellan [9] is extended to the relativistic generalization of a thermal distribution of particles; the generalization is prescribed by the Maxwell-Jüttner distribution [78]. It is found that for parameters relevant to magnetospheric chorus, coherent right-handed circularly polarized waves propagating parallel to the background magnetic field trigger large, non-diffusive pitch-angle scatterings for a significant fraction ($1\% - 5\%$) of the energetic particles. The scaling of this fraction with the wave amplitude may also explain the association of relativistic microbursts to large-amplitude chorus [24]. A new condition for large pitch-angle scattering is also presented; this condition is a certain range related to Eq. 6.1, but may or may not include exact resonance depending on the particle initial conditions. Test-particle simulations corroborate the predictions made by this analysis. It is also demonstrated that the widely-used second-order trapping theory [110, 113, 115, 116, 144] is a simplified approximation of the theory presented in this chapter and that this simplified approximation effectively misses critical details of the wave-particle interaction. The present study illustrates that coherent whistler waves are an important cause of non-diffusive pitch-angle scattering and provides an accurate condition for this scattering.

6.1 Two-Valley Motion Review

Let us begin with a brief review of the large pitch-angle scattering mechanism presented in Bellan [9]. A thorough comprehension of this single-particle mechanism is essential for understanding the ensuing analysis presented here. It is assumed that the wave is right-handed circularly polarized and travels parallel to a uniform background magnetic field, so the total magnetic field can be expressed as $\mathbf{B} = B_0\hat{z} + \tilde{\mathbf{B}}$ where

$$\tilde{\mathbf{B}} = \kappa B_0 \left[\hat{x}\sin(kz - \omega t) + \hat{y}\cos(kz - \omega t)\right]. \tag{6.2}$$

Here κ is the wave amplitude relative to the background B_0. Faraday's law determines the wave electric field to be

$$\tilde{\mathbf{E}} = -\frac{\omega}{k}\hat{z} \times \tilde{\mathbf{B}} = \frac{\omega}{k}\tilde{B}\left[\hat{x}\cos(kz - \omega t) - \hat{y}\sin(kz - \omega t)\right]. \tag{6.3}$$

The relativistic Lorentz force equation determines the motion of a charged particle:

$$\frac{d}{dt}(\gamma\boldsymbol{\beta}) = \frac{q}{m}\left(\frac{\tilde{\mathbf{E}}}{c} + \boldsymbol{\beta} \times \mathbf{B}\right), \tag{6.4}$$

where $\boldsymbol{\beta} = \mathbf{v}/c$ and $\gamma = \left(1 - \beta^2\right)^{-1/2}$.

In Bellan [9], a left-handed circularly polarized wave was used although the study was intended for right-handed waves. However, the result therein is unaffected by this apparent error because the sign of the particle charge was unspecified. Although it was not explicitly stated, the analysis was carried out assuming that the charge is positive, e.g., for positrons or ions. If the charge is assumed to be negative, the same wave-particle interaction arises when the wave is assumed to have a right-handed polarization. Therefore, the theory in Bellan [9] describes wave-particle interactions between positively charged particles and left-handed waves, and equivalently between negatively charged particles and right-handed waves — or electrons and right-handed whistler waves. This equivalence can also be seen using charge-parity-time symmetry, which is a fundamental law of any Lorentz-invariant system [58]; making the changes $z \to -z$ and $t \to -t$ in Eqs. 6.2 and 6.3 changes the sense of rotation of the wave, and the relevant physics must be equivalent when the change $q \to -q$ is made.

In this chapter, the analysis in Bellan [9] with the left-handed wave and positively charged particles will be used for two reasons. First, the analysis can then be kept general for any particle with any sign of charge. Second, the derivation of a separate theory for negatively charged particles will merely be a matter of some sign changes

and is not worth the additional complexity in understanding the core points of this chapter.

In Bellan [9], a "frequency mismatch" parameter

$$\xi = 1 + \alpha\gamma\left(n\beta_z - 1\right) \tag{6.5}$$

was defined, where $\alpha = \omega/\Omega$ is the normalized frequency, $\beta_z = v_z/c$ is the normalized parallel velocity, and $n = ck/\omega$ is the refractive index. Equation 6.1 is satisfied when $\xi = 0$, so ξ is a measure of the departure from resonance. An exact rearrangement of Eq. 6.4 leads to an equation of motion for a particle moving in ξ-space [9]:

$$\frac{1}{\Omega'}\frac{d^2\xi}{dt'^2} = -\frac{\partial\psi}{\partial\xi}, \tag{6.6}$$

where

$$\psi\left(\xi\right) = \frac{1}{8}\xi^4 + \left(\kappa'^2 - \frac{\xi_0^2}{2} - s\kappa'\sin\phi_0\right)\frac{\xi^2}{2} - \kappa'^2\xi \tag{6.7}$$

is the pseudo-potential for ξ-space motion. Here the primed quantities are calculated in the wave frame, i.e., a frame moving with a velocity $\hat{z}\omega/k$. The subscript 0 refers to the value at the initial time $t = t' = 0$ and there are two parameters, namely s and ϕ_0. The parameter s is defined as $s = \alpha n\beta_{\perp 0}\gamma_0/\gamma_T$ where $\gamma_T = \left(1 - n^{-2}\right)^{-1/2}$ is the Lorentz factor of the wave. The parameter ϕ_0 is defined as the initial angular orientation of the perpendicular velocity in the $x - y$ plane, i.e., the angle between $\boldsymbol{\beta}_{\perp 0}$ and $\tilde{\mathbf{E}}(t = 0, z = 0)$. The shape of the pseudo-potential is entirely determined by the initial conditions of the particle with respect to the wave as prescribed by ξ_0, s, and ϕ_0. Note that s is an initial condition of the particle because α and n are fixed parameters in the present analysis.

Multiplying Eq. 6.6 by $d\xi/dt'$ and integrating with respect to t' yields the particle pseudo-energy,

$$W = \frac{1}{2\Omega'^2}\left(\frac{d\xi}{dt'}\right)^2 + \psi\left(\xi\right), \tag{6.8}$$

which is a constant of the motion. For certain initial conditions, $\psi\left(\xi\right)$ consists of two valleys separated by a hill in between. If the initial particle pseudo-energy is sufficiently large to go over the hill between the two valleys, then the particle undergoes two-valley motion in ξ-space. This motion involves large changes in ξ and thus in β_z, $\beta_\perp$ and the pitch-angle $\theta_{\text{pitch}} = \tan^{-1}\beta_\perp/\beta_z$.

6.2 Two-Valley Motion Condition

Let us now derive the conditions for two-valley motion for a given particle. The conditions consist of two parts: $\psi(\xi)$ must first be two-valleyed, and the particle must have sufficient pseudo-energy to overcome the hill between the two-valleys. The initial particle kinetic pseudo-energy can be expressed as [9]

$$\frac{1}{2\Omega'^2}\left(\frac{d\xi}{dt'}\right)^2_{t'=t=0} = \frac{1}{2}s^2\kappa'^2\cos^2\phi_0, \tag{6.9}$$

so the total pseudo-energy is

$$W = \frac{1}{2}s^2\kappa'^2\cos^2\phi_0 - \frac{\xi_0^4}{8} + \frac{\xi_0^2}{2}\kappa'\left(\kappa' - s\sin\phi_0\right) - \kappa'^2\xi_0. \tag{6.10}$$

We write Eq. 6.7 as $\psi(\xi) = \xi^4/8 + b\xi^2/2 - \kappa'^2\xi$ where $b = \kappa'^2 - \xi_0^2/2 - s\kappa'\sin\phi_0$. Then $d\psi/d\xi = \xi^3/2 + b\xi - \kappa'^2$, so one extremum is at small $\xi \simeq \kappa'^2/b$ and two extrema are at large $\xi \simeq \pm\sqrt{-2b}$. Since $d^2\psi/d\xi^2 = 3\xi^2/2 + b$, for $b < 0$ the large extrema are local minima (two valleys) and the small extremum is a local maximum (a hill). For $b \geq 0$, the large extrema are undefined, so there is a minimum at $\xi \simeq \kappa'^2/b$. Figure 6.1a shows an example of a two-valley $\psi(\xi)$ for which $b < 0$, and Fig. 6.1b shows a one-valley $\psi(\xi)$ for which $b \geq 0$.

We now make the assumption

$$\kappa' \ll s, \tag{6.11}$$

which will be shown in Section 6.4 to be appropriate for relevant magnetospheric situations. Then, $b \simeq -\xi_0^2/2 - s\kappa'\sin\phi_0$ is negative for

$$\xi_0^2 \geq -2s\kappa'\sin\phi_0. \tag{6.12}$$

All particles having $\sin\phi_0 > 0$ satisfy this equation because ξ_0^2 is non-negative. Particles having $\sin\phi_0 \leq 0$ satisfy Eq. 6.12 only if they are in a certain distance away from exact resonance ($\xi = 0$).

Now, inserting $\xi = \kappa'^2/b$ in Eq. 6.7, we have the height of the hill to be $\psi_{max} \simeq -\kappa'^4/(2b)$. Therefore, the particle has enough pseudo-energy to cross over the hill if

$$\frac{1}{2}s^2\kappa'^2\cos^2\phi_0 - \frac{\xi_0^4}{8} + \frac{\xi_0^2}{2}\kappa'\left(\kappa' - s\sin\phi_0\right) \geq \kappa'^2\xi_0 - \frac{\kappa'^4}{2b}. \tag{6.13}$$

We now assume and justify later that the terms on the right-hand side of Eq. 6.13 are much smaller than those on the left-hand side. Using Eq. 6.11, Eq. 6.13 becomes

$$\frac{1}{2}s^2\kappa'^2\cos^2\phi_0 - \frac{\xi_0^4}{8} - \frac{\xi_0^2}{2}\kappa' s\sin\phi_0 \geq 0, \tag{6.14}$$

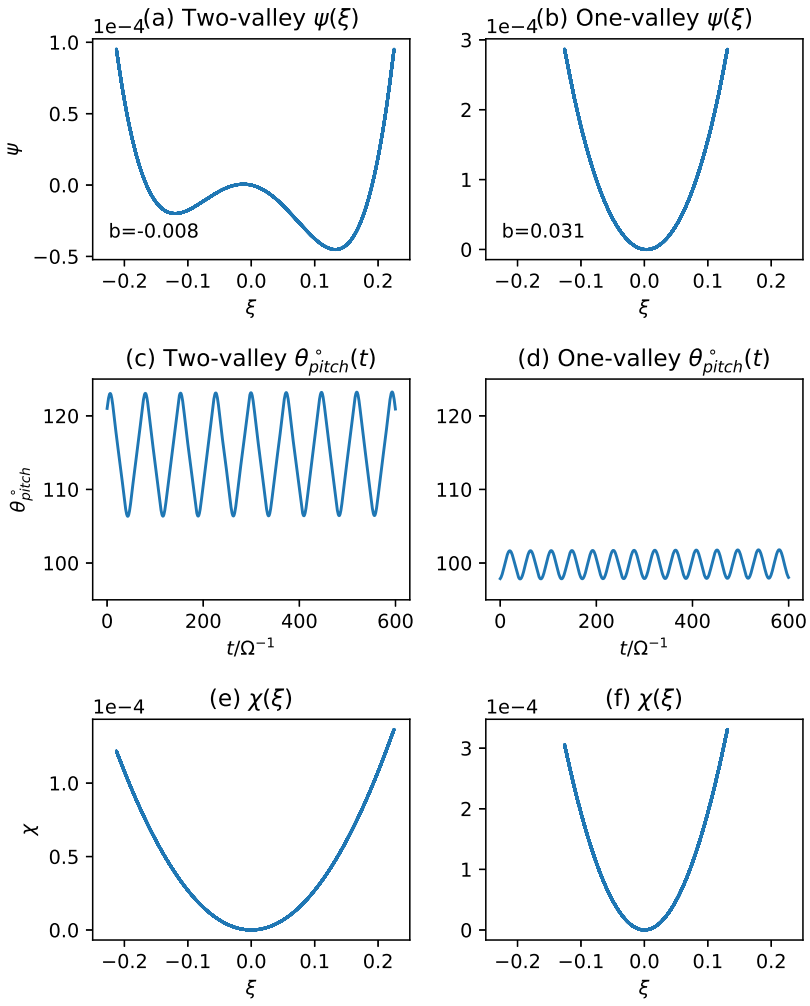

Figure 6.1: (a) An example of a two-valley $\psi(\xi)$ for which $b = -0.008 < 0$. (b) An example of a one-valley $\psi(\xi)$ for which $b = 0.031 \geq 0$. (c) The time-dependent pitch-angle of the particle undergoing two-valley motion, and (d) that of the particle undergoing one-valley motion. The wave parameters were $\kappa = 0.01$, $\alpha = 0.25$, and $n(\alpha) = 18$ from Eq. 6.27. (e), (f) The approximated pseudo-potentials χ obtained by keeping only the term involving $s\kappa'$ in Eq. 6.7 for the respective particles.

whose solution is

$$\xi_0^2 \leq 2s\kappa' (1 - \sin\phi_0) . \tag{6.15}$$

Now we derive the conditions for which the assumptions regarding Eq. 6.13 are valid. This is done by using the solution (i.e., Eq. 6.15) obtained under the assumptions and deriving the conditions for which the terms on the right-hand side of Eq. 6.13 are indeed small compared to those on the left-hand side. Using Eq. 6.15 as an equality, it is seen that each term on the left-hand side of Eq. 6.13 is $O\left(s^2\kappa'^2\right)$ except for the $\kappa'^2\xi_0^2/2$ term which is ignored by Eq. 6.11. On the right-hand side, $\kappa'^2\xi_0 = O\left(\sqrt{s\kappa'^5}\right)$ so it can be ignored if $\kappa' \ll s^3$. Examining the second term, $\kappa'^4/2b = O\left(\kappa'^3/s\right)$ because $b = O(s\kappa')$, so it can be ignored if $\kappa' \ll s$. Since $\kappa' \ll 1$ for linear waves, $\kappa' \ll s^3$ and $\kappa' \ll s$ are both true for $s \geq 1$, and $\kappa' \ll s^3$ is a stronger statement than $\kappa' \ll s$ if $s < 1$. Therefore, for $\kappa' \ll s^3$—which will later be demonstrated to be valid for relevant magnetospheric parameters—the following gives the condition for which a particle undergoes two-valley motion and thus a large pitch-angle scattering:

$$-2s\kappa' \sin\phi_0 \leq \xi_0^2 \leq 2s\kappa' (1 - \sin\phi_0) . \tag{6.16}$$

Equation 6.16 is one of the main results of this chapter. For $\phi_0 \geq 0$, Eq. 6.16 becomes Eq. 6.15 and specifies a certain range around $\xi_0 = 0$. However, for $\phi_0 < 0$ that statistically represents half of the particle population, Eq. 6.16 does not include $\xi_0 = 0$, which means that particles further away from exact resonance undergo two-valley motion and thus large pitch-angle scattering. Therefore, Eq. 6.16 specifies the exact range of the initial distance from resonance that leads to two-valley motion.

Figure 6.1c shows the time-dependent pitch-angle $\theta^\circ_{\text{pitch}}(t)$ of the particle that has enough pseudo-energy to undergo two-valley motion in the two-valley pseudo-potential in Fig. 6.1a. Figure 6.1d shows $\theta^\circ_{\text{pitch}}(t)$ of the particle moving in the one-valley pseudo-potential. The particle in Fig. 6.1c experiences a much larger change in pitch-angle than that in Fig. 6.1d. The rate of change of the pitch-angle in Fig. 6.1c is also very large; the wave period is $T_{\text{wave}}\Omega = 2\pi/\alpha \simeq 25$, so the pitch-angle changes by $\sim 15^\circ$ in $t\Omega \simeq 40$ or in about one to two wave periods.

6.3 Distribution of ξ

The initial particle distribution in ξ-space will now be derived. The subscript zero will henceforth be dropped because only the initial conditions are being examined. The thermal distribution is assumed to be the Maxwell-Jüttner distribution [78]

with an isotropic temperature. This distribution is a considerable simplification, and repercussions of this simplification and possible remedies will be discussed in Section 6.6. This is the relativistic generalization of the Maxwell-Boltzmann distribution and can be expressed in terms of the Lorentz factor γ as

$$f_\gamma = \frac{\gamma^2\sqrt{1-1/\gamma^2}}{\theta K_2(1/\theta)} \exp\left(-\frac{\gamma}{\theta}\right), \tag{6.17}$$

where $\theta = k_B T/mc^2$ is the normalized temperature and K_n is the modified Bessel function of the second kind of order n. Using $\gamma = \sqrt{1+p^2/m^2c^2} = \sqrt{1+\rho^2}$ where $\boldsymbol{\rho} = \mathbf{p}/mc$ is the normalized particle momentum, Eq. 6.17 can be expressed as

$$f_{\boldsymbol{\rho}} = \frac{1}{4\pi\theta K_2(1/\theta)} \exp\left(-\frac{\sqrt{1+\rho^2}}{\theta}\right). \tag{6.18}$$

Integrating Eq. 6.18 in ρ_z and over all angles gives $f_{\rho_\perp}$:

$$f_{\rho_\perp} = \frac{\rho_\perp\sqrt{1+\rho_\perp^2}}{\theta K_2(1/\theta)} K_1\left(\frac{\sqrt{1+\rho_\perp^2}}{\theta}\right). \tag{6.19}$$

Note that $f_{\boldsymbol{\rho}}$ is defined in 3D $\boldsymbol{\rho}$-space so that $\int f_{\boldsymbol{\rho}} d^3\boldsymbol{\rho} = 1$, whereas $f_{\rho_\perp}$ is defined in 1D $\rho_\perp$-space so that $\int f_{\rho_\perp} d\rho_\perp = 1$. Integrating Eq. 6.18 in ρ_x and ρ_y gives f_{ρ_z}:

$$f_{\rho_z} = \frac{\theta}{2K_2(1/\theta)}\left(1+\frac{\sqrt{1+\rho_z^2}}{\theta}\right)\exp\left(-\frac{\sqrt{1+\rho_z^2}}{\theta}\right), \tag{6.20}$$

where $\int f_{\rho_z} d\rho_z = 1$. The details of the derivations of $f_{\rho_\perp}$ and f_{ρ_z} are given in Appendices F.1 and F.2, respectively.

Now, noting that $\gamma\boldsymbol{\beta} = \gamma\mathbf{v}/c = \mathbf{p}/mc = \boldsymbol{\rho}$, the mismatch parameter (Eq. 6.5) can be expressed as

$$\xi = 1 + \alpha(n\rho_z - \gamma). \tag{6.21}$$

The probability distribution of having a specific ξ is obtained by multiplying the probability distribution of having a certain γ by that of having the corresponding ρ_z which yields the specified ξ, and then integrating over all γ (full derivation given in Appendix F.3). The solution is

$$f_\xi = \int_1^\infty \frac{\gamma^2\sqrt{1-1/\gamma^2}}{2\alpha n K_2^2(1/\theta)}\left(1+\frac{\sqrt{1+\rho_z^2(\gamma,\xi)}}{\theta}\right)\exp\left(-\frac{\gamma+\sqrt{1+\rho_z^2(\gamma,\xi)}}{\theta}\right)d\gamma, \tag{6.22}$$

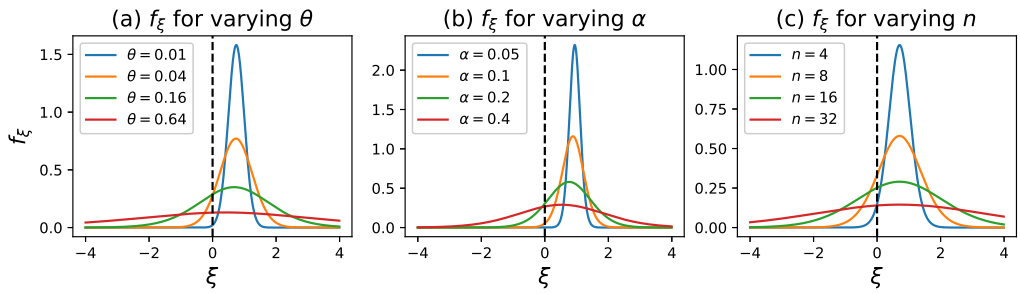

Figure 6.2: f_ξ for different (a) θ, (b) α and (c) n values. The default values are $\theta = 0.1$, $\alpha = 0.25$, and $n = 10$. The black dashed line is the resonant condition $\xi = 0$.

where $\rho_z(\gamma, \xi) = [(\xi - 1)/\alpha + \gamma]/n$ is a rearrangement of Eq. 6.21 and $\int f_\xi d\xi = 1$. Given θ, α and n, Eq. 6.22 is an integral solution for f_ξ.

Figure 6.2 shows f_ξ for different (a) θ, (b) α and (c) n values. The default values are $\theta = 0.1$, $\alpha = 0.25$, and $n = 10$, where $\alpha = 0.25$ and $\theta = 0.1$ are relevant values for the dayside outer magnetosphere [153], and $n = 18 \sim 10$ from the whistler dispersion relation (Eq. 6.27). The black dashed vertical line represents the resonant condition $\xi = 0$ (or equivalently Eq. 6.1). As θ, α, and n increase from zero, f_ξ broadens and more particles are resonant. After a certain threshold, however, too much broadening leads to the decrease of the local magnitude of $f_\xi(\xi = 0)$ and reduces the number of resonant particles. Increasing α significantly changes the mean value of ξ as well, raising this threshold higher.

6.4 Fraction of Particles Undergoing Two-Valley Motion

Before calculating the fraction of particles undergoing two-valley motion, the probability distribution of the limits of integration (Eq. 6.16) must first be derived. Again, the subscript zero will be dropped. Since $s = \alpha n \beta_\perp \gamma / \gamma_T = \alpha\sqrt{n^2 - 1}\rho_\perp$, the relevant distribution is that of $\rho_\perp$ and $\sin\phi$. Equation 6.19 prescribes $f_{\rho_\perp}$, and assuming that ϕ is isotropic, the probability distribution of $\Phi = \sin\phi$ is the Arcsine(-1,1) distribution,

$$f_\Phi = \frac{1}{\pi\sqrt{1 - \Phi^2}}, \tag{6.23}$$

for $\Phi \in (-1, 1)$.

We now have all the ingredients to calculate the fraction of particles that undergo two-valley motion in ξ-space and thus experience large pitch-angle scattering. This fraction can be found by calculating the probability that both Eqs. 6.12 and 6.15

(i.e., Eq. 6.16) are satisfied. In the case $\Phi > 0$ when Eq. 6.12 is always met, after defining a numerical factor $a = 2\alpha\kappa'\sqrt{n^2-1}$ so that $2s\kappa' \sin\phi = a\rho_\perp\Phi$ and $2s\kappa'(1-\sin\phi) = a\rho_\perp(1-\Phi)$, the probability of two-valley motion is

$$p_+ = \int_{\rho_\perp=0}^{\infty}\int_{\Phi=0}^{1} f_{\rho_\perp} f_\Phi \int_{\xi=-\sqrt{a\rho_\perp(1-\Phi)}}^{\sqrt{a\rho_\perp(1-\Phi)}} f_\xi d\xi d\Phi d\rho_\perp. \tag{6.24}$$

In the opposite case where $\Phi \leq 0$, the probability of two-valley motion is,

$$p_- = \int_{\rho_\perp=0}^{\infty}\int_{\Phi=-1}^{0} f_{\rho_\perp} f_\Phi \left(\int_{-\sqrt{a\rho_\perp(1-\Phi)}}^{-\sqrt{-a\rho_\perp\Phi}} f_\xi d\xi + \int_{\sqrt{-a\rho_\perp\Phi}}^{\sqrt{a\rho_\perp(1-\Phi)}} f_\xi d\xi \right) d\Phi d\rho_\perp. \tag{6.25}$$

The total fraction of particles undergoing two-valley motion is then $p_{tv} = p_+ + p_-$.

There are four degrees of freedom when calculating p_{tv}: θ, α, n and κ. However, one degree of freedom can be eliminated by linking α and n through the whistler wave dispersion relation, which, for parallel propagation and $\Omega_p/\Omega \gg 1$ where Ω_p is the electron plasma frequency, is

$$\frac{c^2k^2}{\omega^2} = \frac{\Omega_p^2/\omega^2}{|\Omega|/\omega - 1}. \tag{6.26}$$

In terms of the dimensionless variables used in this chapter, this becomes

$$n = \frac{\Omega_p/\Omega}{\sqrt{\alpha(1-\alpha)}}, \tag{6.27}$$

which can be used to express $n(\alpha)$ if Ω_p/Ω is specified. Using parameters in Tsurutani et al. [153] ($n_e \simeq 10$ cm^{-3},$B_0 \simeq 125$ nT), we obtain $\Omega_p/\Omega \simeq 8$; this value will be used throughout the rest of the analysis.

Let us now calculate p_{tv} for the parameters in the range $0.0001 \leq \kappa \leq 0.01$, $0.1 \leq \alpha \leq 0.8$ and $0.01 \leq \theta \leq 10$ (corresponding to electron thermal energies from 5.11 keV to 5.11 MeV). Since the parameter range is determined, the conditions for which the assumption $\kappa' \ll s^3$ that was used to derive Eq. 6.16 is true can now be determined. Because $n \gg 1$, $\kappa' = \kappa/\gamma_T = \kappa\sqrt{1-1/n^2} \simeq \kappa$ and $s = \alpha\sqrt{n^2-1}\rho_\perp \simeq \alpha n\rho_\perp$. From Eq. 6.27 it follows that $\alpha n = \left(\Omega_p/\Omega\right)\sqrt{\alpha/(1-\alpha)}$. We now compare the largest value of κ to the lowest value of s^3, which involves the smallest values of α and θ. For $\theta \ll 1$, the most likely $\rho_\perp$ is $\sqrt{\theta}$ (see Appendix F.4). Thus, the condition $\kappa' \ll s^3$ can be expressed as

$$\kappa \ll \left(\frac{\Omega_p}{\Omega}\sqrt{\frac{\alpha\theta}{1-\alpha}}\right)^3, \tag{6.28}$$

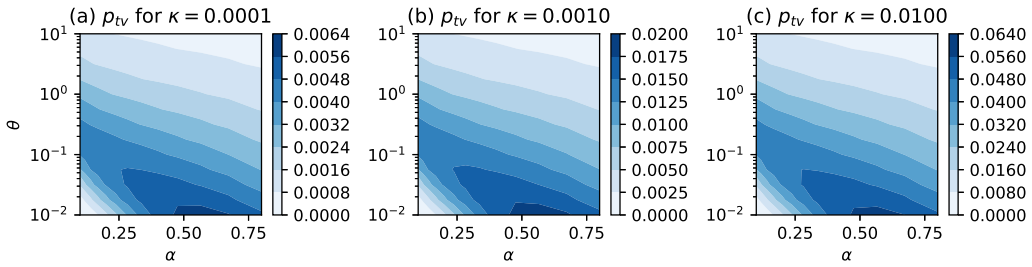

Figure 6.3: p_{tv} as a function of α and θ for different κ values.

or

$$\theta \gg \frac{\kappa^{2/3}}{\left(\Omega_p/\Omega\right)^2 \left(\alpha/(1-\alpha)\right)}. \tag{6.29}$$

Inserting $\alpha = 0.1$ and $\kappa = 0.01$ shows that $\kappa' \ll s^3$ is valid if $\theta \gg 0.0066$. Thus, $0.01 \leq \theta \leq 10$ is consistent with $\kappa' \ll s^3$.

Figure 6.3 shows contours of p_{tv} as a function of α and θ for different κ values. For $\kappa \geq 0.001$, which is typical for magnetospheric chorus [102, 153], a significant fraction (1%−5%) of particles undergo two-valley motion and thus large pitch-angle scattering. However, p_{tv} decreases at high θ ($\theta \gtrsim 1$), and this phenomenon is related to the decrease of the local magnitude of f_ξ ($\xi = 0$) if there is too much broadening of f_ξ, as shown in Fig. 6.2. Figure 6.3 also shows that $p_{tv}(\alpha, \theta)$ has more or less the same shape across a wide range of κ but its magnitude is proportional to $\sqrt{\kappa}$. This is because the limits of the ξ integrals in Eqs. 6.24 and 6.25 scale as $\sqrt{a} \sim \sqrt{\kappa}$, so if the integration range is sufficiently small so that the integrand may be approximated by a linear function, it follows that $p_{tv} \propto \sqrt{\kappa}$.

6.5 Numerical Verification

The analytical predictions presented so far will now be verified via numerical simulations. A computer code was written which solves Eq. 6.4 and $d\mathbf{x}/dt = c\boldsymbol{\beta}$ using the fully implicit Runge-Kutta method of the Radau IIA family of order 5 [64] in the scipy.integrate.solve_ivp package in Python 3.7. This particular method was used because it yielded the smallest numerical error out of the available methods in the Python package, measured by the drift of the average value of the pitch-angle over time which should be zero in principle (see, e.g., Fig. 6.1c where the particle's pitch-angle oscillates around a stationary average value). The error was quantified by using the statistics of the 10,000 particles in Fig. 6.5c. The Radau method with a time step $\Delta t = 0.2$ yielded a median value for the pitch-angle drift of 0.07° with a

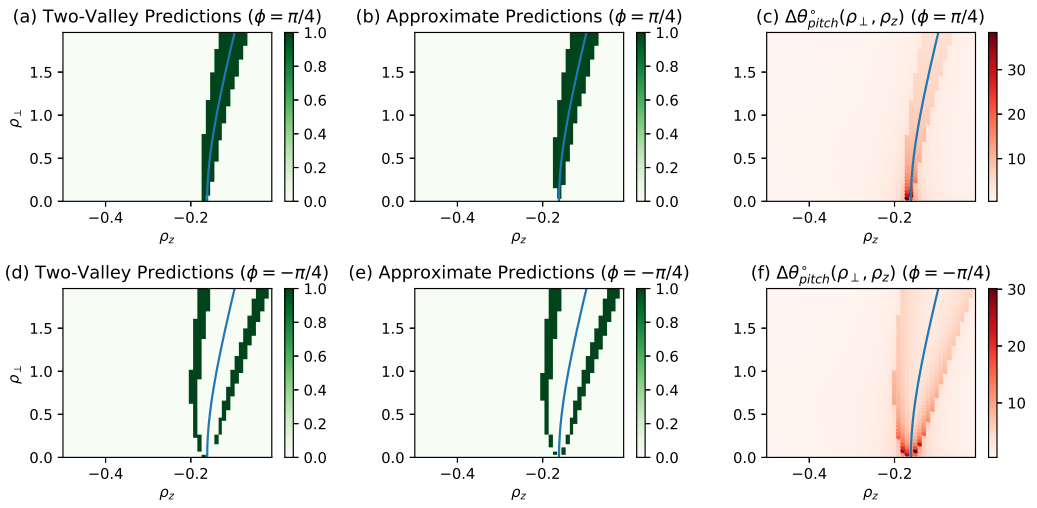

Figure 6.4: (a) Regions of initial momentum space (dark green) that satisfy the unapproximated two-valley criteria (Eqs. 6.13 and $b < 0$) for $\phi = \pi/4$. (b) Regions of this space that satisfy the approximated criterion (Eq. 6.16) for $\phi = \pi/4$. (c) Pitch-angle range (in degrees) within a single particle trajectory for a range of initial particle momenta for $\phi = \pi/4$. (d-f) are the same as (a-c) except for $\phi = -\pi/4$. Blue lines represent the resonance condition (Eq. 6.1; $\xi = 0$). The wave parameters were $\alpha = 0.25$, $\kappa = 0.005$, and $n = 18$ from Eq. 6.27.

standard deviation of 0.14°, which is far smaller than the pitch-angle change of a vast majority of the particles. The electromagnetic fields were prescribed by Eqs. 6.2 and 6.3, which is a simplified model of a whistler wave. The code was parallelized with the multiprocessing package.

It will first be verified that particles which satisfy Eq. 6.16 and thus undergo two-valley motion experience large pitch-angle scattering. 2,500 particle trajectories were numerically integrated, and the initial particle momenta were scanned in the range $\rho_\perp \in [0, 2]$, $\rho_z \in [-0.5, 0]$, and $\phi = \pi/4, -\pi/4$. The wave amplitude was $\kappa = 0.005$, and the wave frequency was $\alpha = 0.25$, which gives $n = 18$ using Eq. 6.27.

Figure 6.4a shows the regions of initial momentum space (dark green) that satisfy the unapproximated two-valley criteria (Eqs. 6.13 and $b < 0$) for $\phi = \pi/4$. Figure 6.4b shows regions of this space that satisfy the approximated criterion (Eq. 6.16). The regions are virtually identical except for $\rho_\perp \lesssim 0.1$ because for sufficiently large $\rho_\perp$, the $\kappa \ll s^3$ approximation holds. Figures 6.4a and 6.4b are effectively predictions of large pitch-angle scattering. The colors in Fig. 6.4c show the pitch-angle range that a particle undergoes for each point in $(\rho_\perp, \rho_z)$ space; this pitch-angle range is

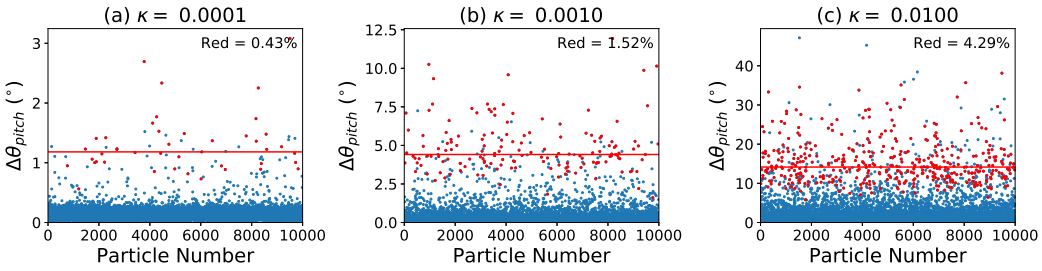

Figure 6.5: Pitch-angle range of 10,000 particles whose initial momenta were randomly sampled from Eq. 6.18 for different κ values. Red points represent particles that meet the two-valley criterion (Eq. 6.16), and the text inside represents the percentage of red particles. The red horizontal lines represents the median $\Delta\theta^{\circ}_{pitch}$ of the red particles

defined by the absolute difference between the maximum and minimum pitch-angles along the particle trajectory. For example, the particle in Fig. 6.1c has a pitch-angle range of $\sim 15^{\circ}$, and that in Fig. 6.1d has a pitch-angle range of $\sim 3^{\circ}$. Figures 6.4d-f are the same as Figs. 6.4a-c except for $\phi = -\pi/4$. It can be clearly seen that if a particle's initial momentum satisfies the two-valley criteria, it undergoes a large pitch-angle scattering.

The blue curves in Fig. 6.4 represent the resonance condition (Eq. 6.1; $\xi = 0$). The curve is found by solving $\xi = 1 + \alpha(n\rho_z - \gamma) = 1 + \alpha(n\rho_z - \sqrt{1 + \rho_\perp^2 + \rho_z^2}) = 0$ for $\rho_\perp(\rho_z)$ and restricting the domain of ρ_z to be consistent with $\gamma = \alpha^{-1} + n\rho_z \geq 1$. In Figs. 6.4d-f, the blue lines do not pass through regions of two-valley motion and large scattering. This fact is consistent with Eq. 6.16 which qualitatively states that for $\phi < 0$, the condition for two-valley motion and large scattering does not include $\xi = 0$.

Next, the analytical prediction for p_{tv} will be verified via the Monte-Carlo method. The trajectories of 10,000 particles whose initial momenta were randomly sampled from Eq. 6.18 were respectively integrated for $\kappa = 0.0001, 0.001$, and 0.01. Other parameters were $\alpha = 0.25$, $n = 18$, and $\theta = 0.1$.

Figure 6.5 shows the pitch-angle range (in degrees) of the randomly sampled particles for different κ values. Red points represent particles that meet the two-valley criterion (Eq. 6.16), and the text inside represents the percentage of red particles. Figure 6.3 shows that for $\alpha = 0.25$ and $\theta = 0.1$, the predicted percentage ranges are $0.4 - 0.48\%$, $1.25 - 1.5\%$, and $4.00 - 4.80\%$ for $\kappa = 0.0001, 0.001$, and 0.01, respectively, which approximately agree with the results in Fig. 6.5. Red points

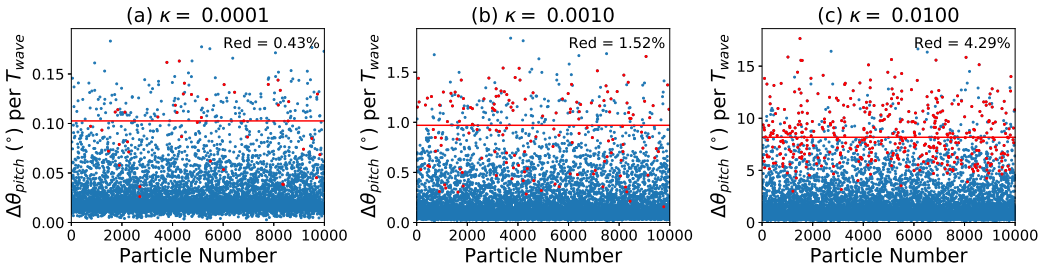

Figure 6.6: Pitch-angle change per wave period of the respective simulations in Fig. 6.5. The red horizontal lines respectively represent the median value of the pitch-angle change per wave period of the red particles.

generally experience significantly larger pitch-angle scattering than other particles, as can be seen from the median value of the red points (red horizontal lines). However, it can be seen that there are blue points that also experience large scattering; examining the pseudo-potential $\psi(\xi)$ for these points shows that these particles have pseudo-energies that are just short of overcoming the two-valley hill, so they "almost" undergo two-valley motion and experience substantial pitch-angle scattering. Therefore, we conclude that p_{tv} is a lower-bound for the fraction of particles with large pitch-angle scattering.

Even if two-valley motion were to cause large pitch-angle scattering, the mechanism would not be significant if this scattering could not occur within a short enough time. Thus, it is necessary to show that the coherent wave lasts sufficiently long for two-valley motion to occur. Figure 6.6 shows the pitch-angle change within a single wave period for the respective simulations in Fig. 6.5. Tsurutani et al. [153] observed in the outer magnetosphere coherent chorus elements with amplitudes $\kappa \simeq 0.0016$ that are $0.1 \sim 0.5$ s long with a frequency of $\sim$ 700Hz. These elements consisted of subelements or packets lasting $5 \sim 10$ ms, corresponding to about 3.5 to 7 wave periods. $\kappa \simeq 0.0016$ approximately corresponds to Fig. 6.6b, which shows that red particles can reach their median pitch-angle range ($\sim 5°$ from Fig. 6.5b) in five wave periods on average. For $\kappa = 0.01$ (Fig. 6.6b), this rate is even faster as the red particles can reach their median pitch-angle range of $\sim 15°$ (Fig. 6.5c) in about two wave periods.

6.6 Discussion

The results presented here may help explain the the association of large-amplitude whistler waves to relativistic microbursts ($\sim$ 1 MeV) [24] and may explain the lack of

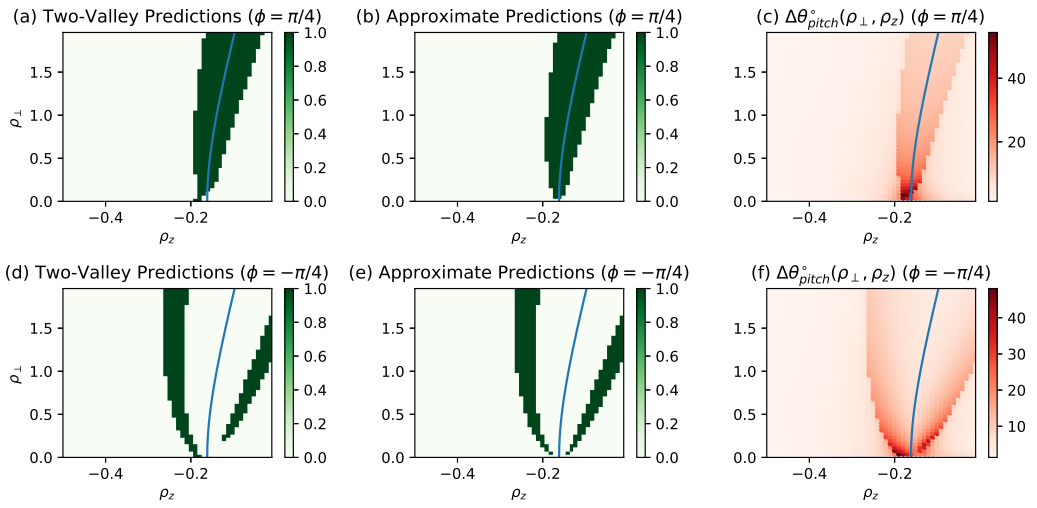

Figure 6.7: Same as Fig. 6.4, but for $\kappa = 0.02$.

such energetic microbursts in small-amplitude chorus [154]. Particle energization is not a subject of this Chapter and thus will not be discussed; it will be assumed that the particles are first energized by some mechanism that yields a relativistic distribution, and then the ensuing pitch-angle dynamics are studied in order to concentrate on one topic. It should be noted, however, that energization and pitch-angle scattering may occur simultaneously.

In Fig. 6.3, for small amplitudes ($0.0001 \leq \kappa \leq 0.001$), only up to 0.5% of particles in a distribution with a temperature of $\sim$ 1 MeV (corresponding to $\theta \simeq 2$) interact with the wave, whereas for large amplitudes ($\kappa \simeq 0.01$), $\sim$2% of such particles do. This is because the range of the two-valley condition in Eq. 6.16 scales with the wave amplitude κ; i.e., as the wave amplitude increases, more particles, including energetic particles, satisfy the two-valley condition.

The interaction of large-amplitude waves with relativistic particles is further explained in Fig. 6.7, which is the same as Fig. 6.4 but for a larger wave amplitude ($\kappa = 0.02$). It can clearly be seen that the predictions of large scattering in Fig. 6.7 are much broader in phase space than those in Fig. 6.4. This is important because in Fig. 6.4, relativistic particles with $\rho \gtrsim 1$ must have large initial pitch-angles to interact with the wave since the two-valley condition is a narrow range related to the exact resonance condition, and thus these particles must undergo extremely large pitch-angle scatterings in order to jump into the loss cone. However, in Fig. 6.7, the range for two-valley motion is much increased, allowing for relativistic particles with

smaller initial pitch-angles to interact with the wave. The deviation of the two-valley condition from the exact resonance condition is because the range in Eq. 6.16 scales with κ. Furthermore, the pitch-angle range itself is significantly increased in Fig. 6.7. Therefore, a larger wave amplitude allows for relativistic particles with lower initial pitch-angles to interact with the wave, while simultaneously increasing the amount of pitch-angle scattering; these two effects lead to more relativistic particles being pitch-angle scattered into the loss-cone.

There are a few limitations to the present analysis that may be subject to future work. First, the Maxwell-Jüttner distribution is a simplification and should not be considered as a distribution representing the entire electron population. The actual distribution is a sum of these Maxwellians or other functions such as the kappa distribution [123]. If the actual distribution can be expressed as a weighted sum of Maxwelll-Jüttner distributions, then the total fraction of particles that undergo two-valley motion is the sum of the partial fractions for each distribution. On the other hand, if the actual distribution is another sufficiently simple function, then an analysis similar to that in Sections 6.3 and 6.4 may be conducted by replacing Eq. 6.17 by the actual distribution.

Second, the particle temperature is assumed for simplicity to be isotropic, whereas observations indicate that electron temperature in the magnetosphere in general is anisotropic and electron distribution functions can be more complex than simple anisotropic distributions [94]. The transition to an anisotropic Maxwell-Jüttner distribution is outlined in Livadiotis [98] and Treumann and Baumjohann [150].

Third, the wave is assumed to have exact parallel propagation, whereas many instances of magnetospheric chorus involve oblique propagation [6, 134]. Also, chorus typically exhibits frequency and amplitude changes over a short time period [153], but the model presented here is based on a plane wave with a fixed frequency and wavenumber (Eqs. 6.2 and 6.3). However, including obliquity and variable frequency makes the analysis considerably more complicated and so would be inappropriate for an inaugural analysis.

6.7 Comparison to Second-order Trapping Theory

A popular theory describing wave-particle interactions is the second-order trapping effect presented in, e.g., Sudan and Ott [144], Nunn [110] and Omura et al. [113]. Omura et al. [115] and Omura et al. [116] present relativistic generalizations of the theory. However, it will now be shown that this previous theory is an approximation

of the theory presented here; this approximation effectively misses the critical two-valley nature of the pseudo-potential.

Omura et al. [113] use the following coupled equations for non-relativistic speeds:

$$\frac{d\zeta}{dt} = k(v_z - V_R), \tag{6.30}$$

$$\frac{d}{dt}(v_z - V_R) = \frac{\omega_t^2}{k}(\sin\zeta + S), \tag{6.31}$$

where

$$V_R = \frac{\omega - \Omega}{k}, \tag{6.32}$$

ζ is the angle between $\mathbf{v}_\perp$ and $\tilde{\mathbf{B}}$, $\omega_t = \sqrt{k v_\perp \Omega \kappa}$ is the trapping frequency, and S is a parameter that is equal to zero when the background magnetic field is spatially uniform and ω is a constant. Therefore, setting $S = 0$, differentiating Eq. 6.31 in time, and using Eq. 6.30,

$$\frac{d^2}{dt^2}(v_z - V_R) = \frac{\omega_t^2}{k}\cos\zeta\frac{d\zeta}{dt}, \tag{6.33}$$

$$= \omega_t^2(v_z - V_R)\cos\zeta. \tag{6.34}$$

Letting $\gamma = 1$ in Eq. 6.5 and rearranging shows that

$$\xi = \frac{k}{\Omega}(v_z - V_R), \tag{6.35}$$

so Eq. 6.34 becomes

$$\frac{d^2\xi}{dt^2} = \xi\omega_t^2\cos\zeta, \tag{6.36}$$

$$= -\frac{\partial}{\partial\xi}\left(-\frac{\xi^2}{2}\omega_t^2\cos\zeta\right), \tag{6.37}$$

$$\frac{1}{\Omega^2}\frac{d^2\xi}{dt^2} = -\frac{\partial\chi(\xi)}{\partial\xi}, \tag{6.38}$$

where $\chi(\xi) = -\xi^2\omega_t^2\cos\zeta/2\Omega^2$ is the pseudo-potential of this system.

Now, let us examine the term involving $s\kappa'$ in Eq. 6.7 assuming $\gamma_0 = \gamma_T = 1$;

$$-s\kappa\sin\phi_0\frac{\xi^2}{2} = -\alpha n\kappa\beta_{\perp 0}\sin\phi_0\frac{\xi^2}{2}, \tag{6.39}$$

$$= -\frac{\omega}{\Omega}\frac{ck}{\omega}\kappa\frac{v_{\perp 0}}{c}\sin\phi_0\frac{\xi^2}{2}, \tag{6.40}$$

$$= -\frac{\omega_{t0}^2}{\Omega^2}\sin\phi_0\frac{\xi^2}{2}, \tag{6.41}$$

$$= \chi_0(\xi), \tag{6.42}$$

because ζ and ϕ are related by $\zeta = \phi - \pi/2$, so $\cos\zeta = \sin\phi$. $\chi_0(\xi)$ is $\chi(\xi)$ except that $v_{\perp 0}$ and ϕ_0 are used instead of $v_\perp$ and ϕ, and the relationship is similar for ω_{t0} and ω_t. Therefore, $\chi(\xi)$ results from keeping only the $s\kappa'$ term in $\psi(\xi)$. This is important because $\chi(\xi)$ only describes either a trapping or a non-trapping potential but not a two-valley potential.

Figure 6.1e and 6.1f plot the approximated pseudo-potentials $\chi(\xi)$ for the particles in Fig. 6.1a and 6.1b, respectively. For both particles, $\chi(\xi)$ is clearly a one-valley potential, whereas the unapproximated $\psi(\xi)$ is two-valleyed for the particle in Fig. 6.1a and thus it undergoes much larger pitch-angle scattering than the particle in Fig. 6.1b . Therefore, if the theory in Omura et al. [113] were to be used, it would be impossible to distinguish between the two particles which clearly have an extremely large difference in the amount of pitch-angle scattering.

Another important problem with the second-order trapping theory is that the time-dependence of the variables is ambiguous at best. Omura et al. [113] imply that $v_\perp$ and thus ω_t are time-dependent but then treat $v_\perp$ as a constant when they state that combining Eqs. 6.30 and 6.31 gives a pendulum equation. Sudan and Ott [144] admit that $v_\perp$ is time-dependent, but then argue that it can be treated as a constant, as specified in the sentence after their Eq. 10. In the present theory, however, the initial variables and the time-dependent ones are explicitly differentiated, so no approximation regarding time-dependence needs to be made. This is an extremely important point because this time-dependence of $v_\perp$ gives the two-valley potential whereas treating it as a constant does not. This fact can be more explicitly illustrated by examining Eq. 26 in Bellan [9] which is an equation for the parallel velocity (recall that $\beta_z = v_z/c$ and prime refers to the wave frame):

$$\frac{1}{\Omega'}\frac{d^2\beta_z'}{dt'^2} = \xi\boldsymbol{\beta}_\perp' \cdot \frac{\tilde{\mathbf{B}}_\perp'}{B_0} - \beta_z'\frac{\tilde{\mathbf{B}}_\perp'}{B_0}\cdot\frac{\tilde{\mathbf{B}}_\perp'}{B_0}. \tag{6.43}$$

The second-order trapping theory effectively drops the last term in Eq. 6.43 and ignores the time-dependence of the first term on the right-hand side. This leads to

$$\frac{1}{\Omega'}\frac{d^2\xi}{dt'^2} = \alpha n\frac{\gamma'}{\gamma_T}\xi\boldsymbol{\beta}_\perp' \cdot \frac{\tilde{\mathbf{B}}_\perp'}{B_0}, \tag{6.44}$$

which is equivalent to Eq. 6.38 if $\gamma' = \gamma_T = 1$ is assumed. However, Eq. 35 of Bellan [9] states that

$$\boldsymbol{\beta}_\perp' \cdot \frac{\tilde{\mathbf{B}}_\perp'}{B_0} = \boldsymbol{\beta}_{\perp 0}' \cdot \frac{\tilde{\mathbf{B}}_{\perp 0}'}{B_0} - \frac{\gamma_T}{2\alpha n\gamma'}\left(\xi^2 - \xi_0^2\right), \tag{6.45}$$

which means that treating $v_\perp$ as a constant effectively misses the ξ-dependence in Eq. 6.45, which is the reason for the two-valley shape of the pseudo-potential.

For example, neglecting the ξ_0^2 term in Eq. 6.45 leads to erroneous conclusions regarding the shape of the potential near $\xi = 0$. In Fig. 6.1e, $\chi(\xi)$ is a valley because $-s\kappa' \sin\phi_0$ is positive in this case. However, the correct pseudo-potential $\psi(\xi)$ in Fig. 6.1a is a hill near $\xi = 0$ because $-\xi_0^2/2 - s\kappa' \sin\phi_0$ in Eq. 6.7 is negative in this case. Also, the ξ^2 term in Eq. 6.45, which leads to the positive ξ^4 term in Eq. 6.7, prevents the pseudo-potential from diverging to $-\infty$ as $\xi \to \pm\infty$. This prevents the particle ξ from veering off to infinity; this phenomenon is unphysically allowed if the approximated $\chi(\xi)$ is used and $\sin\phi_0 > 0$. The term linear in ξ in Eq. 6.7 which affects the asymmetry of the two-valleys is also neglected in $\chi(\xi)$. The fact that $v_\perp$ is not constant can be explicitly seen in Fig. 5g of Bellan [9], where $v_\perp$ of a particle undergoing two-valley motion varies in time by over a factor of three.

It should be noted, however, that for a non-uniform background field and/or time-dependent wave frequencies, S is finite in Eq. 6.31 and this may have an important role in the system additional to the effects described in the present chapter.

6.8 Summary

The interaction of a relativistically-consistent thermal distribution of particles with a coherent right-handed circularly polarized wave has been investigated. Departure from wave-particle resonance for each particle is expressed by a frequency mismatch parameter ξ, where $\xi = 0$ represents perfect resonance. An exact rearrangement of the relativistic particle equation of motion shows that ξ follows pseudo-Hamiltonian dynamics with an associated pseudo-potential $\psi(\xi)$. If $\psi(\xi)$ has two-valleys separated by a hill, and the particle has enough pseudo-energy to overcome the hill, then the particle undergoes two-valley ξ-space motion that produces a large, non-diffusive pitch-angle scattering.

An accurate condition for two-valley motion and thus for large pitch-angle scattering has been derived; this condition is related to but may or may not include the exact resonance condition (Eq. 6.1), and the range of this condition scales with the wave amplitude. Assuming that the particle distribution is Maxwell-Jüttner, which is a relativistic generalization of the Maxwell-Boltzmann distribution, for typical magnetospheric parameters a significant fraction $(1-5\%)$ of the particles undergoes two-valley motion. The pertinent analysis can potentially be used for the actual local electron distribution, which may not be exactly Maxwellian. Numerical simulations

confirm the analytical results. The scaling of the fraction of interacting particles with the wave amplitude may also explain the association of relativistic microbursts to large-amplitude chorus. The present theory is more accurate and exact than the widely-used second-order trapping theory as second-order trapping theory fails to take into account two-valley motion.

Chapter 7

MAGNETIC FIELD DIAGNOSTIC USING TWO-PHOTON DOPPLER-FREE LASER-INDUCED FLUORESCENCE

As can be seen in Chapters 2 through 5, fast magnetic reconnection involves ion skin depth length scales $\sim d_i$ as well as electron skin depth length scales $\sim d_e$. Therefore, any experimental diagnostic that probes magnetic fields in fast reconnection must be able to resolve these scales. However, d_i and d_e in many situations are minute quantities compared to the global scale L of the plasma, as can be seen in Table 7.1. This scale constraint as well as other limitations to existing magnetic field diagnostics impose the need for a new, alternative diagnostic.

A widely-used magnetic field diagnostic is the Faraday pickup coil, which is simply a loop of an arbitrary number of turns made of a conducting wire. Because Faraday's law states that the voltage induced in the loop is proportional to the rate of change of magnetic flux, a Faraday pickup coil can change fluctuating magnetic fields into an electrical signal. Because of the simplicity of their design and application, these coils are frequently used to probe magnetic fields in a plasma [29, 67, 129]. However, when probing smaller length scales, the area through the loop must inevitably become smaller. This smaller area leads to smaller magnetic flux and thus a smaller signal-to-noise ratio, which limits the spatial dimensions of the coil. Another important limitation is that the coil, being a physical wire, essentially perturbs the

Plasma Type	L (m)	n (m^{-3})	d_i (m)	d_e (m)
Flaring Solar Loops	$10^7 - 10^8$	10^{17}	1	10^{-2}
Solar Active Regions	$10^7 - 10^8$	$10^{15} - 10^{16}$	$1 - 10$	$10^{-2} - 10^{-1}$
Fusion Plasmas	$1 - 10$	10^{21}	10^{-2}	10^{-4}
Earth's Magnetotail	$10^8 - 10^9$	10^9	10^4	10^2
Caltech MHD-driven Jet Experiment (Argon)	10^{-1}	10^{22}	10^{-2}	10^{-4}
Magnetic Reconnection Experiment (MRX)	0.5	10^{20}	10^{-1}	10^{-3}

Table 7.1: Plasma parameters of regions where magnetic reconnection occurs or is thought to occur. L is the global length scale of the plasma, n is the density, and d_e is the electron skin depth. Unless specified otherwise, d_i is the ion skin depth assuming that the ion species is hydrogen. Referenced from Refs. [29, 74–76, 109, 127]

plasma; the effect of this perturbation obviously becomes larger as the region of interest becomes smaller. These constraints hinder the usage of pickup coils for investigating magnetic fields at small length scales.

Another magnetic field diagnostic uses Faraday rotation, which is an effect where the plane of polarization of a linearly polarized light wave rotates when passing through a magnetic field in a medium. The amount of this rotation is proportional to the strength of the magnetic field parallel to the light propagation direction, so this method has also been widely used to probe magnetic fields [18, 140]. This method induces little to no physical perturbation to the plasma and can probe small length scales because the size of the light source is arbitrary. However, because the light wave has to pass through a finite region of space for this effect to occur, only line-integrated data can be obtained, i.e., the magnetic field measurement is not 3D-localized.

In this chapter, a new magnetic field diagnostic based on the laser-induced fluorescence (LIF) technique is presented. This diagnostic is essentially non-perturbing, 3D-localized, and can probe arbitrary scale lengths limited only by the diameter of the laser source. The particular scheme suppresses Doppler broadening of the spectral lines, enabling the resolution of Zeeman splitting, which can then be used to infer the magnetic field information. The theoretical background is first presented, followed by a description of a repetitively pulsed radio-frequency plasma source that was constructed in order to test the diagnostic. Preliminary results are then presented.

7.1 Sources of Spectral Broadening

Several textbook sources of spectral broadening will now be described; these effects can be analyzed to yield various properties of the diagnosed plasma [38].

Doppler Broadening

Doppler broadening of a spectral line arises due to the thermal motion of atoms. It is first assumed that the distribution function f is a 1D Maxwellian in the direction of the laser beam, i.e,

$$f(v)dv = \sqrt{\frac{m}{2\pi k_B T}} \exp\left(-\frac{mv^2}{2k_B T}\right) dv, \tag{7.1}$$

where m is the atom mass, v is the atom velocity in the direction of laser propagation, and T is the temperature. In the reference frame of an atom moving at $v \ll c$ where

c is the speed of light, the laser wavelength is Doppler shifted by

$$\lambda = \lambda_0 \left(1 + \frac{v}{c}\right), \tag{7.2}$$

where λ_0 is laser wavelength in the lab frame, or

$$v = c\left(\frac{\lambda - \lambda_0}{\lambda_0}\right), \tag{7.3}$$

$$dv = \frac{c}{\lambda_0} d\lambda. \tag{7.4}$$

Inserting these into Eq. 7.1, we have

$$f(\lambda)d\lambda = \sqrt{\frac{mc^2}{2\pi k_B T \lambda_0^2}} \exp\left(-\frac{mc^2}{2k_B T \lambda_0^2}\left[\lambda - \lambda_0\right]^2\right), \tag{7.5}$$

which has the standard deviation

$$\sigma_\lambda = \sqrt{\frac{k_B T}{mc^2}} \lambda_0. \tag{7.6}$$

This effect is called the Doppler broadening effect. Note that if the atoms are moving at a finite average velocity, a Doppler shift in the center wavelength occurs as well.

Zeeman Splitting

When an atom is subject to an external magnetic field, the interaction between the two effectively splits any energy level to multiple levels. One transition line between two energy levels then splits into multiple transition lines. The energy perturbation is

$$\Delta E = \mu_B g_j m_j \left|\mathbf{B}\right|, \tag{7.7}$$

where $\mu_B = e\hbar/2m_e$ is the Bohr magneton, m_j is the total angular momentum in the z-direction, $\mathbf{B}$ is the external magnetic field, g_j is the Landé g-factor which is a function of the total angular momentum j, the orbital angular momentum l, and the spin angular momentum s. One energy level therefore splits into multiple levels, each corresponding to certain possible values of the quantum numbers. Since the amount of the splitting depends on the magnitude of $\mathbf{B}$, this amount can be used to infer the strength of the magnetic field.

Natural Broadening

Natural broadening inevitably arises due to the Heisenberg uncertainty principle, which effectively relates the lifetime of a particular energy level to the uncertainty of its energy value. The broadening is thus

$$\Delta E \simeq \frac{\hbar}{\tau}, \tag{7.8}$$

where τ is the lifetime of the energy level. The broadening profile is Lorentzian.

Stark Broadening

Stark broadening is analogous to the Zeeman effect in that the electric field instead of the magnetic field perturbs the energy levels. Stark broadening is significant for high plasma densities. For hydrogen lines, Stark broadening scales as $\sim n_e^{2/3}$ where n_e is the electron density, whereas for non-hydrogen lines it scales as $\sim n_e$ [173]. The broadening profile is Lorentzian.

Instrumental Broadening

Instrumental broadening occurs due to limitations of the measurement devices. For example, imperfect focusing inside a spectrometer physically diffuses light, effectively leading to a broadened spectral measurement.

Saturation Broadening

Saturation broadening, or power broadening, occurs when the laser intensity is so high that the population of the base level becomes equal to the excited level. At this saturated point, no further absorption of the laser by the plasma can occur. A spectral absorption probability typically peaks at the center wavelength and is lower at the wings of the profile. Therefore, if the laser intensity is above a threshold, the plasma can no longer absorb the photons at the center wavelength but can absorb those further away from the center wavelength. This effectively leads to a broadened line profile with the width [38]

$$\gamma_s = w\sqrt{1 + \frac{B_{12}\rho(\omega_{12})}{A_{12}}}, \tag{7.9}$$

where w is the original profile width, A_{12} and B_{12} are respectively Einstein coefficients for spontaneous and induced transition between levels 1 and 2, and $\rho(\omega_{12})$ is the spectral energy density of the laser at the transition frequency ω_{12}. The broadening profile is Lorentzian.

Comparison of Broadening Effects

The measured spectral profile is a convolution of all the broadening effects. Depending on the plasma parameters, different effects contribute in different amounts. For example, Table 7.2 shows the contribution of different broadening effects on the 394.539 nm (vacuum; ${}^4D^\circ_{5/2} \rightarrow {}^4 D_{7/2}$) Ar II line for two different plasmas. The Caltech MHD-driven plasma jet [109] has a relatively high density and tem-

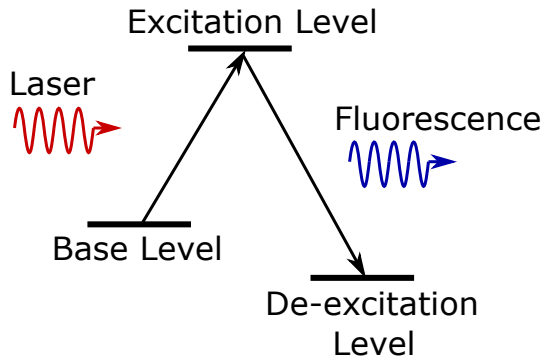

Figure 7.1: A diagram of a laser-induced fluorescence scheme.

perature, so Stark and Doppler effects dominate over Zeeman splitting. The pulsed, inductively-coupled radio-frequency plasma source developed by Chaplin [32] has a lower density and temperature, and so Doppler broadening is comparable to Zeeman splitting while Stark broadening is negligible. Natural broadening (not shown) is negligible for both cases.

7.2 Two-Photon Doppler-Free Laser-Induced Fluorescence

Laser-Induced Fluorescence

Laser-induced fluorescence, or LIF, is an active spectroscopy method in which a laser source excites the electron population at a certain energy level to a higher level [39]. These electrons then de-excite to other lower energy levels, emitting fluorescent signals that can be analyzed to obtain various information such as the temperature, density, and magnetic field of the diagnosed plasma. Figure 7.1 graphically illustrates the scheme.

	n_e (m^{-3})	T_i (eV)	Stark (pm)	Doppler (pm)	Zeeman (pm)
Caltech Jet Experiment	10^{22}	2	2.2	3	0.7
Inductively-Coupled Plasma	10^{19}	0.05	2.2×10^{-3}	0.5	0.7

Table 7.2: Comparison of different broadening effects in two types of plasmas: the Caltech MHD-driven Jet Experiment [29, 105, 109], and a pulsed, inductively-coupled, radio-frequency plasma [32]. Stark broadening is calculated by using the experimentally measured values in Konjević et al. [83] and using the scaling $\propto n_e$ for Argon [173]. Zeeman splitting is calculated by assuming m_j and g_j are of order 1, and $B = 0.1$ T.

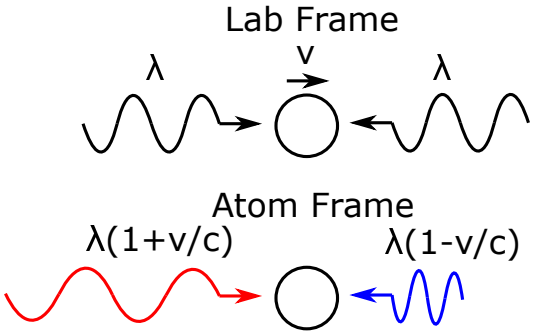

Figure 7.2: Two-photon interaction of an atom in the lab frame and in the atom frame.

Because the absorption of the laser is dependent on the laser wavelength, the population of the excited level and thus the fluorescence intensity is wavelength-dependent. Therefore, the full spectrum can be obtained by scanning the laser wavelength around the spectral line.

The fluorescence intensity depends on the population of the excited level, which in turn depends on the population of the base level and the laser intensity. Therefore, a highly populated base level needs to be chosen in order to maximize the fluorescence signal. An obvious choice is the ground state of the atom, but the transition energy between the ground state and the first excited state is typically too high for any simple, conventional laser. Therefore, a metastable level is typically chosen. By definition, there are no allowed first-order transitions to a lower energy level from metastable levels, so these levels have relatively long lifetimes and so are highly populated.

Two-Photon LIF

As in can be seen in Table 7.2, Doppler broadening can dominate over Zeeman splitting so that the latter is unresolvable. Therefore, in order to resolve Zeeman splitting and thus obtain the magnetic field information, Doppler broadening must be eliminated. Two-photon laser-induced fluorescence achieves this feat by using two counter-propagating laser beams with equal wavelengths [39], as in Fig. 7.2. In the lab frame, the atom is moving with a velocity v and is subject to two counter-propagating photons of wavelength λ. Then, in the frame of the atom, one of the photons is blue-shifted while the other is red-shifted. If both photons are absorbed

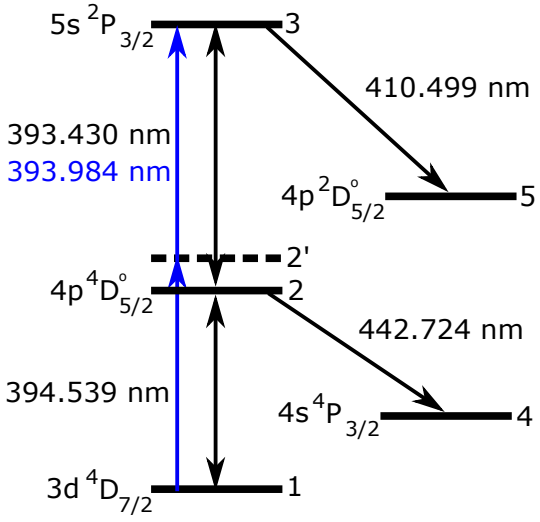

Figure 7.3: Two-photon laser-induced fluorescence scheme for Argon II. Displayed wavelengths are vacuum values.

by the atom, then the absorbed energy is, assuming $v \ll c$,

$$E = \frac{c}{\lambda(1+v/c)} + \frac{c}{\lambda(1-v/c)}, \tag{7.10}$$

$$\simeq \frac{c}{\lambda}\left(1 - \frac{v}{c} + 1 + \frac{v}{c}\right), \tag{7.11}$$

$$= \frac{2c}{\lambda}, \tag{7.12}$$

which does not depend on velocity. Therefore, Doppler broadening is cancelled out in this scheme.

Figure 7.3 shows the proposed two-photon LIF scheme in Argon II. Two counter-propagating laser beams at 393.984 nm pumps the metastable $3d^4D_{7/2}$ level (level 1) to the $5s^2P_{3/2}$ level (level 3) via a virtual level (level 2′). The intermediate level (level 2) is not necessary for two-photon transition but allows it to be achieved with relatively low-power lasers; if the intermediate level does not exist, then high-power lasers are necessary. This fact can be seen by examining the two-photon transition probability A_{13} [39]:

$$A_{13} \propto \frac{\gamma_{13} I_1 I_2}{\left[\omega_{13} - \omega_1 - \omega_2 - \mathbf{v}\cdot(\mathbf{k}_1 + \mathbf{k}_2)\right]^2 + (\gamma_{13}/2)} \times \left| \frac{\overleftrightarrow{\mathbf{D}}_{12}\cdot\hat{e}_1\cdot\overleftrightarrow{\mathbf{D}}_{23}\cdot\hat{e}_2}{\omega_{12} - \omega_1 - \mathbf{v}\cdot\mathbf{k}_1} + \frac{\overleftrightarrow{\mathbf{D}}_{12}\cdot\hat{e}_2\cdot\overleftrightarrow{\mathbf{D}}_{23}\cdot\hat{e}_1}{\omega_{12} - \omega_2 - \mathbf{v}\cdot\mathbf{k}_2} \right|^2, \tag{7.13}$$

where ω_i, $\mathbf{k}_i$, $\hat{e}_i$ and I_i are respectively the angular frequency, the wavevector, the polarization vector, and the intensity of the i-th laser beam, and ω_{ij}, γ_{ij}, and $\overleftrightarrow{\mathbf{D}}_{ij}$

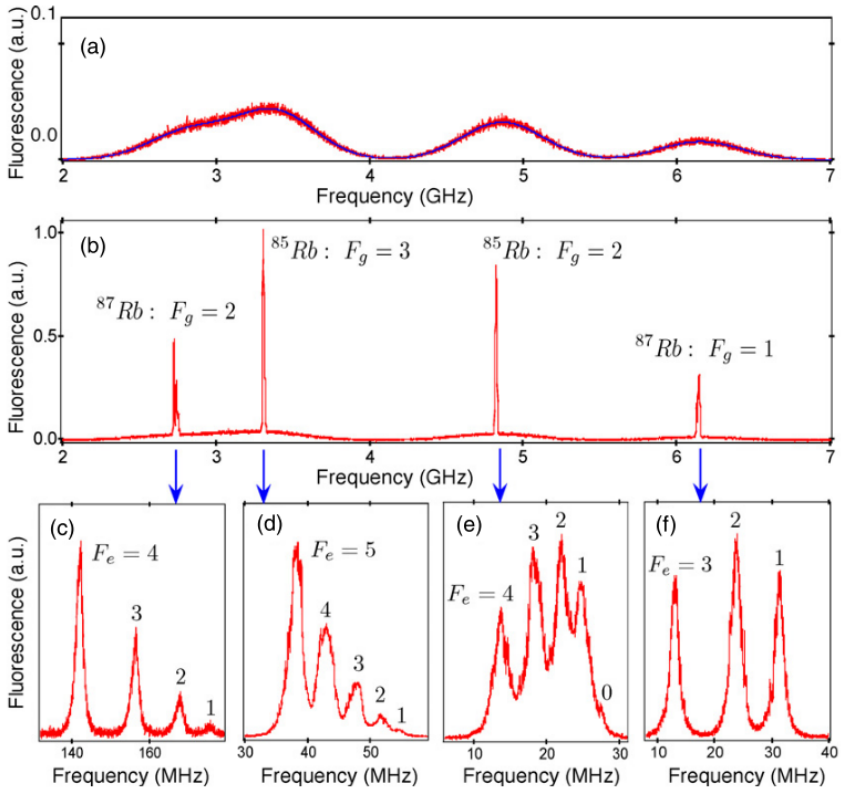

Figure 7.4: Example of two-photon LIF in Rubidium. (a) The original Doppler-broadened spectrum. (b) Result after applying two photons. (c),(d),(e),(f) Zoom-ins of respective peaks, showing hyperfine splittings. Reproduced from Jacques et al. [77]. © European Physical Society. Reproduced by permission of IOP Publishing. All rights reserved.

are the transition angular frequency, the natural linewidth, and the dipole matrix element [38] between energy levels i and j. It can be seen that the second factor increases as ω_1 and ω_2 get closer to ω_{12}.

Two-Photon LIF in Rubidium

There is a well-known two-photon LIF scheme using neutral Rubidium vapors [60, 77, 112]. In particular, Jacques et al. [77] provides a measurement of Zeeman splitting of the hyperfine structure of Rubidium.

Figure 7.4 shows the result of applying two-photon LIF in Rubidium. The Doppler-broadened spectrum is significantly narrowed after application of two-photon LIF, and even hyperfine splittings are resolvable. A Zeeman splitting of the line in Fig. 7.4f is shown in Fig. 7.5. The x-axes in Figs. 7.4 and 7.5 are in relative units, i.e., how far away the laser frequency is from the center value.

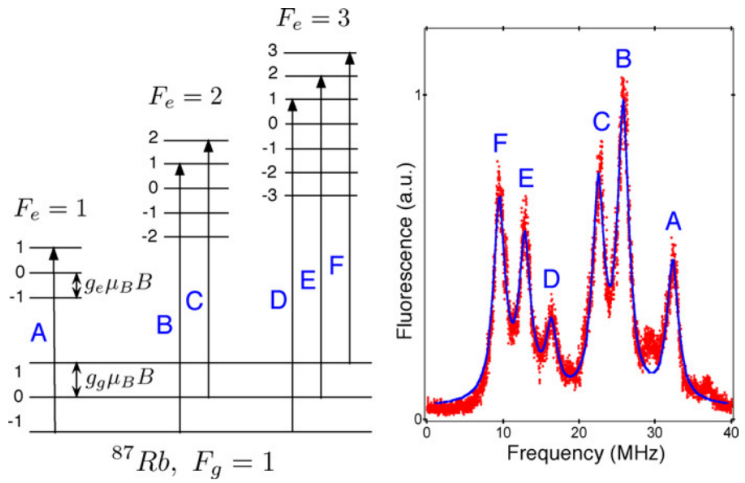

Figure 7.5: Two-photon LIF observation of Zeeman splitting of a Rubidium hyperfine line. Reproduced from Jacques et al. [77]. © European Physical Society. Reproduced by permission of IOP Publishing. All rights reserved.

7.3 Repetitively Pulsed, High-Power, Inductively-Coupled Radio-Frequency Plasma Source

A new plasma source was designed and built as the subject of diagnosis of the proposed two-photon LIF diagnostic. This source is based on the battery-powered pulsed inductively-coupled radio-frequency (RF) plasma source previously developed by Chaplin [32]. The prior source uses a battery rack to charge a capacitor to a high voltage, which is then discharged through a homemade RF generator circuit to deliver an electrical power of 2.7 kW to the load. This power creates a plasma of a relatively high density ($\sim 10^{19}$ m^{-3}) which can last up to about a millisecond. However, this source can be pulsed only once every about 5 seconds, which corresponds to a 0.02% duty cycle. Also, it cannot last for more than about 20 hours before the batteries need to be replaced. Therefore, it is not suitable for experiments that possibly require long averaging times such as LIF experiments.

The new source uses wall power instead of a battery rack and so can be left on indefinitely. The circuit was designed so that the capacitor can be repetitively pulsed at varying frequencies depending on the pulse length. The final design was such that the source was pulsed for 250 μs at 60 Hz, corresponding to a duty cycle of about 1.5%. Figure 7.6 shows a schematic diagram of the RF plasma source. Each of the components comprising the source will now be described in detail.

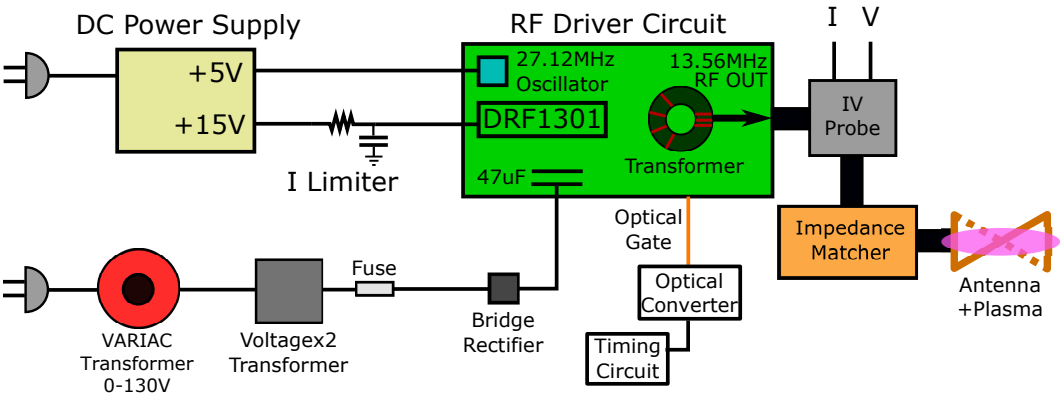

Figure 7.6: A schematic diagram of the RF plasma source.

RF Generator

A commercial power supply converts wall power to +5 V and +15 V DC outputs. The +5 V output is used to power the crystal oscillator which provides the fundamental frequency of 27.12 MHz. The +15 V output is used to power a Microsemi DRF1301 power MOSFET hybrid chip containing two power MOSFETs. A current limiter was put in place to prevent the chip from drawing excessive current from the power supply. Without this current limiter, the power supply would heat up to extremely high temperatures (> 100 C°). The two power MOSFETs inside DRF1301 effectively act as periodic grounds that alternate 180° out-of-phase with each other at 13.56 MHz.

Although not shown in Fig 7.6, the +15 V output is also fed through a DC step-down converter to power a cooling fan at +12 V.

Pulsed Power Driver

A VARIAC (variable AC) transformer rated for 2 kW and 20A converts wall power to AC voltages between 0-130 V. This voltage is then doubled through another transformer. A diode bridge rectifier then flips the negative values of the AC voltage to positive values ($\sin \omega t \rightarrow |\sin \omega t|$). The output of the rectifier is used to charge a 47 μF capacitor rated for 300 V, and because the rectifier does not allow backward current, it can only charge, not discharge, the capacitor. Therefore, the capacitor is charged to a voltage of $\sqrt{2}$ times the VARIAC transformer voltage — recall that AC voltages are rms values — in about 4 ms, which is a quarter of the wall power period.

The gate for the circuit is made optical in order to isolate it from the high-power components. When the gate is open, the main 47 μF capacitor is discharged through

one of the two MOSFETs in an alternating manner. This oscillating discharge is picked up by an on-board transformer made out of a ferrite and wound-up wires. The output of this transformer is the final output of the high-power RF generator.

IV Probe

An IV probe measures the current and voltage outputs of the RF generator. The current was measured by an Ion Physics CM-10-M current monitor. The voltage was measured by a 10x or a 1000x voltage probe, depending on the voltage level of the main capacitor.

Because the current probe and the voltage probe use different measurement leads, an instrumental phase delay is inevitable. This delay, however, can be measured by replacing the impedance matcher and the antenna by a resistor and then probing the current and voltage profiles across it. Because the impedance of a resistor is purely real, there should theoretically be no phase delay between I and V. Therefore, any phase delay across the resistor measured by the IV probe can be considered to be instrumental and thus can be subtracted out from future measurements.

Impedance Matcher

In order for maximal power to be transferred to the load, the load impedance must be equal to the the complex conjugate of the source impedance [32]. Because the source impedance is unknown in the homemade RF generator, the load impedance must be adjusted. Instead of expensive commercial impedance matchers, two binary arrays of ceramic capacitors serve as variable parallel and serial capacitances — C_p and C_s — constituting the impedance matcher. The binary arrays could be adjusted by using copper jumpers to "activate" each of the ceramic capacitors with values of 1 pF, 2 pF, 4 pF, and so on, providing nearly any capacitance value up to C_p = 2604 pF and C_s = 886 pF with 1 pF resolution.

Antenna and Plasma

A half-turn helical (HTH) [139] antenna design is used. Other types of antennas such as Nagoya type III antennas [34] were tested as well, but the HTH antenna proved to be the most efficient in terms of plasma generation. The antenna wraps around a glass tube fed into a vacuum chamber and determines the spatial dimensions of the plasma. Its radius is about 1.27 cm, and its length is about 7.5 cm.

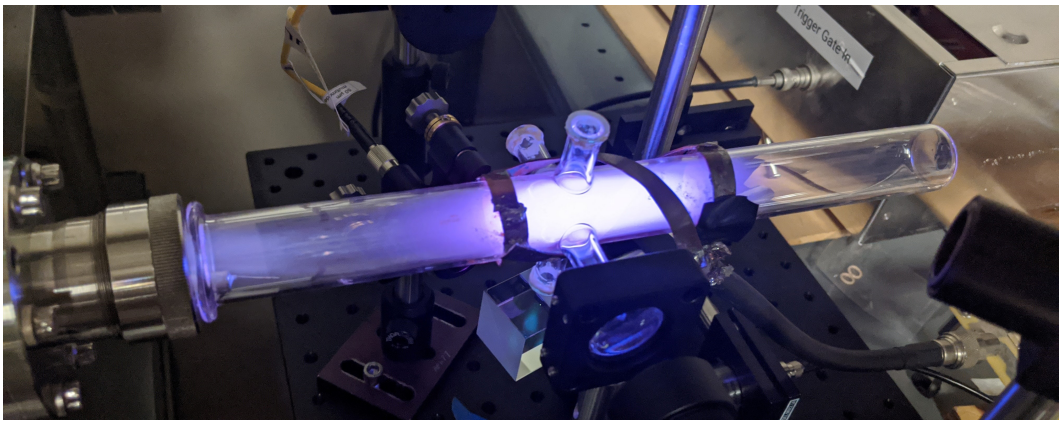

Figure 7.7: The resultant plasma discharge.

Timing Circuit

The timing circuit consists of a trigger generator that determines the frequency of the pulse, which is fed into a pulse generator that determines the gate length of the pulse. The gate is then converted to an optical signal and fed into the RF driver.

An example of the resultant plasma discharge is shown in Fig. 7.7.

7.4 Experimental Setup

Figure 7.8 shows the basic experimental setup for two-photon laser-induced fluorescence.

Laser Excitation System

A tunable diode laser (Sacher Lasertechnik LYNX Littrow Cavity) is controlled by a laser controller, which is in turn controlled by a personal computer (PC). The laser wavelength is controlled by the laser current, temperature, and the piezo voltage, but the piezo voltage was mainly used to scan the wavelength during the main measurements. The other parameters were varied to stabilize the laser during the scans. The diode laser produces a laser beam with a maximum power of 30 mW and a diameter of a few mm. The beam is fed through an acousto-optic modulator (AOM), which deflects the beam if an RF signal is applied. The deflected beam is focused into a multimode optical fiber and is collimated at the output. Therefore, by providing a TTL signal that turns the RF signal on and off at the lock-in frequency $f_{\text{lock-in}}$ via the lock-in amplifier, the output laser beam is modulated (turned on and off) at $f_{\text{lock-in}}$.

A 30:70 beamsplitter directs 30% of the output beam into a wavemeter for wavelength

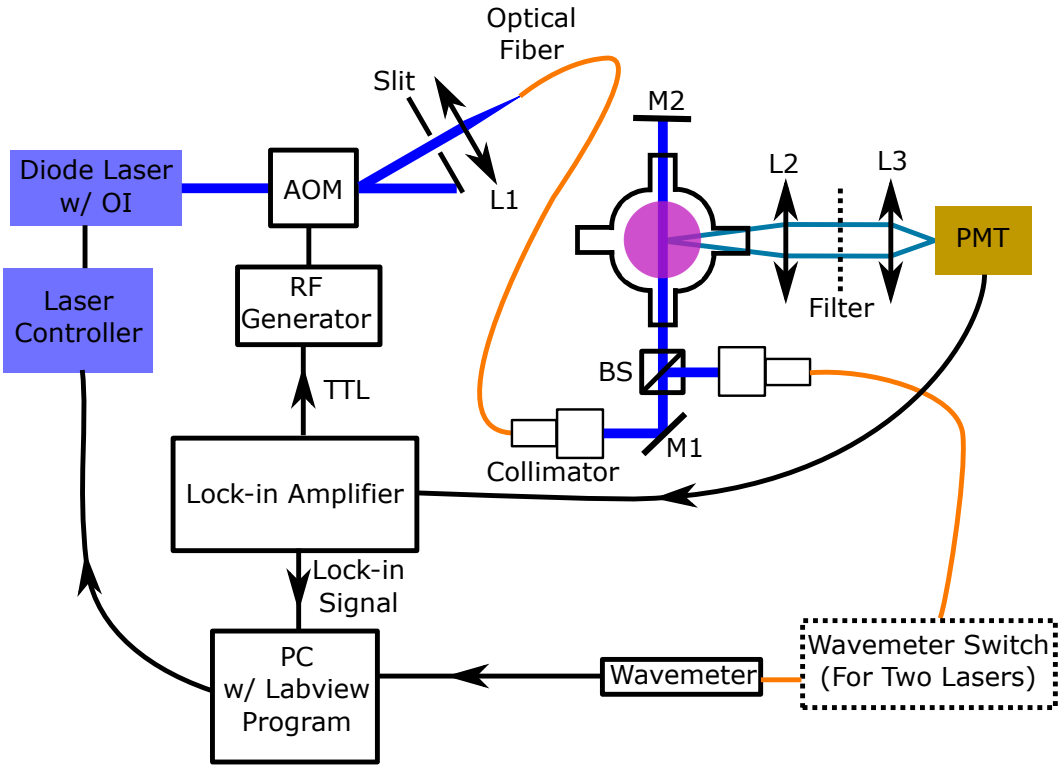

Figure 7.8: Experimental setup for two-photon laser-induced fluorescence. L stands for lens, M for mirror, BS for beam-splitter, AOM for acousto-optic modulator, OI for optical isolator, and PMT for photo-multiplier tube. The purple color is the end-on view of the plasma.

reference. The rest of the beam is directed through the plasma, bounces off of a mirror (M2), and is redirected back into the plasma, providing counter-propagating photons.

Fluorescence Collection System

The laser-induced fluorescence from a single point in the plasma passes through a lens (L2) and is made into a collimated beam, which is in turn passed through a band-pass optical filter of the desired wavelength. The beam is then focused by another lens (L3) into a battery-operated photo-multiplier tube (PMT; Hamatsu H10721-110). In order to maximize the detection of the signal, it is imperative to use a lens to collimate the fluorescence first and then pass it through the filter. This is because the wavelength band of the filter is usually rated at a 90° incident angle and thus is rated for a different wavelength band if the incident angle is different.

Because the laser beam is modulated at $f_{\text{lock-in}}$, the signal is also modulated at $f_{\text{lock-in}}$, provided that the fluorescence rise and decay times are not long compared

to $T_{\text{lock-in}} = 1/f_{\text{lock-in}}$. Thus, the PMT signal is fed into the input of the lock-in amplifier for averaging. The output of the lock-in amplifier is transferred to the PC via a data acquisition system (National Instruments USB-6001).

Wavelength Feedback and Scanning System

A LabVIEW program was written that scans the laser wavelength around a center value at set intervals and collects lock-in data while locking the laser wavelength at each set value. The wavelength locking is performed by feeding the real-time wavemeter measurement back to the laser piezo voltage via the PC. The user inputs the center wavelength, the scan range, the number of data points, and the averaging time, and these are translated into an array of wavelength values for which the data is to be taken. Then, the laser wavelength is sequentially locked at each wavelength value for the duration of the averaging time, and the data from the lock-in is recorded at the end of each averaging time.

For example, let us assume that the center wavelength is 394.538 nm, the scan range is ±4 pm, the number of data points is 200, and the averaging time is 15 seconds. The scan interval is thus $8/200 = 0.04$ pm. So, the program first locks laser wavelength at 394.534 nm for 15 s, records the value of the lock-in output, and then moves the laser wavelength to 394.53404 nm. The process then continues until the laser wavelength reaches 394.542 nm.

Two-Photon LIF with Different Colors

The setup can be altered so that two separate counter-propagating laser beams are respectively tuned to the transition wavelengths of the first (level $1 \rightarrow 2$) and the second (level $2 \rightarrow 3$) transitions. In this case, a second laser + AOM + fiber system is placed at the location of mirror M2 and the laser beam is directed downwards. The beamsplitter directs 30% of the beam into another optical fiber. The two optical fibers that respectively measure the wavelength of the first and the second laser are then fed into a wavemeter switch — a device that allows a single wavemeter to measure multiple wavelengths simultaneously.

7.5 One-Photon LIF Results

In the one-laser setup, the laser wavelength was first scanned around 394.539 nm, which is the transition wavelength of the first transition (level $1 \rightarrow 2$ in Fig. 7.3), and the fluorescence signal of the 442.6 nm line (level $2 \rightarrow 4$ in Fig. 7.3) was measured for different background Argon pressures. This allowed for the testing

of the alignment and the overall setup because the expected signal is theoretically higher for one-photon transition.

Figure 7.9 shows the LIF profiles for background Argon pressures of 1, 5, and 20 mTorr, respectively. Red lines are fitted Voigt profiles, which are a convolution of Gaussian and Lorentzian profiles; i.e.,

$$V(\lambda;\sigma,\gamma) = \int_{-\infty}^{\infty} G(\lambda';\sigma)L(\lambda-\lambda',\gamma)d\lambda', \tag{7.14}$$

where

$$G(\lambda;\sigma) = \frac{1}{\sqrt{2\pi\sigma^2}}\exp\left[-\frac{(\lambda-\lambda_0)^2}{2\sigma^2}\right], \tag{7.15}$$

and

$$L(\lambda;\gamma) = \frac{\gamma}{\pi[(\lambda-\lambda_0)^2+\gamma^2]}. \tag{7.16}$$

Here, γ is the Lorentzian width, σ is the Gaussian width, and λ_0 is the center wavelength.

For background pressures of 5 and 20 mTorr, the broadening is mostly Gaussian. Assuming that this Gaussian profile is entirely due to Doppler broadening, the ion temperatures are respectively 1230 ± 186 K and 756 ± 189 K. Because the input power is fixed, the more ions there are (i.e., higher density), the less power is distributed to individual ions. Therefore, the temperature decreases as the background pressure increases. However, it can be seen that the temperature at 1 mTorr is lower than that at 5 mTorr. This is because the ion-electron collision frequency becomes lower as the density decreases. Since the RF power is primarily transferred to the much lighter electrons, if the number of ion-electron collisions decreases, then electrons transfer less energy to ions.

The fact that the turnaround in the ion temperature is observed can actually be used to estimate the electron (and thus the ion) density. Ion-electron collisions will become negligible when the mean-free-path l_{mfp} is comparable to the plasma length l_{plasma}, which is about 5 cm. From the measured amount of Ar II, the electron temperature is estimated to be around $T_e = 3$ eV. The highest electron density at which collisions are negligible can therefore be estimated to be

$$n_e = \frac{1}{\sigma l_{\text{plasma}}}, \tag{7.17}$$

$$= \frac{2\pi}{l_{\text{plasma}}}\left(\frac{2\epsilon_0 T_e}{e}\right)^2 \frac{1}{\ln\Lambda}, \tag{7.18}$$

$$= 3\times10^{18}\ \text{m}^{-3}, \tag{7.19}$$

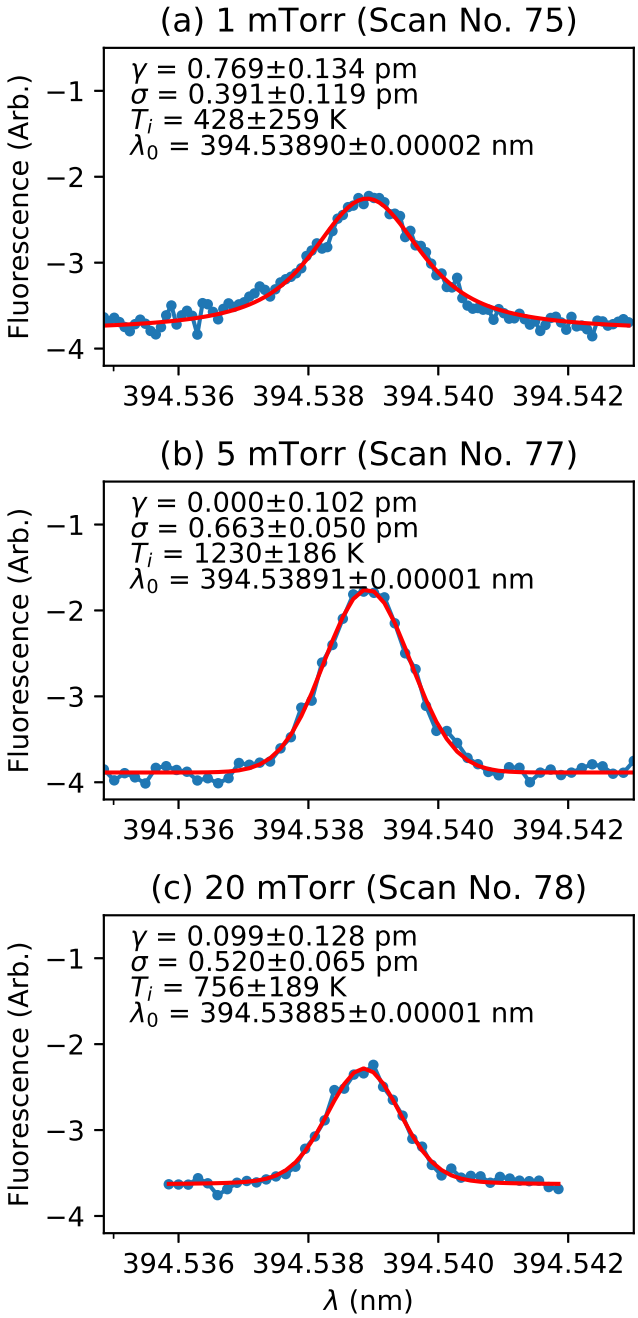

Figure 7.9: One-photon LIF results for 1, 5, and 20 mTorr. The laser wavelength is scanned around the 394.5 nm line in Fig. 7.3 and the plots show the subsequent 442.7 nm fluorescence as a function of the laser wavelength. Red lines are fitted Voigt profiles. γ is the Lorentzian width, σ is the Gaussian width, T_i is the ion temperature calculated from σ, and λ_0 is the center wavelength.

where σ is the collision cross-section, $\ln\Lambda$ is a constant of order 10, and T_e is in units of eV. Above this density, collisions start becoming significant, so electrons start imparting their energies to ions. Previously measured electron densities in a similar setup yielded $\sim 10^{19}$ m^{-3} at $\sim$ 10 mTorr, with which the present estimate agrees well.

The line broadening at 1 mTorr is dominated by a Lorentzian profile. Because the Stark width and the natural width for the given parameters are both $\sim$ 2 fm and so are negligible, it can be concluded that the broadening comes from saturation broadening. This makes sense because if the density is lower, there is a smaller number of atoms that can be excited, so the laser intensity threshold for population saturation becomes lower.

The measured saturation broadening can be used to calculate the laser bandwidth — the spectral uncertainty of the laser wavelength. The Einstein coefficients are related by

$$B_{12} = \frac{\lambda_0^3 A_{12}}{8\pi h}, \tag{7.20}$$

where λ_0 is the transition wavelength and h is Planck's constant. The spectral density is related to the laser intensity by

$$I = \int \rho(\nu) c\, d\nu \simeq \rho c \Delta\nu, \tag{7.21}$$

where I is the laser intensity, ν is the laser frequency, and $\Delta\nu$ is the laser bandwidth. Thus, we have

$$\frac{B_{12}\rho}{A_{12}} = \frac{\lambda_0^3 I}{8\pi h c \Delta\nu}. \tag{7.22}$$

Using Eq. 7.9, we have

$$\Delta\nu = \frac{\lambda_0^3 I}{8\pi h c} \frac{1}{\gamma_s^2/w^2 - 1}. \tag{7.23}$$

In Fig. 7.9a, the total broadened of profile is $\gamma_s = \sqrt{\gamma^2 + \sigma^2} = 0.863 \pm 0.173$, and $w \simeq \sigma$ because other sources of Lorentzian broadening, namely Stark and natural broadening, are negligible. Using the values $\lambda_0 = 394.539$ nm, $I = 10$ mW$/(\pi \times 1$ mm$^2)$ because the laser power at the output of the collimator is $\sim$ 10 mW and the beam radius is $\sim$ 1 mm, we have $\Delta\nu = 10.1 \pm 9.7$ MHz. Although the propagated error is very large, the mean value indicates a laser wavelength bandwidth of $\Delta\lambda = 5.25$ fm, which is very small compared to other dominant effects such as Doppler broadening.

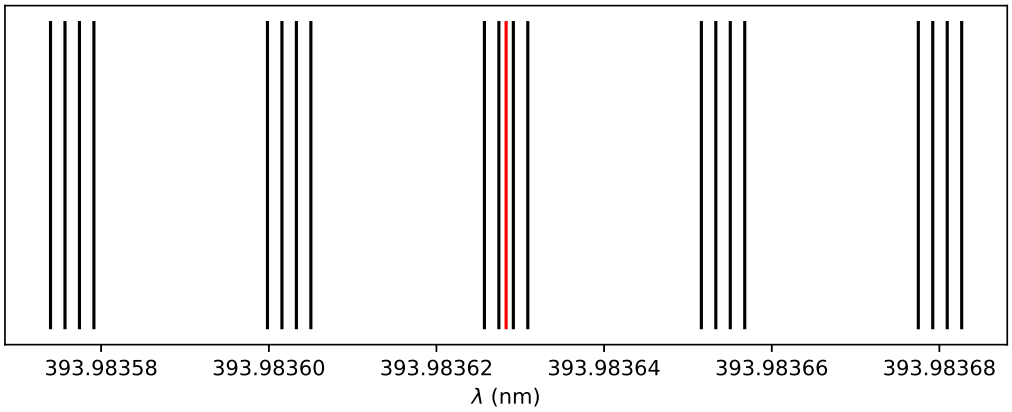

Figure 7.10: The expected locations of the Zeeman splitted transition lines involving the $1 \longrightarrow 3$ transition in Fig. 7.3 for $|\mathbf{B}| = 50$ G. The red line is the original un-splitted line.

7.6 Two-Photon LIF Preliminary Results

In order to observe the two-photon transition, the laser wavelength was shifted to the average of the transition wavelengths $\lambda_{12} = 394.539$ nm and $\lambda_{23} = 393.430$ nm in Fig. 7.3, which is 393.984 nm. The 442.7 nm optical filter that was used in one-photon LIF was replaced by a 410.5 nm filter in order to measure the fluorescence from level 3 to level 5 in Fig. 7.3. A permanent magnet was also placed near the plasma in order to provide a source of magnetic field. The presence of the magnetic field increased the ionization fraction of the plasma source. This could be seen both visibly as the color of the plasma turned bluer (a large fraction of Ar II spectral lines are around 400 nm) and measurably as the natural emission intensity of the 410.499 nm line increased. The explanation is that the magnetic field traps the ionizing electrons for a longer period of time compared to a situation where there is no magnetic field, so they impart more energy to the ions.

The strength of the magnetic field at the location of the collection point was measured by a Hall effect sensor to be around 50 G. Figure 7.10 shows the expected locations of the Zeeman splitted transition lines from level 1 to level 3 for $|\mathbf{B}| = 50$ G. The distance between each line scales linearly with the strength of the magnetic field. Because the selection rule for one-photon Zeeman transition is $m_J = 0, \pm 1$, that for two-photon Zeeman transition is $m_J = 0, \pm 1, \pm 2$.

Figure 7.11 shows the two-photon LIF results of two separate scan instances at 1 mTorr. The red line is the theoretical center transition wavelength, and the

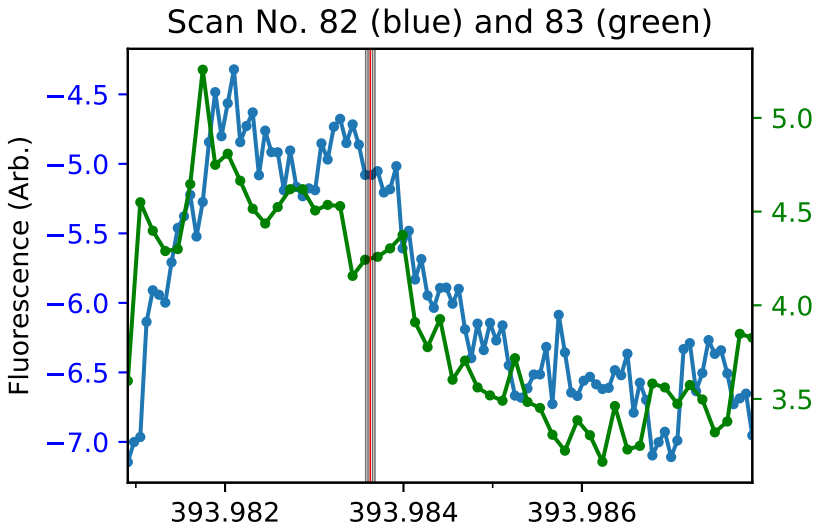

Figure 7.11: Two-photon LIF results of two separate scan instances at 1 mTorr. The red line is the theoretical center transition wavelength, and the grey area is the expected Zeeman splitting for $|\mathbf{B}| = 50$ G.

grey area is the expected Zeeman splitting for $|\mathbf{B}| = 50$ G. Although saturation broadening (~0.8 pm) dominates over Zeeman splitting (~0.04 pm) at this pressure, the former is in fact favorable when trying to find any signal. This is because the measured center wavelength may be shifted from the theoretical result due to, e.g., sources of systematic error such as the uncertainty of the wavemeter. This shift was actually observed in the one-photon LIF results (Fig. 7.9), where the measured center wavelength (~394.5389 nm) is different from the theoretical value (394.5387 nm). A simple analysis of the refractive index of the plasma shows that the predicted fractional wavelength shift due to finite plasma density is 7×10^{-10}, which is negligible compared to other shift effects. Significant broadening allows the detection of a signal even when the laser wavelength is reasonably far from the center value.

It can be seen from Fig. 7.11 the measured peak is shifted to the left, and that there is broadening comparable to that in Fig. 7.9a. Line fitting the measurements to Voigt profiles yielded too big of an error to warrant any analysis. Nevertheless, the peak near 393.9836 nm is evident from the two measurements.

7.7 Suggestions for Further Work

Due to the COVID-19 pandemic in the year 2020 and subsequent restricted access to the laboratory, no further experiments could be done to improve upon the results that have been presented so far. Therefore, some suggestions for further work will now be given that may ultimately lead to the completion of this diagnostic.

First, the center wavelength of the scan must first be shifted to that revealed by the measurements in Fig. 7.11. This allows for the measurement of the complete line profile.

Second, once it is confirmed that the peaks shown in Fig. 7.11 are indeed two-photon LIF signals with saturation broadening, the background gas pressure can then be increased to reduce the broadening. Laser power may be reduced as well, but this will compromise the signal-to-noise ratio of the signal. The elimination of the saturation broadening will reveal sharp two-photon peaks as in Fig. 7.4.

Third, optimization and tests of the signal should be conducted. The amount of Zeeman splitting can be altered by changing the proximity of the magnet, or simply by using a different source of magnetic field such as solenoids. Two-color LIF can also be conducted to increase the signal. The polarization of the laser beam may also be controlled to alter the selection rules.

7.8 Summary

In this chapter, a new laser magnetic field diagnostic was conceived and preliminary results were presented. The method uses the two-photon laser-induced fluorescence (LIF) technique, which allows for the elimination of Doppler broadening arising from finite temperature. The riddance of the dominant broadening effect enables the resolution of Zeeman splitting, which can be used in turn to infer the magnetic field information.

A repetitively-pulsed, inductively-coupled high-power RF plasma source was newly developed as the subject of diagnosis. This source improved upon a previously built battery-powered source and is wall-powered.

One-photon LIF results revealed various properties of the plasma as well as the laser. The temperature of the plasma was measured via Doppler broadening to be around 10^3 K, and this value was dependent on the background gas pressure. The laser bandwidth was measured via saturation broadening to be around 10 MHz.

Finally, Preliminary two-photon LIF results were presented. Initial results indicate

that there is two-photon excitation around the expected wavelength. Although further developments were thwarted by the COVID-19 pandemic, suggestions for improvements on this diagnostic were presented.

Chapter 8

SUMMARY

The progression, properties, and progenies of magnetic reconnection were studied, and a method of probing the magnetic field in a plasma was partially developed in this thesis.

8.1 Progression

Canonical Vorticity Framework

An intuitive framework for explaining the progression of magnetic reconnection was first presented. In order to describe various facets of the process, the framework utilizes a quantity called the electron canonical vorticity $\mathbf{Q}_e$, which is perfectly frozen into the electron flow while the magnetic field **B** is not frozen-in and thus reconnects. A careful analysis of the dynamics of a flux tube defined by $\mathbf{Q}_e$ intuitively explains why magnetic reconnection is an instability, how electrons are accelerated, and how whistler waves are generated. A two-fluid simulation was built to verify the analysis.

When a slight perturbation is applied to a magnetic shear profile, a localized section of a $\mathbf{Q}_e$ flux tube is subject to a stronger out-of-plane electron flow at the center than other parts of the tube. Because the flux tube convects with the electron flow, the localized section is pulled in the out-of-plane direction, in such a way that generates more electron flow toward the center. The process then feeds back to itself, generating an instability.

As the instability progresses and the flux tube is pulled in the out-of-plane direction, it is also lengthened and narrowed in order to conserve its volume, just like a stretching rubber band. This decrease in the circumference of the flux tube, combined with magnetic field cancellation due to magnetic reconnection, increases the electron flow velocity, i.e., accelerates electrons.

Finally, the spatial gradient in the electron flow twists up the $\mathbf{Q}_e$, and this twist is propagated as whistler waves. This is analogous to the generation mechanism of torsional Alfvén waves.

Completion of the Framework

By including the "canonical battery" effect, the canonical vorticity framework of magnetic reconnection was completed down to first principles. Assuming that collisions are ignored, this battery effect is the only non-ideal term that relaxes the topological constraint on $\mathbf{Q}_e$. Different kinetic effects such as electron viscosity and pressure anisotropy are manifested by the canonical battery term and significantly affect the reconnection process. The distinction between a Sweet-Parker-type diffusion process and a purely growing instability could be made by the significance of the canonical battery term. Two-fluid and particle-in-cell simulations aided the analysis.

8.2 Properties

Stochastic Ion Heating in Magnetic Reconnection

Out of the various observed properties of magnetic reconnection, its accompaniment by anomalous ion heating much faster than conventional heating has been a longstanding dilemma.

Stochastic heating — a mechanism in which particles subject to sufficiently strong electric fields undergo chaotic trajectories — is fast enough to account for the observed heating rate. Using the established canonical vorticity framework, the Hall electric fields that develop during reconnection could be calculated. It was then shown that these fields satisfy the stochastic ion heating criterion, and that the ions involved indeed undergo chaotic trajectories. This results in stochastic motion in phase space, which is equivalent to heating. Single-particle simulations were conducted to verify stochastic motion.

Kinetic Verification of Stochastic Ion Heating

The stochastic ion heating mechanism during magnetic reconnection was then kinetically verified through analytical calculations and particle-in-cell simulations. First, it was shown that stochastic ion heating is intrinsic to the Harris equilibrium current sheet, which is profoundly related to magnetic reconnection. Then, it was verified via particle-in-cell simulations that the Hall electric fields that develop during magnetic reconnection indeed satisfy the stochastic ion heating criterion even in the kinetic regime, and that the ion heating profile agreed well with the prediction from the criterion. The mechanism was shown to be valid up to moderate guide fields, and frequently observed features of ion heating were also observed to be consistent with stochastic ion heating.

It was thus confirmed that stochastic ion heating is an intrinsic ion heating mechanism in magnetic reconnection.

8.3 Progenies

A very important progeny of magnetic reconnection is whistler waves, the generation mechanism of which had already been discussed using the canonical vorticity framework. The interaction of whistler waves with relativistic particles, specifically how these waves scatter the pitch-angle of the particles, was examined.

A previous study showed that exact rearrangements of the particle equation of motion under a circularly polarized wave leads to a pseudo-Hamiltonian equation of motion of a frequency mismatch parameter ξ. If the pseudo-potential of this motion is two-valleyed, and the particle has enough pseudo-energy to undergo periodic motion in these two valleys, then the particle was shown to undergo drastic pitch-angle scattering.

Here, the conditions were derived for which the particle undergoes two-valley motion and thus undergoes drastic scattering. The conditions are a certain range related to the exact resonance condition but may or may not include this condition depending on the initial conditions of the particle. It was then shown that if the particle distribution is assumed to be the Maxwell-Jüttner distribution, which the relativistic generalization of the Maxwell-Boltzmann distribution, a significant fraction of the particles undergo large scattering for typical magnetospheric parameters. The scaling of this fraction with the wave amplitude suggests that relativistic microburst events may be explained by the two-valley mechanism. The widely-used second-order trapping theory is shown to be an approximation of the theory presented here and actually misses critical details of the wave-particle interaction.

8.4 Probe

A new magnetic field diagnostic using two-photon Doppler-free laser-induced fluorescence was described and developed to some extent. By using two counter-propagating laser beams, Doppler broadening of a spectral line can be cancelled out, enabling the resolution of Zeeman splitting. This splitting can then be used to extract the magnetic field information.

A repetitively-pulsed, inductively-coupled high-power RF plasma source was newly developed as the subject of diagnosis. One-photon LIF scans of this plasma showed that the temperature of the plasma was around 10^3 K. The laser bandwidth was also

measured via saturation broadening to be around 10 MHz.

Preliminary two-photon LIF results were presented. Initial results indicate that there is two-photon excitation around the expected wavelength. Although further developments were thwarted by the COVID-19 pandemic, improvements on this diagnostic were suggested.

BIBLIOGRAPHY

[1] Ferzan Akalin, D. A. Gurnett, T. F. Averkamp, A. M. Persoon, O. Santolik, W. S. Kurth, and G. B. Hospodarsky. First whistler observed in the magnetosphere of Saturn. *Geophysical Research Letters*, 33(20): L20107, oct 2006. ISSN 0094-8276. doi: 10.1029/2006GL027019. URL http://doi.wiley.com/10.1029/2006GL027019.

[2] J. M. Albert. Evaluation of quasi-linear diffusion coefficients for whistler mode waves in a plasma with arbitrary density ratio. *Journal of Geophysical Research: Space Physics*, 110(A3):1–12, 2005. ISSN 21699402. doi: 10.1029/2004JA010844.

[3] H. Alfvén. Existence of electromagnetic-hydrodynamic waves [7]. *Nature*, 150(3805):405–406, oct 1942. ISSN 00280836. doi: 10.1038/150405d0. URL http://www.nature.com/articles/150405d0.

[4] K. A. Anderson and D. W. Milton. Balloon observations of X rays in the auroral zone: 3. High time resolution studies. *Journal of Geophysical Research*, 69 (21):4457–4479, nov 1964. ISSN 01480227. doi: 10.1029/jz069i021p04457. URL http://doi.wiley.com/10.1029/JZ069i021p04457.

[5] A. V. Artemyev, A. A. Vasiliev, D. Mourenas, O. V. Agapitov, and V. V. Krasnoselskikh. Nonlinear electron acceleration by oblique whistler waves: Landau resonance vs. cyclotron resonance. *Physics of Plasmas*, 20(12): 122901, dec 2013. ISSN 1070-664X. doi: 10.1063/1.4836595. URL http://aip.scitation.org/doi/10.1063/1.4836595.

[6] Anton Artemyev, Oleksiy Agapitov, Didier Mourenas, Vladimir Krasnoselskikh, Vitalii Shastun, and Forrest Mozer. Oblique Whistler-Mode Waves in the Earth's Inner Magnetosphere: Energy Distribution, Origins, and Role in Radiation Belt Dynamics. *Space Science Reviews*, 200(1-4):261–355, 2016. ISSN 15729672. doi: 10.1007/s11214-016-0252-5. URL http://dx.doi.org/10.1007/s11214-016-0252-5.

[7] N. Aunai, G. Belmont, and R. Smets. Proton acceleration in antiparallel collisionless magnetic reconnection: Kinetic mechanisms behind the fluid dynamics. *Journal of Geophysical Research: Space Physics*, 116(9):1–13, 2011. ISSN 21699402. doi: 10.1029/2011JA016688.

[8] D. D. Barbosa and W. S. Kurth. On the generation of plasma waves in Saturn's inner magnetosphere. *Journal of Geophysical Research*, 98(A6):9351, 1993. ISSN 0148-0227. doi: 10.1029/93ja00477. URL http://doi.wiley.com/10.1029/93JA00477.

[9] P. M. Bellan. Pitch angle scattering of an energetic magnetized particle by a circularly polarized electromagnetic wave. *Physics of Plasmas*, 20 (4):042117, apr 2013. ISSN 1070-664X. doi: 10.1063/1.4801055. URL http://aip.scitation.org/doi/10.1063/1.4801055.

[10] P. M. Bellan. Orbits of magnetized charged particles in parabolic and inverse electrostatic potentials. *Journal of Plasma Physics*, 82(1): 615820101, feb 2016. ISSN 0022-3778. doi: 10.1017/S0022377816000064. URL https://www.cambridge.org/core/product/identifier/S0022377816000064/type/journal{_}article.

[11] Paul M. Bellan. *Fundamentals of Plasma Physics*. Cambridge University Press, Cambridge, 2006. ISBN 9780511807183. doi: 10.1017/CBO9780511807183. URL http://ebooks.cambridge.org/ref/id/CBO9780511807183.

[12] Paul M. Bellan. Fast, purely growing collisionless reconnection as an eigenfunction problem related to but not involving linear whistler waves. *Physics of Plasmas*, 21(10):102108, oct 2014. ISSN 1070-664X. doi: 10.1063/1.4897375. URL http://dx.doi.org/10.1063/1.4897375http://aip.scitation.org/doi/10.1063/1.4897375.

[13] Paul M Bellan. *Magnetic Helicity, Spheromaks, Solar Corona Loops, and Astrophysical Jets*. WORLD SCIENTIFIC (EUROPE), apr 2018. ISBN 978-1-78634-514-1. doi: 10.1142/q0151. URL https://www.worldscientific.com/worldscibooks/10.1142/q0151.

[14] Ludwig Biermann and A. Schlüter. Über den Ursprung der Magnetfelder auf Sternen und im interstellaren Raum. *Zeitschrift fur Naturforschung - Section A Journal of Physical Sciences*, 5(2):65–71, 1950. ISSN 18657109. doi: 10.1515/zna-1950-0201. URL http://adsabs.harvard.edu/cgi-bin/nph-data{_}query?bibcode=1950ZNatA...5...65B{&}link{_}type=CITATIONS{%}5Cnpapers://2a2ad0e7-fc2e-4412-9a36-bd8c4bed137e/Paper/p6682.

[15] C.K. Birdsall. *Plasma Physics via Computer Simulation*. CRC Press, oct 2004. ISBN 9781482263060. doi: 10.1201/9781315275048. URL https://www.taylorfrancis.com/books/9781482263060.

[16] J Birn, J. F. Drake, M. A. Shay, B. N. Rogers, R. E. Denton, M. Hesse, M Kuznetsova, Z W Ma, A Bhattacharjee, A Otto, and P L Pritchett. Geospace Environmental Modeling (GEM) Magnetic Reconnection Challenge. *Journal of Geophysical Research: Space Physics*, 106(A3):3715–3719, mar 2001. ISSN 01480227. doi: 10.1029/1999JA900449. URL http://www.sciencedirect.com/science/article/pii/B9780123725066000149http://doi.wiley.com/10.1029/1999JA900449.

[17] D. Biskamp, E. Schwarz, and J. F. Drake. Two-fluid theory of collisionless magnetic reconnection. *Physics of Plasmas*, 4(4):1002–1009, 1997. ISSN 1070664X. doi: 10.1063/1.872211.

[18] A. Bonafede, L. Feretti, M. Murgia, F. Govoni, G. Giovannini, D. Dallacasa, K. Dolag, and G. B. Taylor. The Coma cluster magnetic field from Faraday rotation measures. *Astronomy and Astrophysics*, 513(5):A30, apr 2010. ISSN 0004-6361. doi: 10.1051/0004-6361/200913696. URL http://www.aanda.org/10.1051/0004-6361/200913696.

[19] J. Bortnik, R. M. Thorne, and U. S. Inan. Nonlinear interaction of energetic electrons with large amplitude chorus. *Geophysical Research Letters*, 35(21): L21102, nov 2008. ISSN 0094-8276. doi: 10.1029/2008GL035500. URL http://doi.wiley.com/10.1029/2008GL035500.

[20] R. W. Boswell. Very efficient plasma generation by whistler waves near the lower hybrid frequency. *Plasma Physics and Controlled Fusion*, 26 (10):1147–1162, oct 1984. ISSN 07413335. doi: 10.1088/0741-3335/26/10/001. URL http://stacks.iop.org/0741-3335/26/i=10/a=001?key=crossref.eb755a5ee079398ecf1bb3ffef2fb910.

[21] A. Bourdier and S. Gond. Dynamics of a charged particle in a circularly polarized traveling electromagnetic wave. *Physical Review E - Statistical Physics, Plasmas, Fluids, and Related Interdisciplinary Topics*, 62(3 B): 4189–4206, 2000. ISSN 1063651X. doi: 10.1103/PhysRevE.62.4189.

[22] Sofiane Bourouaine and Benjamin D. G. Chandran. OBSERVATIONAL TEST OF STOCHASTIC HEATING IN LOW-β FAST-SOLAR-WIND STREAMS. *The Astrophysical Journal*, 774(2):96, aug 2013. ISSN 0004-637X. doi: 10.1088/0004-637X/774/2/96. URL http://stacks.iop.org/0004-637X/774/i=2/a=96?key=crossref.d43e975ad84c3808435d2c2097a73004.

[23] J Boussinesq. Essai sur la theorie des eaux courantes. *Memoires presentes par divers savants a l'Academie des Sciences de l'Institut National de France*, XXIII:1–770, 1877.

[24] A. W. Breneman, A. Crew, J. Sample, D. Klumpar, A. Johnson, O. Agapitov, M. Shumko, D. L. Turner, O. Santolik, J. R. Wygant, C. A. Cattell, S. Thaller, B. Blake, H. Spence, and C. A. Kletzing. Observations Directly Linking Relativistic Electron Microbursts to Whistler Mode Chorus: Van Allen Probes and FIREBIRD II. *Geophysical Research Letters*, 44(22):11,265–11,272, 2017. ISSN 19448007. doi: 10.1002/2017GL075001.

[25] S. V. Bulanov, F. Pegoraro, and A. S. Sakharov. Magnetic reconnection in electron magnetohydrodynamics. *Physics of Fluids B*, 4(8):2499–2508, aug 1992. ISSN 08998221. doi: 10.1063/1.860467. URL http://aip.scitation.org/doi/10.1063/1.860467.

[26] BURTIS WJ and HELLIWELL RA. Banded Chorus. a New Type of Vlf Radiation Observed in the Magnetosphere By Ogo 1 and Ogo 3. *J Geophys Res*, 74(11):3002–3010, jun 1969. ISSN 01480227. doi: 10.1029/JA074i011p03002. URL http://doi.wiley.com/10.1029/JA074i011p03002.

[27] E. Cafaro, D. Grasso, F. Pegoraro, F. Porcelli, and A. Saluzzi. Invariants and Geometric Structures in Nonlinear Hamiltonian Magnetic Reconnection. *Physical Review Letters*, 80(20):4430–4433, may 1998. ISSN 0031-9007. doi: 10.1103/PhysRevLett.80.4430. URL https://link.aps.org/doi/10.1103/PhysRevLett.80.4430.

[28] C. Cattell, J. R. Wygant, K. Goetz, K. Kersten, P. J. Kellogg, T. von Rosenvinge, S. D. Bale, I. Roth, M. Temerin, M. K. Hudson, R. A. Mewaldt, M. Wiedenbeck, M. Maksimovic, R. Ergun, M. Acuna, and C. T. Russell. Discovery of very large amplitude whistler-mode waves in earth's radiation belts. *Geophysical Research Letters*, 35(1):1–7, 2008. ISSN 00948276. doi: 10.1029/2007GL032009.

[29] Kil-Byoung Chai, Xiang Zhai, and Paul M. Bellan. Extreme ultra-violet burst, particle heating, and whistler wave emission in fast magnetic reconnection induced by kink-driven Rayleigh-Taylor instability. *Physics of Plasmas*, 23(3):032122, mar 2016. ISSN 1070-664X. doi: 10.1063/1.4944390. URL http://dx.doi.org/10.1063/1.4944390http://aip.scitation.org/doi/10.1063/1.4944390.

[30] B. D. G. Chandran, D. Verscharen, E. Quataert, J. C. Kasper, P. A. Isenberg, and S. Bourouaine. STOCHASTIC HEATING, DIFFERENTIAL FLOW, AND THE ALPHA-TO-PROTON TEMPERATURE RATIO IN THE SOLAR WIND. *The Astrophysical Journal*, 776(1):45, sep 2013. ISSN 0004-637X. doi: 10.1088/0004-637X/776/1/45. URL http://stacks.iop.org/0004-637X/776/i=1/a=45?key=crossref.4f827fd36c5cc243533f783bb229e5f4.

[31] Benjamin D.G. Chandran, Bo Li, Barrett N. Rogers, Eliot Quataert, and Kai Germaschewski. Perpendicular ion heating by low-frequency Alfvén-wave turbulence in the solar wind. *Astrophysical Journal*, 720(1):503–515, 2010. ISSN 15384357. doi: 10.1088/0004-637X/720/1/503.

[32] Vernon H. Chaplin. *Battery-Powered RF Pre-Ionization System for the Caltech Magnetohydrodynamically-Driven Jet Experiment: RF Discharge Properties and MHD-Driven Jet Dynamics*. PhD thesis, California Institute of Technology, 2015.

[33] F.F. Chen and R.W. Boswell. Helicons-the past decade. *IEEE Transactions on Plasma Science*, 25(6):1245–1257, 1997. ISSN 00933813. doi: 10.1109/27.650899. URL http://ieeexplore.ieee.org/document/650899/.

[34] R T S Chen, R A Breun, S Gross, N Hershkowitz, M K J Hsieh, and J Jacobs. Experimental studies of multimode helicon plasma waves. *Plasma Sources Science and Technology*, 4(3):337–344, aug 1995. ISSN 0963-0252. doi: 10.1088/0963-0252/4/3/003. URL http://stacks.iop.org/0963-0252/4/i=3/a=003?key=crossref.b6db19176a30445fcd15f41191ad9065.

[35] G. F. Chew, M. L. Goldberger, and F. E. Low. The Boltzmann equation an d the one-fluid hydromagnetic equations in the absence of particle collisions. *Proceedings of the Royal Society of London. Series A. Mathematical and Physical Sciences*, 236(1204):112–118, jul 1956. ISSN 0080-4630. doi: 10.1098/rspa.1956.0116. URL http://www.royalsocietypublishing.org/doi/10.1098/rspa.1956.0116.

[36] F. V. Coroniti, C. F. Kennel, F. L. Scarf, and E. J. Smith. Whistler mode turbulence in the disturbed solar wind. *Journal of Geophysical Research*, 87 (A8):6029, 1982. ISSN 0148-0227. doi: 10.1029/ja087ia08p06029. URL http://doi.wiley.com/10.1029/JA087iA08p06029.

[37] D. Del Sarto, F. Califano, and F. Pegoraro. Secondary Instabilities and Vortex Formation in Collisionless-Fluid Magnetic Reconnection. *Physical Review Letters*, 91(23):2350011–2350014, 2003. ISSN 00319007. doi: 10.1103/PhysRevLett.91.235001.

[38] Wolfgang Demtröder. *Laser Spectroscopy*. Springer Berlin Heidelberg, Berlin, Heidelberg, 1996. ISBN 978-3-662-08262-1. doi: 10.1007/978-3-662-08260-7. URL http://link.springer.com/10.1007/978-3-662-08260-7.

[39] Wolfgang Demtröder. *Laser Spectroscopy 2*. Springer Berlin Heidelberg, Berlin, Heidelberg, 2015. ISBN 978-3-662-44640-9. doi: 10.1007/978-3-662-44641-6. URL http://link.springer.com/10.1007/978-3-662-44641-6.

[40] X. H. Deng and H. Matsumoto. Rapid magnetic reconnection in the Earth's magnetosphere mediated by whistler waves. *Nature*, 410(6828):557–560, mar 2001. ISSN 0028-0836. doi: 10.1038/35069018. URL http://www.nature.com/articles/35069018.

[41] J. Derouillat, A. Beck, F. Pérez, T. Vinci, M. Chiaramello, A. Grassi, M. Flé, G. Bouchard, I. Plotnikov, N. Aunai, J. Dargent, C. Riconda, and M. Grech. Smilei : A collaborative, open-source, multi-purpose particle-in-cell code for plasma simulation. *Computer Physics Communications*, 222:351–373, jan 2018. ISSN 00104655. doi: 10.1016/j.cpc.2017.09.024. URL https://linkinghub.elsevier.com/retrieve/pii/S0010465517303314.

[42] J. F. Drake. Formation of Electron Holes and Particle Energization During Magnetic Reconnection. *Science*, 299(5608):873–877, feb 2003.

ISSN 00368075. doi: 10.1126/science.1080333. URL http://www.sciencemag.org/cgi/doi/10.1126/science.1080333.

[43] J. F. Drake, R. G. Kleva, and M. E. Mandt. Structure of Thin Current Layers: Implications for Magnetic Reconnection. *Physical Review Letters*, 73(9): 1251–1254, aug 1994. ISSN 0031-9007. doi: 10.1103/PhysRevLett.73.1251. URL https://link.aps.org/doi/10.1103/PhysRevLett.73.1251.

[44] J F Drake, D Biskamp, and A Zeiler. Breakup of the electron current layer during 3-D collisionless magnetic reconnection. *Journal of Geophysical Research: Space Physics*, 24(22):2921–2924, 1997. doi: 10.1029/97GL52961.

[45] J. F. Drake, M. A. Shay, and M. Swisdak. The Hall fields and fast magnetic reconnection. *Physics of Plasmas*, 15(4):042306, 2008. ISSN 1070664X. doi: 10.1063/1.2901194. URL http://scitation.aip.org/content/aip/journal/pop/15/4/10.1063/1.2901194.

[46] J. F. Drake, P. A. Cassak, M. A. Shay, M. Swisdak, and E. Quataert. A MAGNETIC RECONNECTION MECHANISM FOR ION ACCELERATION AND ABUNDANCE ENHANCEMENTS IN IMPULSIVE FLARES. *The Astrophysical Journal*, 700(1):L16–L20, jul 2009. ISSN 0004-637X. doi: 10.1088/0004-637X/700/1/L16. URL http://stacks.iop.org/1538-4357/700/i=1/a=L16?key=crossref.84f266691542cc226326ca2ea699f3da.

[47] J. F. Drake, M. Swisdak, T. D. Phan, P. A. Cassak, M. A. Shay, S. T. Lepri, R. P. Lin, E. Quataert, and T. H. Zurbuchen. Ion heating resulting from pickup in magnetic reconnection exhausts. *Journal of Geophysical Research: Space Physics*, 114(5):1–14, 2009. ISSN 21699402. doi: 10.1029/2008JAO13701.

[48] J. F. Drake, M. Swisdak, and R. Fermo. The power-law spectra of energetic particles during multi-island magnetic reconnection. *Astrophysical Journal Letters*, 763(1):1–5, 2013. ISSN 20418205. doi: 10.1088/2041-8205/763/1/L5.

[49] J. Egedal, W. Fox, N. Katz, M. Porkolab, M. Øieroset, R. P. Lin, W. Daughton, and J. F. Drake. Evidence and theory for trapped electrons in guide field magnetotail reconnection. *Journal of Geophysical Research: Space Physics*, 113(A12):n/a–n/a, dec 2008. ISSN 01480227. doi: 10.1029/2008JA013520. URL http://doi.wiley.com/10.1029/2008JA013520.

[50] A. G. Emslie. Energy partition in two solar flare/CME events. *Journal of Geophysical Research*, 109(A10):A10104, 2004. ISSN 0148-0227. doi: 10.1029/2004JA010571. URL http://doi.wiley.com/10.1029/2004JA010571.

[51] G. Fiksel, A. F. Almagri, B. E. Chapman, V. V. Mirnov, Y. Ren, J. S. Sarff, and P. W. Terry. Mass-Dependent Ion Heating during Magnetic Reconnection in a Laboratory Plasma. *Physical Review Letters*, 103(14):145002, sep 2009.

ISSN 0031-9007. doi: 10.1103/PhysRevLett.103.145002. URL https://link.aps.org/doi/10.1103/PhysRevLett.103.145002.

[52] R. K. Fisher and R. W. Gould. Resonance cones in the field pattern of a short antenna in an anisotropic plasma. *Physical Review Letters*, 22(21):1093–1095, may 1969. ISSN 00319007. doi: 10.1103/PhysRevLett.22.1093. URL https://link.aps.org/doi/10.1103/PhysRevLett.22.1093.

[53] Terry G. Forbes. Flares caught in the act. *Nature Physics*, 9(8):456–457, aug 2013. ISSN 1745-2473. doi: 10.1038/nphys2703. URL http://www.nature.com/articles/nphys2703.

[54] Keizo Fujimoto and Richard D. Sydora. Whistler waves associated with magnetic reconnection. *Geophysical Research Letters*, 35(19):L19112, oct 2008. ISSN 0094-8276. doi: 10.1029/2008GL035201. URL http://doi.wiley.com/10.1029/2008GL035201.

[55] X. Gao, W. Li, R. M. Thorne, J. Bortnik, V. Angelopoulos, Q. Lu, X. Tao, and S. Wang. Statistical results describing the bandwidth and coherence coefficient of whistler mode waves using THEMIS waveform data. *Journal of Geophysical Research: Space Physics*, 119(11):8992–9003, nov 2014. ISSN 21699380. doi: 10.1002/2014JA020158. URL http://doi.wiley.com/10.1002/2015JA021094http://doi.wiley.com/10.1002/2014JA020158.

[56] Gregory P. Ginet and Michael A. Heinemann. Test particle acceleration by small amplitude electromagnetic waves in a uniform magnetic field. *Physics of Fluids B*, 2(4):700–716, apr 1990. ISSN 08998221. doi: 10.1063/1.859307. URL http://aip.scitation.org/doi/10.1063/1.859307.

[57] M. V. Goldman, G. Lapenta, D. L. Newman, S. Markidis, and H. Che. Jet Deflection by Very Weak Guide Fields during Magnetic Reconnection. *Physical Review Letters*, 107(13):135001, sep 2011. ISSN 0031-9007. doi: 10.1103/PhysRevLett.107.135001. URL https://link.aps.org/doi/10.1103/PhysRevLett.107.135001.

[58] O. W. Greenberg. <math display="inline"> <mi>C</mi> <mi>P</mi> <mi>T</mi> </math> Violation Implies Violation of Lorentz Invariance. *Physical Review Letters*, 89(23):231602, nov 2002. ISSN 0031-9007. doi: 10.1103/PhysRevLett.89.231602. URL https://link.aps.org/doi/10.1103/PhysRevLett.89.231602.

[59] W. Grotian. Zur Frage der Deutung der Linien im Spektrum der Sonnenkorona. *Die Naturwissenschaften*, 27(13):214, mar 1939. ISSN 00281042. doi: 10.1007/BF01488890. URL http://link.springer.com/10.1007/BF01488890.

[60] T T Grove, V Sanchez-Villicana, B C Duncan, S Maleki, and P L Gould. Two-photon two-color diode laser spectroscopy of the Rb 5 D 5/2 state. *Physica Scripta*, 52(3):271–276, sep 1995. ISSN 0031-8949. doi: 10.1088/0031-8949/52/3/008. URL http://stacks.iop.org/1402-4896/52/i=3/a=008?key=crossref.16e81e7d77fb01e934f637cf1cd5ecc8.

[61] Fan Guo, Yi Hsin Liu, William Daughton, and Hui Li. Particle Acceleration and Plasma Dynamics During Magnetic Reconnection in the Magnetically Dominated Regime. *Astrophysical Journal*, 806(2):167, 2015. ISSN 15384357. doi: 10.1088/0004-637X/806/2/167. URL http://dx.doi.org/10.1088/0004-637X/806/2/167.

[62] D. A. Gurnett and B. J. O'Brien. High-latitude geophysical studies with satellite Injun 3: 5. Very-low-frequency electromagnetic radiation. *Journal of Geophysical Research*, 69(1):65–89, jan 1964. ISSN 01480227. doi: 10.1029/jz069i001p00065. URL http://doi.wiley.com/10.1029/JZ069i001p00065.

[63] C. C. Haggerty, M. A. Shay, J. F. Drake, T. D. Phan, and C. T. McHugh. The competition of electron and ion heating during magnetic reconnection. *Geophysical Research Letters*, 42(22):9657–9665, 2015. ISSN 19448007. doi: 10.1002/2015GL065961.

[64] Ernst Hairer, Syvert Paul Nrsett, and Gerhard Wanner. *Solving Ordinary Differential Equations: Nonstiff problems. v. 2: Stiff and differential-algebraic problems*, volume 14 of *Springer Series in Computational Mathematics*. Springer Berlin Heidelberg, Berlin, Heidelberg, 2010. ISBN 3642081584. doi: 10.1007/978-3-662-09947-6. URL http://link.springer.com/10.1007/978-3-319-32452-4{_}4http://link.springer.com/10.1007/978-3-662-09947-6.

[65] J. D. Hare, L. Suttle, S. V. Lebedev, N. F. Loureiro, A. Ciardi, G. C. Burdiak, J. P. Chittenden, T. Clayson, C. Garcia, N. Niasse, T. Robinson, R. A. Smith, N. Stuart, F. Suzuki-Vidal, G. F. Swadling, J. Ma, J. Wu, and Q. Yang. Anomalous Heating and Plasmoid Formation in a Driven Magnetic Reconnection Experiment. *Physical Review Letters*, 118(8):085001, feb 2017. ISSN 0031-9007. doi: 10.1103/PhysRevLett.118.085001. URL https://link.aps.org/doi/10.1103/PhysRevLett.118.085001.

[66] E. G. Harris. On a plasma sheath separating regions of oppositely directed magnetic field. *Il Nuovo Cimento Series 10*, 23(1):115–121, 1962. ISSN 00296341. doi: 10.1007/BF02733547.

[67] Magnus A. Haw, Byonghoon Seo, and Paul M. Bellan. Laboratory Measurement of Large-Amplitude Whistler Pulses Generated by Fast Magnetic Reconnection. *Geophysical Research Letters*, 46(13):7105–7112, jul 2019. ISSN 0094-8276. doi: 10.1029/2019GL082621. URL https://onlinelibrary.wiley.com/doi/abs/10.1029/2019GL082621.

[68] R. A. Helliwell and T. L. Crystal. A feedback model of cyclotron interaction between whistler-mode waves and energetic electrons in the magnetosphere. *Journal of Geophysical Research*, 78(31):7357–7371, nov 1973. ISSN 01480227. doi: 10.1029/ja078i031p07357. URL http://doi.wiley.com/10.1029/JA078i031p07357.

[69] Michael Hesse. Dissipation in magnetic reconnection with a guide magnetic field. *Physics of Plasmas*, 13(12), 2006. ISSN 1070664X. doi: 10.1063/1.2403784.

[70] H. Hietala, J. F. Drake, T. D. Phan, J. P. Eastwood, and J. P. McFadden. Ion temperature anisotropy across a magnetotail reconnection jet. *Geophysical Research Letters*, 42(18):7239–7247, 2015. ISSN 19448007. doi: 10.1002/2015GL065168.

[71] R. B. Horne and R. M. Thorne. Relativistic electron acceleration and precipitation during resonant interactions with whistler-mode chorus. *Geophysical Research Letters*, 30(10), may 2003. ISSN 00948276. doi: 10.1029/2003GL016973. URL http://doi.wiley.com/10.1029/2003GL016973.

[72] Masahiro Hoshino. Stochastic particle acceleration in multiple magnetic islands during reconnection. *Physical Review Letters*, 108(13):1–4, 2012. ISSN 00319007. doi: 10.1103/PhysRevLett.108.135003.

[73] G. B. Hospodarsky, T. F. Averkamp, W. S. Kurth, D. A. Gurnett, J. D. Menietti, O. Santolik, and M. K. Dougherty. Observations of chorus at Saturn using the Cassini Radio and Plasma Wave Science instrument. *Journal of Geophysical Research: Space Physics*, 113(A12), dec 2008. ISSN 01480227. doi: 10.1029/2008JA013237. URL http://doi.wiley.com/10.1029/2008JA013237.

[74] S. C. Hsu, G. Fiksel, T. A. Carter, H. Ji, R. M. Kulsrud, and M. Yamada. Local Measurement of Nonclassical Ion Heating during Magnetic Reconnection. *Physical Review Letters*, 84(17):3859–3862, apr 2000. ISSN 0031-9007. doi: 10.1103/PhysRevLett.84.3859. URL https://link.aps.org/doi/10.1103/PhysRevLett.84.3859.

[75] J. D. Huba. NRL Plasma Formulary. Technical report, Naval Reserach Laboratory, 2006. URL https://apps.dtic.mil/dtic/tr/fulltext/u2/a447173.pdf.

[76] C. M. Jackman, C. S. Arridge, N. André, F. Bagenal, J. Birn, M. P. Freeman, X. Jia, A. Kidder, S. E. Milan, A. Radioti, J. A. Slavin, M. F. Vogt, M. Volwerk, and A. P. Walsh. Large-Scale Structure and Dynamics of the Magnetotails of Mercury, Earth, Jupiter and Saturn. *Space Science Reviews*, 182(1-4):85–154, aug 2014. ISSN 0038-6308. doi: 10.1007/s11214-014-0060-8. URL http://link.springer.com/10.1007/s11214-014-0060-8.

[77] V. Jacques, B. Hingant, A. Allafort, M. Pigeard, and J. F. Roch. Nonlinear spectroscopy of rubidium: an undergraduate experiment. *European Journal of Physics*, 30(5):921–934, sep 2009. ISSN 0143-0807. doi: 10.1088/0143-0807/30/5/001. URL http://stacks.iop.org/0143-0807/30/i=5/a=001?key=crossref.a85323f9f6623e69b22f87d1099edd2d.

[78] Ferencz Jüttner. Das Maxwellsche Gesetz der Geschwindigkeitsverteilung in der Relativtheorie. *Annalen der Physik*, 339(5):856–882, 1911. ISSN 15213889. doi: 10.1002/andp.19113390503. URL http://doi.wiley.com/10.1002/andp.19113390503.

[79] Homa Karimabadi, W. Daughton, and J. Scudder. Multi-scale structure of the electron diffusion region. *Geophysical Research Letters*, 34(13):n/a–n/a, jul 2007. ISSN 00948276. doi: 10.1029/2007GL030306. URL http://doi.wiley.com/10.1029/2007GL030306.

[80] C. F. Kennel and H. E. Petschek. Limit on stably trapped particle fluxes. *Journal of Geophysical Research*, 71(1):1–28, jan 1966. ISSN 01480227. doi: 10.1029/jz071i001p00001. URL http://doi.wiley.com/10.1029/JZ071i001p00001.

[81] C. F. Kennel and R. M. Thorne. Electron pitch–angle diffusion driven by oblique whistler-mode turbulence. *Journal of Plasma Physics*, 6(3):589–606, dec 1971. ISSN 14697807. doi: 10.1017/S0022377800006310. URL https://www.cambridge.org/core/product/identifier/S0022377800006310/type/journal{_}article.

[82] K. Knizhnik, M. Swisdak, and J. F. Drake. The acceleration of ions in solar flares during magnetic reconnection. *Astrophysical Journal Letters*, 743(2):1–6, 2011. ISSN 20418205. doi: 10.1088/2041-8205/743/2/L35.

[83] N. Konjević, A. Lesage, J. R. Fuhr, and W. L. Wiese. Experimental Stark Widths and Shifts for Spectral Lines of Neutral and Ionized Atoms (A Critical Review of Selected Data for the Period 1989 Through 2000). *Journal of Physical and Chemical Reference Data*, 31(3):819–927, sep 2002. ISSN 0047-2689. doi: 10.1063/1.1486456. URL http://aip.scitation.org/doi/10.1063/1.555847http://aip.scitation.org/doi/10.1063/1.1486456.

[84] Steven E. Koonin, Dawn C. Meredith, and William H. Press. Computational Physics: Fortran Version . *Physics Today*, 44(10):112–113, oct 1991. ISSN 0031-9228. doi: 10.1063/1.2810288. URL http://physicstoday.scitation.org/doi/10.1063/1.2810288.

[85] T. W. Kornack, P. K. Sollins, and M. R. Brown. Experimental observation of correlated magnetic reconnection and Alfvénic ion jets. *Physical Review E*, 58(1):R36–R39, jul 1998. ISSN 1063-651X. doi: 10.1103/PhysRevE.58.R36. URL https://link.aps.org/doi/10.1103/PhysRevE.58.R36.

[86] Russell M. Kulsrud. Magnetic reconnection in a magnetohydrodynamic plasma. *Physics of Plasmas*, 5(5):1599–1606, may 1998. ISSN 1070-664X. doi: 10.1063/1.872827. URL http://aip.scitation.org/doi/10.1063/1.872827.

[87] G. S. Lakhina, B. T. Tsurutani, O. P. Verkhoglyadova, and J. S. Pickett. Pitch angle transport of electrons due to cyclotron interactions with the coherent chorus subelements. *Journal of Geophysical Research: Space Physics*, 115 (A8), aug 2010. ISSN 01480227. doi: 10.1029/2009JA014885. URL http://doi.wiley.com/10.1029/2009JA014885.

[88] A. Le, J. Egedal, W. Daughton, W. Fox, and N. Katz. Equations of State for Collisionless Guide-Field Reconnection. *Physical Review Letters*, 102 (8):085001, feb 2009. ISSN 0031-9007. doi: 10.1103/PhysRevLett.102.085001. URL https://link.aps.org/doi/10.1103/PhysRevLett.102.085001.

[89] A. Le, J. Egedal, O. Ohia, W. Daughton, H. Karimabadi, and V. S. Lukin. Regimes of the Electron Diffusion Region in Magnetic Reconnection. *Physical Review Letters*, 110(13):135004, mar 2013. ISSN 0031-9007. doi: 10.1103/PhysRevLett.110.135004. URL http://linkinghub.elsevier.com/retrieve/pii/S1499404611006142https://link.aps.org/doi/10.1103/PhysRevLett.110.135004.

[90] J. A. Le Roux, G. P. Zank, G. M. Webb, and O. Khabarova. A kinetic transport theory for particle acceleration and transport in regions of multiple contracting and reconnecting inertial-scale flux ropes. *Astrophysical Journal*, 801(2):1–24, 2015. ISSN 15384357. doi: 10.1088/0004-637X/801/2/112.

[91] J. A. le Roux, G. P. Zank, G. M. Webb, and O. V. Khabarova. Combining Diffusive Shock Acceleration With Acceleration By Contracting and Reconnecting Small-Scale Flux Ropes At Heliospheric Shocks. *The Astrophysical Journal*, 827(1):47, 2016. ISSN 1538-4357. doi: 10.3847/0004-637X/827/1/47. URL http://stacks.iop.org/0004-637X/827/i=1/a=47?key=crossref.4075f5f0d48618f0a0efc715e7a970bd.

[92] M. P. Leubner. On Jupiter's whistler emission. *Journal of Geophysical Research*, 87(A8):6335, 1982. ISSN 0148-0227. doi: 10.1029/ja087ia08p06335. URL http://doi.wiley.com/10.1029/JA087iA08p06335.

[93] Bin Li and Ritoku Horiuchi. Electron Force Balance in Steady Collisionless-Driven Reconnection. *Physical Review Letters*, 101(21):215001, nov 2008. ISSN 0031-9007. doi: 10.1103/PhysRevLett.101.215001. URL https://link.aps.org/doi/10.1103/PhysRevLett.101.215001.

[94] W. Li, R. M. Thorne, Y. Nishimura, J. Bortnik, V. Angelopoulos, J. P. McFadden, D. E. Larson, J. W. Bonnell, O. Le Contel, A. Roux, and U. Auster.

THEMIS analysis of observed equatorial electron distributions responsible for the chorus excitation. *Journal of Geophysical Research: Space Physics*, 115(A6), jun 2010. ISSN 01480227. doi: 10.1029/2009JA014845. URL http://doi.wiley.com/10.1029/2009JA014845.

[95] Xing Li, Shadia Rifai Habbal, John L. Kohl, and Giancarlo Noci. The Effect of Temperature Anisotropy on Observations of Doppler Dimming and Pumping in the Inner Corona. *The Astrophysical Journal*, 501(1):L133–L137, jul 1998. ISSN 0004637X. doi: 10.1086/311428. URL http://arxiv.org/abs/astro-ph/9805021http://stacks.iop.org/1538-4357/501/i=1/a=L133.

[96] R. P. Lin, S. Krucker, G. J. Hurford, D. M. Smith, H. S. Hudson, G. D. Holman, R. A. Schwartz, B. R. Dennis, G. H. Share, R. J. Murphy, A. G. Emslie, C. Johns-Krull, and N. Vilmer. RHESSI Observations of Particle Acceleration and Energy Release in an Intense Solar Gamma-Ray Line Flare. *The Astrophysical Journal*, 595(2):L69–L76, oct 2003. ISSN 0004-637X. doi: 10.1086/378932. URL http://stacks.iop.org/1538-4357/595/i=2/a=L69.

[97] T. V. Liseikina, F. Pegoraro, and E. Yu Echkina. Foliation and mixing of the electron drift-kinetic distribution function in nonlinear two-dimensional magnetic reconnection. *Physics of Plasmas*, 11(7):3535–3545, 2004. ISSN 1070664X. doi: 10.1063/1.1758231.

[98] George Livadiotis. Modeling anisotropic Maxwell–Jüttner distributions: derivation and properties. *Annales Geophysicae*, 34(12):1145–1158, dec 2016. ISSN 1432-0576. doi: 10.5194/angeo-34-1145-2016. URL https://www.ann-geophys.net/34/1145/2016/.

[99] N. F. Loureiro, A. A. Schekochihin, and S. C. Cowley. Instability of current sheets and formation of plasmoid chains. *Physics of Plasmas*, 14(10):100703, oct 2007. ISSN 1070-664X. doi: 10.1063/1.2783986. URL http://aip.scitation.org/doi/10.1063/1.2783986.

[100] A. M. Lyapunov. The general problem of the stability of motion. *International Journal of Control*, 55(3):531–534, mar 1992. ISSN 13665820. doi: 10.1080/00207179208934253. URL http://www.tandfonline.com/doi/abs/10.1080/00207179208934253.

[101] Lawrence R. Lyons. Pitch Angle And Energy Diffusion Coefficients From Resonant Interactions With Ion—Cyclotron And Whistler Waves. *Journal of Plasma Physics*, 12(3):417–432, dec 1974. ISSN 14697807. doi: 10.1017/S002237780002537X. URL https://www.cambridge.org/core/product/identifier/S002237780002537X/type/journal{_}article.

[102] E. Macúšová, O. Santolík, N. Cornilleau-Wehrlin, and K. H. Yearby. Bandwidths and amplitudes of chorus-like banded emissions measured by the TC-1 Double Star spacecraft. *Journal of Geophysical Research: Space Physics*, 120(2):1057–1071, feb 2015. ISSN 21699380. doi: 10.1002/2014JA020440. URL http://doi.wiley.com/10.1002/2014JA020440.

[103] R. M. Magee, D. J. Den Hartog, S. T. A. Kumar, A. F. Almagri, B. E. Chapman, G. Fiksel, V. V. Mirnov, E. D. Mezonlin, and J. B. Titus. Anisotropic Ion Heating and Tail Generation during Tearing Mode Magnetic Reconnection in a High-Temperature Plasma. *Physical Review Letters*, 107(6):065005, aug 2011. ISSN 0031-9007. doi: 10.1103/PhysRevLett.107.065005. URL https://link.aps.org/doi/10.1103/PhysRevLett.107.065005.

[104] M. E. Mandt, R. E. Denton, and J. F. Drake. Transition to whistler mediated magnetic reconnection. *Geophysical Research Letters*, 21(1): 73–76, jan 1994. ISSN 19448007. doi: 10.1029/93GL03382. URL http://doi.wiley.com/10.1029/93GL03382.

[105] R. S. Marshall, M. J. Flynn, and P. M. Bellan. Hard x-ray bursts observed in association with Rayleigh-Taylor instigated current disruption in a solar-relevant lab experiment. *Physics of Plasmas*, 25(11):112101, nov 2018. ISSN 1070-664X. doi: 10.1063/1.5054927. URL http://aip.scitation.org/doi/10.1063/1.5054927.

[106] G. M. Mason. 3He-rich solar energetic particle events. *Space Science Reviews*, 130(1-4):231–242, 2007. ISSN 00386308. doi: 10.1007/s11214-007-9156-8.

[107] W. H. Matthaeus, J. J. Ambrosiano, and M. L. Goldstein. Particle Acceleration by Turbulent Magnetohydrodynamic Reconnection. *Physical Review Letters*, 53(15):1449–1452, oct 1984. ISSN 00319007. doi: 10.1103/PhysRevLett.53.1449. URL https://link.aps.org/doi/10.1103/PhysRevLett.53.1449.

[108] J. M. McChesney, R. A. Stern, and P. M. Bellan. Observation of fast stochastic ion heating by drift waves. *Physical Review Letters*, 59(13):1436–1439, 1987. ISSN 00319007. doi: 10.1103/PhysRevLett.59.1436.

[109] Auna L. Moser and Paul M. Bellan. Magnetic reconnection from a multiscale instability cascade. *Nature*, 482(7385):379–381, feb 2012. ISSN 0028-0836. doi: 10.1038/nature10827. URL http://www.nature.com/articles/nature10827.

[110] D. Nunn. A self-consistent theory of triggered VLF emissions. *Planetary and Space Science*, 22(3):349–378, mar 1974. ISSN 00320633. doi: 10.1016/0032-0633(74)90070-1. URL https://linkinghub.elsevier.com/retrieve/pii/0032063374900701.

[111] O. Ohia, J. Egedal, V. S. Lukin, W. Daughton, and A. Le. Demonstration of Anisotropic Fluid Closure Capturing the Kinetic Structure of Magnetic Reconnection. *Physical Review Letters*, 109(11):115004, sep 2012. ISSN 0031-9007. doi: 10.1103/PhysRevLett.109.115004. URL https://link.aps.org/doi/10.1103/PhysRevLett.109.115004.

[112] Abraham J. Olson, Evan J. Carlson, and Shannon K. Mayer. Two-photon spectroscopy of rubidium using a grating-feedback diode laser. *American Journal of Physics*, 74(3):218–223, 2006. ISSN 0002-9505. doi: 10.1119/1.2173278. URL http://aapt.scitation.org/doi/10.1119/1.2173278.

[113] Y. Omura, D. Nunn, H. Matsumoto, and M. J. Rycroft. A review of observational, theoretical and numerical studies of VLF triggered emissions. *Journal of Atmospheric and Terrestrial Physics*, 53(5):351–368, may 1991. ISSN 00219169. doi: 10.1016/0021-9169(91)90031-2. URL https://linkinghub.elsevier.com/retrieve/pii/0021916991900312.

[114] Yoshiharu Omura and Danny Summers. Dynamics of high-energy electrons interacting with whistler mode chorus emissions in the magnetosphere. *Journal of Geophysical Research*, 111(A9):A09222, sep 2006. ISSN 0148-0227. doi: 10.1029/2006JA011600. URL http://doi.wiley.com/10.1029/2006JA011600.

[115] Yoshiharu Omura, Naoki Furuya, and Danny Summers. Relativistic turning acceleration of resonant electrons by coherent whistler mode waves in a dipole magnetic field. *Journal of Geophysical Research: Space Physics*, 112(A6), jun 2007. ISSN 01480227. doi: 10.1029/2006JA012243. URL http://doi.wiley.com/10.1029/2006JA012243.

[116] Yoshiharu Omura, Yuto Katoh, and Danny Summers. Theory and simulation of the generation of whistler-mode chorus. *Journal of Geophysical Research: Space Physics*, 113(A4), apr 2008. ISSN 01480227. doi: 10.1029/2007JA012622. URL http://doi.wiley.com/10.1029/2007JA012622.

[117] Y. Ono, M. Yamada, T. Akao, T. Tajima, and R. Matsumoto. Ion Acceleration and Direct Ion Heating in Three-Component Magnetic Reconnection. *Physical Review Letters*, 76(18):3328–3331, apr 1996. ISSN 0031-9007. doi: 10.1103/PhysRevLett.76.3328. URL https://link.aps.org/doi/10.1103/PhysRevLett.76.3328.

[118] Y. Ono, H. Tanabe, Y. Hayashi, T. Ii, Y. Narushima, T. Yamada, M. Inomoto, and C. Z. Cheng. Ion and Electron Heating Characteristics of Magnetic Reconnection in a Two Flux Loop Merging Experiment. *Physical Review Letters*, 107(18):185001, oct 2011. ISSN 0031-9007. doi: 10.1103/PhysRevLett.107.185001. URL https://link.aps.org/doi/10.1103/PhysRevLett.107.185001.

[119] E. N. Parker. Sweet's mechanism for merging magnetic fields in conducting fluids. *Journal of Geophysical Research*, 62(4):509–520, dec 1957. ISSN 01480227. doi: 10.1029/jz062i004p00509. URL http://doi.wiley.com/10.1029/JZ062i004p00509.

[120] Wenbing Pei, Ritoku Horiuchi, and Tetsuya Sato. Ion dynamics in steady collisionless driven reconnection. *Physical Review Letters*, 87(23):235003–1–235003–4, 2001. ISSN 10797114. doi: 10.1103/PhysRevLett.87.235003.

[121] T. D. Phan, J. F. Drake, M. A. Shay, F. S. Mozer, and J. P. Eastwood. Evidence for an Elongated (<math display="inline"> <mo>></mo> <mn>60</mn> </math> Ion Skin Depths) Electron Diffusion Region during Fast Magnetic Reconnection. *Physical Review Letters*, 99(25):255002, dec 2007. ISSN 0031-9007. doi: 10.1103/PhysRevLett.99.255002. URL https://link.aps.org/doi/10.1103/PhysRevLett.99.255002.

[122] T. D. Phan, J. P. Eastwood, M. A. Shay, J. F. Drake, B. U.O. Ö Sonnerup, M. Fujimoto, P. A. Cassak, M. Øieroset, J. L. Burch, R. B. Torbert, A. C. Rager, J. C. Dorelli, D. J. Gershman, C. Pollock, P. S. Pyakurel, C. C. Haggerty, Y. Khotyaintsev, B. Lavraud, Y. Saito, M. Oka, R. E. Ergun, A. Retino, O. Le Contel, M. R. Argall, B. L. Giles, T. E. Moore, F. D. Wilder, R. J. Strangeway, C. T. Russell, P. A. Lindqvist, and W. Magnes. Electron magnetic reconnection without ion coupling in Earth's turbulent magnetosheath. *Nature*, 557(7704):202–206, may 2018. ISSN 14764687. doi: 10.1038/s41586-018-0091-5. URL http://www.nature.com/articles/s41586-018-0091-5.

[123] V. Pierrard and M. Lazar. Kappa Distributions: Theory and Applications in Space Plasmas. *Solar Physics*, 267(1):153–174, nov 2010. ISSN 0038-0938. doi: 10.1007/s11207-010-9640-2. URL http://link.springer.com/10.1007/s11207-010-9640-2.

[124] E. R. Priest, C. R. Foley, J. Heyvaerts, T. D. Arber, J. L. Culhane, and L. W. Acton. Nature of the heating mechanism for the diffuse solar corona. *Nature*, 393(6685):545–547, jun 1998. ISSN 0028-0836. doi: 10.1038/31166. URL http://www.nature.com/articles/31166.

[125] P. L. Pritchett. Onset of magnetic reconnection in the presence of a normal magnetic field: Realistic ion to electron mass ratio. *Journal of Geophysical Research: Space Physics*, 115(10):1–9, 2010. ISSN 21699402. doi: 10.1029/2010JA015371.

[126] Bao-Liang Qian. Relativistic motion of a charged particle in a superposition of circularly polarized plane electromagnetic waves and a uniform magnetic field. *Physics of Plasmas*, 7(2):537–543, feb 2000. ISSN 1070-664X. doi: 10.1063/1.873839. URL http://aip.scitation.org/doi/10.1063/1.873839.

[127] Fabio Reale. Coronal Loops: Observations and Modeling of Confined Plasma. *Living Reviews in Solar Physics*, 11(1), 2014. ISSN 1614-4961. doi: 10.12942/lrsp-2014-4. URL http://link.springer.com/10.12942/lrsp-2014-4.

[128] D. V. Reames and C. K. Ng. Heavy-Element Abundances in Solar Energetic Particle Events. *The Astrophysical Journal*, 610(1):510–522, jul 2004. ISSN 0004-637X. doi: 10.1086/421518. URL http://stacks.iop.org/0004-637X/610/i=1/a=510.

[129] Yang Ren, Masaaki Yamada, Stefan Gerhardt, Hantao Ji, Russell Kulsrud, and Aleksey Kuritsyn. Experimental Verification of the Hall Effect during Magnetic Reconnection in a Laboratory Plasma. *Physical Review Letters*, 95(5):055003, jul 2005. ISSN 0031-9007. doi: 10.1103/PhysRevLett.95.055003. URL https://link.aps.org/doi/10.1103/PhysRevLett.95.055003.

[130] Charles S. Roberts and S. J. Buchsbaum. Motion of a charged particle in a constant magnetic field and a transverse electromagnetic wave propagating along the field. *Physical Review*, 135(2A):A381–A389, jul 1964. ISSN 0031899X. doi: 10.1103/PhysRev.135.A381. URL https://link.aps.org/doi/10.1103/PhysRev.135.A381.

[131] Marshall N. Rosenbluth. Stability of the pinch. 245(1243):435–455, 1956.

[132] Christopher T. Russell, Robert E. Holzer, and Edward J. Smith. OGO 3 observations of ELF noise in the magnetosphere: 1. Spatial extent and frequency of occurrence. *Journal of Geophysical Research*, 74(3):755–777, feb 1969. ISSN 0148-0227. doi: 10.1029/ja074i003p00755. URL http://doi.wiley.com/10.1029/JA074i003p00755.

[133] S. J. Sanders, P. M. Bellan, and R. A. Stern. Observations of fast anisotropic ion heating, ion cooling, and ion recycling in large-amplitude drift waves. *Physics of Plasmas*, 5(3):716–728, mar 1998. ISSN 1070-664X. doi: 10.1063/1.872758. URL http://aip.scitation.org/doi/10.1063/1.872758.

[134] O. Santolík, D. A. Gurnett, J. S. Pickett, J. Chum, and N. Cornilleau-Wehrlin. Oblique propagation of whistler mode waves in the chorus source region. *Journal of Geophysical Research: Space Physics*, 114(A12), dec 2009. ISSN 01480227. doi: 10.1029/2009JA014586. URL http://doi.wiley.com/10.1029/2009JA014586.

[135] D. D. Sentman and C. K. Goertz. Whistler mode noise in Jupiter's inner magnetosphere. *Journal of Geophysical Research: Space Physics*, 83(A7):3151–3165, jul 1978. ISSN 01480227. doi: 10.1029/ja083ia07p03151. URL http://doi.wiley.com/10.1029/JA083iA07p03151.

[136] Byonghoon Seo, Pakorn Wongwaitayakornkul, Magnus A. Haw, Ryan S. Marshall, Hui Li, and Paul M. Bellan. Determination of a macro- to micro-scale progression leading to a magnetized plasma disruption. *Physics of Plasmas*, 27(2):022109, feb 2020. ISSN 1070-664X. doi: 10.1063/1.5140348. URL http://aip.scitation.org/doi/10.1063/1.5140348.

[137] M. A. Shay, J. F. Drake, and M. Swisdak. Two-Scale Structure of the Electron Dissipation Region during Collisionless Magnetic Reconnection. *Physical Review Letters*, 99(15):155002, oct 2007. ISSN 0031-9007. doi: 10.1103/PhysRevLett.99.155002. URL https://link.aps.org/doi/10.1103/PhysRevLett.99.155002.

[138] Kazunari Shibata and Syuniti Tanuma. Plasmoid-induced-reconnection and fractal reconnection. *Earth, Planets and Space*, 53(6):473–482, jun 2001. ISSN 1880-5981. doi: 10.1186/BF03353258. URL http://earth-planets-space.springeropen.com/articles/10.1186/BF03353258.

[139] T. Shoji, Y. Sakawa, S. Nakazawa, K. Kadota, and T. Sato. Plasma production by helicon waves. *Plasma Sources Science and Technology*, 2(1):5–10, feb 1993. ISSN 13616595. doi: 10.1088/0963-0252/2/1/002. URL http://stacks.iop.org/0963-0252/2/i=1/a=002?key=crossref.5aff2e3dc3ab75d92ccaeb840b19b1ba.

[140] J. A. Stamper and B. H. Ripin. Faraday-rotation measurements of megagauss magnetic fields in laser-produced plasmas. *Physical Review Letters*, 34(3):138–141, jan 1975. ISSN 00319007. doi: 10.1103/PhysRevLett.34.138. URL https://link.aps.org/doi/10.1103/PhysRevLett.34.138.

[141] A. Stark, W. Fox, J. Egedal, O. Grulke, and T. Klinger. Laser-Induced Fluorescence Measurement of the Ion-Energy-Distribution Function in a Collisionless Reconnection Experiment. *Physical Review Letters*, 95(23):235005, dec 2005. ISSN 0031-9007. doi: 10.1103/PhysRevLett.95.235005. URL https://link.aps.org/doi/10.1103/PhysRevLett.95.235005.

[142] K. Stasiewicz, R. Lundin, and G. Marklund. Stochastic Ion Heating by Orbit Chaotization on Electrostatic Waves and Nonlinear Structures. *Physica Scripta*, T84(1):60, 2000. ISSN 0031-8949. doi: 10.1238/Physica.Topical.084a00060. URL http://www.physica.org/xml/article.asp?article=t084a00060.xml.

[143] H. R. Strauss. Hyper-resistivity produced by tearing mode turbulence. *Physics of Fluids*, 29(11):3668, 1986. ISSN 00319171. doi: 10.1063/1.865798. URL https://aip.scitation.org/doi/10.1063/1.865798.

[144] R. N. Sudan and E. Ott. Theory of triggered VLF emissions. *Journal of Geophysical Research*, 76(19):4463–4476, jul 1971. ISSN 01480227.

doi: 10.1029/ja076i019p04463. URL http://doi.wiley.com/10.1029/JA076i019p04463.

[145] Danny Summers, Richard M. Thorne, and Fuliang Xiao. Relativistic theory of wave-particle resonant diffusion with application to electron acceleration in the magnetosphere. *Journal of Geophysical Research: Space Physics*, 103 (A9):20487–20500, 1998. ISSN 2169-9402. doi: 10.1029/98ja01740.

[146] H. Tanabe, T. Yamada, T. Watanabe, K. Gi, K. Kadowaki, M. Inomoto, R. Imazawa, M. Gryaznevich, C. Michael, B. Crowley, N. J. Conway, R. Scannell, J. Harrison, I. Fitzgerald, A. Meakins, N. Hawkes, K. G. McClements, T. O'Gorman, C. Z. Cheng, and Y. Ono. Electron and Ion Heating Characteristics during Magnetic Reconnection in the MAST Spherical Tokamak. *Physical Review Letters*, 115(21):1–5, 2015. ISSN 10797114. doi: 10.1103/PhysRevLett.115.215004.

[147] J. B. Taylor. Relaxation of toroidal plasma and generation of reverse magnetic fields. *Physical Review Letters*, 33(19):1139–1141, nov 1974. ISSN 00319007. doi: 10.1103/PhysRevLett.33.1139. URL https://link.aps.org/doi/10.1103/PhysRevLett.33.1139.

[148] A. Tenerani, M. Velli, F. Pucci, S. Landi, and A. F. Rappazzo. 'Ideally' unstable current sheets and the triggering of fast magnetic reconnection. *Journal of Plasma Physics*, 82(5):535820501, oct 2016. ISSN 0022-3778. doi: 10.1017/S002237781600088X. URL https://www.cambridge.org/core/product/identifier/S002237781600088X/type/journal{_}article.

[149] W. Thomson. VI.—On Vortex Motion. *Transactions of the Royal Society of Edinburgh*, 25(1):217–260, jan 1867. ISSN 00804568. doi: 10.1017/S0080456800028179. URL https://www.cambridge.org/core/product/identifier/S0080456800028179/type/journal{_}article.

[150] Rudolf A. Treumann and Wolfgang Baumjohann. Anisotropic Jüttner (relativistic Boltzmann) distribution. *Annales Geophysicae*, 34(9):737–738, sep 2016. ISSN 1432-0576. doi: 10.5194/angeo-34-737-2016. URL https://www.ann-geophys.net/34/737/2016/.

[151] Bruce T. Tsurutani and Edward J. Smith. Postmidnight chorus: A substorm phenomenon. *Journal of Geophysical Research*, 79(1):118–127, 1974. ISSN 0148-0227. doi: 10.1029/ja079i001p00118.

[152] Bruce T. Tsurutani, David J. Southwood, Edward J. Smith, and Andre Balogh. A Survey of Low Frequency Waves at Jupiter: The Ulysses Encounter. *Journal of Geophysical Research*, 98(A12):21203–21216, 1993. ISSN 0148-0227. doi: 10.1029/93ja02586. URL http://doi.wiley.com/10.1029/93JA02586.

[153] Bruce T. Tsurutani, Olga P. Verkhoglyadova, Gurbax S. Lakhina, and Satoshi Yagitani. Properties of dayside outer zone chorus during HILDCAA events: Loss of energetic electrons. *Journal of Geophysical Research: Space Physics*, 114(A3), mar 2009. ISSN 01480227. doi: 10.1029/2008JA013353. URL http://doi.wiley.com/10.1029/2008JA013353.

[154] Bruce T. Tsurutani, Gurbax S. Lakhina, and Olga P. Verkhoglyadova. Energetic electron (>10 keV) microburst precipitation, ˜5-15 s X-ray pulsations, chorus, and wave-particle interactions: A review. *Journal of Geophysical Research: Space Physics*, 118(5):2296–2312, may 2013. ISSN 21699380. doi: 10.1002/jgra.50264. URL http://doi.wiley.com/10.1002/jgra.50264.

[155] C. Vocks, C. Salem, R. P. Lin, and G. Mann. Electron Halo and Strahl Formation in the Solar Wind by Resonant Interaction with Whistler Waves. *The Astrophysical Journal*, 627(1):540–549, jul 2005. ISSN 0004-637X. doi: 10.1086/430119. URL http://stacks.iop.org/0004-637X/627/i=1/a=540.

[156] J. Vranjes and S. Poedts. Solar nanoflares and other smaller energy release events as growing drift waves. *Physics of Plasmas*, 16(9):092902, sep 2009. ISSN 1070-664X. doi: 10.1063/1.3224037. URL http://aip.scitation.org/doi/10.1063/1.3224037.

[157] J. Vranjes and S. Poedts. Electric fields in solar magnetic structures due to gradient-driven instabilities: Heating and acceleration of particles. *Monthly Notices of the Royal Astronomical Society*, 400(4):2147–2152, 2009. ISSN 00358711. doi: 10.1111/j.1365-2966.2009.15612.x.

[158] J. Vranjes and S. Poedts. Kinetic instability of drift-Alfvén waves in solar corona and stochastic heating. *Astrophysical Journal*, 719(2):1335–1342, 2010. ISSN 15384357. doi: 10.1088/0004-637X/719/2/1335.

[159] J. Vranjes and S. Poedts. Drift waves in the corona: Heating and acceleration of ions at frequencies far below the gyrofrequency. *Monthly Notices of the Royal Astronomical Society*, 408(3):1835–1839, 2010. ISSN 00358711. doi: 10.1111/j.1365-2966.2010.17249.x.

[160] G. N. Watson. *A Treatise on the Theory of Bessel Functions*. Cambridge University Press, feb 1995.

[161] J. A. Wesson. Sawtooth reconnection. *Nuclear Fusion*, 30(12):2545–2549, dec 1990. ISSN 17414326. doi: 10.1088/0029-5515/30/12/008. URL http://stacks.iop.org/0029-5515/30/i=12/a=008?key=crossref.2bd9a8474378a2009ca09302dbc9d503.

[162] J. R. Wygant, C. A. Cattell, R. Lysak, Y. Song, J. Dombeck, J. McFadden, F. S. Mozer, C. W. Carlson, G. Parks, E. A. Lucek, A. Balogh, M. Andre,

H. Reme, M. Hesse, and C. Mouikis. Cluster observations of an intense normal component of the electric field at a thin reconnecting current sheet in the tail and its role in the shock-like acceleration of the ion fluid into the separatrix region. *Journal of Geophysical Research: Space Physics*, 110 (A9):1–30, sep 2005. ISSN 01480227. doi: 10.1029/2004JA010708. URL http://doi.wiley.com/10.1029/2004JA010708.

[163] M. Yamada, F. M. Levinton, N. Pomphrey, R. Budny, J. Manickam, and Y. Nagayama. Investigation of magnetic reconnection during a sawtooth crash in a high-temperature tokamak plasma. *Physics of Plasmas*, 1(10): 3269–3276, oct 1994. ISSN 1070664X. doi: 10.1063/1.870479. URL http://aip.scitation.org/doi/10.1063/1.870479.

[164] Masaaki Yamada, Hantao Ji, Scott Hsu, Troy Carter, Russell Kulsrud, and Fedor Trintchouk. Experimental investigation of the neutral sheet profile during magnetic reconnection. *Physics of Plasmas*, 7(5):1781–1787, may 2000. ISSN 1070-664X. doi: 10.1063/1.873999. URL http://aip.scitation.org/doi/10.1063/1.873999.

[165] Masaaki Yamada, Russell Kulsrud, and Hantao Ji. Magnetic reconnection. *Reviews of Modern Physics*, 82(1):603–664, mar 2010. ISSN 0034-6861. doi: 10.1103/RevModPhys.82.603. URL https://link.aps.org/doi/10.1103/RevModPhys.82.603.

[166] Masaaki Yamada, Jongsoo Yoo, Jonathan Jara-Almonte, Hantao Ji, Russell M. Kulsrud, and Clayton E. Myers. Conversion of magnetic energy in the magnetic reconnection layer of a laboratory plasma. *Nature Communications*, 5(May), 2014. ISSN 20411723. doi: 10.1038/ncomms5774.

[167] Kane S. Yee. Numerical Solution of Initial Boundary Value Problems Involving Maxwell's Equations in Isotropic Media. *IEEE Transactions on Antennas and Propagation*, 14(3):302–307, may 1966. ISSN 15582221. doi: 10.1109/TAP.1966.1138693. URL https://www.taylorfrancis.com/books/9781351465953/chapters/10.1201/9781315137650-6http://ieeexplore.ieee.org/document/1138693/.

[168] Jongsoo Yoo, Masaaki Yamada, Hantao Ji, and Clayton E. Myers. Observation of Ion Acceleration and Heating during Collisionless Magnetic Reconnection in a Laboratory Plasma. *Physical Review Letters*, 110(21):215007, may 2013. ISSN 0031-9007. doi: 10.1103/PhysRevLett.110.215007. URL https://link.aps.org/doi/10.1103/PhysRevLett.110.215007.

[169] Young Dae Yoon and Paul M. Bellan. A generalized two-fluid picture of non-driven collisionless reconnection and its relation to whistler waves. *Physics of Plasmas*, 24(5):052114, may 2017. ISSN 1070-664X. doi: 10.1063/1.4982812. URL http://aip.scitation.org/doi/10.1063/1.4982812.

[170] Young Dae Yoon and Paul M. Bellan. An intuitive two-fluid picture of spontaneous 2D collisionless magnetic reconnection and whistler wave generation. *Physics of Plasmas*, 25(5):055704, may 2018. ISSN 1070-664X. doi: 10.1063/1.5016345. URL http://dx.doi.org/10.1063/1.5016345http://aip.scitation.org/doi/10.1063/1.5016345.

[171] Young Dae Yoon and Paul M. Bellan. Fast Ion Heating in Transient Collisionless Magnetic Reconnection via an Intrinsic Stochastic Mechanism. *The Astrophysical Journal Letters*, 868(2): L31, nov 2018. ISSN 2041-8213. doi: 10.3847/2041-8213/aaf0a3. URL http://stacks.iop.org/2041-8205/868/i=2/a=L31?key=crossref.559ad6f22dfdfcdfe3b6e580c7240456.

[172] S. You. A field theory approach to the evolution of canonical helicity and energy. *Physics of Plasmas*, 23(7):72108, jul 2016. ISSN 1070-664X. doi: 10.1063/1.4956465. URL http://aip.scitation.org/doi/10.1063/1.4956465.

[173] Gunsu Soonshin Yun. *Dynamics of Plasma Structures Interacting with External and Self-Generated Magnetic Fields*. PhD thesis, California Institute of Technology, 2008.

[174] G. P. Zank, J. A. le Roux, G. M. Webb, A. Dosch, and O. Khabarova. PARTICLE ACCELERATION VIA RECONNECTION PROCESSES IN THE SUPERSONIC SOLAR WIND. *The Astrophysical Journal*, 797 (1):28, nov 2014. ISSN 1538-4357. doi: 10.1088/0004-637X/797/1/28. URL http://stacks.iop.org/0004-637X/797/i=1/a=28?key=crossref.ab621007c24087e86cee6e20be7d3561.

[175] G. P. Zank, P. Hunana, P. Mostafavi, J. A.Le Roux, Gang Li, G. M. Webb, O. Khabarova, A. Cummings, E. Stone, and R. Decker. DIFFUSIVE SHOCK ACCELERATION and RECONNECTION ACCELERATION PROCESSES. *Astrophysical Journal*, 814(2):137, 2015. ISSN 15384357. doi: 10.1088/0004-637X/814/2/137. URL http://dx.doi.org/10.1088/0004-637X/814/2/137.

[176] Daniel Zwillinger. *Table of Integrals, Series, and Products*. Elsevier, 2015. ISBN 9780123849335. doi: 10.1016/C2010-0-64839-5. URL https://linkinghub.elsevier.com/retrieve/pii/C20100648395.

Appendix A

WHISTLER WAVE ANALYTICAL SOLUTION

The analytical solution for a whistler wave driven by a ring current source will now be derived. Relevant normalizations are described in Table 2.1. It will be assumed that all linear quantities have the dependence $\sim e^{i\mathbf{k}\cdot\mathbf{x}-i\omega t}$. The linearized dimensionless equations are, under uniform $\mathbf{B}_0 = \hat{z}$,

$$\nabla \times \mathbf{E} = -\frac{\partial \mathbf{B}}{\partial t}, \tag{A.1}$$

$$\nabla \times \mathbf{B} = -\mathbf{u}_e + I\delta\left(r-a\right)\delta\left(z\right)e^{-i\Omega t}\hat{\phi}, \tag{A.2}$$

$$\frac{\partial \mathbf{u}_e}{\partial t} = -\mathbf{E} - \mathbf{u}_e \times \hat{z}, \tag{A.3}$$

where $I\delta\left(r-a\right)\delta\left(z\right)e^{-i\Omega t}\hat{\phi}$ is the ring current source with frequency Ω, normalized source strength I, and radius a. Also, $D\mathbf{u}_e/Dt = \partial\mathbf{u}_e/\partial t + \mathbf{u}_e \cdot \nabla\mathbf{u}_e \simeq \partial\mathbf{u}_e/\partial t$ because $\mathbf{u}_e$ is a linear quantity. Because the background magnetic field and the ring current source has no dependence on ϕ, there is cylindrical symmetry; therefore, the wavevector $\mathbf{k} = k_r\hat{r} + k_z\hat{z}$, i.e., $k_\phi = 0$, and $k^2 = k_r^2 + k_z^2$. Fourier analyzing in space, the source term $S\left(\mathbf{r}\right) = \delta\left(r-a\right)\delta\left(z\right)$ turns into

$$S\left(\mathbf{k}\right) = \int_{r=0}^{\infty}\int_{\phi=0}^{2\pi}\int_{z=-\infty}^{\infty}\delta\left(r-a\right)\delta\left(z\right)e^{-ik_r r\cos(k_\phi-\phi)-ik_z z}r\,dr\,d\phi\,dz, \tag{A.4}$$

$$= \int_{r=0}^{\infty}\int_{\phi=0}^{2\pi}\delta\left(r-a\right)e^{-ik_r r\cos\phi}r\,dr\,d\phi, \tag{A.5}$$

$$= \int_{\phi=0}^{2\pi} a e^{-ik_r a\cos\phi}\,d\phi, \tag{A.6}$$

$$= 2\pi a J_0\left(k_r a\right), \tag{A.7}$$

where J_n is the Bessel function of the first kind of order n. Fourier analyzing the time dependence of the source,

$$\int_{-\infty}^{\infty} e^{-i\Omega t+i\omega t}\,dt = 2\pi\delta\left(\Omega-\omega\right). \tag{A.8}$$

Thus, Fourier analyzing the relevant equations, i.e., $\nabla \longrightarrow i\mathbf{k}$ and $\partial/\partial t \longrightarrow -i\omega$, gives

$$\mathbf{k}\times\mathbf{E} = \omega\mathbf{B}, \tag{A.9}$$

$$i\mathbf{k}\times\mathbf{B} = -\mathbf{u}_e + I\left(2\pi\right)^2 a J_0\left(k_r a\right)\delta\left(\Omega-\omega\right)\hat{\phi}, \tag{A.10}$$

$$-i\omega\mathbf{u}_e = -\mathbf{E} - \mathbf{u}_e\times\hat{z}. \tag{A.11}$$

We will now define $I(2\pi)^2 aJ_0(k_r a)\delta(\Omega-\omega)=\alpha$ to reduce clutter. Taking $\mathbf{k}\times$ of the Eq. A.10:

$$i\mathbf{k}\times(\mathbf{k}\times\mathbf{B}) = -\mathbf{k}\times\mathbf{u}_e + \alpha\mathbf{k}\times\hat{\phi}, \tag{A.12}$$

$$-ik^2\mathbf{B} = -\mathbf{k}\times\mathbf{u}_e + \alpha k_r\hat{z} - \alpha k_z\hat{r}, \tag{A.13}$$

where $\nabla\cdot\mathbf{B} = i\mathbf{k}\cdot\mathbf{B} = 0$ was used.

Now taking $\mathbf{k}\times$ of Eq. A.11 and using $\mathbf{k}\cdot\mathbf{u}_e = 0$ for incompressible electrons:

$$-i\omega\mathbf{k}\times\mathbf{u}_e = -\mathbf{k}\times\mathbf{E} - \mathbf{k}\times(\mathbf{u}_e\times\hat{z}), \tag{A.14}$$

$$-i\omega\mathbf{k}\times\mathbf{u}_e = -\omega\mathbf{B} - k_z\mathbf{u}_e + (\mathbf{k}\cdot\mathbf{u}_e)\hat{z}, \tag{A.15}$$

$$-i\omega\mathbf{k}\times\mathbf{u}_e = -\omega\mathbf{B} - k_z\mathbf{u}_e. \tag{A.16}$$

Using Eq. A.13 and Eq. A.10,

$$-i\omega\left(ik^2\mathbf{B} + \alpha k_r\hat{z} - \alpha k_z\hat{r}\right) = -\omega\mathbf{B} - k_z\left(-i\mathbf{k}\times\mathbf{B} + \alpha\hat{\phi}\right), \tag{A.17}$$

$$\omega\left(k^2+1\right)\mathbf{B} = ik_z\mathbf{k}\times\mathbf{B} - i\alpha\omega k_z\hat{r} - \alpha k_z\hat{\phi} + i\alpha\omega k_r\hat{z}, \tag{A.18}$$

$$\omega\left(k^2+1\right)\mathbf{B} = ik_z\mathbf{k}\times\mathbf{B} + \mathbf{C}, \tag{A.19}$$

where

$$\mathbf{C} = -i\alpha\omega k_z\hat{r} - \alpha k_z\hat{\phi} + i\alpha\omega k_r\hat{z}. \tag{A.20}$$

Taking $\mathbf{k}\times$ of Eq. A.19 and using Eq. A.19,

$$\omega\left(k^2+1\right)\mathbf{k}\times\mathbf{B} = ik_z\mathbf{k}\times(\mathbf{k}\times\mathbf{B}) + \mathbf{k}\times\mathbf{C}, \tag{A.21}$$

$$\omega\left(k^2+1\right)\mathbf{k}\times\mathbf{B} = -ik_zk^2\mathbf{B} + \mathbf{k}\times\mathbf{C}, \tag{A.22}$$

$$\omega\left(k^2+1\right)ik_z\mathbf{k}\times\mathbf{B} = k_z^2k^2\mathbf{B} + ik_z\mathbf{k}\times\mathbf{C}, \tag{A.23}$$

$$\omega\left(k^2+1\right)\left[\omega\left(k^2+1\right)\mathbf{B} - \mathbf{C}\right] = k_z^2k^2\mathbf{B} + ik_z\mathbf{k}\times\mathbf{C}, \tag{A.24}$$

$$\left[\omega^2\left(k^2+1\right)^2 - k_z^2k^2\right]\mathbf{B} = \omega\left(k^2+1\right)\mathbf{C} + ik_z\mathbf{k}\times\mathbf{C}, \tag{A.25}$$

$$\mathbf{B} = \frac{\omega\left(k^2+1\right)\mathbf{C} + ik_z\mathbf{k}\times\mathbf{C}}{\omega^2\left(k^2+1\right)^2 - k_z^2k^2}. \tag{A.26}$$

Let us examine the ϕ direction. Since

$$(\mathbf{k}\times\mathbf{C})_\phi = k_zC_r - k_rC_z, \tag{A.27}$$

$$= -i\alpha\omega\left(k_z^2 + k_r^2\right), \tag{A.28}$$

$$= -i\alpha\omega k^2, \tag{A.29}$$

it follows that

$$\omega\left(k^2+1\right)\mathbf{C}+ik_z\mathbf{k}\times\mathbf{C}=-\alpha\omega\left(k^2+1\right)k_z+k_z\alpha\omega k^2, \tag{A.30}$$

$$=\alpha\omega k_z, \tag{A.31}$$

$$=I\left(2\pi\right)^2 aJ_0\left(k_r a\right)\delta\left(\Omega-\omega\right)\omega k_z. \tag{A.32}$$

The solution for B_ϕ is thus

$$B_\phi\left(\omega,\mathbf{k}\right)=\frac{-I\left(2\pi\right)^2 a\delta\left(\Omega-\omega\right)\omega J_0\left(k_r a\right)k_z}{\omega^2\left(k^2+1\right)^2-k_z^2k^2}. \tag{A.33}$$

The inverse transform in space gives

$$B_\phi\left(\omega,\mathbf{r}\right)=-I\left(2\pi\right)^2 a\delta\left(\Omega-\omega\right)\omega\left(\frac{1}{2\pi}\right)^3 \tag{A.34}$$

$$\times\int_{k_r=0}^{\infty}\int_{k_\phi=0}^{2\pi}\int_{k_z=-\infty}^{\infty}\frac{J_0\left(k_r a\right)k_z}{\omega^2\left(k^2+1\right)^2-k_z^2k^2}e^{ik_r r\cos\left(k_\phi-\phi\right)}e^{ik_z z}k_r dk_r dk_\phi dk_z, \tag{A.35}$$

$$=Ia\delta\left(\Omega-\omega\right)\omega i\frac{\partial}{\partial z}\int_{k_r=0}^{\infty}\int_{k_z=-\infty}^{\infty}\frac{J_0\left(k_r a\right)J_0\left(k_r r\right)k_r}{\omega^2\left(k^2+1\right)^2-k_z^2k^2}e^{ik_z z}dk_r dk_z. \tag{A.36}$$

Let us now do a contour integral for the k_z integral. Solving for the poles:

$$\omega^2\left(k^2+1\right)^2-k_z^2k^2=0, \tag{A.37}$$

$$\omega^2\left(k^4+2k^2+1\right)-k_z^2k^2=0, \tag{A.38}$$

$$\omega^2\left(k_z^2+k_r^2\right)^2+2\omega^2\left(k_z^2+k_r^2\right)+\omega^2-k_z^2\left(k_z^2+k_r^2\right)=0, \tag{A.39}$$

$$\omega^2k_z^4+2\omega^2k_z^2k_r^2+\omega^2k_r^4+2\omega^2k_z^2+2\omega^2k_r^2+\omega^2-k_z^4-k_z^2k_r^2=0, \tag{A.40}$$

$$\left(\omega^2-1\right)k_z^4+\left(2\omega^2k_r^2+2\omega^2-k_r^2\right)+\omega^2k_r^4+2\omega^2k_r^2+\omega^2=0, \tag{A.41}$$

$$\left(\omega^2-1\right)k_z^4+\left(2\omega^2\left[1+k_r^2\right]-k_r^2\right)+\omega^2\left(1+k_r^2\right)^2=0, \tag{A.42}$$

whose solution for k_z is

$$k_z^2=\frac{-2\omega^2\left[1+k_r^2\right]+k_r^2\pm\sqrt{\left(2\omega^2\left[1+k_r^2\right]-k_r^2\right)^2-4\left(\omega^2-1\right)\omega^2\left(1+k_r^2\right)^2}}{2\left(\omega^2-1\right)}. \tag{A.43}$$

Here, the determinant is

$$D = \left(2\omega^2\left[1+k_r^2\right]-k_r^2\right)^2 - 4\omega^2\left(\omega^2-1\right)\left(1+k_r^2\right)^2, \tag{A.44}$$

$$= 4\omega^4\left(1+k_r^2\right)^2 - 4\omega^2\left(1+k_r^2\right)k_r^2 + k_r^4 - 4\omega^4\left(1+k_r^2\right)^2 + 4\omega^2\left(1+k_r^2\right)^2, \tag{A.45}$$

$$= -4\omega^2\left(1+k_r^2\right)k_r^2 + k_r^4 + 4\omega^2\left(1+k_r^2\right)^2, \tag{A.46}$$

$$= -4\omega^2\left(1+k_r^2\right)\left(k_r^2-1-k_r^2\right) + k_r^4, \tag{A.47}$$

$$= 4\omega^2\left(1+k_r^2\right) + k_r^4. \tag{A.48}$$

Therefore, there exist 4 poles at

$$k_z = \pm\sqrt{\frac{2\omega^2\left(1+k_r^2\right)-k_r^2 \pm \sqrt{4\omega^2\left(1+k_r^2\right)+k_r^4}}{2\left(1-\omega^2\right)}}. \tag{A.49}$$

To check the complexity of the poles, we need to check the following:

$$2\omega^2\left(1+k_r^2\right)-k_r^2 < \sqrt{4\omega^2\left(1+k_r^2\right)+k_r^4}, \tag{A.50}$$

in which case there are at least two imaginary poles. The right-hand side is always positive, so if the following is true,

$$2\omega^2\left(1+k_r^2\right) > k_r^2, \tag{A.51}$$

$$\omega^2 > \frac{k_r^2}{2\left(1+k_r^2\right)}, \tag{A.52}$$

then $2\omega^2\left(1+k_r^2\right)-k_r^2$ is also positive. In this case, by squaring both sides Eq. A.50,

$$4\omega^4\left(1+k_r^2\right)^2 - 4\omega^2k_r^2\left(1+k_r^2\right) + k_r^4 < 4\omega^2\left(1+k_r^2\right) + k_r^4, \tag{A.53}$$

$$4\omega^4\left(1+k_r^2\right) - 4\omega^2k_r^2 < 4\omega^2, \tag{A.54}$$

$$4\omega^4\left(1+k_r^2\right) < 4\omega^2\left(1+k_r^2\right), \tag{A.55}$$

$$\omega^2 < 1, \tag{A.56}$$

so for $\frac{k_r^2}{2\left(1+k_r^2\right)} < \omega^2 < 1$, two poles are real and two poles are imaginary.

In the opposite case where

$$\omega^2 < \frac{k_r^2}{2\left(1+k_r^2\right)}, \tag{A.57}$$

two poles are real if and only if

$$\left|2\omega^2\left(1+k_r^2\right)-k_r^2\right| < \sqrt{4\omega^2\left(1+k_r^2\right)+k_r^4}, \tag{A.58}$$

$$k_r^2-2\omega^2\left(1+k_r^2\right) < \sqrt{4\omega^2\left(1+k_r^2\right)+k_r^4}, \tag{A.59}$$

which actually has the solution $\omega^2 < 1$.

Therefore, there are two real and two imaginary poles, respectively, for $\omega^2 < 1$, which is true by assumption for whistler waves (recall from Table 2.1 that $\omega^2 < 1$ means $\omega^2 < \omega_{ce}^2$ in dimensional quantities, which is true for whistler waves).

Therefore, there exist 4 simple poles which will be called A, $-A$, iB, and $-iB$, where $A, B > 0$. The integral in Eq. A.36 now becomes

$$B_\phi(\omega,\mathbf{r}) = Ia\delta(\Omega-\omega)\,\omega i \tag{A.60}$$

$$\times\int_{k_r=0}^{\infty} dk_r J_0(k_r a)\,k_r e^{ik_r r\cos\left(k_\phi-\phi\right)} \tag{A.61}$$

$$\times\frac{\partial}{\partial z}\int_{k_z=-\infty}^{\infty} dk_z \frac{e^{ik_z z}}{\left(1-\omega^2\right)(k_z-A)(k_z+A)(k_z-iB)(k_z+iB)}. \tag{A.62}$$

The $\left(1-\omega^2\right)$ term in the denominator exists because the coefficient of the quadratic term of equation for k_z is $\left(1-\omega^2\right)$. Doing the complex contour integral from $k_z=-\infty$ to $+\infty$, we pick up half the residues at A and $-A$, and the full residue at iB. With respect to the k_z integral, the residues at A, $-A$, and iB are, respectively,

$$Res(A) = \frac{e^{iAz}}{\left(1-\omega^2\right)(A+A)(A-iB)(A+iB)}, \tag{A.63}$$

$$= \frac{e^{iAz}}{2A\left(1-\omega^2\right)\left(A^2+B^2\right)}, \tag{A.64}$$

$$Res(-A) = \frac{e^{-iAz}}{-2A\left(1-\omega^2\right)\left(A^2+B^2\right)}, \tag{A.65}$$

$$Res(iB) = \frac{e^{-Bz}}{\left(1-\omega^2\right)(iB+A)(iB-A)2iB}, \tag{A.66}$$

$$= \frac{e^{-Bz}}{-2iB\left(1-\omega^2\right)\left(A^2+B^2\right)}. \tag{A.67}$$

It can be inferred from Eq. A.49 that

$$A^2 = \frac{2\omega^2\left(1+k_r^2\right) - k_r^2 + \sqrt{4\omega^2\left(1+k_r^2\right)+k_r^4}}{2\left(1-\omega^2\right)}, \tag{A.68}$$

$$B^2 = \frac{-2\omega^2\left(1+k_r^2\right) + k_r^2 + \sqrt{4\omega^2\left(1+k_r^2\right)+k_r^4}}{2\left(1-\omega^2\right)}, \tag{A.69}$$

$$A^2 + B^2 = \frac{\sqrt{4\omega^2\left(1+k_r^2\right)+k_r^4}}{1-\omega^2}. \tag{A.70}$$

Thus, the k_z integral evaluates to

$$\frac{\pi i}{\sqrt{4\omega^2\left(1+k_r^2\right)+k_r^4}}\left(\frac{e^{iAz}-e^{-iAz}}{2A} - \frac{e^{-Bz}}{iB}\right) = \frac{\pi}{\sqrt{4\omega^2\left(1+k_r^2\right)+k_r^4}}\left(-\frac{\sin Az}{A} - \frac{e^{-Bz}}{B}\right). \tag{A.71}$$

Doing the partial z derivative,

$$\frac{\pi}{\sqrt{4\omega^2\left(1+k_r^2\right)+k_r^4}}\left(-\cos Az + e^{-Bz}\right). \tag{A.72}$$

The solution for B_ϕ is now

$$B_\phi(\omega, \mathbf{r}) = -I\pi a\delta(\Omega-\omega)\,\omega i\int_{k_r=0}^{\infty} \frac{J_0(k_r a)\,J_0(k_r r)\,k_r}{\sqrt{4\omega^2\left(1+k_r^2\right)+k_r^4}}\left[\cos(Az) - e^{-Bz}\right]dk_r. \tag{A.73}$$

Because $A, B > 0$, this is a sum of an oscillating solution and an evanescent solution.

Figure A.1 shows the analytical solution for B_ϕ in Eq. A.73 for a source with $\omega = 0.35$, $a = 1$, and an arbitrary amplitude. The red vertical line represents the location and extent of the ring current source. The numerical integration was carried out using the scipy.integrate.quad package in Python 3.7. The result of the integral at $r = 0$ (black horizontal dashed line) does not converge fast enough and is thus dubious. The cone-like structures emanating from the source are called "resonance cones" [52]. These arise from the frequency dependence of the plasma dielectric tensor; their angles have the following relation in dimensional quantities [52]:

$$\sin^2\theta = \frac{\Omega^2\left(\omega_{pe}^2 + \omega_{ce}^2 - \Omega^2\right)}{\omega_{ce}^2\omega_{pe}^2}, \tag{A.74}$$

where θ is the cone angle, ω_{pe} is the electron plasma frequency, ω_{ce} is the electron cyclotron frequency, and Ω is the frequency of the source. In the limit $\omega_{pe} \gg \omega_{ce}$,

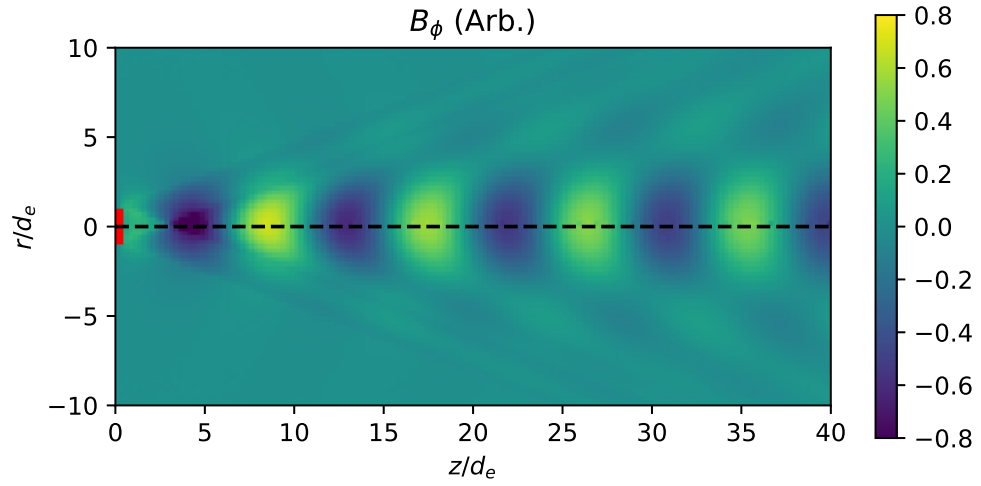

Figure A.1: Analytical solution for B_ϕ in Eq. A.73 of an arbitrary magnitude. The red vertical line at $z = 0$ represents the ring current source. The numerical integration of Eq. A.73 is dubious at $r = 0$ (black dashed line).

which is equivalent to ignoring the displacement current (see Eq. 3.16), and $\Omega \ll \omega_{ce}$ for whistler waves, the relation becomes

$$\sin^2\theta = \frac{\Omega^2}{\omega_{ce}^2}, \tag{A.75}$$

which shows that $\theta = 0.35 = 21^\circ$ for $\Omega/\omega_{ce} = 0.35$. The cone-angle in Fig. A.1 is approximately $\theta = \arctan(9/25) = 0.35$, which agrees with the prediction.

Reverting back to dimensionless quantities, the whistler dispersion relation in Eq. 2.63 can be expressed as an equation for k_z:

$$\Omega^2 = \frac{k_z^2\left(k_z^2 + k_r^2\right)}{\left(1 + k_r^2 + k_z^2\right)^2}, \tag{A.76}$$

$$\Omega^2\left(1 + k_r^2 + k_z^2\right)^2 = k_z^4 + k_z^2 k_r^2, \tag{A.77}$$

$$\Omega^2\left(1 + k_r^2\right)^2 + 2\Omega^2\left(1 + k_r^2\right)k_z^2 + \Omega^2 k_z^4 = k_z^4 + k_z^2 k_r^2, \tag{A.78}$$

$$\left(1 - \Omega^2\right)k_z^4 + \left[k_r^2 - 2\Omega^2\left(1 + k_r^2\right)\right]k_z^2 - \Omega^2\left(1 + k_r^2\right)^2 = 0. \tag{A.79}$$

The solution for k_z is

$$k_z^2 = \frac{2\Omega^2\left(1 + k_r^2\right) - k_r^2 + \sqrt{k_r^4 + 4\Omega^2\left(1 + k_r^2\right)}}{2(1 - \Omega^2)}, \tag{A.80}$$

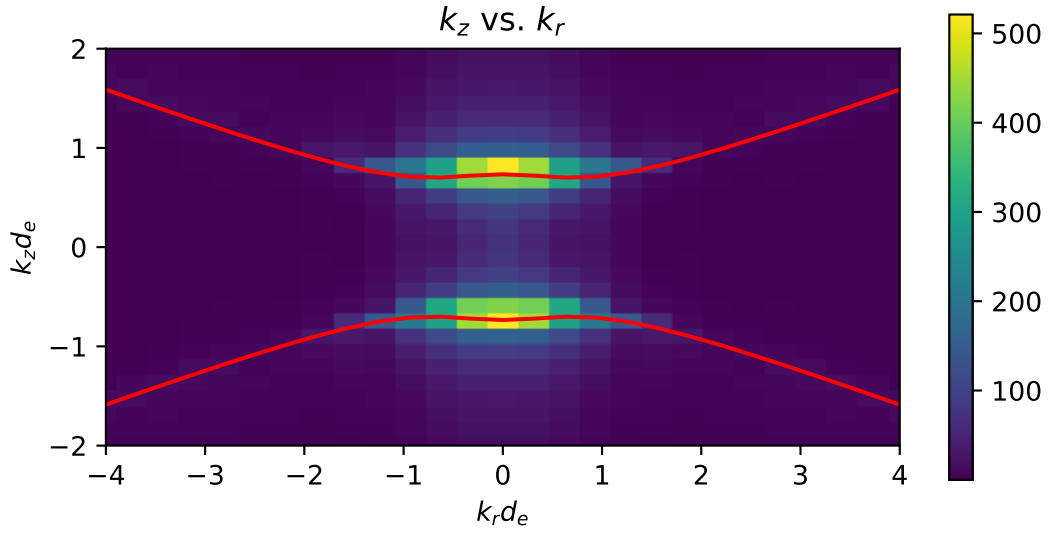

Figure A.2: The fast Fourier transform of the result in Fig. A.1. The red lines represent the dispersion relation in Eq. A.80 for $\Omega = 0.35$.

which, for a particular value of Ω, yields a relation between k_z and k_r.

Figure A.2 shows the fast Fourier transform of the result in Fig. A.1. The red lines represent the dispersion relation in Eq. A.80 for $\Omega = 0.35$. It can be seen that the areas with high magnitude follow the red lines. The match is not perfect, of course, because the dispersion relation is based on plane waves.

An analytical solution for a whistler wave excited by a delta function ring current source has thus been presented.

Appendix B

ALGORITHM TEST USING WHISTLER WAVES

The algorithm presented in Section 2.3 should yield whistler waves similar to that in Appendix A. A 3D code that mimics the current source in Appendix A.73 was constructed.

Because it is difficult to realize a delta function in a numerical simulation, the current source was approximated by a Gaussian of the form

$$j_\phi = \hat{\phi}\epsilon \exp\left(-\frac{(r-a)^2 + z^2}{2\sigma^2}\right) \sin \Omega t, \tag{B.1}$$

where ϵ is the current amplitude, a is the ring radius, and σ is the ring thickness. A Cartesian grid of dimensions $(x, y, z) = (80, 80, 320) = (20, 20, 80)d_e$ was used, and the time step was $\Delta t = 0.05$. The source parameters were $a = 1$, $\sigma = 0.5$, $\epsilon = 0.1$, and $\Omega = 0.35$. Periodic boundary conditions were used.

Figure B.1 shows B_ϕ from the numerical simulation at $t = 80|\omega_{ce}|^{-1}$. The general spatial structure is similar to that in Fig. A.1, except for at $r = 0$. The cone angle is slightly wider ($\theta = 0.4$), which may be due to the fact that here the current source is not a perfect delta function.

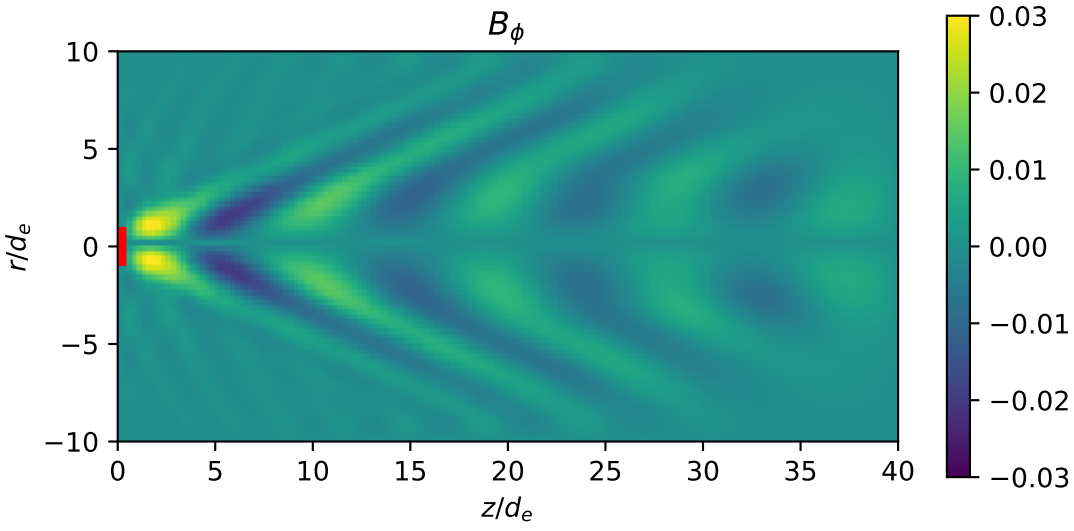

Figure B.1: B_ϕ at $t = 80|\omega_{ce}|^{-1}$

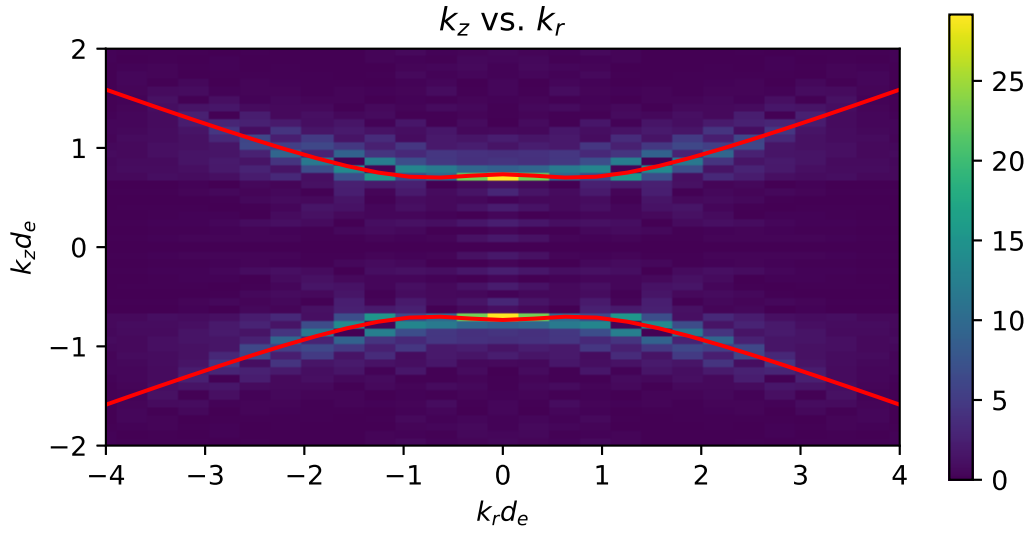

Figure B.2: The fast Fourier transform of the results in Fig. B.1. The red lines represent the dispersion relation in Eq. A.80 for $\Omega = 0.35$.

Figure B.2 shows the fast Fourier transform of the results in Fig. B.1. The red lines represent the dispersion relation in Eq. A.80 for $\Omega = 0.35$. The regions of high magnitude follow the red lines, arguably more closely than those in Fig. A.2.

It has thus been confirmed that the algorithm and simulation described in Section 2.3 produce whistler waves as expected.

Appendix C

CANONICAL HELICITY DENSITY AND THE LAGRANGIAN DENSITY IN ELECTRON-MAGNETOHYDRODYNAMICS

Relevant normalizations are carried out according to Section 2.3. The normalized electron canonical momentum and canonical vorticity are defined as, respectively,

$$\mathbf{P}_e = \mathbf{u}_e - \mathbf{A}, \tag{C.1}$$

$$\mathbf{Q}_e = \nabla \times \mathbf{P}_e, \tag{C.2}$$

$$= \nabla \times \mathbf{u}_e - \mathbf{B}. \tag{C.3}$$

The normalized electron equation of motion is

$$\frac{\partial \mathbf{u}_e}{\partial t} + \mathbf{u}_e \cdot \nabla \mathbf{u}_e = -\mathbf{E} - \mathbf{u}_e \times \mathbf{B} - \nabla p_e, \tag{C.4}$$

or, in terms of $\mathbf{Q}_e$,

$$\frac{\partial \mathbf{u}_e}{\partial t} + \nabla \left(\frac{u_e^2}{2} \right) = -\mathbf{E} + \mathbf{u}_e \times \mathbf{Q}_e - \nabla p_e, \tag{C.5}$$

where scalar electron pressure and uniform electron density were assumed. Also, because both ion and electron densities are assumed to be uniform, the electrostatic potential $\phi = 0$, so $\mathbf{E} = -\partial \mathbf{A}/\partial t$. Examining the time evolution of the normalized electron canonical helicity density $\kappa_Q = \mathbf{P}_e \cdot \mathbf{Q}_e$,

$$\frac{\partial \kappa_Q}{\partial t} = \frac{\partial \mathbf{P}_e}{\partial t} \cdot \mathbf{Q}_e + \mathbf{P}_e \cdot \frac{\partial \mathbf{Q}_e}{\partial t}, \tag{C.6}$$

$$= \left(\frac{\partial \mathbf{u}_e}{\partial t} - \frac{\partial \mathbf{A}}{\partial t} \right) \cdot \mathbf{Q}_e + \mathbf{P}_e \cdot \nabla \times (\mathbf{u}_e \times \mathbf{Q}_e), \tag{C.7}$$

$$= \left(\frac{\partial \mathbf{u}_e}{\partial t} + \mathbf{E} \right) \cdot \mathbf{Q}_e + \nabla \cdot ([\mathbf{u}_e \times \mathbf{Q}_e] \times \mathbf{P_e}) + \cancel{(\mathbf{u}_e \times \mathbf{Q}_e) \cdot (\nabla \times \mathbf{P}_e)}, \quad \mathbf{u}_e \times \mathbf{Q}_e \cdot \mathbf{Q}_e = 0 \tag{C.8}$$

$$= \left(-\nabla \left(\frac{u_e^2}{2} \right) + \cancel{\mathbf{u}_e \times \mathbf{Q}_e} - \nabla p_e \right) \cdot \mathbf{Q}_e + \nabla \cdot (\mathbf{Q}_e \left[\mathbf{u}_e \cdot \mathbf{P}_e \right] - \mathbf{u}_e \left[\mathbf{P}_e \cdot \mathbf{Q}_e \right]), \tag{C.9}$$

$$= \mathbf{Q}_e \cdot \nabla \left(-\frac{u_e^2}{2} - p_e + \mathbf{u}_e \cdot \mathbf{P}_e \right) - \mathbf{u}_e \cdot \nabla \kappa_Q, \tag{C.10}$$

where $\nabla \cdot \mathbf{Q}_e = \nabla \cdot \mathbf{u}_e = 0$ has been used. Expressing this in terms of the convective derivative and using $\mathbf{u}_e \cdot \mathbf{P}_e = u_e^2 - \mathbf{u}_e \cdot \mathbf{A}$,

$$\frac{D \kappa_Q}{D t} = \mathbf{Q}_e \cdot \nabla \left(\frac{u_e^2}{2} - p_e - \mathbf{u}_e \cdot \mathbf{A} \right). \tag{C.11}$$

Now we prove that $\mathcal{L} = \frac{u_e^2}{2} - p_e - \mathbf{u}_e \cdot \mathbf{A}$ is the Lagrangian density of the system. The Euler-Lagrange equation

$$\nabla_x L - \frac{D}{Dt}\nabla_u L = 0, \tag{C.12}$$

where $L(\mathbf{x}, \mathbf{u}_e, t) = \int \mathcal{L}(\mathbf{x}, \mathbf{u}_e, t)\, dV$ is the Lagrangian, must give the equation of motion of the system (Eq. C.4). ∇_x is the spatial gradient and ∇_u is the gradient in velocity space. Here,

$$\nabla_x L = \int \left[-\nabla_x p_e - \nabla_x (\mathbf{u}_e \cdot \mathbf{A})\right] dV, \tag{C.13}$$

$$= \int \left[-\nabla_x p_e - \mathbf{u}_e \cdot \nabla_x \mathbf{A} - \mathbf{u}_e \times (\nabla_x \times \mathbf{A})\right] dV, \tag{C.14}$$

$$= \int \left[-\nabla_x p_e - \mathbf{u}_e \cdot \nabla_x \mathbf{A} - \mathbf{u}_e \times \mathbf{B}\right] dV, \tag{C.15}$$

since only p_e and $\mathbf{A}$ are explicitly spatially dependent. Also,

$$\nabla_u L = \int \nabla_u \mathcal{L} dV, \tag{C.16}$$

$$= \int (\mathbf{u}_e - \mathbf{A})\, dV. \tag{C.17}$$

So,

$$\frac{D}{Dt}\nabla_u L = \int \frac{\partial}{\partial t}(\mathbf{u}_e - \mathbf{A})\, dV + \int (\mathbf{u}_e - \mathbf{A})(\mathbf{u}_e \cdot d\mathbf{s}), \tag{C.18}$$

$$= \int \left(\frac{\partial \mathbf{u}_e}{\partial t} - \frac{\partial \mathbf{A}}{\partial t}\right) dV + \int \nabla_x \cdot \left[\mathbf{u}_e (\mathbf{u}_e - \mathbf{A})\right] dV, \tag{C.19}$$

$$= \int \left(\frac{D\mathbf{u}_e}{Dt} + \mathbf{E} - \mathbf{u}_e \cdot \nabla_x \mathbf{A}\right) dV. \tag{C.20}$$

Therefore,

$$\nabla_x L - \frac{D}{Dt}\nabla_u L = \int \begin{bmatrix} -\nabla_x p_e - \mathbf{u}_e \cdot \nabla_x \mathbf{A} - \mathbf{u}_e \times \mathbf{B} \\ -\frac{D\mathbf{u}_e}{Dt} - \mathbf{E} + \mathbf{u}_e \cdot \nabla_x \mathbf{A} \end{bmatrix} dV, \tag{C.21}$$

$$= \int \left[-\nabla_x p_e - \mathbf{u}_e \times \mathbf{B} - \frac{D\mathbf{u}_e}{Dt} - \mathbf{E}\right] dV, \tag{C.22}$$

$$= 0. \tag{C.23}$$

Setting the integrand to zero gives us the original normalized equation of motion (Eq. C.4):

$$\frac{D\mathbf{u}_e}{Dt} = -\mathbf{E} - \mathbf{u}_e \times \mathbf{B} - \nabla p_e. \tag{C.24}$$

Therefore, $\mathcal{L}$ is the Lagrangian density of the system and

$$\frac{D\kappa_Q}{Dt} = \mathbf{Q}_e \cdot \nabla \mathcal{L}. \tag{C.25}$$

Also, integrating this equation over a volume and writing the total canonical helicity as $K_Q = \int_V \kappa_Q dV$,

$$\frac{DK_Q}{Dt} = \int_V \mathbf{Q}_e \cdot \nabla \mathcal{L} dV, \tag{C.26}$$

$$= \int_V \nabla \cdot (\mathbf{Q}_e \mathcal{L})\, dV, \tag{C.27}$$

$$= \oint_S \mathcal{L} \mathbf{Q}_e \cdot d\mathbf{s}. \tag{C.28}$$

Therefore, if $\mathbf{Q}_e$ does not penetrate the volume at the boundary, K_Q is a conserved quantity.

Appendix D

IMPLICIT PARTICLE INTEGRATOR

An algorithm [15] will now be illustrated that implicitly solves the particle equation of motion

$$m\frac{d\mathbf{v}}{dt} = q\mathbf{E} + q\mathbf{v}\times\mathbf{B}. \tag{D.1}$$

Defining $\mathbf{\Omega} = q\mathbf{B}/m$ and $\Sigma = q\mathbf{E}/m$,

$$\frac{d\mathbf{v}}{dt} = \Sigma + \mathbf{v}\times\mathbf{\Omega}. \tag{D.2}$$

Now, velocity is defined at integer time steps, and position is defined at half-integer time steps. The time derivative of the velocity is evaluated at the half-integer time step, i.e.,

$$\frac{\mathbf{v}_{t+1}-\mathbf{v}_t}{\Delta t} = f\left(\frac{\mathbf{v}_{t+1}+\mathbf{v}_t}{2}\right), \tag{D.3}$$

$$= \Sigma_{t+1/2} + \frac{\mathbf{v}_{t+1}+\mathbf{v}_t}{2}\times\mathbf{\Omega}_{t+1/2}. \tag{D.4}$$

This equation may be expressed as

$$\mathbf{v}_{t+1} + \mathbf{A}\times\mathbf{v}_{t+1} = \mathbf{C}, \tag{D.5}$$

where

$$\mathbf{A} = \frac{\mathbf{\Omega}_{t+1/2}\Delta t}{2}, \tag{D.6}$$

and

$$\mathbf{C} = \mathbf{v}_t + \Delta t\left(\Sigma_{t+1/2} + \frac{\mathbf{v}_t}{2}\times\mathbf{\Omega}_{t+1/2}\right). \tag{D.7}$$

Now, dotting Eq. D.5 with $\mathbf{A}$,

$$\mathbf{v}_{new}\cdot\mathbf{A} = \mathbf{C}\cdot\mathbf{A}. \tag{D.8}$$

Crossing Eq. D.5 with $\mathbf{A}$,

$$\mathbf{v}_{t+1}\times\mathbf{A} + (\mathbf{A}\times\mathbf{v}_{t+1})\times\mathbf{A} = \mathbf{C}\times\mathbf{A}, \tag{D.9}$$

$$\mathbf{v}_{t+1}\times\mathbf{A} + \mathbf{v}_{t+1}A^2 - \mathbf{A}\,(\mathbf{v}_{t+1}\cdot\mathbf{A}) = \mathbf{C}\times\mathbf{A}, \tag{D.10}$$

$$\mathbf{v}_{t+1} - \mathbf{C} + \mathbf{v}_{t+1}A^2 - \mathbf{A}\,(\mathbf{C}\cdot\mathbf{A}) = \mathbf{C}\times\mathbf{A}, \tag{D.11}$$

$$\mathbf{v}_{t+1} = \frac{\mathbf{C} + \mathbf{A}\,(\mathbf{C}\cdot\mathbf{A}) + \mathbf{C}\times\mathbf{A}}{1+A^2}, \tag{D.12}$$

which can be used to update a given $\mathbf{v}_t$.

The new position is given by

$$\mathbf{x}_{t+3/2} = \mathbf{x}_{t+1/2} + \mathbf{v}_{t+1}\Delta t. \tag{D.13}$$

Appendix E

HARRIS EQUILIBRIUM PLASMA SHEATH DERIVATION

The Harris equilibrium is a specific stationary solution of the Vlasov equation, Gauss's law, and Ampère's law [66]. It is assumed that the spatial dependence is only in the x-direction, i.e., only $\partial/\partial x$ is finite, and that $\mathbf{A} = A_z\hat{z}$. It then follows that $\mathbf{B} = B_y\hat{y}$ and $\mathbf{E} = E_x\hat{x}$. Equations to solve are

$$0 = v_x\frac{\partial f_\sigma}{\partial x} + \frac{q_\sigma}{m_\sigma}\left(\mathbf{E} + \mathbf{v}_\sigma \times \mathbf{B}\right)\cdot\frac{\partial f_\sigma}{\partial \mathbf{v}_\sigma}, \tag{E.1}$$

$$\frac{\partial E_x}{\partial x} = \frac{1}{\epsilon_0}\sum_\sigma q_\sigma \int f_\sigma d^3\mathbf{v}_\sigma, \tag{E.2}$$

$$\frac{\partial B_y}{\partial x} = \mu_0\sum_\sigma q_\sigma \int f_\sigma v_z d^3\mathbf{v}_\sigma. \tag{E.3}$$

In terms of the electrostatic and vector potentials ϕ and A_z,

$$0 = v_x\frac{\partial f_\sigma}{\partial x} + \frac{q_\sigma}{m_\sigma}\left(\mathbf{E} + \mathbf{v}_\sigma \times \mathbf{B}\right)\cdot\frac{\partial f_\sigma}{\partial \mathbf{v}_\sigma}, \tag{E.4}$$

$$\frac{\partial^2\phi}{\partial x^2} = -\frac{1}{\epsilon_0}\sum_\sigma q_\sigma \int f_\sigma d^3\mathbf{v}_\sigma, \tag{E.5}$$

$$\frac{\partial^2 A_z}{\partial x^2} = -\mu_0\sum_\sigma q_\sigma \int f_\sigma v_z d^3\mathbf{v}_\sigma. \tag{E.6}$$

Now, because the system is independent of y and z coordinates, the canonical momenta p_y and p_z are constants of the motion, as well as the total energy. In other words,

$$W = \frac{1}{2}m\left(v_x^2 + v_y^2 + v_z^2\right) + q\phi, \tag{E.7}$$

$$p_y = mv_y, \tag{E.8}$$

$$p_z = mv_z + qA_z \tag{E.9}$$

are constants of motion for each species. Now consider the distribution function

$$f_\sigma = \left(\frac{m_\sigma}{2\pi k_B T_\sigma}\right)^{3/2} n_0 \exp\left[-\frac{m_\sigma}{2k_B T_\sigma}\left(v_x^2 + v_y^2 + (v_z - V_\sigma)^2 + \frac{2q}{m_\sigma}\left(\phi - A_z V_\sigma\right)\right)\right], \tag{E.10}$$

where T_σ is the temperature of each species, n_0 is the reference density, and V_σ is the average velocity of each species in the z-direction. Because

$$v_x^2 + v_y^2 + (v_z - V_\sigma)^2 + \frac{2q_\sigma}{m_\sigma}(\phi - A_z V_\sigma) = \frac{2W}{m_\sigma} - \frac{2p_z}{m_\sigma} + V_\sigma^2 \tag{E.11}$$

is a function of constants of motion only, Eq. E.10 is a solution of Eq. E.4 by Liouville's theorem. Thus we have

$$\int f_\sigma d^3\mathbf{v} = n_0 \exp\left[-\frac{q_\sigma}{k_B T_\sigma}(\phi - A_z V_\sigma)\right], \tag{E.12}$$

$$\int v_z f_\sigma d^3\mathbf{v} = n_0 V_\sigma \exp\left[-\frac{q_\sigma}{k_B T_\sigma}(\phi - A_z V_\sigma)\right]. \tag{E.13}$$

Inserting these into Eqs. E.5 and E.6,

$$\frac{\partial^2\phi}{\partial x^2} = -\frac{en_0}{\epsilon_0}\left[\exp\left[-\frac{e}{k_B T_i}(\phi - A_z V_i)\right] - \exp\left[\frac{e}{k_B T_e}(\phi - A_z V_e)\right]\right], \tag{E.14}$$

$$\frac{\partial^2 A_z}{\partial x^2} = -\mu_0 e n_0\left[V_i \exp\left[-\frac{e}{k_B T_i}(\phi - A_z V_i)\right] - V_e \exp\left[\frac{e}{k_B T_e}(\phi - A_z V_e)\right]\right]. \tag{E.15}$$

It is now assumed that $V_i = -V_e = V$, which can be done by moving to a frame where the average velocities of ions and electrons are equal in magnitude and opposite. It is also assumed that $T_i = T_e = T$ for simplicity; the situation where $T_i \neq T_e$ is described in Ref. [164]. Then,

$$\frac{\partial^2\phi}{\partial x^2} = -\frac{en_0}{\epsilon_0}\exp\left[\frac{e}{k_B T}A_z V\right]\left(\exp\left[-\frac{e\phi}{k_B T}\right] - \exp\left[\frac{e\phi}{k_B T}\right]\right), \tag{E.16}$$

$$\frac{\partial^2 A_z}{\partial x^2} = -\mu_0 e n_0 V \exp\left[\frac{e}{k_B T}A_z V\right]\left[\exp\left[-\frac{e\phi}{k_B T}\right] + \exp\left[\frac{e\phi}{k_B T}\right]\right]. \tag{E.17}$$

Since the first equation is trivially solved by $\phi = 0$, the only equation to solve is

$$\frac{\partial^2 A_z}{\partial x^2} = -2\mu_0 e n_0 V \exp\left[\frac{e}{k_B T}A_z V\right]. \tag{E.18}$$

The solution to this equation is

$$A_z = -\frac{2k_B T}{eV}\ln\cosh\left(\frac{Vx}{\sqrt{2}c\lambda_D}\right), \tag{E.19}$$

where

$$\lambda_D = \left(\frac{1}{\lambda_{Di}^2} + \frac{1}{\lambda_{De}^2}\right)^{-\frac{1}{2}} = \sqrt{\frac{\epsilon_0 k_B T}{2n_0 e^2}} \tag{E.20}$$

is the Debye length.

Using Eq. E.19, the solution for the magnetic field is

$$B_y = -\frac{\partial A_z}{\partial x} = \frac{2k_BT}{ec}\sqrt{\frac{n_0e^2}{\epsilon_0 k_BT}}\tanh\left(\frac{Vx}{\sqrt{2}c\lambda_D}\right), \tag{E.21}$$

$$= 2\sqrt{\mu_0 n_0 k_BT}\tanh\left(\frac{Vx}{\sqrt{2}c\lambda_D}\right), \tag{E.22}$$

$$= B_0\tanh\left(\frac{Vx}{\sqrt{2}c\lambda_D}\right). \tag{E.23}$$

The magnitude of the equilibrium magnetic field illustrates that the magnetic pressure is balance by the thermal pressure, i.e.,

$$\frac{B_0^2}{2\mu_0} = 2n_0k_BT = p_i + p_e, \tag{E.24}$$

where p_i and p_e are ion and electron pressures, respectively.

Finally, inserting Eq. E.19 and $\phi = 0$ into Eq. E.12 gives the equilibrium density

$$n = n_0\cosh^{-2}\left(\frac{Vx}{\sqrt{2}c\lambda_D}\right), \tag{E.25}$$

which shows that the density is peaked at $x = 0$ and goes to zero as $x \to \pm\infty$. This is why the Harris equilibrium is also called the Harris "sheath."

Appendix F

ONE-DIMENSIONAL AND TWO-DIMENSIONAL MAXWELL-JÜTTNER DISTRIBUTIONS AND THE DISTRIBUTION OF ξ

F.1 Derivation of $f_{\rho_\perp}$

In cylindrical coordinates, Eq. 6.18 is equivalent to

$$f_{\boldsymbol{\rho}} d^3\boldsymbol{\rho} = \frac{1}{4\pi\theta K_2(1/\theta)} \exp\left(-\frac{\sqrt{1+\rho^2}}{\theta}\right) \rho_\perp d\rho_\perp d\phi d\rho_z. \tag{F.1}$$

Integrating in ρ_z gives

$$\int_{\rho_z=-\infty}^{\infty} f_{\boldsymbol{\rho}} \rho_\perp d\rho_\perp d\phi d\rho_z = \int_{\rho_z=-\infty}^{\infty} \frac{1}{4\pi\theta K_2(1/\theta)} \exp\left(-\frac{\sqrt{1+\rho_\perp^2+\rho_z^2}}{\theta}\right) \rho_\perp d\rho_\perp d\phi d\rho_z \tag{F.2}$$

$$= \rho_\perp d\rho_\perp d\phi \int_{\rho_z=0}^{\infty} \frac{1}{2\pi\theta K_2(1/\theta)} \exp\left(-\frac{\sqrt{1+\rho_\perp^2+\rho_z^2}}{\theta}\right) d\rho_z, \tag{F.3}$$

where $\rho^2 = \rho_\perp^2 + \rho_z^2$. Defining

$$a^2 = \frac{1+\rho_\perp^2}{\theta^2} \tag{F.4}$$

and

$$t = \frac{\rho_z}{\theta}, \tag{F.5}$$

the ρ_z-integral in Eq. F.3 becomes

$$\frac{1}{2\pi K_2(1/\theta)} \int_0^\infty \exp\left(-\sqrt{a^2+t^2}\right) dt. \tag{F.6}$$

Now we define

$$t = a \sinh z, \tag{F.7}$$

so $\sqrt{a^2+t^2} = a\sqrt{1+\sinh^2 z} = a\cosh z$ and $dt = a\cosh z dz$. Equation F.6 is now

$$\frac{a}{2\pi K_2(1/\theta)} \int_0^\infty \cosh z \exp(-a\cosh z)\, dz. \tag{F.8}$$

The z-integral in Eq. F.8 evaluates to $K_1(a)$ where K_n is the modified Bessel function of the second kind of order n [176, Section 8.432, 1.].

Therefore, Eq. F.3 is now

$$\frac{\sqrt{1+\rho_\perp^2}}{2\pi\theta K_2(1/\theta)} K_1\left(\frac{\sqrt{1+\rho_\perp^2}}{\theta}\right)\rho_\perp d\rho_\perp d\phi. \tag{F.9}$$

Integrating in ϕ yields the final result:

$$f_{\rho_\perp} d\rho_\perp = \frac{\rho_\perp\sqrt{1+\rho_\perp^2}}{\theta K_2(1/\theta)} K_1\left(\frac{\sqrt{1+\rho_\perp^2}}{\theta}\right) d\rho_\perp, \tag{F.10}$$

which is Eq. 6.19.

F.2 Derivation of f_{ρ_z}

In cylindrical coordinates, Eq. 6.18 is equivalent to

$$f_{\boldsymbol{\rho}} d^3\boldsymbol{\rho} = \frac{1}{4\pi\theta K_2(1/\theta)} \exp\left(-\frac{\sqrt{1+\rho^2}}{\theta}\right)\rho_\perp d\rho_\perp d\phi d\rho_z. \tag{F.11}$$

Integrating in all ϕ and $\rho_\perp$, Eq. F.11 becomes

$$f_{\rho_z} d\rho_z = \int_{\rho_\perp=0}^{\infty} \frac{1}{2\theta K_2(1/\theta)} \exp\left(-\frac{\sqrt{1+\rho_\perp^2+\rho_z^2}}{\theta}\right)\rho_\perp d\rho_\perp d\rho_z. \tag{F.12}$$

Letting $\eta^2 = 1+\rho_\perp^2+\rho_z^2$ while keeping ρ_z constant so that

$$\eta d\eta = \rho_\perp d\rho_\perp, \tag{F.13}$$

we have

$$f_{\rho_z} d\rho_z = \int_{\eta=\sqrt{1+\rho_z^2}}^{\infty} \frac{1}{2\theta K_2(1/\theta)} \exp\left(-\frac{\eta}{\theta}\right)\eta d\eta d\rho_z. \tag{F.14}$$

Using the integral formula [176, Section 3.351, 2.]

$$\int_u^\infty x^n e^{-\mu x} dx = e^{-u\mu}\sum_{k=0}^{n}\frac{n!}{k!}\frac{u^k}{\mu^{n-k+1}}, \tag{F.15}$$

where $x = \eta$, $u = \sqrt{1+\rho_z^2}$, $\mu = 1/\theta$, and $n = 1$ in this case, we have

$$f_{\rho_z} d\rho_z = \frac{1}{2\theta K_2(1/\theta)} \left(\theta^2 + \theta\sqrt{1+\rho_z^2}\right) \exp\left(-\frac{\sqrt{1+\rho_z^2}}{\theta}\right), \tag{F.16}$$

$$= \frac{\theta}{2K_2(1/\theta)} \left(1 + \frac{\sqrt{1+\rho_z^2}}{\theta}\right) \exp\left(-\frac{\sqrt{1+\rho_z^2}}{\theta}\right), \tag{F.17}$$

which is Eq. 6.20.

F.3 Derivation of f_ξ

ξ is defined as

$$\xi = 1 + \alpha\left(n\rho_z - \gamma\right) = 1 + \alpha\zeta, \tag{F.18}$$

where $\zeta = n\rho_z - \gamma$.

f_ζ will first be derived. Defining $R = n\rho_z$ (so $d\rho_z = dR/n$ and $\zeta = R - \gamma$), we have

$$f_{\rho_z}(\rho_z) d\rho_z = f_{\rho_z}\left(R/n\right) \frac{dR}{n} \tag{F.19}$$

$$= \frac{\theta}{2nK_2\left(1/\theta\right)} \left(1 + \frac{\sqrt{1+R^2/n^2}}{\theta}\right) \exp\left(-\frac{\sqrt{1+R^2/n^2}}{\theta}\right) dR \tag{F.20}$$

$$= f_R(R) dR. \tag{F.21}$$

Now, in order for $\zeta = R - \gamma$ to be true, the value of R has to equal $\zeta + \gamma$ for a given value of γ. The probability distribution of this occurrence integrated over all values of γ gives f_ζ:

$$f_\zeta(\zeta) = \int_1^\infty f_\gamma\left(\gamma\right) f_R\left(\zeta + \gamma\right) d\gamma \tag{F.22}$$

$$= \int_1^\infty \frac{\gamma^2\sqrt{1-1/\gamma^2}}{2nK_2^2\left(1/\theta\right)} \left(1 + \frac{\sqrt{1+\left(\zeta+\gamma\right)^2/n^2}}{\theta}\right) \exp\left(-\frac{\gamma + \sqrt{1+\left(\zeta+\gamma\right)^2/n^2}}{\theta}\right) d\gamma. \tag{F.23}$$

Finally, rearranging Eq. F.18 yields $\zeta\left(\xi\right) = \left(\xi - 1\right)/\alpha$ so that $d\zeta = d\xi/\alpha$. It follows

that

$$f_\zeta(\zeta)d\zeta = f_\zeta\left([\xi-1]/\alpha\right)\frac{d\xi}{\alpha} \tag{F.24}$$

$$= \int_1^\infty \frac{\gamma^2\sqrt{1-1/\gamma^2}}{2\alpha n K_2^2\left(1/\theta\right)}\left(1+\frac{\sqrt{1+\left(\zeta\left(\xi\right)+\gamma\right)^2/n^2}}{\theta}\right)\exp\left(-\frac{\gamma+\sqrt{1+\left(\zeta\left(\xi\right)+\gamma\right)^2/n^2}}{\theta}\right)d\gamma d\xi \tag{F.25}$$

$$= f_\xi(\xi)d\xi. \tag{F.26}$$

Writing $\rho_z\left(\gamma,\xi\right) = \left(\zeta\left(\xi\right)+\gamma\right)/n$ yields a more compact expression:

$$f_\xi(\xi) = \int_1^\infty \frac{\gamma^2\sqrt{1-1/\gamma^2}}{2\alpha n K_2^2\left(1/\theta\right)}\left(1+\frac{\sqrt{1+\rho_z^2\left(\gamma,\xi\right)}}{\theta}\right)\exp\left(-\frac{\gamma+\sqrt{1+\rho_z^2\left(\gamma,\xi\right)}}{\theta}\right)d\gamma, \tag{F.27}$$

which is Eq. 6.22.

F.4 Derivation of non-relativistic $f_{\rho_\perp}$

From Eq. F.10,

$$f_{\rho_\perp} = \frac{\rho_\perp\sqrt{1+\rho_\perp^2}}{\theta K_2\left(1/\theta\right)}K_1\left(\frac{\sqrt{1+\rho_\perp^2}}{\theta}\right). \tag{F.28}$$

For $\rho_\perp \ll 1$,

$$\sqrt{1+\rho_\perp^2} \simeq 1+\frac{\rho_\perp^2}{2}. \tag{F.29}$$

For $\theta \ll 1$, it is seen that [160, Section 7.23]

$$K_2\left(1/\theta\right) \simeq \sqrt{\frac{\pi\theta}{2}}e^{-1/\theta}, \tag{F.30}$$

and for small $\theta \ll 1$ and $\rho_\perp \ll 1$,

$$K_1\left(\frac{\sqrt{1+\rho_\perp^2}}{\theta}\right) \simeq K_1\left(\frac{1}{\theta}+\frac{\rho_\perp^2}{2\theta}\right) \tag{F.31}$$

$$\simeq \sqrt{\frac{\pi\theta}{2+\rho_\perp^2}}\exp\left(-\frac{1}{\theta}-\frac{\rho_\perp^2}{2\theta}\right), \tag{F.32}$$

so to lowest order,

$$f_{\rho_\perp} \simeq \frac{\rho_\perp}{\theta}\sqrt{1+\frac{\rho_\perp^2}{2}}\exp\left(-\frac{\rho_\perp^2}{2\theta}\right) \tag{F.33}$$

$$\simeq \frac{\rho_\perp}{\theta}\exp\left(-\frac{\rho_\perp^2}{2\theta}\right). \tag{F.34}$$

The most likely $\rho_\perp$ value given this probability distribution function is

$$\rho_{\perp,\mathrm{ML}} = \sqrt{\theta}. \tag{F.35}$$